The relationship between supergranulation flows, magnetic field evolution and network flares

Von der Fakultät für Elektrotechnik, Informationstechnik, Physik
der Technischen Universität Carolo-Wilhelmina zu Braunschweig

zur Erlangung des Grades eines
Doktors der Naturwissenschaften (Dr. rer. nat.)

genehmigte Dissertation

von Raphael Attie

aus Bayonne, Frankreich

eingereicht am: 10.09.2014

Disputation am: 08.01.2015

1. Referentin oder Referent: Prof. Dr. Sami K. Solanki
2. Referentin oder Referent: Prof. Dr. Karl-Heinz Glaßmeier

Druckjahr: 2015

Bibliografische Information der Deutschen Nationalbibliothek

Die Deutsche Nationalbibliothek verzeichnet diese Publikation in der Deutschen Nationalbibliografie; detaillierte bibliografische Daten sind im Internet über `http://dnb.d-nb.de` abrufbar.

Dissertation an der Technischen Universität Braunschweig,
Fakultät für Elektrotechnik, Informationstechnik, Physik

ISBN 978-3-944072-09-8

uni-edition GmbH 2015
http://www.uni-edition.de

Printed in Germany

Publications and presentations

Publications

Attie, R., Innes, D., 2008, Explosive Event in the Quiet Sun Seen by XRT-EIS and SUMER, in First Results From Hinode, (Eds.) S. A. Matthews, J. M. Davis, L. K. Harra, vol. 397 of Astronomical Society of the Pacific Conference Series, pp. 155

Innes, D. E., Attie, R., Hara, H., Madjarska, M. S., 2008, EIS/ Hinode Observations of Doppler Flow Seen through the 40 arcsec Wide-Slit, Sol. Phys., 252, 283-292

Attie, R., Innes, D. E., Potts, H. E., 2009, Evidence of photospheric vortex flows at super- granular junctions observed by FG/SOT (Hinode), A&A, 493, L13-L16

Innes, D. E., Genetelli, A., Attie, R., Potts, H. E., 2009, Quiet Sun mini-coronal mass ejections activated by supergranular flows, A&A, 495, 319-323

Attie, R., Innes, D. E., 2014, Magnetic Balltracking: tracking the photospheric magnetic flux, A&A (submitted)

Oral presentations and posters

Attie, R., Innes, D., Explosive Event in the Quiet Sun Seen by XRT-EIS and SUMER, First Results From Hinode, Trinity College, Dublin, Ireland, August 20-24, 2007. (Poster)

Attie, R., Innes, D., Coronal Heating by Small Scale Eruptive Events on Quiet sun Investigated By Coaligned Observations From Soho and Hinode, AGU Fall Meeting, San Francisco, USA, Dec. 10-14, 2007. (Poster)

Attie, R., Innes, D., Explosive Events in the Not-so-quiet Sun: The Hinode View, 12th European Solar Physics Meeting, Freiburg, Germany, September, 8-12, 2008 (oral)

Attie, R., Innes, D., Coronal Heating from Not-so-quiet-Sun Explosive Events, Second Hinode Science Meeting, Boulder, Colorado, USA, Sep. 29 - Oct. 3, 2008 (oral)

Attie, R., Innes, D., Potts, H., Soft X-ray Emission in the Quiet Sun Related to Magnetic Reconnection, 38th COSPAR Scientific Assembly, Bremen, Germany, July 15-18, 2010 (oral)

Attie, R., Innes, D., Predicting the All Clear: New perspectives from SoHO-Hinode-Stereo observations, Prospects for surveys with SDO, All Clear Workshop, April 22-24, 2009, NCAR, Boulder, Colorado, USA (oral)

Attie, R. Potts, H., Innes, D. Tracking flow fields and magnetic flux with the SDO/HMI pipeline, Solar Image Processing Workshop V, Sep. 12-16, 2010, Les Diablerets, Switzerland (oral)

Contents

Summary **9**

1 Introduction **11**

1.1 The photospheric flows 11
  1.1.1 Multi-scale convection: from granulation to supergranulation . . . 11
  1.1.2 Measuring the plasma flows 12
1.2 Photospheric magnetic field 13

2 Methods for analyzing photospheric observations **15**

2.1 Local Correlation Tracking 15
2.2 Balltracking: an efficient way to track the photospheric flows 17
  2.2.1 In a nutshell 17
  2.2.2 Phase 1: rescaling 2D images into 3D surfaces 19
  2.2.3 Phase 2: main tracking phase 19
  2.2.4 Phase 3: filling the gaps 26
  2.2.5 Phase 4: calibration of the velocity field 32
2.3 Error analysis 33
  2.3.1 Effects of the input parameters 33
  2.3.2 Random error due to sampling limitations 38
2.4 Advantages of Balltracking with respect to LCT 41
2.5 Physical validation examples 43
  2.5.1 Limitations for using the divergence and vorticity fields 45
  2.5.2 Extracting the boundaries of the convection cells 46
  2.5.3 Variability of the supergranular flows 50
  2.5.4 Comparison with the magnetograms 50
2.6 Magnetic Balltracking: tracking the photospheric magnetic flux 51
  2.6.1 Phase 1: preprocessing of the magnetograms 52
  2.6.2 Phase 2: initialization 53
  2.6.3 Phase 3: main tracking phase 53
  2.6.4 Phase 4: detection of emerging flux 58
  2.6.5 Primary application: segmentation of the magnetic features . . . 60

2.6.6 Secondary application: tracking magnetic field-lines 63
2.7 Summary 64

3 Practical applications on case studies 67
3.1 Balltracking on granulation 67
3.1.1 Observations 67
3.1.2 Results 69
3.1.3 Discussion 71
3.2 Magnetic Balltracking on flux emergence 76
3.2.1 Observation of flux emergence 76
3.2.2 Detection and quantification 78
3.2.3 About the thresholding 80
3.3 User-friendly software for Balltracking and Magnetic Balltracking 80
3.4 Summary 82

4 Soft-X-ray emission related to photospheric flows and coronal magnetic field 83
4.1 Multi-instrument observations 83
4.2 Protocol for near 1-arcsec co-alignment 84
4.2.1 Registration of MDI data 88
4.2.2 Registration of BFI/SOT dataset 88
4.2.3 Co-alignment of NFI/SOT with MDI high-res. 91
4.2.4 Co-alignment of NFI magnetograms with the Blue continuum images from BFI 94
4.2.5 Co-alignment of the SoHO and Hinode data 97
4.2.6 Overall co-alignment 97
4.3 Calibration of the magnetograms from NFI/SOT 97
4.3.1 Rejection of artifacts 99
4.3.2 Least-squares fits 99
4.4 Flows, magnetic field, and X-ray emission 102
4.4.1 Detection of X-ray transients 102
4.4.2 Transients in MDI-XRT FOV 105
4.4.3 Transients in SOT-XRT FOV 105
4.4.4 Energy of the X-ray transients 118

5 Discussion 127
5.1 Converging flux model 127
5.1.1 Definition of the model parameters 129
5.1.2 Results 130
5.1.3 Comparisons of E_{th} and W_{free} 131
5.2 Effect of the funnels and the vortices 131

5.2.1 Shearing motions 131
5.2.2 Large-scale vortices and funnels 134
5.3 Qualitative model of X-ray network flares 135
5.3.1 Magnetic field configuration 135
5.3.2 Model of X-ray network flares 136
5.4 Prospects for future studies 138
5.4.1 Quiet Sun 138
5.4.2 Active Regions and large scale dynamics 139

6 Conclusion **141**

A Zeeman effect and measurement of photospheric magnetic field **143**

B Object-oriented implementation of the Balltracking algorithms **147**
B.1 GUI for Balltracking 147
B.2 GUI for Magnetic Balltracking 148
B.2.1 module of Magnetic Balltracking and region-growing algorithm . 148
B.2.2 Module for field-lines tracking 149
B.2.3 Computing power 150

Bibliography **153**

Acknowledgements **158**

Curriculum Vitae **160**

Summary

The quiet Sun may be the biggest laboratory to isolate and study physical elementary processes of fundamental importance to space plasma. The advantage is the continuous availability of small-scale events, carrying the micro-physics that is responsible for but often hidden in larger-scale phenomena. By small-scale events, we mean spatial dimensions of a few Mm at most, and durations of less than an hour.

The work presented here is an attempt to describe and understand the coupling between the photospheric flows, the photospheric magnetic flux, and small-scale energetic transient events. The latter are observed in soft X-Ray, have an intensity of at least 1 order of magnitude above the background level, and occur high up in the quiet Sun atmosphere. After a brief introduction on photospheric observations in Chapter 1, Chapter 2 describes new numerical methods to analyze them. These methods are summarized as followed:

- We adapted a highly efficient numerical method, called Balltracking, to derive the photospheric flows from images of the granulation. The method is described in detail and is compared to other algorithms.

- To study the dynamics of magnetic flux, and more precisely, its cancellation at relevant sites, we developed a new tool called "Magnetic Balltracking", similar to the Balltracking algorithm, to track and tag the photospheric magnetic elements present in high-resolution magnetograms of both SoHO and Hinode. The algorithm can detect and measure flux emergence and flux cancellation. It can also be applied to track magnetic field lines in the framework of magnetic field extrapolation.

We present the main results of these new methods in Chapter 3:

- The balltracking algorithm is applied to observations in the blue continuum from the Solar Optical Telescope (SOT) of Hinode. We reveal the existence of large-scale photospheric vortex flows at the junctions of the supergranular lanes. Typical sizes are 20 Mm in diameter, and last for a duration of at least 30 min, up to several hours.

- Applications of Magnetic Balltracking are shown on magnetograms from both SoHO and Hinode, at high resolution (below 1 arcsec). An example of detection and quantification of flux emergence is also presented, in combination with co-spatial observations of soft X-ray loops associated with the emergence.

In Chapter 4, the Balltracking and Magnetic Balltracking are used in a multi-instrument study, to analyze the triggering mechanism of small-scale X-ray network flares.

- Co-spatial and co-temporal observations in soft X-rays are used to identify transient events in the low-corona. A total of 5 instruments (MDI and EIT from SoHO, SOT-NFI, SOT-BFI, XRT from Hinode) and 7 independent datasets are involved in the co-alignment. We present a detailed protocol on how all the datasets must be co-aligned to an accuracy near 1 arcsec.
- With XRT, we identified several small-scale X-ray network flares. The energy released by these transient events ranges within $10^{24} - 10^{26}$ erg in a few minutes. 5 cases are analyzed in detail, and the conclusions are extended to the 11 most intense events in a 4-hours time series, within an area of ~1/8 the solar disk.
- Balltracking and Magnetic Balltracking are used to investigate what triggers the network flares. Balltracking directly relates the flows with cancelling longitudinal magnetic flux, while the cancelling flux is tracked and quantified with Magnetic Balltracking. The cancellation is viewed as a result of magnetic reconnection. The amount of longitudinal flux that has cancelled at the onset of the transient X-ray events ranges from 10% to 40%. Illustrative magnetic field extrapolations show possible field configurations and their relationships with the hot plasma released in the low corona.

From this study, we identify two patterns of the horizontal flows that act as catalysts for efficient magnetic reconnection, and appear as a necessary-but-not-sufficient condition in triggering X-ray network flares:

- The first pattern has funnel-shaped streamlines of the horizontal flow in which the magnetic flux is carried. Magnetic flux of opposite polarities move together and inevitably reconnect. These horizontal funnels form in the network, usually along supergranular lanes and end up at their intersection.
- The second pattern has large-scale vortices at the intersection of the network lanes, in which distant magnetic features of opposite polarities are sucked in and ultimately cancel. As the flux is swept in, it gets easily stressed, which explains the higher energy released at these sites.

Finally, these results are discussed in Chapter 5:
The photospheric flows are usually pictured as acting randomly on the field until it reaches a topology that can ignite an energy burst. Our new conclusions are confronted with existing models and, instead, emphasize that the identified flow patterns fulfill specific conditions when carrying the magnetic field, which makes the energy release more efficient. While we have performed this analysis in soft X-ray, similar work has been done in EUV using lower-resolution instrumentation, and revealing small-scale CME-like eruptions, all over the quiet Sun. It seems possible that the network flares observed so far may be the X-ray counterpart of these EUV events. Statistical studies on the Solar Dynamic Observatory (SDO) are under investigation to test this hypothesis.

1 Introduction

1.1 The photospheric flows

1.1.1 Multi-scale convection: from granulation to supergranulation

The photosphere of the quiet Sun is easily identified by the presence of small convection cells, called "granules" or "granulation" (Fig.1.1). They are the result of a radiative-convective process in the solar upper convection zone. Stein and Nordlund (1989) established the first consistent model. The granulation rises from the ascension of plasma in the density-stratified convection zone, where regions of higher temperatures have a larger pressure scale height. When buoyant parcels of plasma ascend in the convection zone, their higher pressure forces them to expand horizontally. This horizontal expansion is blocked or deflected by the growth of neighboring convection cells. The radiative energy loss makes the plasma overturn at the edge of the cells, where downflows are observed. The granule is the idealized concept of this ascending and overturning parcel of fluid. Temperature gradients from the center to the edge of the convection cells make the center of the cells brighter in white light continuum than the edge. The latter are the so-called "intergranular" lanes and appear darker.

The granules are dynamic objects in constant renewal. They move, grow, shrink, and sometimes explode. The average velocity of these motions is $\sim$800 m s^{-1} (Roudier et al. 1999), and they can even be supersonic or close to it. They have a typical size of $\sim$1 Mm and a typical lifetime of $\sim$6 min, that can last up to 20 min.

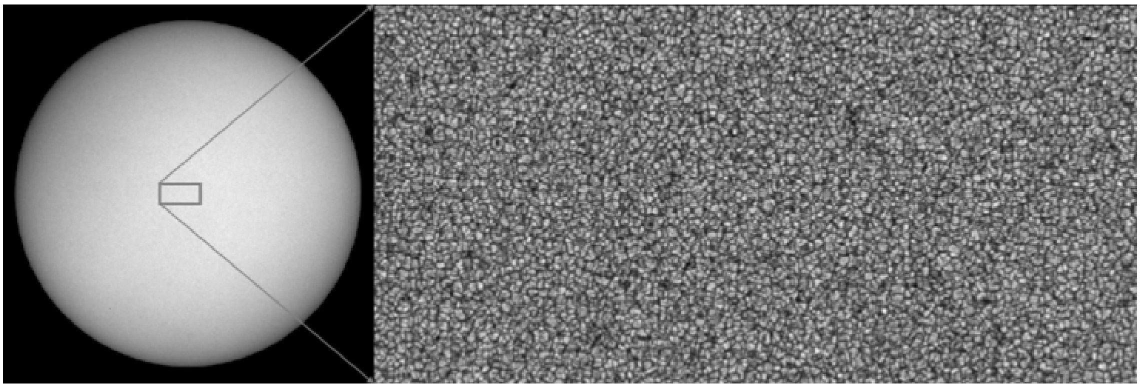

Figure 1.1: White light continuum image of the solar photosphere taken with MDI/SoHO, with a close-up taken at higher resolution by SOT/Hinode. The latter shows the granulation.

In addition to the granulation, the photospheric convection also exists at larger scales. Between 5 to 10 Mm, the mesogranulation was revealed by measuring the time-averaged velocity field (~60 $\mathrm{m\,s^{-1}}$ on average), with a minimum lifetime of 2 hr (November et al. 1981). At even greater scales, about 10 to 50 Mm, the "supergranulation" was reported with a much greater lifetime of up to 2 days (Leighton et al. 1962), and horizontal velocity up to a few hundred $\mathrm{m\,s^{-1}}$. Contrary to granules, mesogranules and supergranules are not directly visible in photospheric images, and their existence is revealed in time-averaged flow fields, and more indirectly on time-averaged observations of the solar magnetic field (magnetograms). They are both believed to rise at deeper layers in the convection zone (Stein and Nordlund 1989). Several convection theories are focusing on the supergranulation as a genuine convective process (Simon and Weiss 1968, Vickers 1971, van der Borght 1979, Gierasch 1985). However, the actual origin of mesogranulation and supergranulation is still under debate. Indeed, mesogranulation is also thought of as an intrinsic property of the granulation, and not a true scale of solar convection (Rieutord et al. 2000), while supergranulation is believed to be caused by prograde waves with 6-9 days-period (Gizon et al. 2003). A common origin of both mesogranulation and supergranulation was proposed in a simplified model by Rast (2003), by considering the advection of small-scale granular downflow plumes (Rast 1995). Using an N-body simulation, it was shown that the collective interaction of the downflow plumes give rise to specific convection scales, comparable to mesogranulation and supergranulation. Thus the theories up till now are quite contradictory, and understanding the multi-scale solar convection is still a great challenge.

In our framework, the supergranular flows are studied with particular attention, as they are closely related to the magnetic field in the quiet Sun. Analyses of the photospheric flows are used to study the coupling between the plasma motions and the magnetic field. Indeed, as it will be shown in this thesis, this coupling often occurs at the footpoints of relatively energetic releases of energy observed high up in the solar atmosphere.

1.1.2 Measuring the plasma flows

By using time series of images in white light, individual granules can easily be resolved over a wide FOV and it is possible to measure an average "plane-of-sky" component of the velocity field (in the plane of the CCD) by tracking the granular pattern. Near disk center, effects of spherical projection become negligible and the plane-of-sky component of these motions approximates to the horizontal component. Doppler shifts from photospheric spectral lines can provide the vertical component of the photospheric flows (Leighton et al. 1962). However, here, we concentrate on the horizontal flows. From now on, unless stated otherwise, any mention of the photospheric flows will imply its horizontal component.

The first assumption in tracking photospheric flows is to consider the granules as tracers of the velocity field on top of which they are constantly flowing. Due to the very dynamic evolution of the granules (growing, shrinking, colliding, exploding), granules have intrinsic stochastic motions. For this reason, they introduce random errors in the velocity field. As mentioned earlier, photospheric flows exist at different temporal, and geometrical scales. Supergranules have a lifetime of up to 2 days and sizes of up to

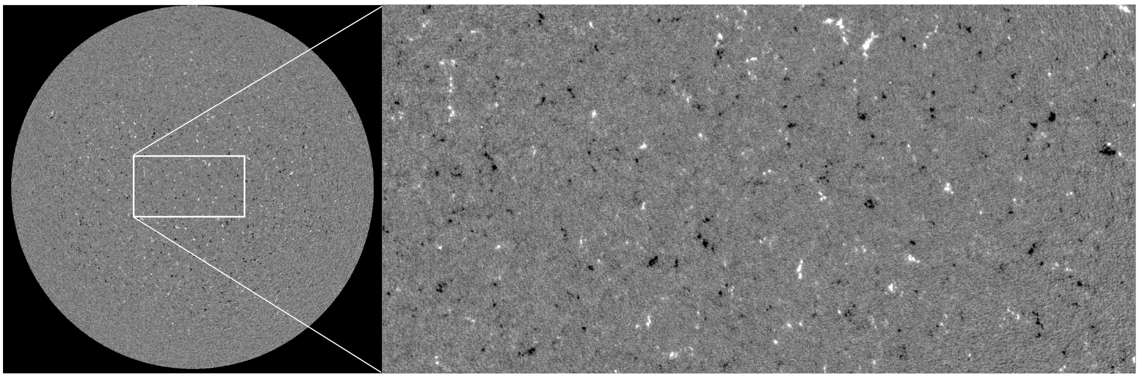

Figure 1.2: *Magnetogram from MDI/SoHO. Full-disk (left) and at higher-resolution (right). The black and white intensity correspond to opposite polarities of the longitudinal magnetic field*

50 Mm. Typical mean velocities are about 400 m s^{-1}. Thus by tracking faster-evolving granules only 1 Mm wide, with an average lifetime of ~6 min, it is a priori difficult to reveal the supergranulation as it stays "hidden" within the granulation. Therefore time averaging and spatial smoothing of the data are necessary to bring out the supergranular scales of the flow. In addition, based on simulated velocity fields of granular motions, Rieutord et al. (2001) found out that the granules become reliable tracers of the velocity field only if their motions are averaged over at least 2.5 Mm, and on temporal scales of at least 30 min. These are theoretical thresholds that we use as lower limits of the smoothing and of the averaging of the velocity fields. Below these thresholds, the velocity still contains too much of the stochastic motions of the granules, and it would not yield the velocity field above which they evolve. For an exhaustive review on measurements and theories of the Sun's supergranulation, we refer to Rieutord and Rincon (2010).

1.2 Photospheric magnetic field

Measurements of the solar magnetic field are routine in the photosphere and it can also be measured in the chromosphere. In the quiet Sun, where granules are observed, the weakest magnetic elements have a field strength of the order of a few 10^{-1} mT – 1 mT, and a lifetime of the order of few minutes up to several hours. These values, however, are subject to instrumental selection. More details can be found in Stenflo et al. (1998), Emonet and Cattaneo (2001). The coronal magnetic field can be measured locally, but more global estimates of the coronal magnetic field vector are mostly obtained by indirect estimates and extrapolation of the photospheric magnetic field. See for example Thalmann (2010).

In this study we are using magnetograms. They are obtained from direct measurements of the polarimetric signal of the photospheric radiation, and only provide the observer with the line-of-sight (LOS) component of the magnetic field, also referred to as the longitudinal component. The Zeeman splitting is computed from the line shift of left and right circularly polarized light, using the Stokes parameters V and I. A brief development of the Zeeman effect is given in the appendix A. More detailed descriptions can be found in Stix (1989), del Toro Iniesta (2003) and Condon and Shortley (1963). In the present thesis, we use the magnetograms of the Michelson Doppler Imager (MDI) onboard SoHO

(Scherrer et al. 1995) (Fig.1.2), and of the Narrow-band-Filter Imager (NFI) of the Solar Optical Telescope (SOT) onboard Hinode (Tsuneta et al. 2008).

The present thesis focuses on analyzing the relationships between the photospheric flows, the magnetic field and eruptive events outside active regions, in the so-called "quiet Sun". To do so, we have adapted an existing algorithm to measure the photospheric flows, and we developed a new algorithm to track the magnetic flux. They are presented in Chapters 2 and 3. In Chapter 4, we use these algorithms in a multi-instrument analysis of small eruptive events observed in soft-X-ray. The results are discussed in Chapter 5.

2 Methods for analyzing photospheric observations

Different techniques and algorithms are used to derive the photospheric flows by tracking the motions of granules, such as the Local Correlation Tracking (LCT) originally developed by November and Simon (1988), the Coherent Structure Tracking (Roudier et al. 1999), and the "Balltracking" (Potts et al. 2004). In Section 2.1 and 2.2, we present two of them, the "Local Correlation Tracking" (LCT)", and the "Balltracking", with a special emphasis on the latter which was chosen for the present thesis. In Section 2.3 we carry out an error analysis of the Balltracking, followed by a description of its computational advantages in Section 2.4. Section 2.5 presents a qualitative validation of our version of the code. In the last section, we present a new technique of our own, designed to track the magnetic flux from the magnetograms, called "Magnetic Balltracking".

2.1 Local Correlation Tracking

One of the first algorithms that were used to track the motions of granules is Local Correlation Tracking (LCT) developed by November and Simon (1988).

It consists in calculating the correlation of small parts of images within a time series. These small parts are like "tracking windows" or "tracking areas" (Fig.2.1). The algorithm takes the intensity in these tracking areas as the random variable X. X_j^1 is a specific value of X for the j^{th} pixel in the first image. X_{j+k}^2 is the intensity at the $j+k^{th}$ pixel of the second image. If the mean intensity of the selected part of an image f is $\overline{X^f}$, with N pixels, its standard deviation is defined as:

$$\sigma_{X^f} = \sqrt{\frac{1}{N-1}\sum_{i=1}^{N}(X_i^f - \overline{X^f})^2} \tag{2.1}$$

The correlation between the selected part of image 1 and image 2 would then be :

$$R(k) = \frac{\sigma_{X^1X^2}}{\sigma_{X^1}\sigma_{X^2}} \tag{2.2}$$

More explicitly, it gives :

$$R(k) = \frac{\sum_{i=1}^{N}\left[(X_i^1 - \overline{X^1})(X_{i+k}^2 - \overline{X^2})\right]}{\sqrt{\sum_{i=1}^{N}(X_i^1 - \overline{X^1})^2}\sqrt{\sum_{i=1}^{N}(X_i^2 - \overline{X^2})^2}} \tag{2.3}$$

The local correlations are computed between image 1 and image 2, within several tracking areas, until it covers the whole image. In each area, the local correlation is recalculated for as many different pixel k (Eq.2.3) as necessary to cover the whole window. Fig.2.1 illustrates how they are used for the simple case of granules whose shape does not vary in time. For simplicity, the inter-granular space has been exaggerated, and we represent only iso-contours of granules and granules of equal intensity.

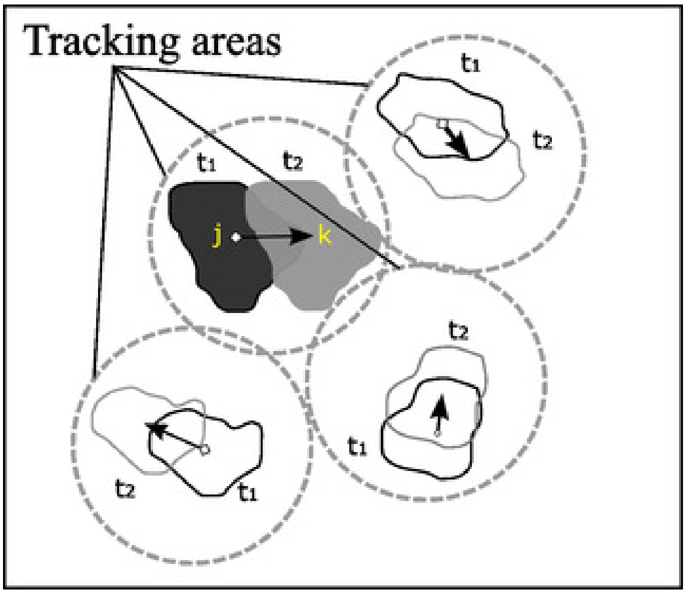

Figure 2.1: Illustration on how the tracking areas are set on images containing moving granules. t_1 and and t_2 are the time of respectively, image 1 and image 2. j and k in yellow, are the center of the granules at the respective times.

Next, we consider one tracking area. At t_1, the position of the center of a feature is the j^{th} pixel. At t_2, the feature has moved and its center is at the m^{th} pixel, with $1 \leq m \leq N$. In this case, the correlation coefficient is computed for $k = 1, ..., N$ and is maximum for $k = m$. The vector defined by the position of the j^{th} and the m^{th} pixel defines the displacement of the feature from the first to the second image. Dividing the displacement by the time difference, we derive the velocity vector. Doing the same for all the time series will give a time series of velocity fields. From Fig.2.1 one can see that the size of the tracking areas must be chosen carefully. If it is chosen too small, the displaced feature may fall outside the tracking area, or the noise gets too high to resolve any displacement. In either case, the algorithm eventually fails as the correlation $R(k)$ gets too low. If the window is chosen too large, the resolution of the velocity field will be degraded. In practice, some smoothing is applied to the data falling within the tracking window and several tests are sometimes necessary to set a reasonable size of the tracking windows. This can be a disadvantage with large data sets of hundreds or even thousands of images. In addition, with images from MDI/SoHO (Scherrer et al. 1995), the granules are not resolved as much as they need to be. This motivated Potts et al. (2004) to develop an alternate method called "Balltracking" which overcomes this limitation, and which we present in detail in the next section.

2.2 Balltracking: an efficient way to track the photospheric flows

2.2.1 In a nutshell

Compared to LCT, the Balltracking algorithm aims at handling the noise better, and at improving the computing time for large data sets (Potts et al. 2004). This algorithm considers the intensity of the images as a geometrical height. The granules become tridimensional geometrical tracers, and define a constantly evolving carpet full of bumps, that could also be compared to an agitated sea.

Next, user-defined balls are dispatched on this surface. The initial depth at which the balls are dropped depends on the Signal-to-Noise ratio (S/N) and the contrast of the data. The balls are given a constant size, a mass, and damping characteristics are associated with the whole system. Within the 3D box, a user-defined gravity is set, and the balls obey an equation of motion, involving a numerical buoyancy, a gravity force (different from the solar gravity), and a damping force. The latter is mainly used for tuning the stability of the balls on noisy data. Each ball rests on several data points (pixels) in the image, and each data point (indexed as i) exerts an elementary buoyancy force. This force is radially oriented toward the ball center, and is acting on a submerged point at a known radial depth d_i. In what follows, the index i always refers to the i^{th} pixel among all the pixels over which the ball is floating. The three forces governing the motion of the balls can simply be expressed with the vectorial equation:

$$m\dot{\mathbf{v}} = \sum_i \mathbf{f}_i(d_i) - mg\mathbf{e_z} - \gamma\mathbf{v} \tag{2.4}$$

where $\mathbf{v}$ is the velocity of the ball, $\dot{\mathbf{v}}$ its time derivative, $\sum_i \mathbf{f}_i(d_i)$ is the sum over all the elementary buoyancy forces exerted by the data point at the i^{th} pixel. The user-defined gravity field g sets the maximum acceleration that a ball can possibly reach. It is oriented downward, in a 3D cartesian frame of reference where $\mathbf{e_z}$ is a unit vector pointing upward. γ is the damping coefficient. At this stage, $\mathbf{v}$ does not correspond to the velocity of the granules that the balls are meant to track. The general principle for deriving the velocity of the granules is sketched in Fig.2.2, where the forces and the integration of the position of one ball is represented across two consecutive images at the times t_1 and t_2. On this sketch, the velocity of a tracked granule (drawn as a blue wave moving from left to right) would be the difference between the final positions of the balls, after a few integration steps of Eq.2.4 in each image, $X^2_{\text{final}} - X^1_{\text{final}}$, divided by the time interval between two

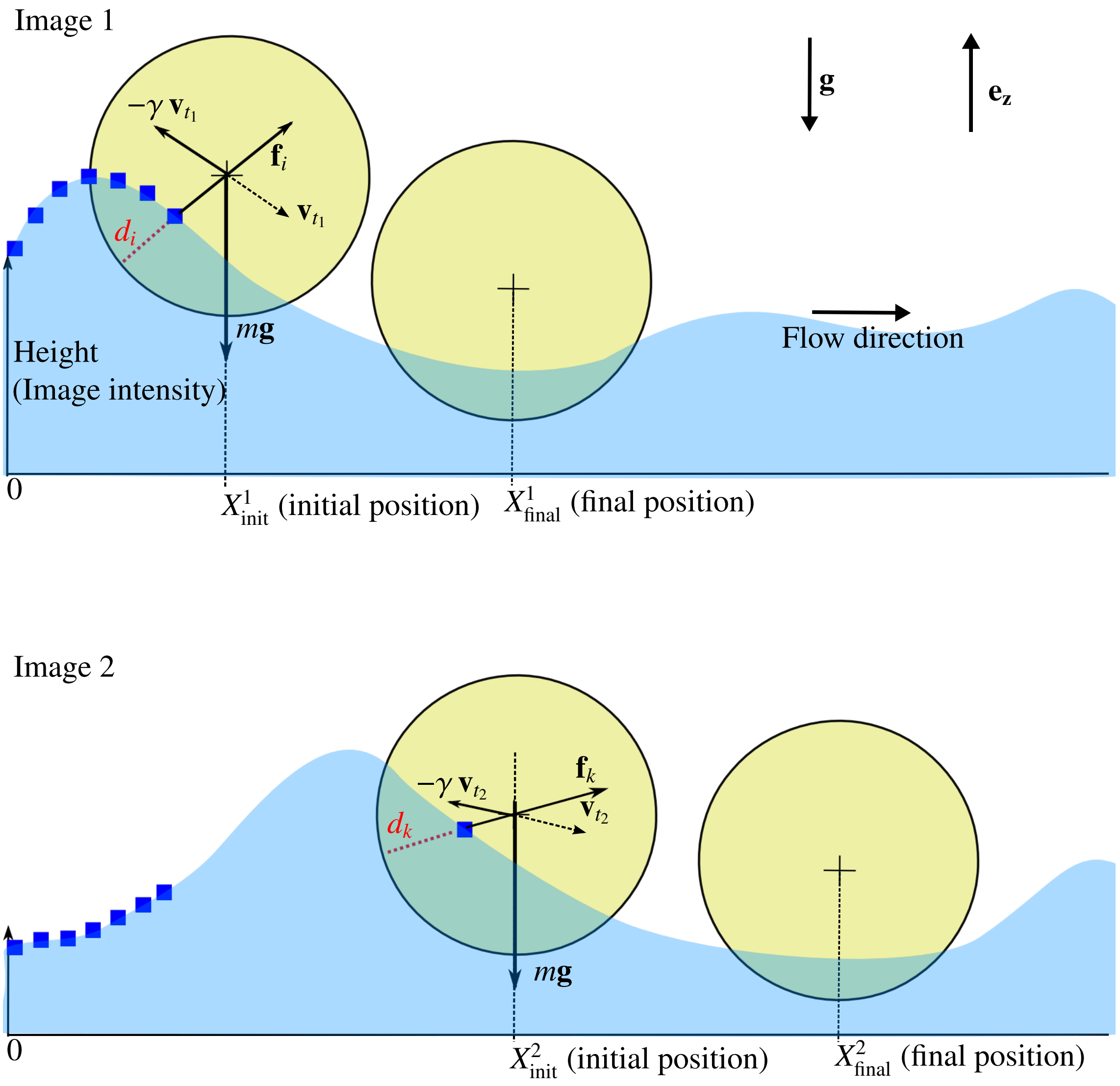

Figure 2.2: *General concept of the Balltracking algorithm for one ball. The ball, while floating on the data surface, is pushed by the granules, represented by the blue wave. The blue squares represent the pixels drawn at a height equal to the associated image intensity. Only a few of them are represented.*

consecutive frames.

In this thesis, the original algorithm defined in Potts et al. (2004) has been re-written, with further developments of our own, and with the help of its original authors. In the next four sections (§ 2.2.2 to § 2.2.5), we describe our version of the algorithm that we have divided in four main phases.

To clear out any semantic confusion in what follows, the words "image" and "frame" are used interchangeably: they both designate a two-dimensional map of scalar values, or of vector quantities.

2.2.2 Phase 1: rescaling 2D images into 3D surfaces

The intensity of the images of the granulation is given in Data Number units (DN units), and typically ranges over hundreds of DN. Since the balls are spheres designed to track circular tracers (the idealized granules), the conversion of the intensity into a vertical axis must be consistent with the horizontal dimensions of the granules. More precisely, the vertical amplitude obtained from the difference between the bright summits and the dark edges of the granules must be of the same order of magnitude as the average width of the granules (~1 Mm). This can be achieved easily by considering that the horizontal gradient of their emission is somewhat related to their spatial dimension. In the basic picture of radiative-convective phenomena, the convected hot material reaches the top of the convection cell before it cools by radiative loss and flows down to the edge. A two dimensional cut in the vertical plane would show a nearly circular pattern. Thus we consider that the vertical extension of this process is of the same order of magnitude as its horizontal extension. Potts et al. (2004) chose to set the vertical dimension as the intensity re-scaled by the standard deviation of the intensity of the image, which corresponds to the average deviation of the intensity from the mean of the image. The image may also be subtracted by its mean, in order to conveniently define the average surface level at an altitude of zero. Fig.2.3 shows this conversion. The upper panel contains the original and calibrated data from SOT/Hinode (Tsuneta et al. 2008), with a spatial light curve taken across the middle of the image. The amplitude of the intensity is spanning over hundreds of DN. The bottom panel shows the same data subtracted by the mean value of the intensity, and divided by the standard deviation $\sigma \approx 230$ DN. The re-scaled intensity now spans over a few times the standard deviation, and counted in units of the latter (σ-units) on Z-axis, which is here plotted with the same aspect radio as the X-axis (the geometric length of 1 px equals the geometric length of 1 σ). If we consider the maximum amplitude, the "tallest" features in the image are about 4 σ-high. In the images, the average width of the granules (1 Mm) corresponds to ~6 px, which makes this scaling very appropriate. Fig.2.4 presents the result of the conversion from the 2D image to the 3D surface, using Hinode data.

2.2.3 Phase 2: main tracking phase

Here we review the equations and geometry as used in the original algorithm from Potts et al. (2004). Some notations may vary to maintain consistency with other notations used throughout this thesis. Nonetheless, the final equations are equivalent to the ones at the end of the original paper (Potts et al. (2004), annex A.2, Eq.A.14). Since the algorithm is designed to track granules represented in 3D, a pre-requisite of the code is to know their geometrical characteristics in the images. From this geometry, the appropriate characteristics of the balls are defined, as well as the scaling parameters for Eq.2.4.

First, we need to define the buoyancy force $\mathbf{f}_i$, in a form consistent with the data. We consider one ball in equilibrium on a flat surface, floating at a maximum depth D_p as

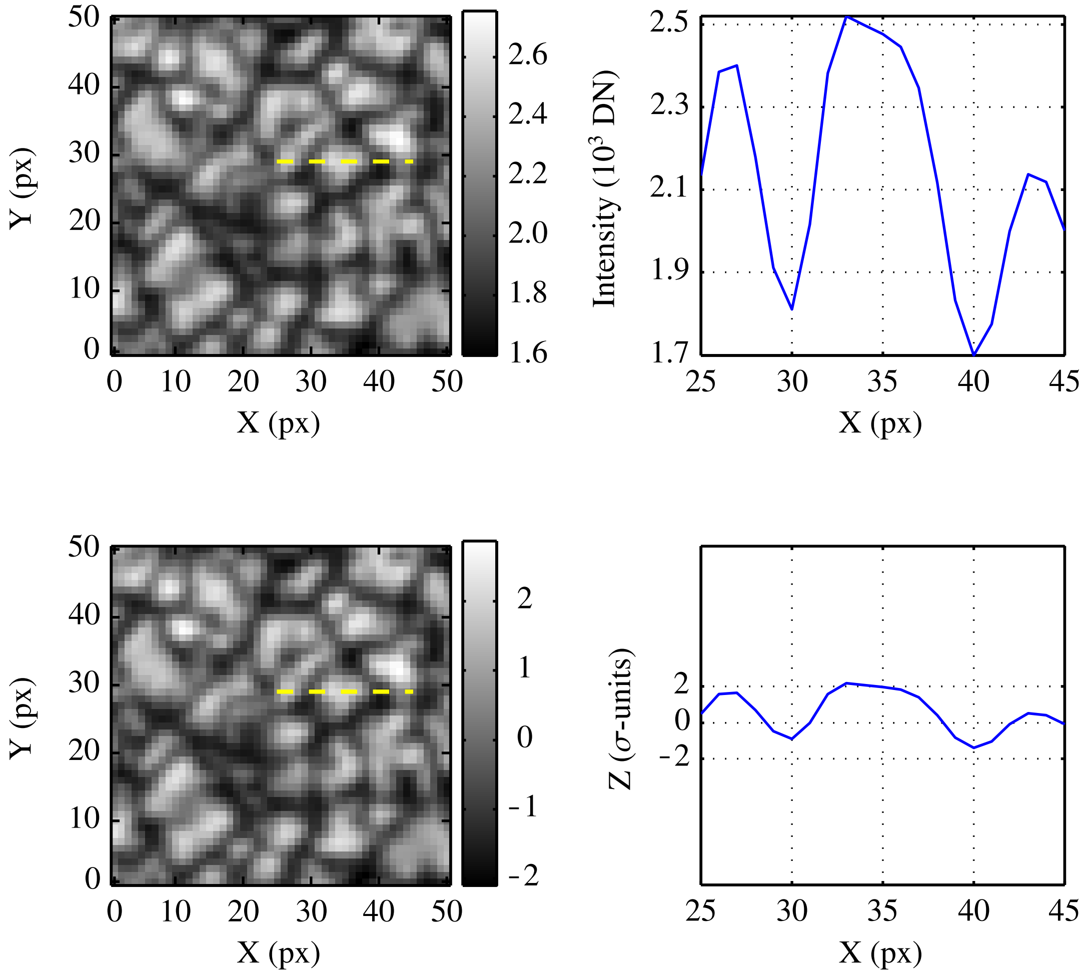

Figure 2.3: *Top: Original, non-scaled image (left) of the granulation taken by Hinode with a light curve (top right) taken across the x-axis (yellow lines on the left images). The units are Data Number (DN). Bottom: Same image subtracted by its mean, and scaled to its standard deviation* σ*. The intensity (bottom right) is spanning over a few times the standard deviation, and is considered as the vertical dimension Z.*

shown in Fig.2.5, in which we use the following definitions:

R_s : Sphere radius
D_p : Maximum penetration depth
$d_i(\theta)$: Radial penetration depth at pixel i
θ_w : Angle at surface piercing point
$A_i(\theta)$: Area of the spherical annulus (red) at radial depth $d_i(\theta)$
$f_i(\theta)$: arbitrary buoyancy force applied on the ball center due to the pressure forces applied on A_i

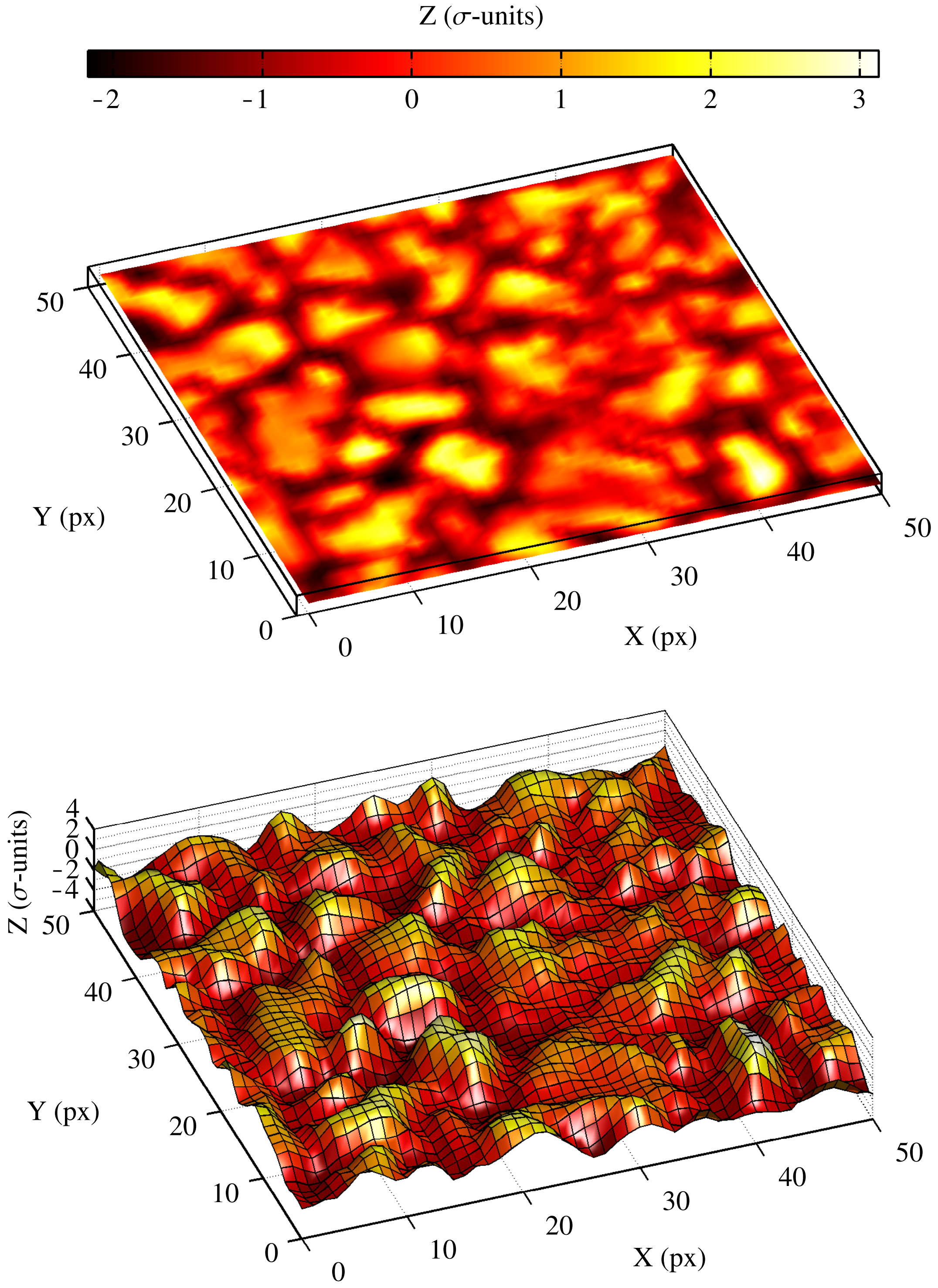

Figure 2.4: Preprocessing of the images before Balltracking. Top: 2D sample of an image of the granulation. Bottom: Same sample converted to a 3D surface.

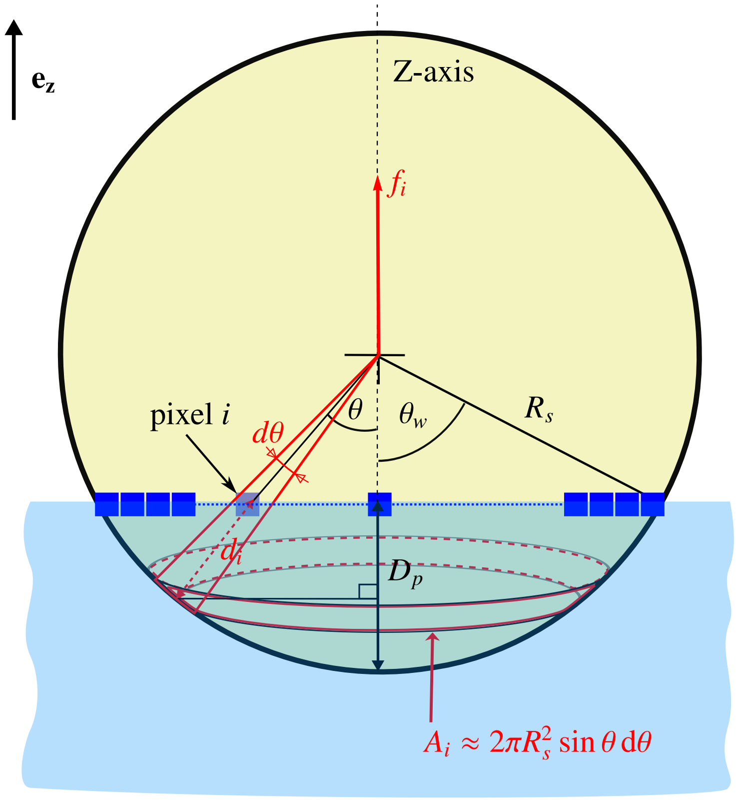

Figure 2.5: *Description of the geometry of a ball as used in Balltracking. The ball is floating on a flat surface. The blue squares represent pixels in the image.*

The algorithm uses dimensionless parameters. Each quantity defined in Fig.2.5 is scaled by characteristic parameters:

d_c : characteristic length (pixel size)
t_c : characteristic time (time interval between each image)

and the dimensionless parameter associated with Fig.2.5 defines as:

$$\widetilde{R_s} \equiv R_s/d_c \tag{2.5}$$

$$\widetilde{D_p} \equiv D_p/R_s \tag{2.6}$$

$$\widetilde{d_i} \equiv d_i/R_s \tag{2.7}$$

Now we must define the pressure on an elementary spherical annulus of width $R_s\, d\theta$ at a radial penetration depth d_i (shown in red in Fig.2.5) making an angle θ with the vertical axis of the ball, and equal to:

$$d_i = R_s - \frac{R_s - D_p}{\cos\theta} \tag{2.8}$$

In units of sphere radius R_s, d_i gives:

$$\widetilde{d_i} = 1 - \frac{1 - \widetilde{D_p}}{\cos\theta} \tag{2.9}$$

We now define the pressure applied to the annulus as:

$$P_i = k\,\widetilde{d_i} \tag{2.10}$$

where k is the force scaling factor. In the present situation, we are only interested in tracking the position of the center of the balls. All the forces must be defined in relation to this point. Additional effects like spinning motions are of no interest in this framework. The total arbitrary buoyancy, by definition, is oriented upward, so we only express the elementary buoyancy force f_i as a function of d_i. Due to the symmetry around the vertical axis on the flat surface, and considering the pressure applied on the whole area A_i of an elementary spherical annulus, we have:

$$\begin{aligned} f_i &= P_i \cos\theta\, A_i \\ &= k\,\widetilde{d_i}\cos\theta\, A_i \\ &= k\left(1 - \frac{1-\widetilde{D_p}}{\cos\theta}\right) 2\pi R_s^2\, \cos\theta \sin\theta\, \mathrm{d}\theta \end{aligned} \tag{2.11}$$

Now we derive the force scaling factor k in terms of the parameters introduced above, by using the equilibrium between the gravity force and the total buoyancy force. The gravity force is not related to the solar gravity. It is another factor intrinsic to the algorithm, noted g, used only to balance the buoyancy force. The total buoyancy force is obtained by integrating f_i over all the submerged elementary annuli.

$$mg = \int_0^{\theta_w} f_i\, \mathrm{d}\theta \tag{2.12}$$

$$= 2\pi k R_s^2 \left[\frac{1}{2}\sin^2\theta + (1 - \widetilde{D_p})\cos\theta\right]_0^{\theta_w} \tag{2.13}$$

where θ_w is the angle between the bottom vertical axis of the sphere and the surface, which satisfies:

$$\cos\theta_w = \frac{R_s - D_p}{R_s} = 1 - \widetilde{D_p} \tag{2.14}$$

$$\tag{2.15}$$

Finally, we obtain an equation for k:

$$k = \frac{mg}{\pi R_s^2 \widetilde{D_p}^2} \tag{2.16}$$

The above derivation is only used to find a suitable definition of k, which is a constant characteristics of the balls, and does not depend on how the surface is shaped. A horizontal surface allows the easiest calculations. The horizontal motion arises from the asymmetric topology of a non-flat surface.

On discrete data, there is a finite number of data points N_d acting on the ball, and the total buoyancy force $\mathbf{f_b}$ is defined as:

$$\begin{aligned} \mathbf{f_b} &= \sum_{i=1}^{N_d} k\widetilde{\mathbf{d_i}} \\ &= \sum_{i=1}^{N_d} \frac{mg}{\pi R_s^2 \widetilde{D_p}^2}\widetilde{\mathbf{d_i}} \end{aligned} \tag{2.17}$$

Note that k scales the buoyancy force. The latter is thus proportional to the arbitrary gravity g, and is also scaled by the level at which the ball is in equilibrium when it is floating on a flat surface (Eq.2.13). This level is set by $\widetilde{D_p}$.
For stability we need to introduce a damping force that slows down the balls proportionally to their velocity such that in the absence of other forces, the velocity satisfies:

$$\begin{aligned} m\frac{\mathbf{dv}}{dt} &= -\gamma\mathbf{v} \\ \mathbf{v} &= \mathbf{v_0}\exp\left(\frac{-t}{\widetilde{T_d}}\right) \end{aligned} \tag{2.18}$$

in which $\widetilde{T_d} = m/\gamma$ is the characteristic damping time, and $\mathbf{v_0}$ is the initial velocity. Note that this is also the solution of the homogenous form of Eq.2.4, which accounts for the effect of the damping force. So if we know the initial velocity, the displacement $\mathbf{x}(t_1) - \mathbf{x}(t_0)$ between two consecutive times t_1 and t_0 can be integrated analytically as:

$$\mathbf{x}(t_1) - \mathbf{x}(t_0) = \int_{t_0}^{t_1} \mathbf{v(t)}dt \tag{2.19}$$

$$= \int_{t_0}^{t_1} \mathbf{v_0}\exp\left(\frac{-t}{\widetilde{T_d}}\right)dt \tag{2.20}$$

$$= \mathbf{v_0}\exp\left(\frac{-t_1}{\widetilde{T_d}}\right)\widetilde{T_d}\left[1 - \exp\left(\frac{-(t_1 - t_0)}{\widetilde{T_d}}\right)\right] \tag{2.21}$$

$$= \mathbf{v_1}\widetilde{T_d}\left[1 - \exp\left(\frac{-\delta t}{\widetilde{T_d}}\right)\right] \tag{2.22}$$

where $\mathbf{v_1} = \mathbf{v_0}\exp\left(\frac{-t_1}{\widetilde{T_d}}\right)$ according to Eq.2.18, and $\delta t = t_1 - t_0$.

In fact, the damping force is used to maintain some stability (Potts et al. 2004). It is applied only after the buoyancy force acts on the balls. Before it is applied, the velocity change between two time steps derives as:

$$\delta\mathbf{v} = \delta t\,(\mathbf{f_b} - g\mathbf{e_z}) \tag{2.23}$$

The positions of the balls are updated at each new image by integrating Eq.2.23 iteratively. At the end of each integration step, the damping is applied using Eq.2.22. In fact, each integration of the positions is decomposed in four consecutive calculations:

- The buoyancy force is calculated with Eq.2.17.
- The new velocity is integrated with the buoyancy force calculated above, according to Eq.2.23.
- The new position is integrated according to Eq.2.22.
- The damped velocity is calculated explicitly using Eq.2.18 so it is used as the initial velocity at the next time step.

In the algorithm, $\delta t = 1$, as one image corresponds to one time step. For simplicity, the mass of the balls is set to 1. The balls have no initial velocity ($\mathbf{v}_0 = 0$), and are initially positioned in the first image at $\mathbf{x_1} \equiv (x_1, y_1, z_1)$. z_1 is set at a height that satisfies that the bottom point of each ball is submerged by 0.5 D_p. The horizontal spacing of the balls is equal to one ball diameter (2 R_s) which ensures that the balls do not overlap at the beginning of the tracking.

In what follows we associate the time t with the image number n, so that $\mathbf{v}(t) \equiv \mathbf{v}_n$ and $\mathbf{f_b}(t) \equiv \mathbf{f_b}_n$. If we unroll the integration of the velocities and positions at the first image, the four steps described above give:

$$\mathbf{f_b}_1 = k \sum_{i=1}^{N_d} \mathbf{d}_{i1} \tag{2.24}$$

$$\mathbf{v}_1 = \mathbf{f_b}_1 - g\mathbf{e_z} \tag{2.25}$$

$$\mathbf{x}_1 = \mathbf{x}_0 + \mathbf{v}_1 \widetilde{T}_d \left[1 - \exp\left(\frac{-1}{\widetilde{T}_d} \right) \right] \tag{2.26}$$

$$\mathbf{v}_1^* = \mathbf{v}_1 \exp\left(\frac{-1}{\widetilde{T}_d} \right) \tag{2.27}$$

where we have introduced the asterisk symbol * to distinguish the damped velocity at the fourth step from its non-damped value at the second step. At the next image we will have:

$$\mathbf{f_b}_2 = k \sum_{i=1}^{N_d} \mathbf{d}_{i2} \tag{2.28}$$

$$\mathbf{v}_2 = \mathbf{v}_1^* + \mathbf{f_b}_2 - g\mathbf{e_z} \tag{2.29}$$

$$\mathbf{x}_2 = \mathbf{x}_1 + \mathbf{v}_2 \widetilde{T}_d \left[1 - \exp\left(\frac{-1}{\widetilde{T}_d} \right) \right] \tag{2.30}$$

$$\mathbf{v}_2^* = \mathbf{v}_2 \exp\left(\frac{-1}{\widetilde{T}_d} \right) \tag{2.31}$$

Henceforth, the integration of the position at the n^{th} frame knowing the velocity and position at the $(n-1)^{th}$ frame, with $\delta t = n_2 - n_1 = 1$ gives:

$$\mathbf{f_b}_n = k \sum_{i=1}^{N_d} \mathbf{d}_{in} \tag{2.32}$$

$$\mathbf{v}_n = \mathbf{v}^*_{n-1} + \mathbf{f_b}_n - g\mathbf{e_z} \tag{2.33}$$

$$\mathbf{x}_n = \mathbf{x}_{n-1} + \mathbf{v}_n \widetilde{T}_d \left[1 - \exp\left(\frac{-1}{\widetilde{T}_d}\right)\right] \tag{2.34}$$

$$\mathbf{v}_n = \mathbf{v}^*_n \exp\left(\frac{-1}{\widetilde{T}_d}\right) \tag{2.35}$$

With real data, the surface is defined by the intensity of the image, which is not flat, thus we define D_p as a characteristic depth. If the ball floats at a different depth than D_p, the vertical component of the buoyancy force will move the ball to satisfy the equilibrium defined in Eq.2.13. In the meantime, the two horizontal components of the total buoyancy force move the ball horizontally. When the ball falls in the intergranular lanes, it will settle in and follow the net motion of the set of granules that define these lanes. These steps are presented in Fig.2.6.

2.2.4 Phase 3: filling the gaps

At the end of the integration of the ball positions, there can be places where they overlay. By continuity, this also creates gaps larger than the initial spacing between the balls at the initialization (one ball diameter between the centers of the nearest neighbors), which leaves parts of the images not sampled. Potts et al. (2004) "regulated" this in two steps before each new integration of the positions of the balls:

- Neighboring balls will eventually settle to the same local minima, causing an "over-population" at different grid points of the frame where the balls overlay (see the overlaying circles in Fig.2.8). Such balls are detected by computing the histogram of the position of all the balls. These balls and their position on the grid are flagged for relocation.

- For any empty grid point, it is filled with one of the previously flagged balls. The positions of the relocated balls are also flagged when differentiating the final positions: this ensures that the differentiation does not act on the previous positions of relocated balls (as these could have been anywhere before their relocation).

In the original version of the code, we realized that the number of gaps and of overlays were not balanced: after the two steps above, there were still much more of the former than there were of the latter. This is illustrated in Fig.2.7 where we have plotted the gaps (black) before (top) and after (bottom) the two steps of the "gap filling" procedure, at a given time. Note that because of the original square grid spacing (one ball diameter of,

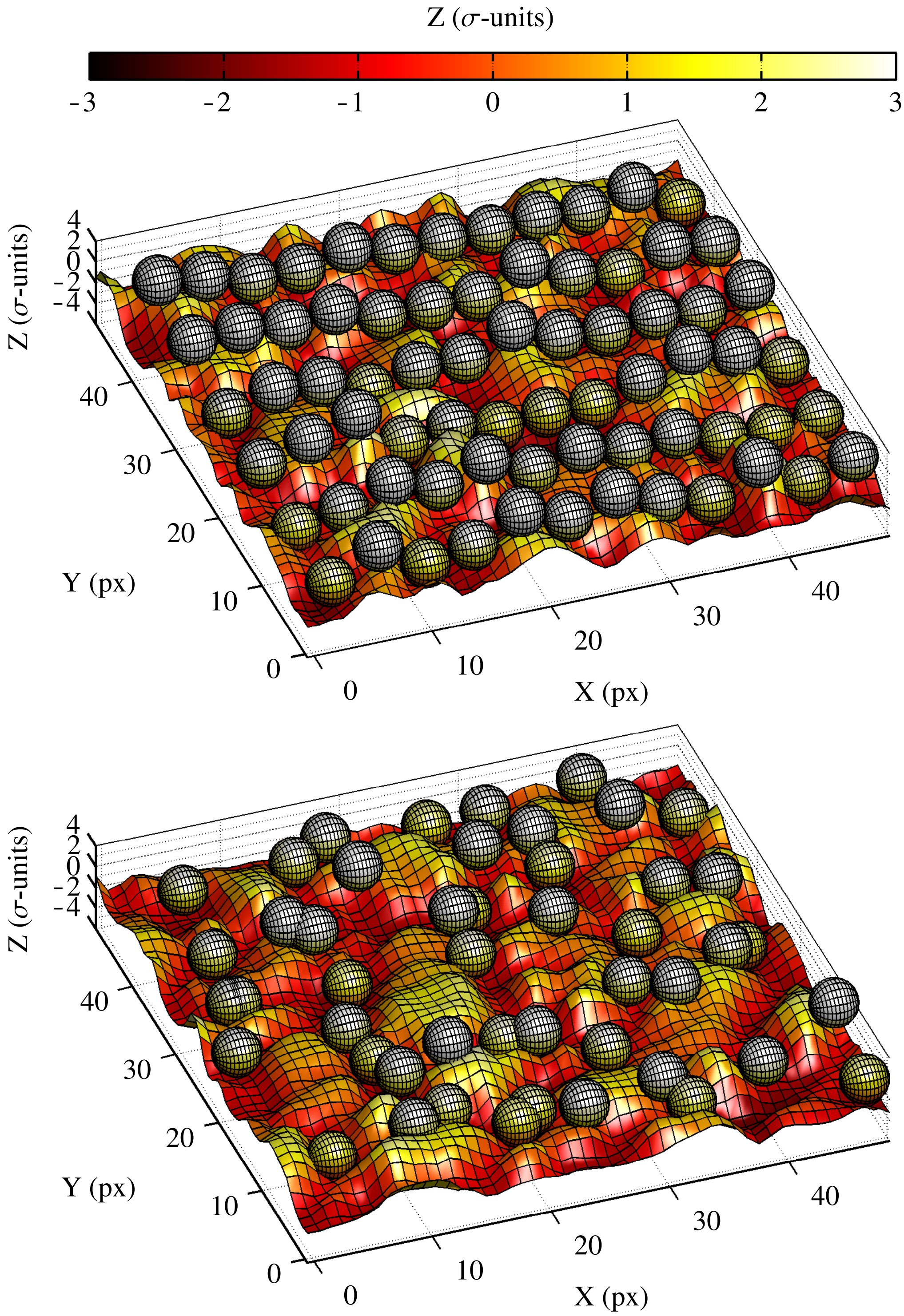

Figure 2.6: *Status of Balltracking at two different times. Top: The balls are placed on the 3D surface. Bottom: the balls have moved over 6 images of the granulation, recorded every* 2 min. *The color scaling and Z-scaling are in units of standard deviation (σ-units)*

here, 4 px), the gaps are drawn as squares of 4 × 4 px^2. One can see that there is still a significant part of the grid that is not populated. The number of empty blocks (black) is given in the title of each image. Here it is initially equal to 287, and reduces to 140. This leaves in this case 22% of the initial grid not sampled, and this discrepancy stays throughout the whole time series. According to the continuity principle, this should not be the case, as the gaps are created only because some balls converge to the same areas and overlay, (the image on the bottom should be blank). In Potts et al. (2004), this was compensated using weighted average so this effect was minimized. In our implementation of the code, we realized that the balance between gaps and overlays could easily be enforced, ensuring that the number of relocated balls from the overlays is always enough to re-fill all the gaps. This was solved using a more consistent communication between the two steps described above, that is consistent with the continuity principle, and, in a least proportion, by taking into account the possible loss of balls due to edge effects. This also ultimately results in a finer sampling of the images, which allows us to make a consistent error analysis (more on that in Section 2.3).

In addition to the two steps that minimizes the number of gaps, Potts et al. (2004) improved the statistics by tracking the granules back in time, starting from the last image, and tracking the motions back to the first image. The timeline of the final positions is reversed to recover the real timeline. This tracking is referred to as the "backward tracking". This provides a different set of sampled grid points, that is added to the first one, the latter being referred to as the "forward tracking". This was kept in our version of the code. Indeed, even if our modifications made the initial sampling grid better preserved across the images (i.e, no additional gaps are created), we cannot guarantee that the balls sample evenly all the pixels of all the local minima (the intergranular lanes) during the forward tracking. This in fact depends on the data themselves. With the backward tracking, the balls eventually follow different tracks than in the forward tracking, and this increases the quality of the sampling.

Nonetheless, this method only tracks the motion of the flow by tracking the intergranular lanes. Whether we use the forward or the backward tracking, the balls will only track the darker intergranular lanes, and not the bright center of the granules. This again leaves these parts of the data surface not sampled. Therefore, in the present thesis, another improvement was made to fill these gaps: by considering the inverted images (referred to as the "back-side" images), the local minima map to the centroids of the granules which were the local maxima in the non-inverted images (the "top-side" image). The Balltracking applied to both sets of images provides a finer sampling of the flows. Fig.2.9 shows a sample of the tracking on both sides, in 3D, of the larger image in Fig.2.8 (yellow rectangle). The latter pictures how the image is actually sampled by the balls after merging both sets of the final positions. After a few integration steps, the balls have settled in the integranular lanes during the top-side tracking (green circles in Fig.2.8, and Fig.2.9, top), and in the centroids of the granules in the back-side image (red circles in Fig.2.8, and Fig.2.9, top). Since the pixels at, and around the centroid of the granules are different from the pixels at the intergranular lanes, the data sampled during the "top-side" tracking are independent from the data sampled during the"back-side" tracking. The resulting velocity fields can be averaged to reduce the error, provided that both sets of results are calibrated properly. This is discussed in the next section.

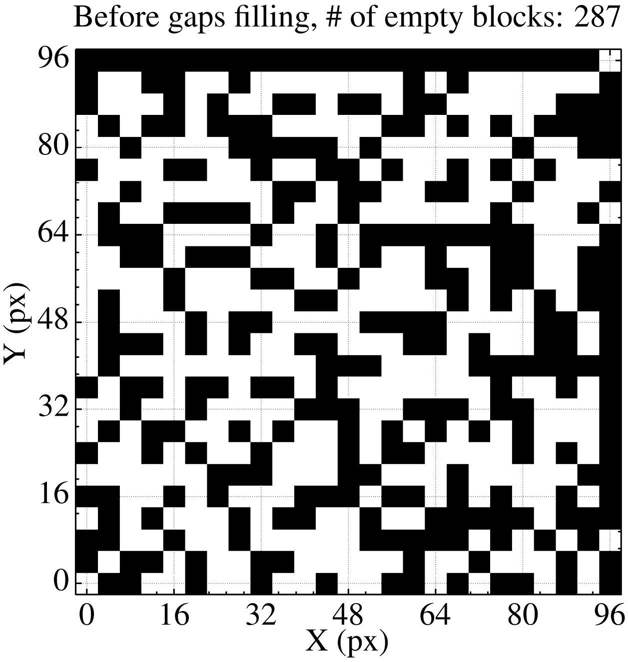

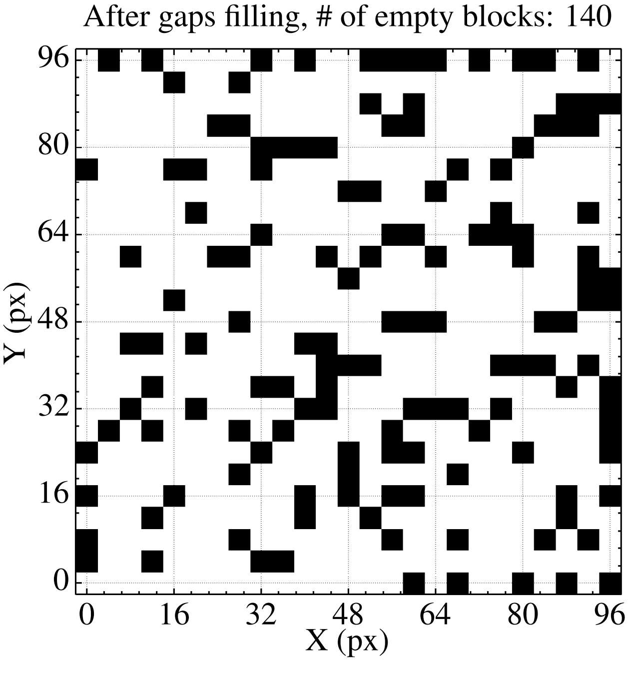

Figure 2.7: *Illustration of the gaps filling step in phase 3 of Balltracking, showing how the image is actually sampled. The black blocks are the gaps, i.e, areas of the grid without any ball. Top: 287 gaps appear at the end of the integration of the balls positions. Bottom: after re-filling the gaps, there are still 140 empty blocks. The field-of-view is the same as the one in Fig.2.8.*

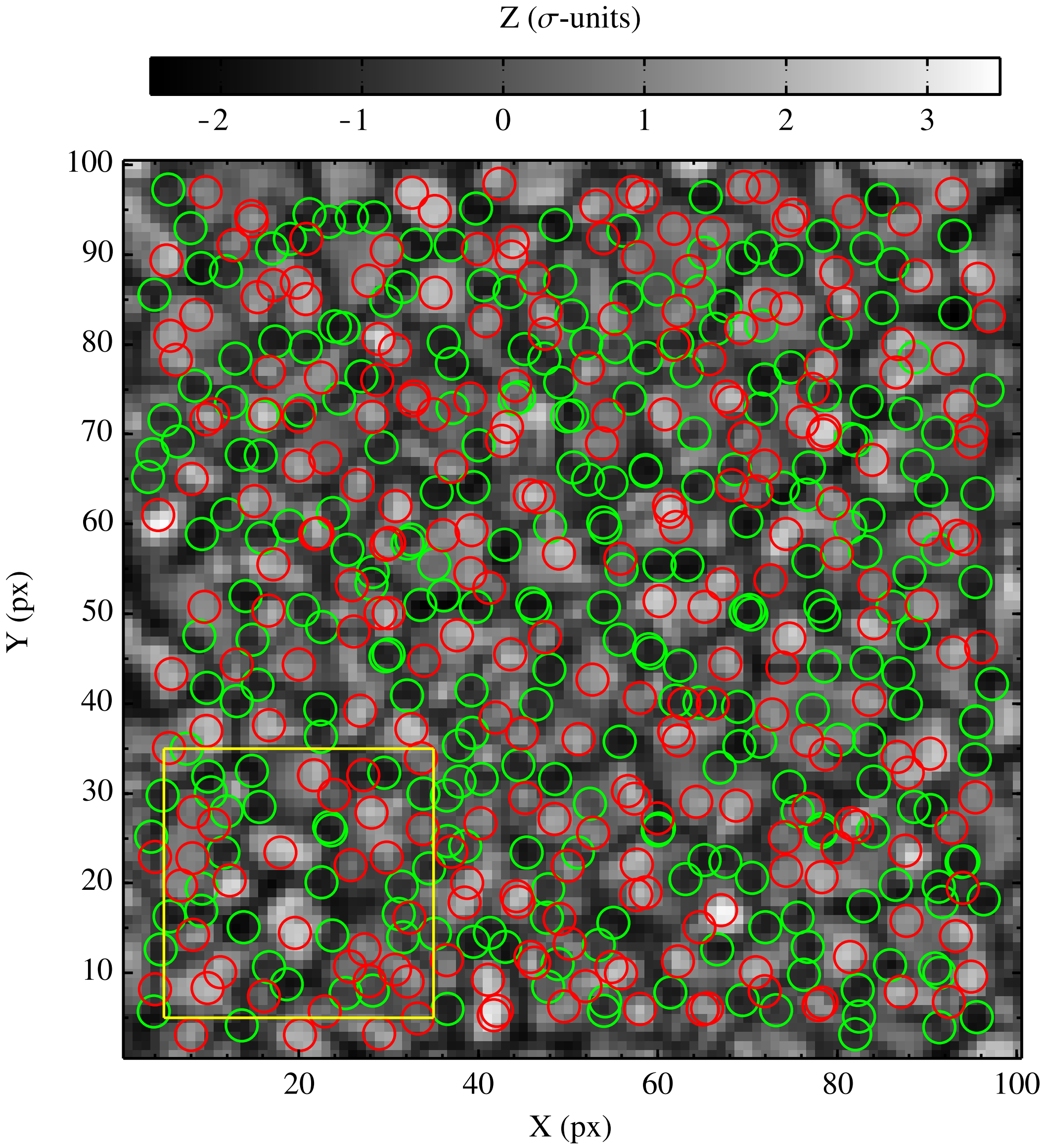

Figure 2.8: *Image of the granulation with the final positions of the balls after a few integration steps. In this colormap, the black areas correspond to the minimum "height", i.e, the intergranular lanes. The balls from the top-side tracking (green circles) have settled in them. The clearer, white areas are the granules, in which the balls from back-side tracking (red circles) have also settled at the centroid. The yellow rectangle corresponds to the field-of-view pictured in Fig.2.9.*

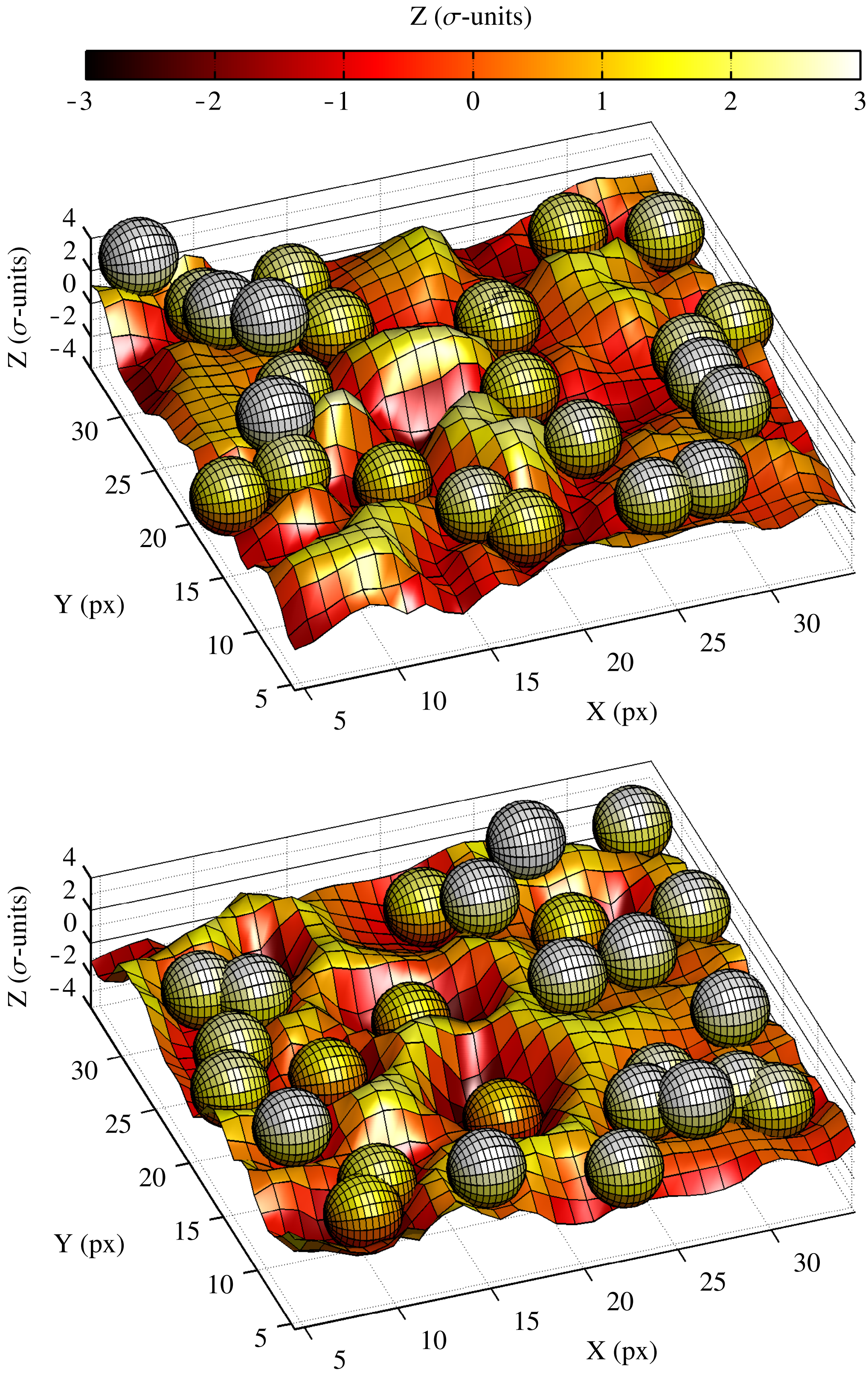

Figure 2.9: *Illustration of the top-side tracking (top) and back-side tracking (bottom). The field-of-view corresponds to the yellow rectangle in the larger frame in Fig.2.8.*

2.2.5 Phase 4: calibration of the velocity field

One must not confuse the velocity in Eqs.2.18 to 2.33 as the final output velocity. Instead, we output the final positions of the balls after the integration in each frame (Eq.2.35). These positions are, in fact, calculated in a Lagrangian frame of reference (the equation of motion follows each single ball), whereas the so-called "velocity field" (also referred to as "flow fields") must be calculated in a Eulerian frame of reference (the velocity of the fluid is observed at fixed locations) in a post-processing phase. Potts et al. (2004) does the conversion as follows:

- The final positions of the balls at two consecutive frames are differentiated.
- The average positions of the balls between these two frames are used as the grid points of the Euler frame of reference.
- Spatial smoothing and time averaging are applied over the velocity fields, in order to clear out the fast and stochastic small-scale motions of the granules, as discussed in Section 1.1.
- The conversion of the velocity to physical units is done at the end of the computation, by multiplying its two horizontal components V_x and V_y by the pixel size d_c and dividing by the time interval t_c between the images (which will be sometimes referred to as the instrumental "cadence" of the imager).

Note that the conversion above assumes a cartesian frame of reference, with a constant length of the pixel size projected onto the solar surface. This is, in fact, a tangential approximation of the spherical frame of reference valid only within a limited field-of-view (FOV). In the present thesis, we consider FOVs of, respectively, ~600 arcsec-wide with MDI/SoHO, and of ~250 arcsec with SOT/Hinode. The error on the pixel size of the farthest pixel of the CCD, induced by the solar spherical curvature, with respect to the pixel in the middle of the CCD, is of ~10%, and of ~1%, respectively. Only the results from SOT, and the co-spatial sub-region of the MDI's CCD is used in this thesis for quantitative analyses. Higher precision within wider FOVs, provided that enough granules are resolved, will need to account for a more precise map of the coordinates of all the pixels. Regardless, as we will see in Section 2.3, the random error intrinsic to the tracking of granules is much greater, which makes such corrections (i.e, the use of more precise maps of coordinates) unnecessary within the scope of this thesis.

In addition, since the balls take some time to settle in the local minima (the intergranular lanes), the velocities are, on average, underestimated. Therefore another calibration step is necessary to compensate for this systematic error. This was originally carried out by using the results from LCT (Section 2.1) to properly rescale the results from Balltracking by a linear coefficient (Potts et al. 2004). In the present thesis, we chose to use a more independent method. It consists in applying a known uniform velocity, in a specific direction, either the East-West direction (X-axis) or the North-South direction (Y-axis), by shifting subsets of the images. This emulates a constant large-scale drift, which would be picked-up as an offset on the average velocity. Balltracking is then performed on the drifting subsets. This process is repeated for different values of the drift velocity. Next,

V_x and V_y are averaged over the FOV of these subsets. Repeating the operation at the different values of the drift velocity reveals that the calculated velocity has a linear response to the drift. The calibration consists in dividing or multiplying[1] the velocity by this linear coefficient.
This coefficient depends on the characteristics of the data, like the pixel size, the noise level, the filter, the cadence of the imager, or the input parameters of the algorithm. If these conditions do not change, the same calibration coefficient can be used. Should any of them be changed at any time, this calibration should be carried out again. This includes the "top-side" and "back-side" tracking. The calibration must be done in each case. An example of this calibration for MDI and SOT is given in Fig.2.10. Note the linear response, and the different coefficients associated with each tracking (top-side and back-side). The linear response (here $R^2 > 0.99$ in all cases) is the necessary condition for this calibration, and the flow fields, to be meaningful. The value of the calibration coefficient is also an estimator of how fast the balls are able to respond to the changes of the flow fields. This property is discussed in more details in the next section.

2.3 Error analysis

The results of the top-side and back-side tracking are not strictly identical. They exhibit some discrepancies which can be used to estimate the measurement error. Because the method of using a top-side and back-side tracking is an improvement to the original algorithm, this error analysis not only measures the precision of the final output, it also quantifies the dependency of the results on the input parameters, and further justifies how to choose them. This is done in Section 2.3.1. In Section 2.3.2, we will use the theoretical model derived by Potts et al. (2004) to find out more about the accuracy of the tracking, which is the measure of how close the output velocity fields are to the true value of the flow fields underneath the granules. Note that we used the terms, "precision" and "accuracy", as distinct, and as defined in textbooks of error analysis (see for instance Bevington 1969, § 1.1). This distinction will be kept throughout this document.

In what follows, unless stated otherwise, the use of "pixel size" and "resolution" are used interchangeably as we rule out any manipulation that would decrease the pixel size without any gain in resolution, or increase the pixel size without the equal loss in resolution.

2.3.1 Effects of the input parameters

In order to assess how each parameter affects the results, we first need a formal definition of the measurement error of the velocity.
One measurement of the velocity at the i^{th} grid point (x_i, y_i) is the set of its 2 components: $(V_x(x_i, y_i)\ ,\ V_y(x_i, y_i))$, in units of "px/frame". The top-side tracking (T) and the back-side tracking (B), respectively, provide two independent measurements: $(V_x(x_i, y_i)\ ,\ V_y(x_i, y_i))_T$ and $(V_x(x_i, y_i)\ ,\ V_y(x_i, y_i))_B$, respectively. The discrepancy on the velocity components at

---

[1] Whether the velocity is either divided or multiplied by the calibration coefficient depends on how the user orders the measurements and the reference data in the linear fit.

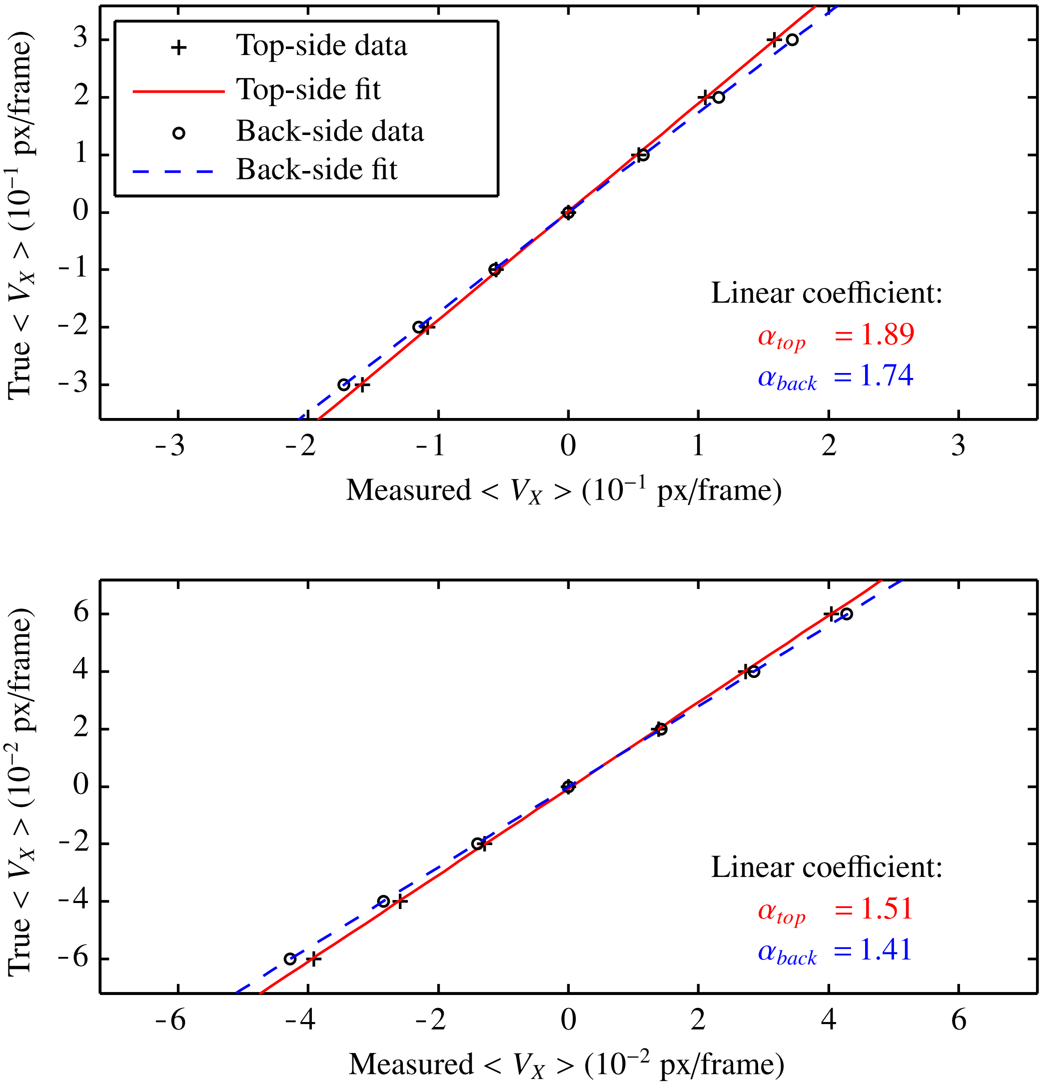

Figure 2.10: *Linear fit for the calibration of the velocity with images from two different instruments: SOT/Hinode (top) and MDI/SoHO (bottom).*

the i^{th} grid point defines as:

$$\delta V_x = V_x(x_i, y_i)_T - V_x(x_i, y_i)_B \tag{2.36}$$

$$\delta V_y = V_y(x_i, y_i)_T - V_y(x_i, y_i)_B \tag{2.37}$$

and referred to as $\delta V_k(x_i, y_i)$ with $k = x, y$. In what follows, for simplicity and unless stated otherwise, the index k always refers to the x and y component of the velocity.
In terms of velocity magnitude we will have:

$$\delta|V| = |V|(x_i, y_i)_T - |V|(x_i, y_i)_B \tag{2.38}$$

where $|V| = \sqrt{V_x^2 + V_y^2}$.

The above discrepancies are random, and their distributions across the N grid points $(x_i, y_i)_{i=1,\ldots N}$ approximate the normal distribution centered on zero.

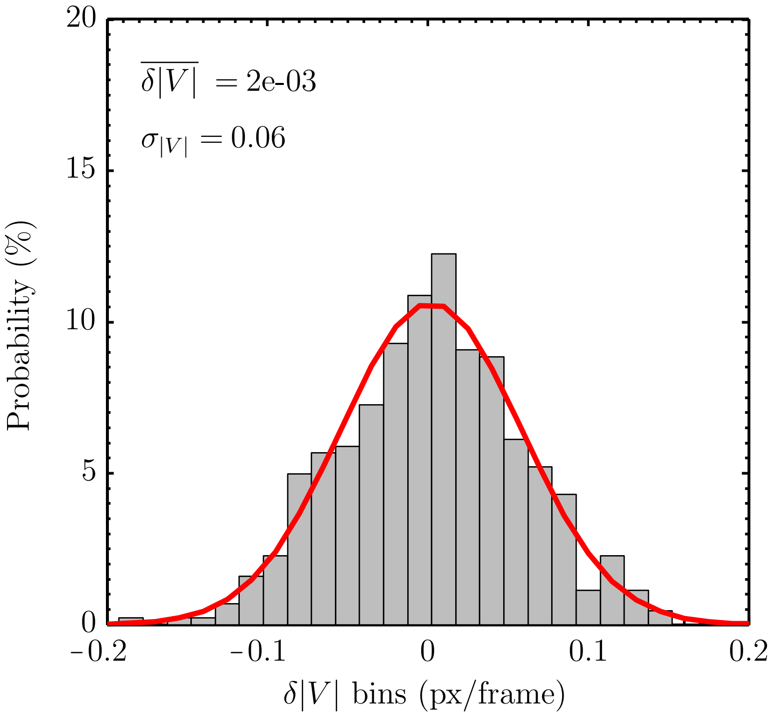

Figure 2.11: *Distribution of the discrepancies (gray bars) and the fitted normal distribution (red) for the two components of the velocity V_x and V_y.*

Then we define the standard error in the 2 components of the velocity as the standard deviation of the discrepancies, noted σ_{V_k}, such that:

$$\sigma_{V_k} = \sqrt{\frac{1}{N-1}\sum_{i=1}^{N}\left(\delta V_k(x_i, y_i) - \overline{\delta V_k}\right)^2} \tag{2.39}$$

where $\overline{\delta V_k}$ is the mean discrepancy over the N grid points which is negligible with respect to the velocity magnitude. In Fig.2.11, we show an example of the standard error on the velocity magnitude ($\sigma_{|V|}$) from real data (SOT/hinode). Here $\sigma_{|V|} = 0.06$ px/frame and $\overline{\delta|V|} = 2\,10^{-3}$, from a flow field with a mean velocity magnitude of $\overline{|V|} = 0.3$ px/frame.

Since the same algorithm is used to track the velocity at each grid point (x_i, y_i), and there is no interaction between the balls, the measurements at each grid point are independent from each other. In addition, the top-side and back-side tracking are also independent as the features that are being tracked are different. Indeed, on the "top-side" images, the balls settle in the local minima of the intergranular lanes and track the motions of the latter, whereas on the "back-side" images, they track the centroid of the granules. Thus by averaging the results of the tracking on both sides as:

$$V_k^*(x, y) = \frac{V_k(x, y)_T + V_k(x, y)_B}{2} \tag{2.40}$$

the standard error of the mean measurements $\sigma^*_{V_k}$ at each grid point reduces to:

$$\sigma^*_{V_k} = \frac{\sigma_{V_k}}{\sqrt{2}} \tag{2.41}$$

In Fig.2.11, this reduces the standard error $\sigma_{|V|}$ to $\sigma^*_{|V|} \sim 0.04$, and to a percentage error $\frac{\sigma^*_{|V|}}{|V|}$ of 13%. We can now estimate the velocity components within a 1σ-uncertainty by:

$$V_k(x, y) = V^*_k(x, y) \pm \sigma^*_{V_k} \tag{2.42}$$

The above derivations are applied to real data, using images from SOT with a pixel size of 0.16 Mm, and a field-of-view $500 \times 500\,\mathrm{px}^2$. The velocity field is the result of a time average of 1 hr and of a gaussian smoothing over a full-width-at-half-maximum (FWHM) of 24 px (~4 Mm). Each velocity map is binned, with a square bin size equal to the FWHM in order to provide uncorrelated samples (the value at each bin is the average of all the values within). $\sigma^*_{V_k}$ is calculated after different runs of Balltracking on the same series of images, with different sets of input parameters. To give more generalized results for comparisons in future studies, the uncertainty is normalized. In order to avoid divisions by zeros, it is normalized to the mean velocity magnitude $\langle\ |\boldsymbol{V}(x, y)|\ \rangle$ (where $\langle\ \rangle$ represents the spatial average over x and y), which is always positive, and the standard error is expressed as a standard "relative error", noted $\sigma^*_{nV_k}$ and expressed as a percentage in Fig.2.12. In addition to these results, each change in parameters space requires a new calibration. The calibration coefficients of the top-side and back-side tracking are plotted in Fig.2.13. We remind that these values also measure how fast the balls react to the velocity changes in the flows. The closer they are to 1, the faster they react. Below are the interpretations of these results for each input parameter, which complements the discussion on the choice of parameters in the original paper (see Potts et al. 2004, §2.4).

Sphere radius ($\widetilde{R}_s$) The uncertainty $\sigma^*_{nV_k}$ is minimized down to ~12% at $\widetilde{R}_s = 2$ px. At higher values, the uncertainty slightly increases by a few percents. The optimum value of $\widetilde{R}_s$ directly relates to the size of the features we need to track, and to the resolution of the images: the size of the balls need to be small enough to settle between the granules (top-side tracking), and within the granule centroid (back-side tracking). Thus too great a radius defeats the purpose. Too small a radius can nearly double the uncertainty with $\sigma^*_{nV_k}(1.2) = 21\%$, because the balls do not have enough pixels under them to really track anything coherent: the motions remain dominated by the small-scale random noise of the images, regardless of the amount of time and spatial average.

Gravity (g) It is used to maintain stability. The buoyancy forces are proportional to it (Eq.2.18). In Fig.2.12, $\sigma^*_{nV_k}$ significantly increases at $g > 1$. If it is too high, the balls move faster than the changes in the flow. Hence the increase of the standard error from $\sigma^*_{nV_k}(0.2) \simeq 10\%$ to $\sigma^*_{nV_k}(1.5) \simeq 25\%$. Values lower than 0.8 should be avoided too, despite the apparent "better precision" implied by the graphs of $\sigma^*_{nV_k}(g)$. Indeed, as mentioned earlier, there is a difference between "precision" and "accuracy". Consider Eqs.2.16 and 2.17 and the extreme case of $g = 0$. The buoyancy forces would vanish

too, and all the balls would stand still. The discrepancies between the top-side and the back-side would subsequently be zero, and so would $\sigma^*_{nV_k}$. The latter corresponds to a very "precise" measurement, but it also corresponds to the worse accuracy with respect to the real motions of the granules that are definitely moving! See Fig.2.13, in which the lower the value of g, the greater the calibration coefficients, which we mention earlier is to be interpreted as greater reaction times (i.e, the balls react more slowly). If the balls were rigidly following the granules, the calibration coefficients would be closer to 1.
So, decreasing g slows down the balls, and increases their reaction time to the changes in the flows. Therefore g should be set to the highest possible value that doe not get $\sigma^*_{nV_k}$ to increase significantly. According to Fig.2.12, $0.8 \geq g \geq 1$.

Number of intermediate frames N_{int} Due to the granules mean life time of 5 min, a time interval of 2 min between the images is a bit low: the shape and positions of the granules can significantly evolve between two consecutive frames. Before the integration at the next image, with a damping time of, e.g., $\widetilde{T}_d = 1$, the balls would still have ∼36% (damping by e^{-1} in Eq.2.33) of their last calculated velocity, in the absence of other forces. This affects the next displacements that they are supposed to catch. This influence is of course lower at a higher cadence (i.e, smaller time interval between the images) because the granules would evolve less between two consecutive images. To compensate for a low cadence (i.e, a large time interval between the images), Potts et al. (2004) linearly interpolates intermediate images to give the balls more time to track the granules, and make them anticipate the changes in the next image. Note that this does not improve the time resolution of the velocity map, as the missing information cannot be created, but this improves the precision of the measurements. In Fig.2.12, with 2 intermediate frames between the real images (the ones actually recorded by the instrument), the uncertainty decreases from 20% (0 interpolated frame) to 13%. In Fig.2.13, note that with no interpolated frame, the tracking is really slow at catching up the displacements with $\alpha_{T,B} > 3$. At 3 intermediate frames, $\alpha_{T,B} < 2$. So increasing the number of interpolated frames decreases the reaction time, in the same manner as the gravity g does. With a low cadence of 2 min, we need 2 to 3 intermediate frames. Interpolating more images than this does not improve the precision, neither does it improve the balls reaction time significantly, while it still increases the computational time.

Characteristic damping times ($\widetilde{T}_d$, $\widetilde{T}_{dz}$) The damping forces are necessary to stabilize the balls against rapid changes in the data, such as short wavelength noise (Potts et al. 2004). In addition, the stochastic motions of the granules are also short wavelength data with respect to the size of the field-of-view, and they are everything but noise: the average motions that rises from these stochastic displacements are precisely the useful data embedded in the final velocity fields (Section 2.2.5). $\widetilde{T}_d$ and $\widetilde{T}_{dz}$ are the times after which the horizontal and vertical velocity decreases by e in the absence of other forces, and it physically means that the balls have a "limited memory" of their past motions, which preserves some of the stochastic behavior that we need. Their effects on the final results are similar to the effects of g: they establish a compromise between stability and reaction time. Lower values reduce $\sigma^*_{nV_k}$ (Fig.2.12), but also reduce the responsiveness of the tracking according to Fig.2.13. Note that the damping times are in units of time interval

Inputs	R_s	$\widetilde{T}_d$	$\widetilde{T}_{dz}$	$\widetilde{D}_p$	N_{int}	$\sigma^*_{nV_k}$
value	2	3	0.3	0.2	3	13%

Table 2.1: *Chosen value of each input parameter of Balltracking for the images of SOT/Hinode used in this thesis.*

between the frames. Interpolating images reduces this time interval. Note also the range of $\widetilde{T}_{dz}$. It needs to be one order of magnitude less than $\widetilde{T}_d$ (Potts et al. 2004). Here we choose $\widetilde{T}_d = 3$ and $\widetilde{T}_{dz} = 0.3$. A very simple explanation for this difference is to compare the situation with a surfboard on a wave. To follow the motions of the wave at a given buoyancy, the surfboard is optimized so it is easier to glide horizontally than vertically. This is modeled by giving it a lot of damping in the vertical axis (low $\widetilde{T}_{dz}$), and much less horizontal damping ($\widetilde{T}_d > \widetilde{T}_{dz}$). Another comparison would be with the paraglider: in order to follow the horizontal component of the wind more efficiently than the vertical component, the paraglider acts on the strings of his parachute to increase the vertical damping with respect to the horizontal damping, which is precisely what we need to do.

Characteristic penetration depth ($\widetilde{D_p}$) It corresponds to the depth of submergence of the ball at which the latter is in equilibrium on a flat surface. $\widetilde{D_p} = 0$ means that the ball is not submerged at all. $\widetilde{D_p} = 1$ means it is entirely below the surface. On real data, it corresponds to an average penetration depth. To maximize the number of data points under the sphere, the latter should not be more than half submerged. It should not be too emerged either. Otherwise there are too few data points to compute coherent buoyancy forces, which reduces the reaction time. From Figs. 2.12 and 2.13, we can see that the penetration depth should be set to: $0.2 \leq \widetilde{D_p} \leq 0.3$.

Table 2.1 wraps up the best input values and the uncertainty for the tested series of images from SOT. These data will be used for science studies in the next chapters.

The discussion above showed how the precision can be improved by an appropriate choice of parameter values which reduces $\sigma^*_{nV_k}$. However, no matter how great the precision can get, the accuracy of the final results is constrained by physical limitations of the granules themselves. This is explained in the following section.

2.3.2 Random error due to sampling limitations

As mentioned in Section 1.1, Rieutord et al. (2001) observe that tracking granules gives relevant underlying flows only at spatial scales of more than 2.5 Mm and on temporal scales of at least 30 min. Thus observations of the velocity fields below these values may not be meaningful. At these thresholds, Potts et al. (2004) estimate from a theoretical model (see § 3.1 of the publication for a complete derivation) that whatever the tracking algorithm used, for 1 min cadenced data, with an instrumental resolution of 1.2 arcsec (MDI data), and assuming perfect tracking of the granules, the random error on the de-

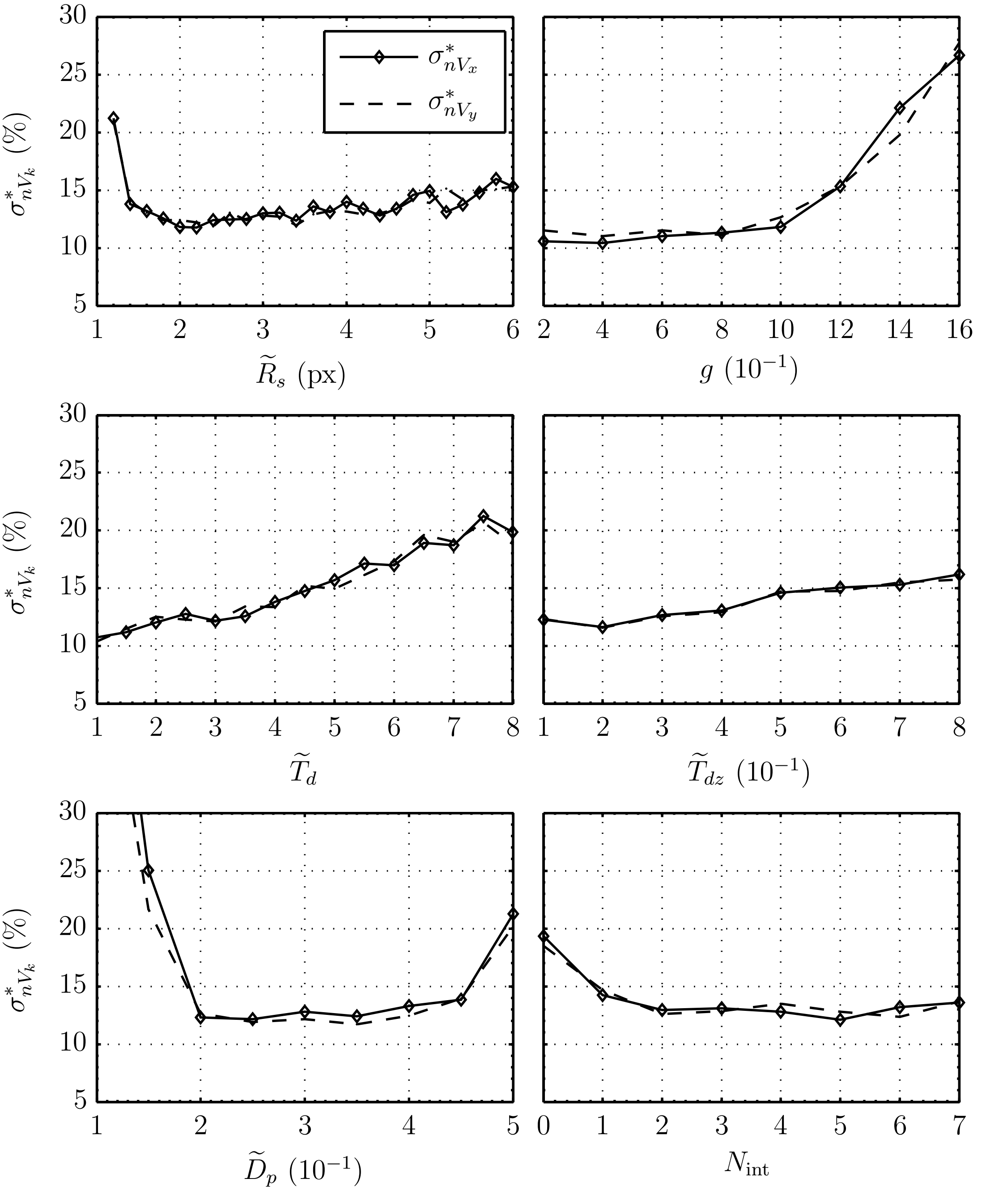

Figure 2.12: *Standard errors on the velocity components V_x and V_y, normalized to the mean velocity magnitude, for different values of the input parameters of Balltracking. The plots share the same vertical axis scaling, and the same legend as the one in the top left panel.*

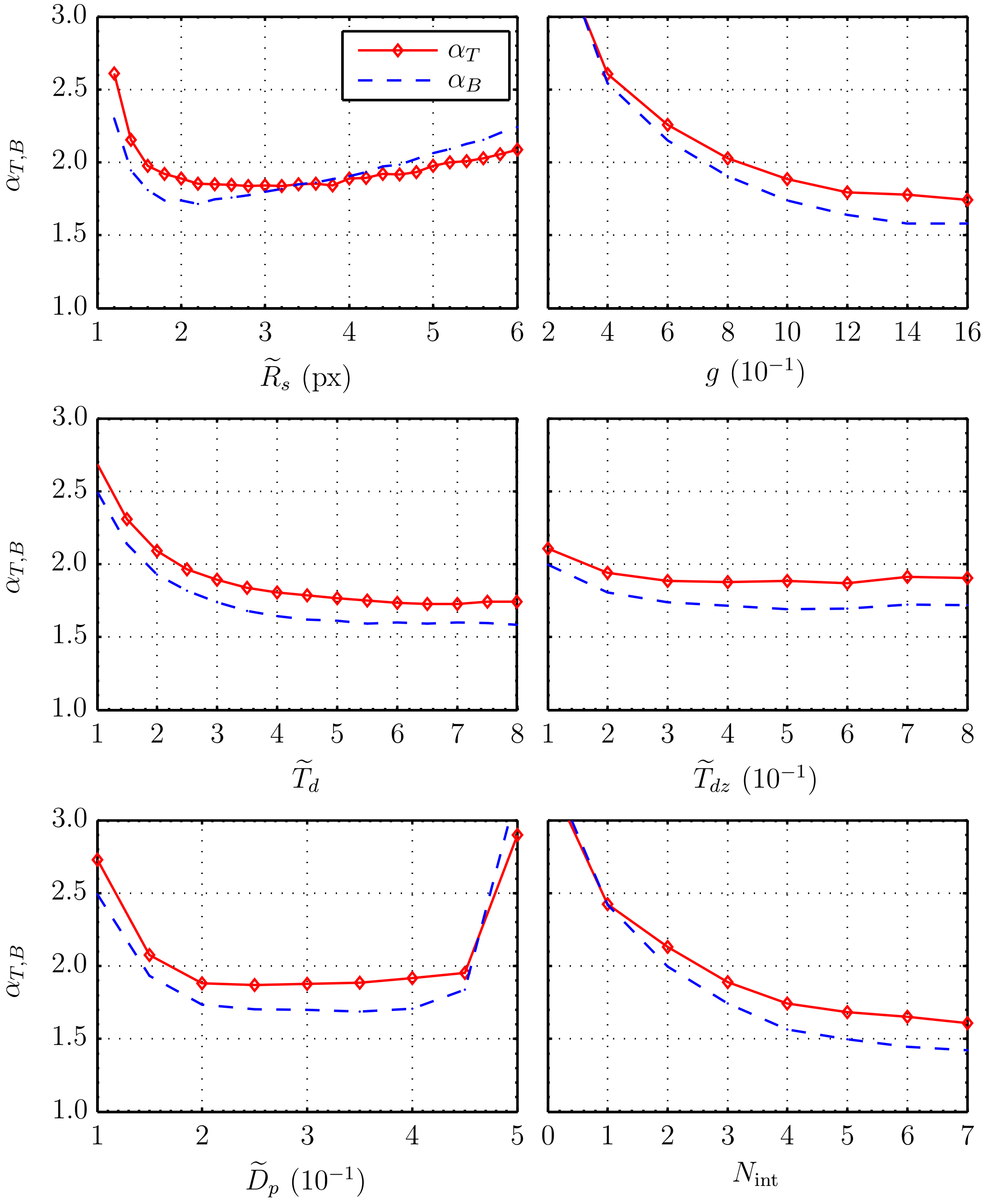

Figure 2.13: *Calibration coefficients* α_T *and* α_B *as a function of the input parameters. Each coefficient is derived with the same method as the one used in Fig.2.10, and as described in Section 2.2.5*

rived velocity flows would be ∼150 m s^{-1}. This uncertainty accounts for the finite scale of the granulation, in time and space, which makes the measurements spatially and temporally correlated. In sampling theory, it means that the effective number of independent data points is smaller than the number of samples taken by the instrument. Therefore, to keep the random error low enough for meaningful analysis at a given resolution in time and space, the spatial smoothing and time averaging must be chosen with caution.

As a look-up table for the next chapters, Fig.2.14 displays the theoretical random error on the velocity field derived with Balltracking using MDI and SOT data, as a function of both the time average and the spatial smoothing. The difference in the error between MDI and SOT observations is mainly due to a finer resolution of SOT, whose effect on the error compensates the effect of its lower cadence. In this example, the SOT cadence is 2 min, and the MDI cadence is 1 min. For typical photospheric flow fields of ∼400 m s^{-1} (on everage), and using the same time average (1 hr) and spatial smoothing (4 Mm) used in our error analysis in the previous section, Fig.2.14 gives an error of ∼60 m s^{-1}, i.e, a relative error of 15%. Note that this is a measure of the accuracy, which is of the order of the precision calculated earlier (13%). This means that the true accuracy is impaired by these measurement errors, and it also means that no matter how precise the measurements are, our results will have at least 15% error. A better accuracy will be obtained at the expense of either time resolution or spatial resolution, or of both. Note that the theoretical random error analytically derived by Potts et al. (2004) is not related to the tracking algorithm. It is a theoretical limitation, intrinsic to the granules and to the instrumentation used to record the images, regardless of the tracking technique used to process the data.

2.4 Advantages of Balltracking with respect to LCT

Balltracking and LCT are different methods to measure flow fields, that theoretically, given perfect data, and within the error bars of their respective measurement errors, are supposed to output the same results. However, with real images, the data can be biased by cosmic rays, hot or dead pixels, missing data, etc... across which LCT and Balltracking behave differently. In addition, on large data sets, there are intrinsic differences. These differences lead to significant advantages when using Balltracking. Some of the advantages were discussed by Potts et al. (2004) but our own implementation of the code offer other ones, which we describe below:

- The top-side and back-side tracking that we have used in this thesis provide a unique way to estimate the tracking precision from real data, which is not possible with LCT, whose precision and accuracy is assessed using simulations and by comparisons with other algorithms (Potts et al. 2004, Roudier et al. 1999).
- The original algorithm was using explicit "for-loops" over each single ball in the integration of the positions, as well as in the "gap filling" phase (Section 2.2.4). The whole code was written in the Matlab language. By vectorizing these codes (i.e, the removal of "for-loop" using faster matrix linear algebra), and by writing the core of the algorithm in Fortran and C, we have reduced the compute time by more than one order of magnitude, which makes possible real time analyses for long-term surveys (hours of observation take less than a minute to be computed).

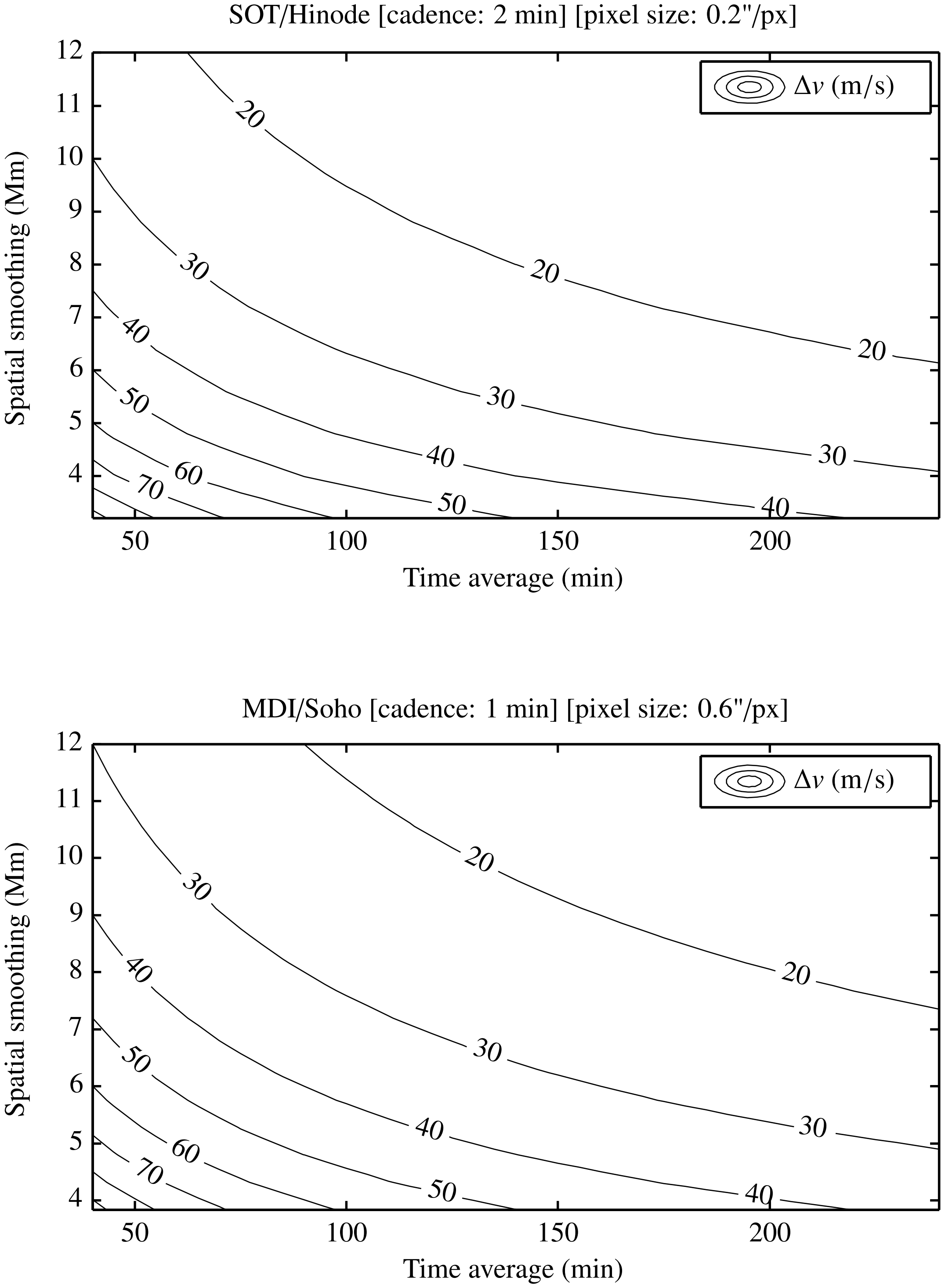

Figure 2.14: *Theoretical random error on the velocity fields derived from Balltracking, at different time averages and spatial smoothings, for SOT (top) and MDI (bottom). For this calculation, the SOT images are taken every* 2 min*, while MDI images are taken every minute. The instrumental characteristics used here (time cadence and pixel size of the images) are given in the figure titles. Adapted from Potts et al. (2004).*

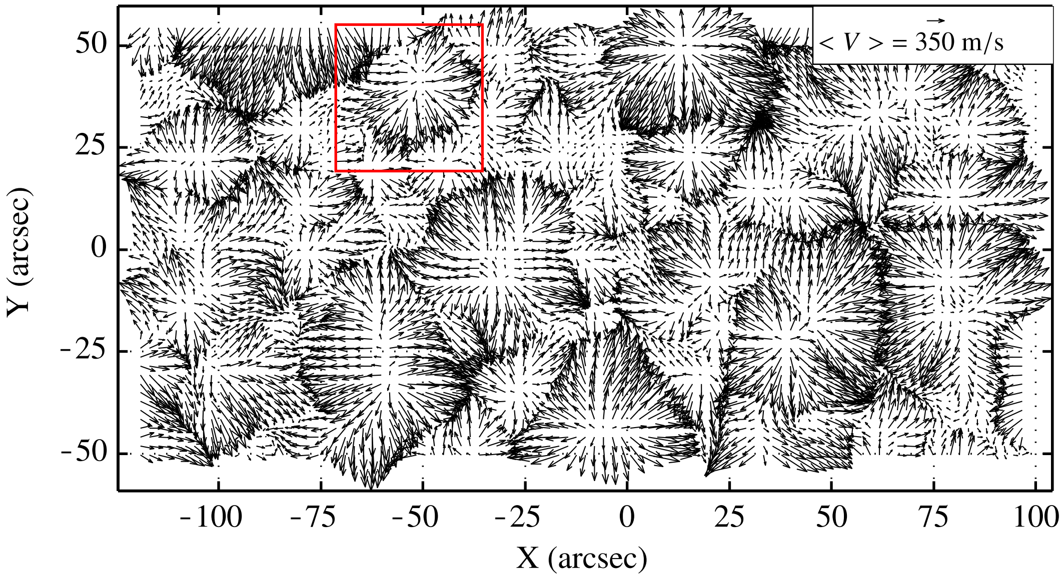

Figure 2.15: *Example of a velocity field output by Balltracking for the whole FOV of SOT/Hinode (*~216 × 107 arcsec^2 ~157 × 78 Mm^2*). Time average is* 4 hr. *Smoothing is applied with FWHM of* 4 Mm. *The axes are in heliocentric coordinates. At disk center,* 1 arcsec ≈ 0.16 Mm. *The red rectangle is* ~26 Mm*-wide, and encompasses a small supergranule. The corresponding close-up is displayed in Fig.2.17.*

- We also made the code more suitable for parallel computing. The forward and backward tracking, as well as the top-side and back-side tracking, can be carried out independently until their final output are averaged. The very simple independent equations of motion, and the quite low usage of memory make the whole code more suitable for execution within a cheap Graphical Processing Unit (GPU) and its hundreds of cores, instead of more expensive CPUs of usually less than 8 cores. The benefit in computational time between both hardwares will increase as the volumes of data will increase in the future.

2.5 Physical validation examples

Ultimately, the output obtained with Balltracking must be consistent with what is already known about the photospheric flows. It is necessary not only to validate the algorithm itself, but to make sure that we have re-written it and tuned it properly. One way to do it is first to consider the large-scale flows. When averaging over several hours and over a few Mm, the large-scale convection cells (i.e, the supergranules) should be easily visible. Fig.2.15 is a 4 hr-averaged velocity field obtained with Balltracking on images of SOT/Hinode, and smoothed over 4 Mm (FWHM). The associated divergence field is plotted in Fig.2.16. Fig.2.17 is a close-up on a supergranule (black rectangle in Fig.2.15). The streamlines of the flow are overlaid on a colored background of the magnitude of the horizontal velocity (V_h). In this 2D view, the center of the convection cell, and its boundaries are characterized by a slower velocity (red).

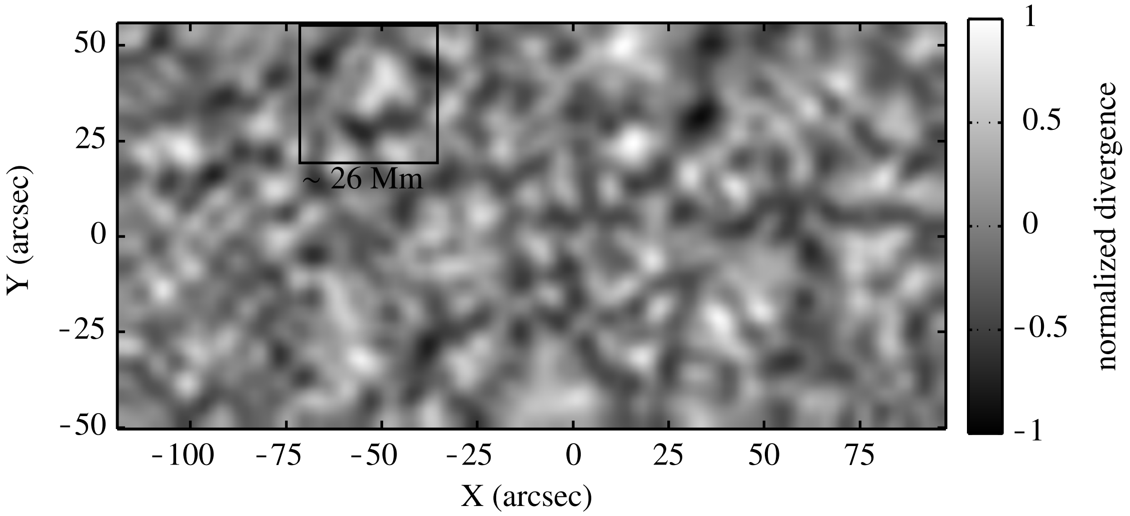

Figure 2.16: *Divergence of the velocity field in Fig.2.15. The black rectangle is at the same location. The divergence is normalized to the maximum value.*

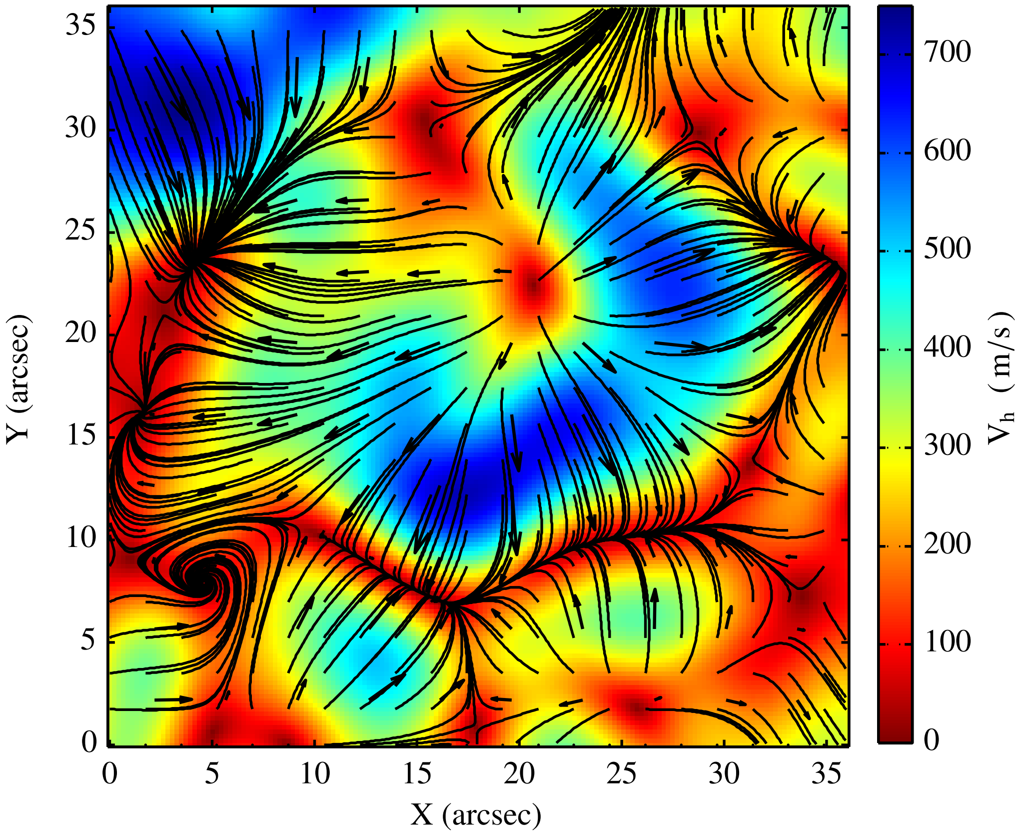

Figure 2.17: *Close-up of the supergranule in Fig.2.15. The colored background is the magnitude of the horizontal velocity* V_h*. The black lines are the streamlines, and the arrows indicate the direction of the flow.*

2.5.1 Limitations for using the divergence and vorticity fields

In Fig.2.15, one identifies a bounded network formed by the convergence of the flows of neighboring supergranules. It is less visible in the divergence field Fig.2.16, where it is seen as blurry dark lanes in regions of negative divergence, although to locate the regions of convergence of the flow, the divergence field would have been somewhat more natural, by definition, than using only a graphical proxy consisting in a map of hundreds of arrows. The fact that, surprisingly, the divergence field only gives a very blurry picture of the boundaries of the supergranules is due to the complex structure of the small scale flows, and to the random error that impairs the scalar field of local derivatives like the divergence and the vorticity.

In fact, these random errors simply originate from the propagation of those defined in Eqs.2.39 and 2.41 and can be calculated using the general rules of error propagation (e.g. Taylor 1996, Chapter 3 and 5). For this, let us consider the velocity components impaired by the standard error $\sigma^*_{V_k}$. The divergence field of our 2D velocity vector field is defined by:

$$\nabla \cdot \boldsymbol{V} = \frac{\partial V_x}{\partial x} + \frac{\partial V_y}{\partial y} \tag{2.43}$$

Written numerically, with a grid spacing equal to unity, the divergence is computed as $\nabla \cdot \boldsymbol{V} = \Delta V_x + \Delta V_y$ where ΔV_k is the difference between two adjacent grid points of the velocity component V_k. If we define the i^{th} and $i+1^{th}$ grid points at the coordinates (x_i, y_i) and (x_{i+1}, y_{i+1}), according to Eq.2.42 we have $V_{k_i} = V^*_{k_i} \pm \sigma^*_{V_k}$ and $V_{k_{i+1}} = V^*_{k_{i+1}} \pm \sigma^*_{V_k}$. Accounting for the quadratic propagation of the uncertainty σ^*_V, any differentiation of a given velocity component between two adjacent grid points will derive as:

$$\begin{aligned} \Delta V_k &= V_{k_{i+1}} - V_{k_i} \\ &= V^*_{k_{i+1}} - V^*_{k_i} \pm \sqrt{\sigma^{*2}_{V_x} + \sigma^{*2}_{V_y}} \end{aligned} \tag{2.44}$$

Here we have used a forward difference, but the results regarding the error are the same with a backward or central difference.

For simplicity we assume that in the disk center the x and y component are equivalent regarding the random error, and so $\sigma^*_{V_x} \sim \sigma^*_{V_y} \equiv \sigma^*_{V_k}$. In the divergence field, we use differentiation and sum, so the errors $\sigma^*_{V_k}$ are added quadratically four times.

This finally gives:

$$\begin{aligned} \nabla \cdot \boldsymbol{V}_i &= V_{x_{i+1}} - V_{x_i} + V_{y_{i+1}} - V_{y_i} \\ \nabla \cdot \boldsymbol{V}_i &= V^*_{x_{i+1}} - V^*_{x_i} + V^*_{y_{i+1}} - V^*_{y_i} \pm \sqrt{2\sigma^{*2}_{V_x} + 2\sigma^{*2}_{V_y}} \\ \nabla \cdot \boldsymbol{V}_i &= \nabla \cdot \boldsymbol{V}^*_i \pm \sqrt{4\sigma^{*2}_{V_k}} \\ \nabla \cdot \boldsymbol{V}_i &= \nabla \cdot \boldsymbol{V}^*_i \pm 2\sigma^*_{V_k} \\ \nabla \cdot \boldsymbol{V}_i &= \nabla \cdot \boldsymbol{V}^*_i \pm \sigma_{\mathrm{div}} \end{aligned} \tag{2.45}$$

where we have introduced the "true" value of the divergence $\nabla \cdot \boldsymbol{V}^*_i$, impaired by a random error σ_{div} which is the quadratic sum of the random errors in 4 independent values used in the differentiation of the velocity components. We have hereby proved that the divergence field can only be derived with an uncertainty $\sigma_{\text{div}} = 2\sigma^*_{V_k}$, which is twice the error in the velocity fields. The proof of the uncertainty in the vorticity $\nabla \times \boldsymbol{V}$ yields the same result, as it involves the same number of data samples (and neglecting second order errors).

We have shown earlier that the relative error in the velocity is typically between 10% and 20% (Table 2.1) with a smoothing of the order of few Mm and time averages of ~1 hr. Then the relative error at 1σ in the divergence field would range between 20% to 40%, which explains why Fig.2.16 is not very helpful to locate the supergranular boundaries accurately. This can only be down-scaled by larger smoothing and longer time averages, which would significantly degrade the spatial and time resolution of the velocity fields. This is not possible in this study since we are interested in features of a few Mm, with a time resolution of ~1 hr.

Yet we still need to extract the network formed by the large convection cells. Indeed, a step forward in the physical validation of Balltracking is to compare them with the magnetograms, which also outline the magnetic network at the boundaries of the supergranules. This process is explained in the next section.

2.5.2 Extracting the boundaries of the convection cells

In the photosphere of the quiet Sun, the flows continuously sweep out the magnetic flux toward the supergranular boundaries where it accumulates, and forms a magnetic network on supergranular scales (Simon and Leighton 1964). Extracting the boundaries of the large scale flows allows a direct comparison with this magnetic network, from an independent dataset (the magnetograms). This is done by using an algorithm that detects the boundaries of the supergranules from the flow fields. It was developed by Potts and Diver (2008a), and summarized as follows:

The position of test particles are computed by integrating a given velocity field, back in time. The test particles back-track the streamlines of the flows, until they reach a final position. If the velocity field is consistent with the topology of supergranular flows, test particles lying initially within the same supergranule would all converge toward its center. At the end of the integration, the final position (x_f, y_f) of the particles are mapped to their initial position (x_i, y_i), so that $x_f \equiv x_f(x_i, y_i)$, and $y_f \equiv y_f(x_i, y_i)$. Then we use Eq.2.46 which gives the relative variation $L(x_i, y_i)$ of the final distance of initially neighboring particles, with respect to the difference between their initial separation:

$$L(x_i, y_i) = \sqrt{\left(\frac{\Delta x_f}{\Delta x_i}\right)^2 + \left(\frac{\Delta y_f}{\Delta y_i}\right)^2} \tag{2.46}$$

where Δx_f, Δy_f are the difference between the final horizontal coordinates of the test particles with initial separation $\Delta x_i, \Delta y_i$, and mapped to their initial coordinates (x_i, y_i). For instance, in the algorithm of Potts and Diver (2008a), the central differences are used to derive Δx_f and Δy_f at a given pixel i, so that:

$$\Delta x_f(x_i, y_i) = x_f(x_i + 1, y_i) - x_f(x_i - 1, y_i) \tag{2.47}$$

$$\Delta y_f(x_i, y_i) = y_f(x_i, y_i + 1) - y_f(x_i, y_i - 1) \tag{2.48}$$

At the edges of the frame, single-sided differences are used. Thus $L(x_i, y_i)$, at a given pixel i, depends on the final coordinates of the two pairs of particles that left the four nearest neighbors. Typically, $\Delta x_i = \Delta y_i = 2\,\text{px}$ when one uses central differences, and $\Delta x_i = \Delta y_i = 1\,\text{px}$ with single-sided differences.

One can see that if there is no motion at all, the final positions are identical to the initial positions, and so $x_f = x_i$, $y_f = y_i$, $\Delta x_f = \Delta x_i$, $\Delta y_f = \Delta y_i$, and thus $L(x_i, y_i) = 1$. On the other hand, two pairs of neighboring test particles, initially positioned at two different sides of a thin supergranular lane, would end up at completely different positions, e.g, the top of adjacent supergranules. In this situation, the difference between the final positions, divided by the difference between the initial positions, is maximum (considering the absolute value). This difference is minimal for two pairs of neighboring particles starting from within the same supergranule, and converging to the same center. The scalar value of $L(x_i, y_i)$ is a relative distance, without physical dimension. The greater its value at (x_i, y_i) is, the more apart the test particles, initially around this starting point, at the end of the integration on the time-reversed velocity field.

The algorithm initially positions one test particle at every pixel, and outputs a 2D map of the lanes (see Fig.2.20) which outlines the sharp boundaries of the large-scale convection cells. These lanes are simply the loci of greater convergence of the flow. Note that this is a much sharper representation of the convection cells than the one in Fig.2.16, where we use the same velocity field to process both figures. The true nature of the flow, and the number of integration steps will affect the sharpness of these boundaries, as all the test particles may not have reached the top of the convection cell at the end of the integration. Fig.2.18 contains four snapshots of this integration in the same close-up shown in Fig.2.17 which encompasses the flow field of a supergranule. The test particles are positioned on a regular grid. Each test particle belongs to a streamline from where they start to backtrack the flows. After 5 integration steps, the boundaries of large-scale convection cells start to emerge. After 10 steps, the boundaries of the convection cells have joined up. Beyond this, increasing the number of integration steps only sharpens the image, which is useful to us for later use as contour maps of the supergranular lanes, on top of other co-spatial observations.

The first and last step of this algorithm, in a wider FOV (same as Figs.2.15 and 2.16), are visible in Fig.2.19. The trajectories that the test particles follow during the integration are also displayed (thin black lines). The red dots are the initial (top) and final positions (bottom) of the test particles. The color scaling, and the associated color-bars in the images of the lanes give, as explained above, the relative traveled distance between the test particles, with respect to their initial position (see Eq.2.46). As explained earlier, when two particles originating from 2 contiguous pixels travel together, over the same distance, the intensity of $L(x_i, y_i)$ is low. When they are advected in opposite directions, e.g., when they originate from either side of a narrow lane, the intensity is higher.

In Fig.2.20 (top), some supergranular cells of different sizes appear to be merged to other ones, forming even bigger cells, like if their boundaries were partially "resolved" by the algorithm. This comes from the limited resolution of the velocity field. The merging of cells on these maps occurs when the time averaging and/or the spatial smoothing is too high, so that it reveals the bigger convection patterns, but leaves the smaller ones somewhat blurry. Another reason is that the flows may really not have clear convection

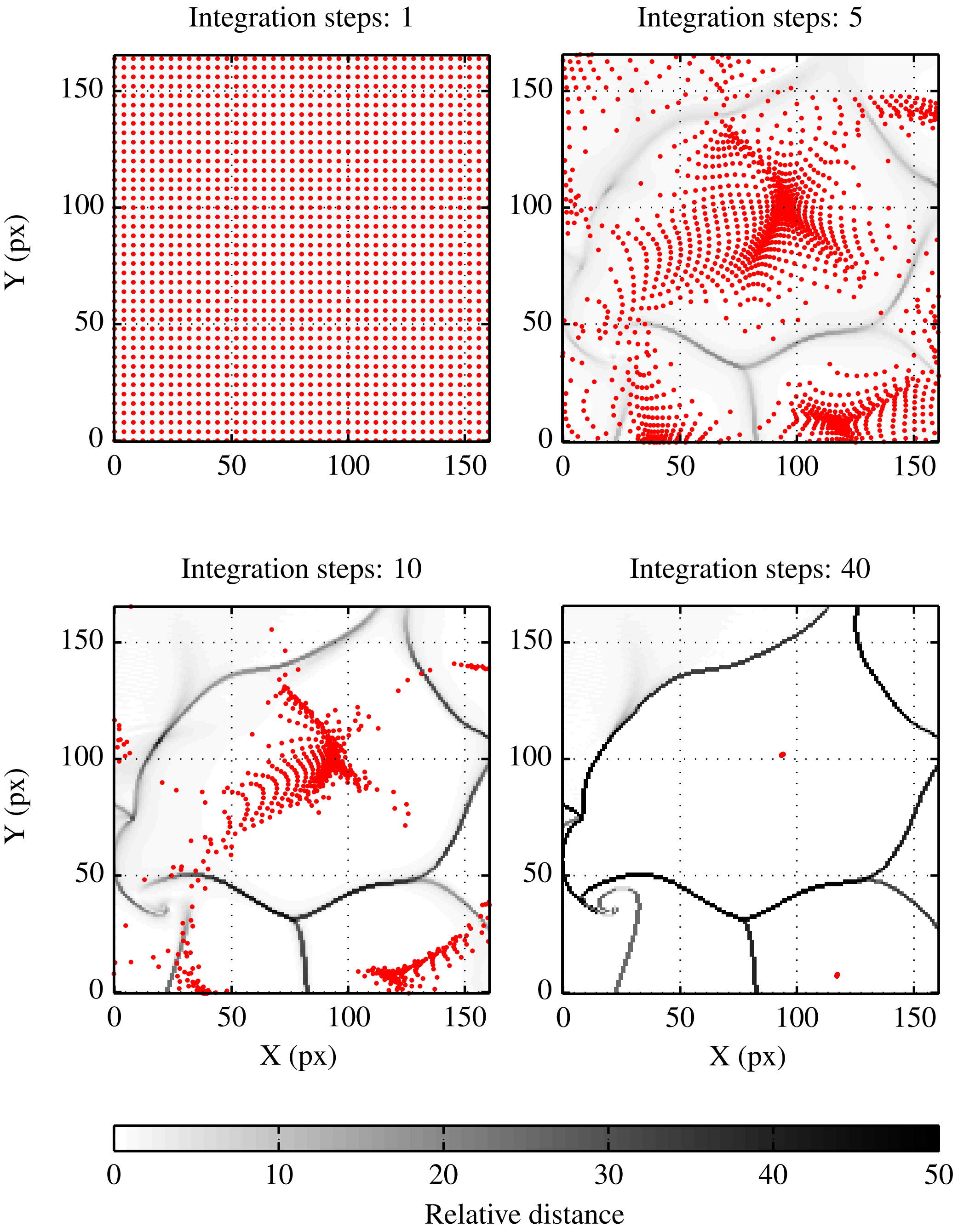

__Figure 2.18:__ Snapshots at several integration steps of the lane-recognition algorithm.

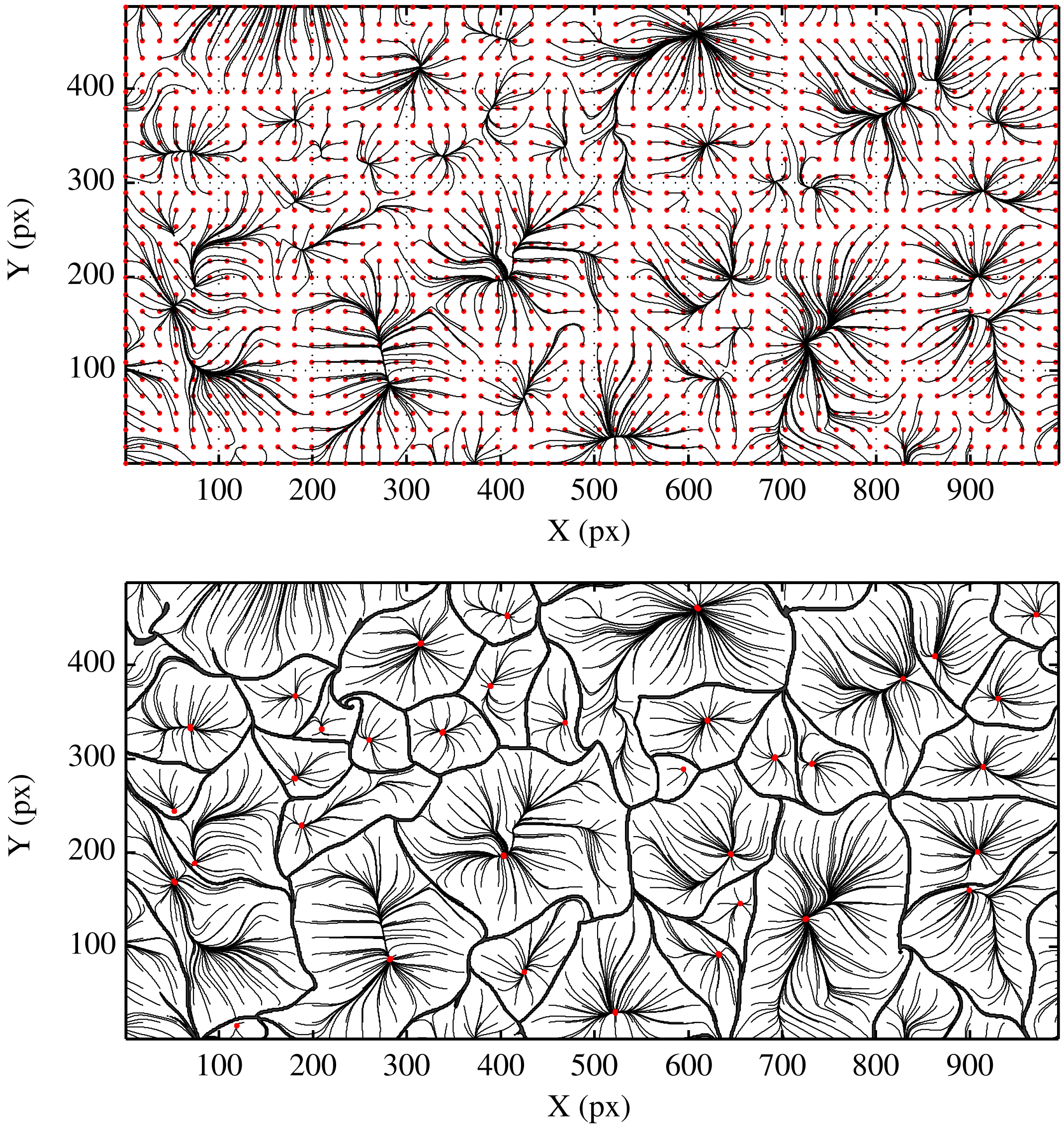

Figure 2.19: *Top: test particles are positioned on a regular grid. Each particle will backtrack the flow along the streamlines (black thin lines). Here, the particles are represented on a coarser grid than the actual computation grid (1 particle per pixel). Bottom: contour map of the convection cells (black thick lines), output by the algorithm, are overlaid on the streamlines.*

boundaries, in which case these "blurry" lines have a physical meaning. This problem is the same as making a picture of boiling water. The longer the time exposure, the more merged the cells appear. Similarly, regardless of the time exposure, smoothing the picture afterwards blurs the boundaries as well. We also mentioned that averaging the velocity field (in time and space) is necessary to reduce the random error. The drawback is that the scales of the flows that can be revealed cannot be much smaller than the averaging scales. No matter how perfect is the segmentation used afterwards to reveal the convection cells, the latter will only be approximate components of the actual flow fields.

2.5.3 Variability of the supergranular flows

The "segmentation" equation defined by Eq.2.46 that provides a map of the supergranular boundaries only operates on "snapshots" of the reversed velocity field. Yet it is important to account for the variability of the flows over time. Indeed, the integration is done along the streamlines of the reversed velocity. In stationary flows, the streamlines and the trajectories are equivalent but the photospheric flows are time-dependent, which is why we choose to produce a time series of dynamic velocity fields. In order to account for the variability of the flow within the longer period of observations used in this thesis (several hours), we produce time series of velocity fields from which we integrate several snapshots of the supergranular lanes, and that are finally averaged.
For example, in Fig.2.20, we have used a running average of 13 velocity fields within 4 hr. Each of the velocity fields is an average over 40 min, with a time interval of 16 min between each of the 13 frames. From each of them, a map of the lanes is produced. Fig.2.20 (bottom) shows the average of the 13 maps of the lanes. In such a figure, the spatial spreading of the lanes carries the variability of the velocity field, in both time and space, in a single map. As a consequence of the averaging, the lanes that are wide-spread are lighter (lower relative distance), and come from more dynamic flows compared to steadier flows that exhibit sharper, darker averaged lanes. Compare it with Fig.2.20 (top) which shows the lanes computed from a single 4 hr-average flow field. The lanes are much sharper. Averaging the flows over 4 hr leaves only the most persistent boundaries, but we have no information on their variations over that time interval.

In this thesis, we use this new visualization method to relate the fine structures of the photospheric convection to the evolution of the magnetic field.

2.5.4 Comparison with the magnetograms

We now have a map of the regions where the flows converge. When available, we can overlay the average magnetograms on the images of the supergranular lanes. MDI/SOHO provides magnetograms and continuum images of the granulation using the same CCD, so the magnetograms and the map of the lanes are already co-aligned.
In Fig.2.21, the lanes are plotted as yellow contour lines over the magnetograms, averaged over the same time (4 hr). Note how the magnetic flux concentrates toward the supergranular lanes. This averaged magnetogram outlines a pattern (known as the "network"), aligned with the supergranular lanes (yellow), which are expected to spatially coincide (Leighton et al. 1962, Simon and Leighton 1964). For this reason, we will sometimes refer to these "lanes" as "supergranular lanes" or "network lanes", interchangeably. We also interpret this alignment of the supergranular lanes and the magnetic network as a qualitative validation of a consistent implementation of all the algorithms that we have described in this chapter.

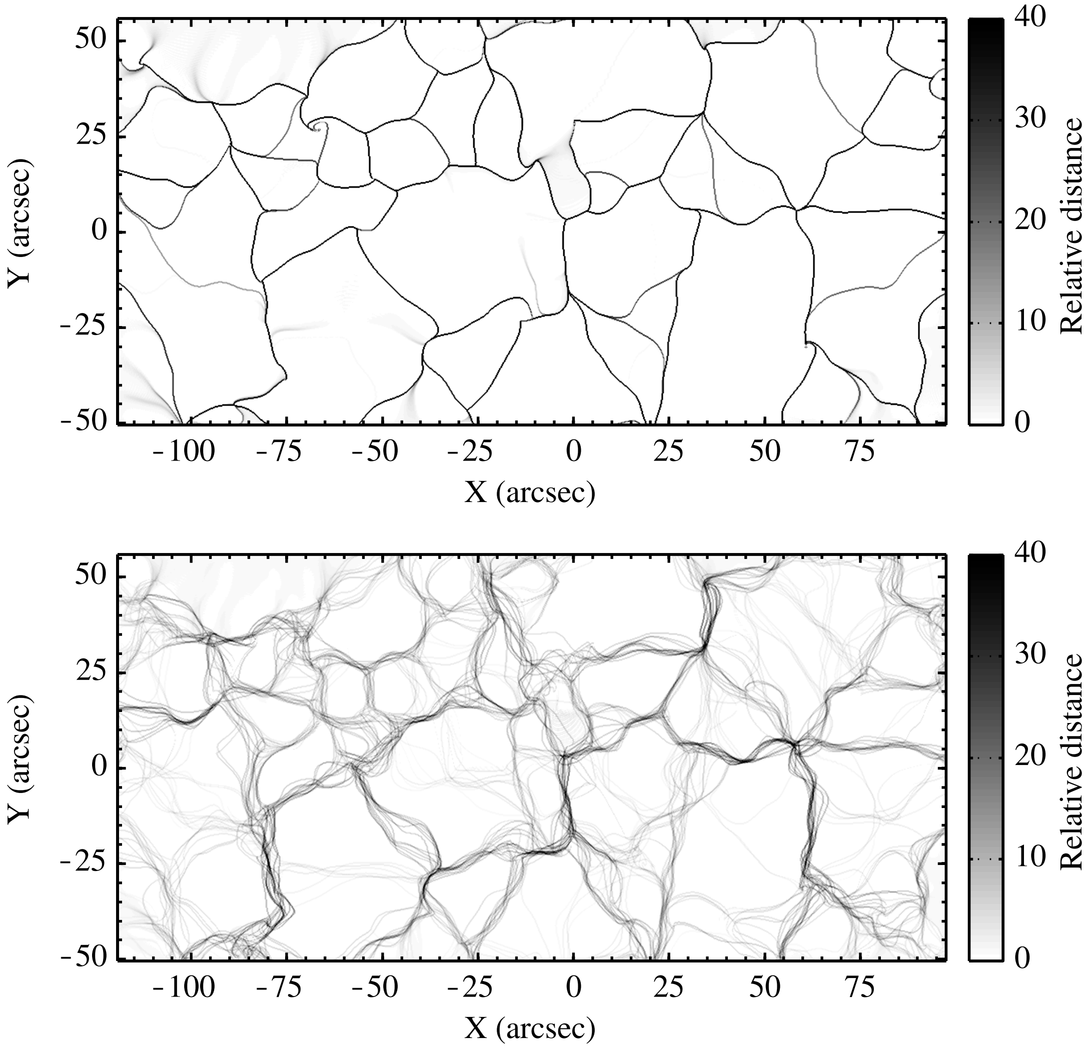

Figure 2.20: *Averaged maps of the supergranular lanes. Top:* 4 hr-*average from the velocity field shown in Fig.2.15. Bottom: average map from the time series of thirteen* 40 min-*average velocity fields, with a time interval of 16 min. The axes are in heliocentric coordinates. The FOV on the top image is the same as on the bottom image.*

2.6 Magnetic Balltracking: tracking the photospheric magnetic flux

One aspect of understanding the origin of small-scale X-ray emission, and more generally, the dynamics of the low corona of the quiet Sun, is to quantify the evolution of the small-scale magnetic flux. This section presents our singular attempt at investigating the evolution of the broad variety of small-scale magnetic features. The latter are not different from those that have been routinely observed in the quiet photosphere, and which were given various names, e.g, pores, knots, magnetic patches.
For a detailed review on their various observational characteristics, see for example Solanki (1993, § 5.6) and the references therein.

Using a method derived from Balltracking, we have developed a new technique to

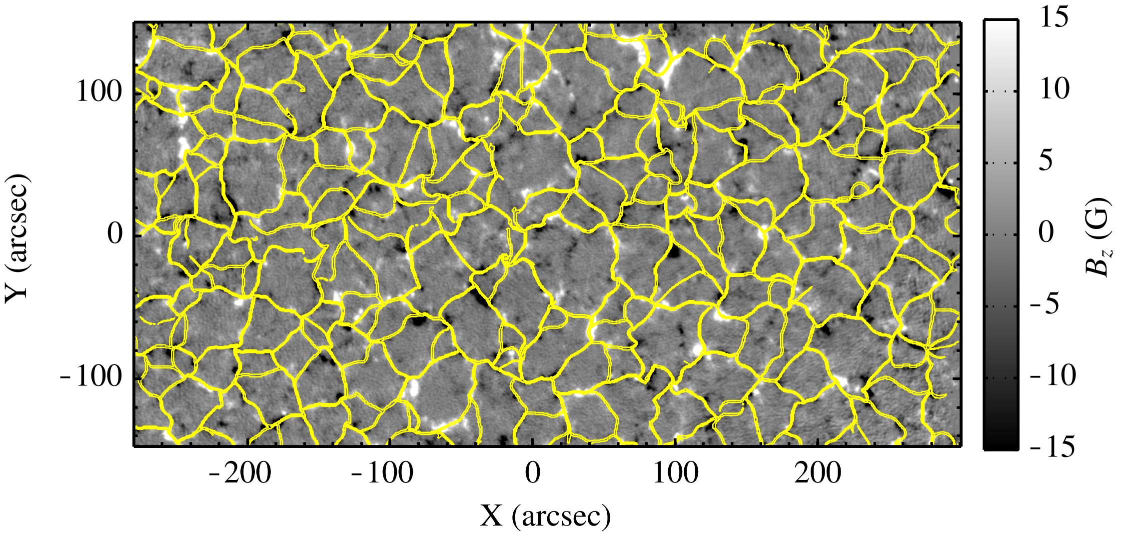

Figure 2.21: *Supergranular lanes represented by the yellow contours on the magnetograms from MDI/SoHO. The gray colormap is scaled between* $-15\,\mathrm{G}$ *and* $+15\,\mathrm{G}$ *to enhance the contrast. The axes are in heliocentric coordinates.*

track the evolution of the individual magnetic features from magnetograms, called "Magnetic Balltracking", with a precision of one px to a few px. This method uses the same basic concept and equations of motion of the "normal" Balltracking that we have presented earlier. We remind that the latter is suited to track features (like granules) whose apparent geometry and displacements are relatively well constrained within three dimensions of similar sizes. The magnetic features that are picked up in the high-resolution Stokes V/I filtergrams (~0.3 arcsec per pixel) from NFI-SOT (Tsuneta et al. 2008) in the quiet Sun, as well as the MDI magnetograms, satisfy these conditions. The so-called "filtergrams" are called "magnetograms" once they have been calibrated into Gauss units (whose procedure will be explained later in this document).

We have divided the Magnetic Balltracking into 4 phases, presented in the next 4 sections (§ 2.6.1 to § 2.6.4). In the last two sections (§ 2.6.5 and § 2.6.6), we present two practical applications of the Magnetic Balltracking.

2.6.1 Phase 1: preprocessing of the magnetograms

With Magnetic Balltracking, the aim is to make the balls able to track the magnetic features. The main change from the "standard" Balltracking is to account for the signed values of the magnetograms, and for the more contrasted intensity, spanning typically over more than 2 orders of magnitude in the quiet Sun (from a few G to hundreds of G). So we have to rescale the magnetograms in order to rescale the magnetic features vertically into "holes" of reasonable depth, either positively or negatively signed, which will allow the balls to settle inside them. This is the purpose of the following preprocessing (see also Figs.2.22 and 2.23).

To start with, let us consider a single magnetogram as a scalar field $B_z(x,y)$, like the one in Fig.2.22 (top). B_z is first reverse-scaled (non linearly) into:

$$B_z^* = max(\sqrt{|B_z|}) - \sqrt{|B_z|}$$

B_z^* is then offset by its mean value and normalized to its standard deviation $\sigma_{B_z^*}$:

$$B_{zn}^* = \frac{B_z^* - < B_z^* >}{\sigma_{B_z^*}}$$

B_{zn}^* is displayed in Fig.2.22 (bottom), with an intensity spanning over a few units, which is of the order of the horizontal size of the magnetic features that we want to track. This rescaled intensity can be seen as a geometrical height. In a 3D plot (Fig.2.23), the magnetic features look like holes into which the balls can settle easily.

2.6.2 Phase 2: initialization

Once the magnetograms are rescaled, the balls are initially positioned at the pixels whose absolute intensity in the original (not rescaled) magnetogram is above a given threshold. This initialization is illustrated in Fig.2.24 (top) where the balls center are plotted on the original magnetograms (small red crosses).
With the magnetograms from NFI/SOT, the threshold is usually set between 10 G and 20 G. These values are chosen so we do not track random noise. In addition, this saves some computational time by reducing the number of balls which is much smaller than the total number of pixels. In the Magnetic Balltracking, we do not make assumptions on the size of the magnetic features, and the minimum length between the ball centers, within each magnetic feature, is 1 px at any time.

Once the balls are positioned on the magnetic features, or "magnetic holes", the polarity of these features is retrieved from the signed intensity of the original magnetogram, at the positions of the ball (i.e, at the coordinates of their center). This polarity (plus or minus) is stored, and is a constant associated with each ball. It is referred to as the initial "ball polarity". Next, a few integration steps, typically 10 to 20 depending on the size of the features, are performed between the first and second frame, so the balls have time to converge down into the local minima.

Because a segmentation algorithm will be used on the tracked magnetic features (more on that later), it is not necessary to have several balls within the same feature. If several balls have converged to the same local minima, only one ball is kept. After this stage, it is still possible to have one large magnetic feature being tracked by several balls, if for instance the feature has several local minima. This is illustrated in Fig.2.24 (bottom). Note that this significantly reduces the number of balls between the first (top) and the next frame (bottom), as much as the computational time.

2.6.3 Phase 3: main tracking phase

After the initialization, the next frames are loaded, and the balls track the local minima (the "magnetic holes") like they do within intergranular lanes with the Balltracking.

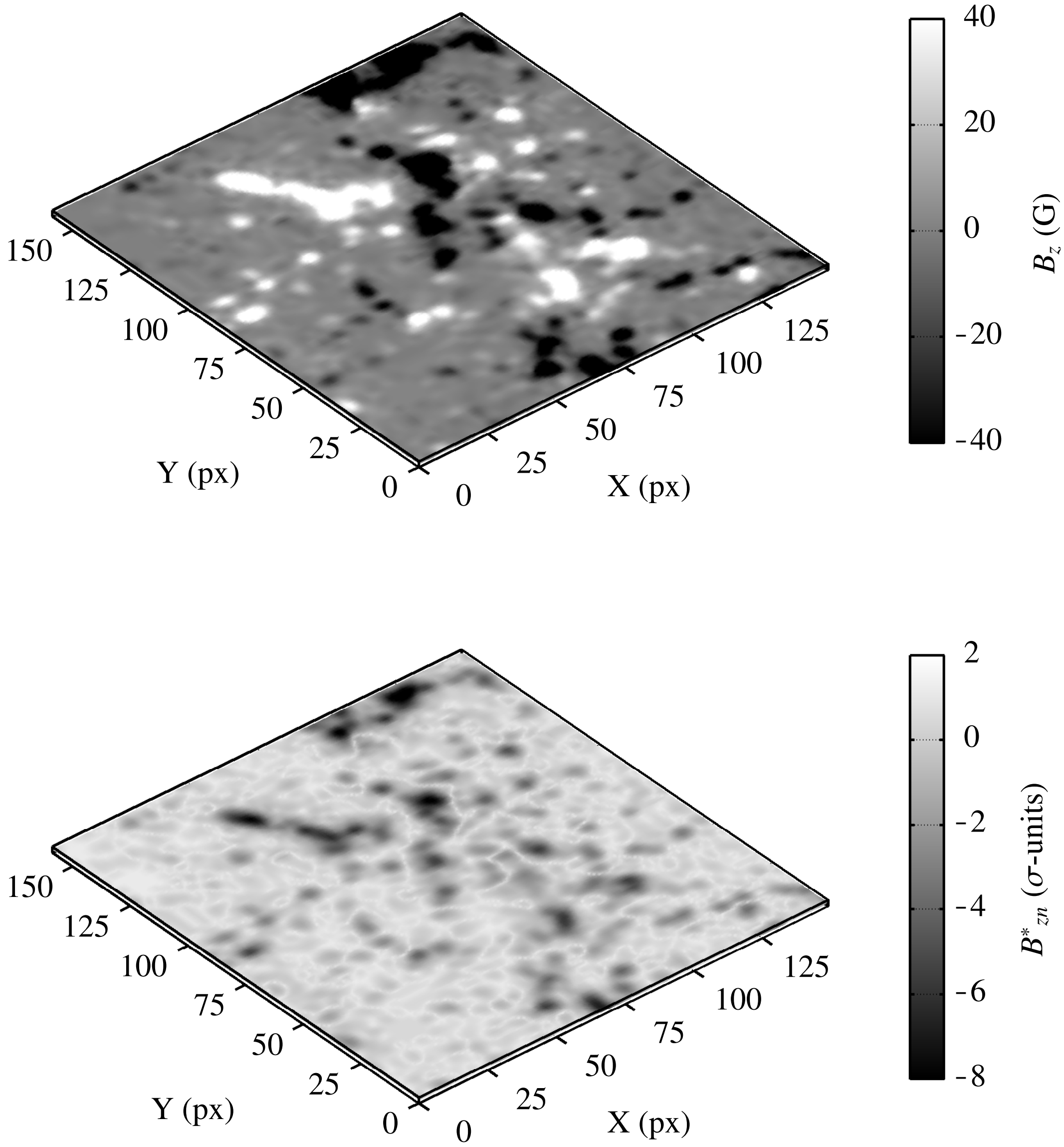

Figure 2.22: *Preprocessing of the Magnetic Balltracking. Top: Initial NFI filtergram* B_z*, calibrated into Gauss units, scaled between* $-40\,\mathrm{G}$ *and* $+40\,\mathrm{G}$*. Bottom:* B^*_{zn} *obtained after rescaling* B_z*.*

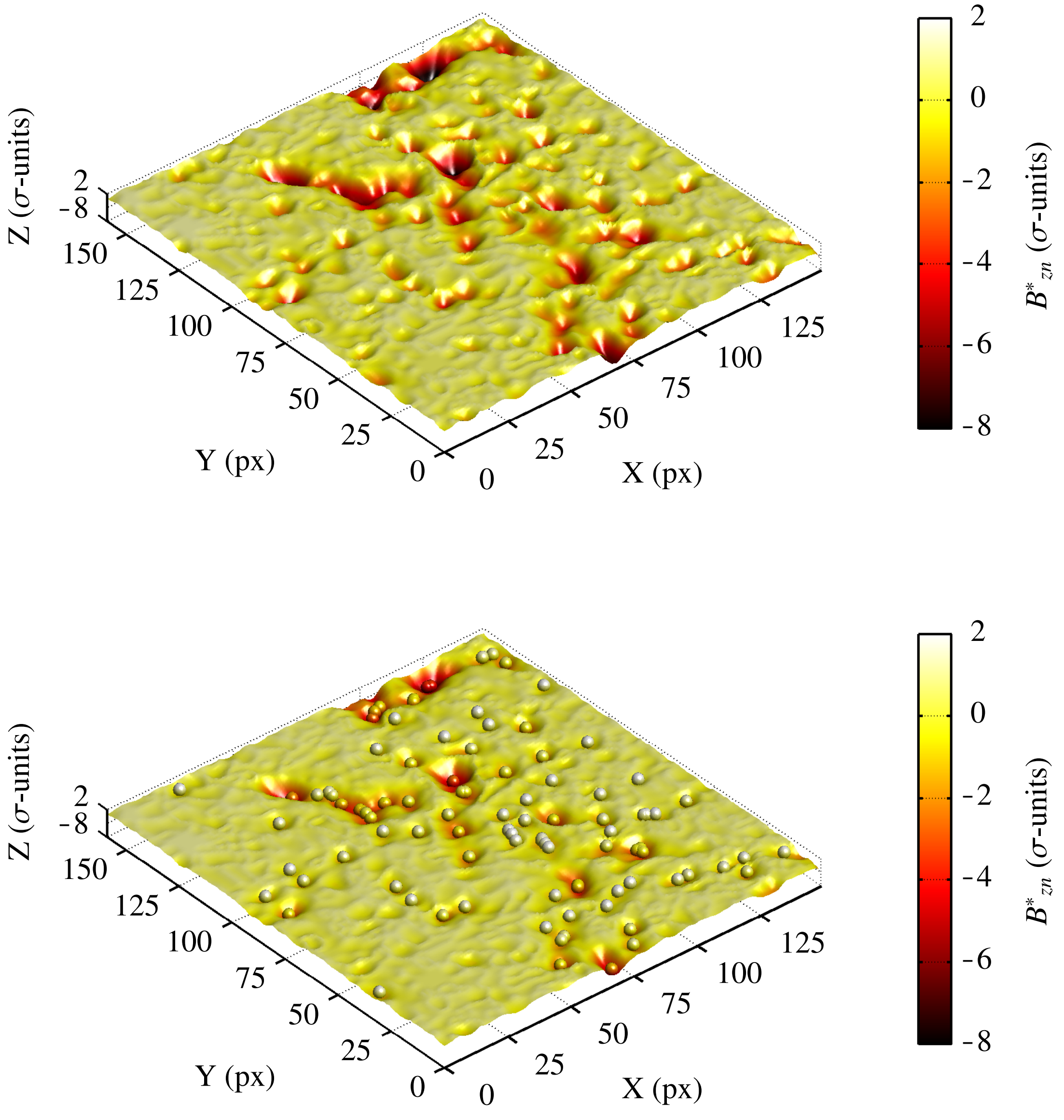

Figure 2.23: *Top: B^*_{zn} in 3D, using the same data as in the bottom of Fig.2.22, with the intensity used as a geometrical height. The colormap is scaled exactly as the intensity. Bottom: same as the top figure, with balls that have settled in the "magnetic holes" after a few integration steps. The position of these balls on the original 2D magnetograms are shown in Fig.2.24.*

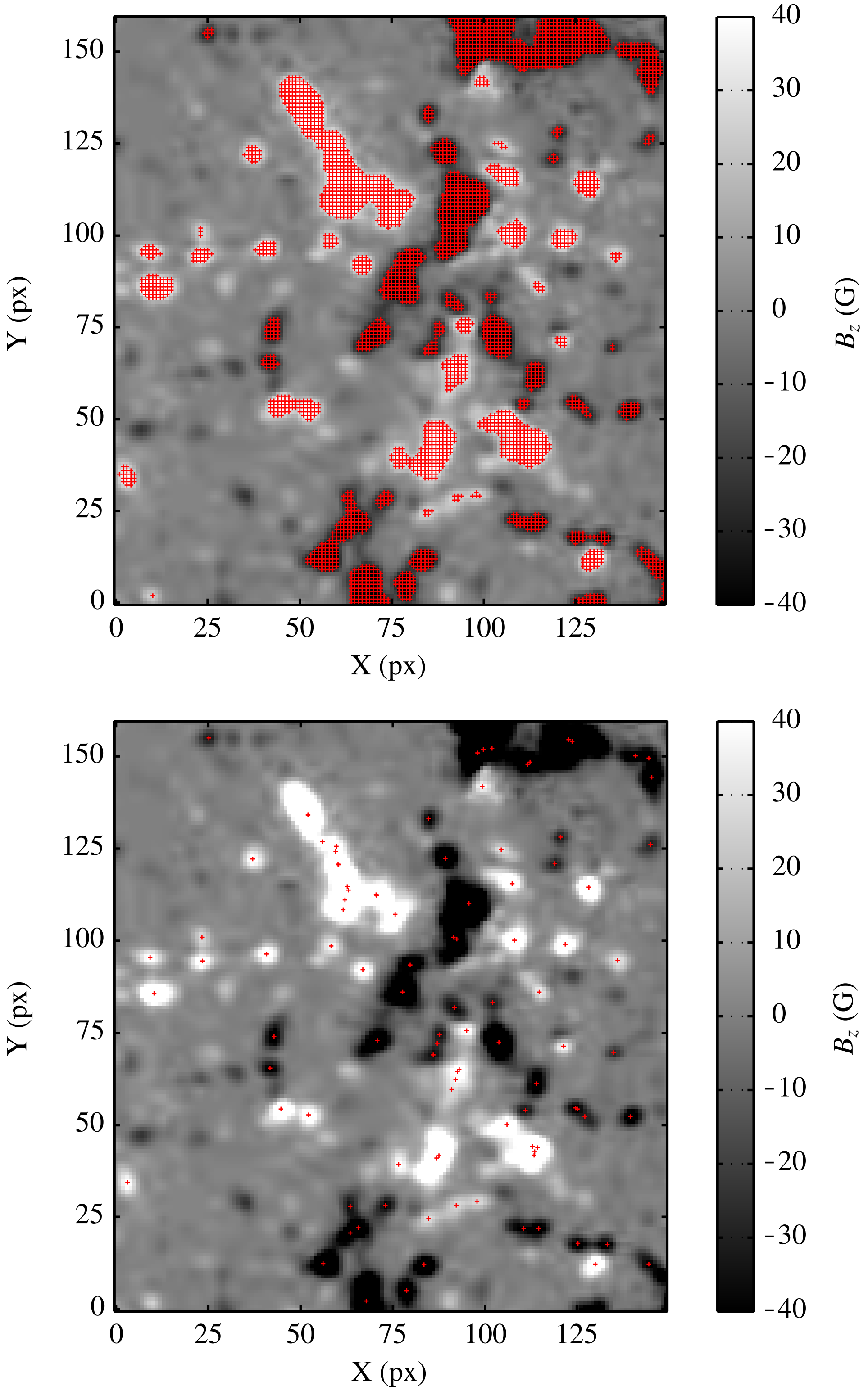

Figure 2.24: *Initialization of the Magnetic Balltracking. Top: The values in the original magnetogram B_z are used to dispatch the balls on pixels above* 20 G *(red crosses). Bottom: New positions of the balls, after integrating the equations of motion, on the same magnetogram.*

In the original magnetograms, the local minima of the rescaled frame correspond, respectively, to the local maxima and minima of the signed intensity (plus and minus, respectively) of the magnetic flux. At any time, the position of the ball is known, and each ball is tagged with a unique number. The positions can be plotted on-the-fly, so that one can check by eye the quality of the tracking. An example of the main tracking phase is visible in the snapshots of Fig.2.25.

When a magnetic feature is moving too rapidly, the balls do not have time to settle in the local minima. In this situation, at worst, they may be delayed by a few frames, and several integration steps between each frame are necessary to make sure that the balls do not get lost. This gives them more time to "catch up" on the fastest features. Typically, for magnetograms taken at cadences of up to 3 min, 10 to 20 intermediate integration steps of the equation of motion are used between each frame. This may or may not be the same number of intermediate steps used for the initialization phase, these are indeed two independent "tuning" parameters.

For large connected magnetic features, the shape of the magnetic features looks like a carpet full of holes, where each hole can be filled with a ball (see Fig.2.23). This is very convenient to track clustering flux, as it has been reported quite often that large magnetic patches cluster into several pieces that are swept out by the supergranular flows (Solanki 1993). The algorithm can follow each of these clustering pieces.

At each tracking step, the polarity under the current position of the ball center is compared to the ball polarity. The tracking of a ball ends as soon as this polarity is reversed with respect to the initial one (the ball polarity). This strategy has several advantages. Indeed, to "see" a reversed polarity, a ball needs either to keep tracking down to the noise level until the first opposite value appears (this current value is taken in the original magnetograms), or it needs to encounter a magnetic feature of opposite polarity. Each of these two conditions are described below separately. If none are fulfilled, the ball keeps tracking until the last magnetogram is processed.

Condition 1: tracking down to the noise level

Tracking down to the noise level makes the algorithm use the true sensitivity of the instrument. Indeed, even if the initialization step uses a threshold, the features are tracked until they cannot be detected by the instrument, i.e, to values below the threshold. Should we ever need to track the faintest magnetic features from the beginning, the threshold may simply be lowered down to the noise level, which has the only consequence of increasing the computing time (more balls will be added).

Another advantage is that this allows any ball to track any faint feature with weak flux, which seems like skimming under and above the noise level, and which makes it disappear for about 1 or 2 frames. When it happens, the ball simply drifts on the flat surface with whatever momentum and inertia it had from the previous state, which makes it stay on its last track for a limited time (determined by the damping time T_d). This limited time sometimes (but not always) is enough to keep track of the weak flickering flux that we observe in NFI/SOT. If not even the weakest flux is detected after this limited time, which means that the ball is floating over pure random noise, the sign of the intensity in the original magnetograms eventually reverses, in which case the ball is removed.

Condition 2: no crossing of reverse polarity

Another issue we had to solve is how to prevent the ball from crossing a feature with positive flux to a neighboring one with negative flux. This would occur for example if the ball is in a local minima, and if it has kept enough momentum to reach another close-by local minima of opposite polarity at the next integration step. This can also occur, if the close-by local minima move quickly toward the ball, like for example in the case of the two footpoints of a loop being submerged.
This problem can be thought of as a "numerical tunnel effect", in the sense that at one time a ball is in a magnetic hole, and at the next, it has crossed a barrier and lies within the second magnetic hole.
The solution is as follows: because the true polarity of each pixel is known from the original magnetogram, the local minima are always associated with a polarity, which is compared to the initial ball polarity (see § 2.6.2) at the end of each integration step. Should a ball lie in a magnetic hole with a polarity opposite to the ball polarity, the ball is removed.

Condition 1 and 2 are checked independently for each ball. If any of these two conditions is fulfilled for a given ball, its tracking ends, so that the lifetime of a ball corresponds to the lifetime of the magnetic feature tracked so far. This does not end the whole algorithm which continues as long as other balls remain.

Note also that the magnetic features may exist at very irregular places (see Fig.2.24, top), and consequently, the balls usually get moved to very irregular locations. Therefore, contrary to Balltracking (see § 2.2.5), the conversion of the velocity initially calculated in a Lagrangian frame of reference, to a Eulerian frame of reference, cannot happen. In other words, this method tracks and follows the individual motions of the magnetic features. It cannot output a "flow field", with the values of the velocity at any given time on fixed positions, on a regular grid. This is simply because there are parts of the frame where the magnetic flux is not detected, and thus, there is no velocity to be defined there. At best, such Eulerian flow fields can only be derived locally, in regions where there are enough magnetic features that allow a "reasonable" sampling.

2.6.4 Phase 4: detection of emerging flux

The algorithm permanently scans for new pixels that would rise above the initialization threshold. When it happens, new balls are added on these areas so that emerging flux can be tracked. The rest of the tracking is exactly the same as for the other balls. Thus, the balls are able to detect emerging flux, and track them until the flux disappears again. An example is given with the ball 5450 in Fig.2.25 (starting from frame 5, near the upper right corner, seen as a small yellow cross). It is tracking emerging flux that, before frame 5, was below the initialization threshold of 10 G. When the magnetic feature emerges above 10 G, this new ball locks onto it and tracks it until the last frame. This phase makes the algorithm useful not only to track the flux visible from the start, until its cancellation, but also to track the emerging one.

In this thesis, we use the positions of the balls for two purposes. The first one is to track the time-dependent displacements of the local extrema of the flux. These positions

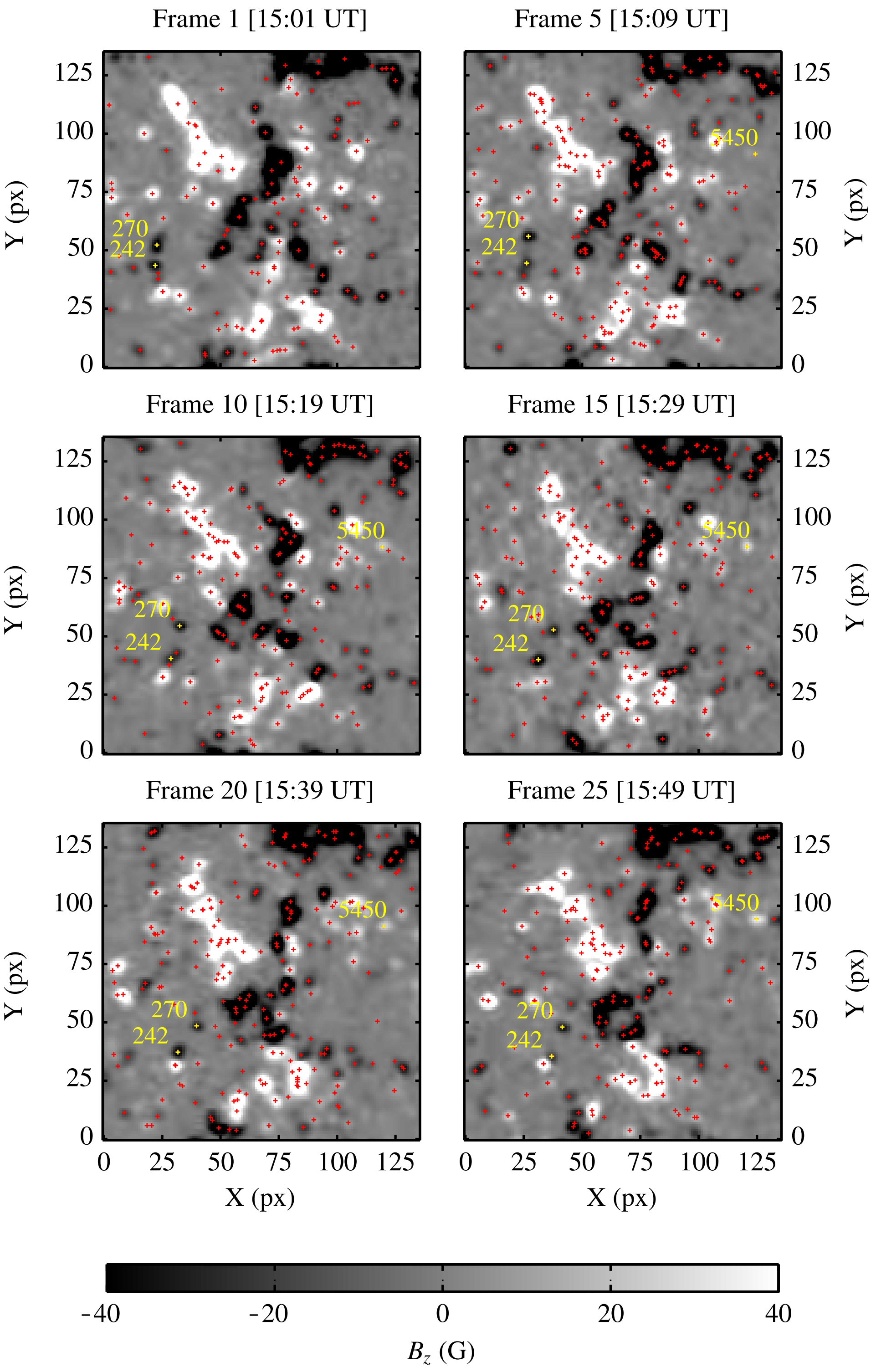

Figure 2.25: *Magnetic Balltracking of a small field of view of NFI, at different time steps. The numbers bound to the crosses (yellow) are the tags that are unique to each ball.*

are then used in a segmentation algorithm to integrate the flux over the area of the tracked features. The second purpose is to track magnetic field lines when performing magnetic field extrapolation. These two applications are explained in the next two sections.

2.6.5 Primary application: segmentation of the magnetic features

As mentioned earlier, the magnetic features can be very clustered in the quiet Sun, and quantifying the evolution of each bit of such magnetic structures that can be near the limit of the instrumental resolution is quite challenging. As explained in the previous sections, the Magnetic Balltracking tracks the time-dependent positions of the local extrema of individual magnetic features. Thus the next step in describing their evolution is to integrate the magnetic flux of these features. An easy way to do this is by applying a "region extraction" algorithm. The technique is also known as "region growing", and has many names and variations that depend on the scientific field in which this segmentation technique is applied. It is one of the basic algorithms detailed in textbooks of digital image processing (see for example Gonzalez and Woods 2008, Chapter 10, § 10.4).

This "region growing", here, consists in extracting the magnetic features that have been tracked, from the rest of the magnetograms, so we can easily integrate the intensity of the flux over the extracted area. We use the tracked positions (the final positions of the balls in each frame) that we call "seed points". For each position (or each "seed point"), the difference between the intensity of the neighboring pixels and the one of the initial pixel (the seed) is compared to a given threshold. If the comparison is true (in the logical sense), it is added to a list of pixels connected with each other, including the seed, which "grows" a region and thus segments the magnetic feature from the rest of the magnetogram. If the comparison is false, the pixel is not added to the list. The region stops growing when there are no more connected pixels. The output of the region-growing algorithm is a binary mask: an array of logical values, co-spatial with the magnetograms, where the pixels in the grown region are set to 1, and the other pixels are set to 0. These masks can directly be used to extract the features from the magnetogram in order to integrate the flux of the tracked features. Such extracted features are visible in Fig.2.26, which used the tracked positions (i.e, the seeds) previously illustrated in Fig.2.25 as the input of this segmentation.

As mentioned in the previous section, several balls may track wide magnetic features, with as many balls as there are local extrema in it. As the position of these balls are used as seed points, they will ultimately extract the same connected pixels, and output identical masks. So we have to get rid of the duplicates, which we do by using a logical "or" (equivalent to a logical "union") between all the extracted masks. If the same masks of connected pixels are output for different balls, the logical "or" reduce them to one unique mask before integrating the flux. This makes sure that, when looping over the extracted regions to integrate their flux, we do not integrate it over the same region more than once.

Finally, each magnetogram is integrated over these masks. This gives the flux of each tracked feature, in each single frame. Repeating this for all the magnetograms provides the time-dependent flux of all the tracked features, including the emerging one if any has been detected during the tracking. The ball numbers are like tags of the magnetic features,

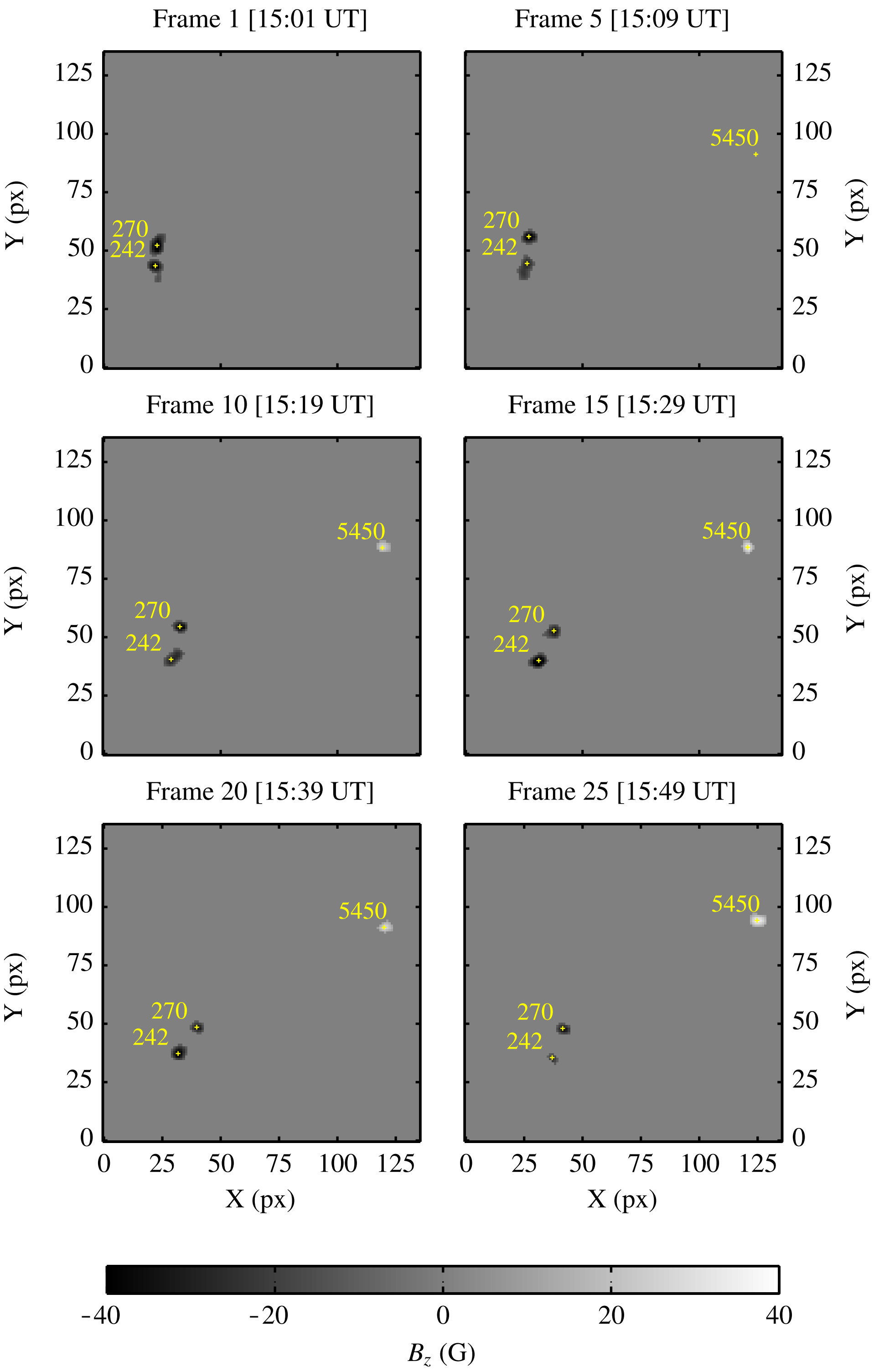

Figure 2.26: *Region of the magnetograms extracted using the region-growing algorithm onto the balltracked seed-points of Fig.2.25.*

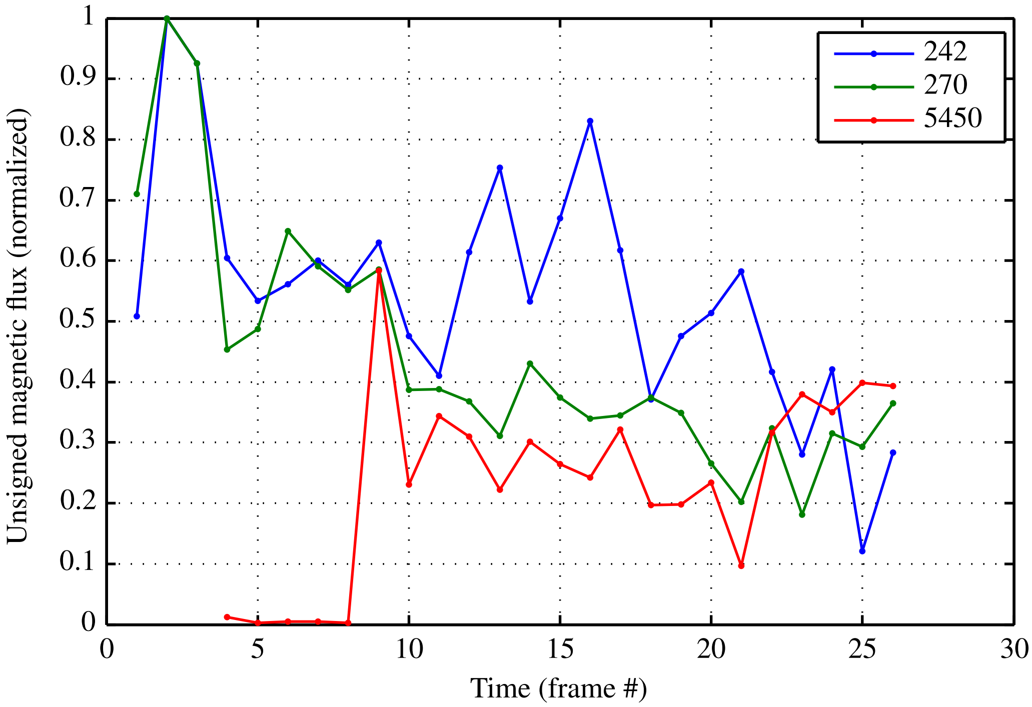

Figure 2.27: *Absolute value of the integrated intensity over the positive and negative areas, for the balls used in Fig.2.25, and using their respective masks in Fig.2.26. The X-axis is the time axis, in units of frames, with one frame taken every* 2 min.

which gives also the ability to select them individually. This way we can choose which one to extract with the region-growing algorithm, but it is also possible to simply take all of the tracked features for more global statistical analyzes. The result of this integration is given in the graph of Fig.2.27 for features manually selected with the tags (i.e, the ball numbers) in Fig.2.26. The X-axis is in unit of frames, with 2 min between each frame. Notice the emerging flux that has been detected by the ball 5450 during phase 4, and that has been automatically extracted by the segmentation algorithm. In Fig.2.27, the raw results are plotted, and show discontinuities and oscillations. These are caused by the too coarse time sampling of the magnetograms (taken every 2 minutes). A possible source of oscillations in the different curves could be a side effect of the p-modes oscillations (Leighton et al. 1962), and that would contaminate the spectro-polarimetric measurements. As an indirect consequence we expect the signed intensity in the magnetograms to skim above and below the threshold set in the region-growing algorithm. However the current limitations of our segmentation algorithm makes this explanation still very speculative. In this hypothesis however, when the balls track areas with low intensity, the time-dependent fluxes such as the ones in Fig.2.27 may oscillate at p-modes frequencies close to 3.3 mHz (i.e, a period of 5 min).

One limitation of this method is that it cannot grow a region using too low thresholds, otherwise, close but probably non-connected regions may be added to the list of "good" pixels. This leads to a wrong segmentation, and ultimately a biased estimation of the flux. This could probably be solved using a more sophisticated segmentation algorithm. For consistency, we use thresholds close, but not necessarily equal to the thresholds used in the previous phases of the Magnetic Balltracking (defined in phase 2). They are between, typically, 5 G and 15 G. We found these values by "try and error" and they turned out to be optimal in the very clustered flux of the quiet Sun. A direct unfortunate consequence is that no flux is integrated below these thresholds.

Other algorithms designed to track magnetic features exist, such as in Démoulin and Berger (2003) and Welsch et al. (2004), which are focused in deriving averaged velocity flows in magnetized regions. The Magnetic Balltracking, instead, is used here to track and tag individual features, which we use to quantify the flux in clustered field where a more global approach does not provide enough resolution. Indeed, as we have already mentioned, the displacements are calculated in the Lagrangian frame of reference, and are averaged neither in space, nor in time, which makes our method offer nearly as much resolution as given by the instruments.

Another application of the Magnetic Balltracking is the time-dependent and coherent tracking of magnetic field lines obtained from magnetic field extrapolations. This is presented in the next section.

2.6.6 Secondary application: tracking magnetic field-lines

The magnetic field vector **B** in the corona can be obtained by extrapolating the measurements in the photosphere, using magnetograms (longitudinal component of **B**) or vector magnetograms (3D **B**) as the boundary condition (see Thalmann 2010, Chapter 2). The extrapolation models often used are the ones assuming force-free conditions, in which the currents **J** are aligned with the magnetic field ($\mathbf{J} = \alpha\mathbf{B}$), so that the $\mathbf{J} \times \mathbf{B}$ force vanishes, and where the linear coefficient α defines three extrapolation schemes:

- $\alpha = 0$: Potential field extrapolation (no current).
- $\alpha =$ constant : Linear Force-Free Extrapolation (LFFE)
- $\alpha = \alpha(z)$ where z is the altitude above the photosphere : Non-Linear Force-Free Extrapolation (NLFFE).

Another application of the Magnetic Balltracking is the time-dependent tracking of 3D magnetic field lines obtained from an extrapolation method like the ones mentioned above. As described earlier, the algorithm tracks the local maxima of the magnetic flux, and tags the corresponding magnetic elements by a unique number (the ball number), which is kept during its whole lifetime. If the positions of the corresponding balls are used as the footpoints of 3D magnetic field lines, one can automatically track, and trace the field lines passing through the local maxima, while the latter are being advected by the flows.

For example, by using an extracted set of magnetic features as footpoints, one can track a group of closed field-lines (or even a flux tube), and distinguish, over time, which ones have reconnected, or reconfigured, to other field-lines from one magnetogram to the next, and which ones have not, and therefore we keep track of the evolution of the magnetic topology.

Since we dispose here of magnetograms, the LFFE is used for illustrative purposes only, and for demonstrating the capabilities of the Magnetic Balltracking. We also use

LFFE with $\alpha = 0$ for potential field solutions. Our algorithm is an implementation of the solution from Seehafer (1978), where the magnetograms are used as the bottom boundary condition. They also are mirrored on each side to satisfy the condition of flux balance. Thus extrapolated magnetic field near the edges of the magnetograms is less meaningful, since it accounts for much less information than the field extrapolated from the center of the magnetograms. We do not intend to justify the validity of force-free, or potential conditions in the quiet Sun, but we use the method only to emphasize the applications of the Magnetic Balltracking. More details on the implementation of LFFE are in Wiegelmann et al. (2005a,b). For more discussion on the force-free conditions in magnetic field extrapolation, one can also refer to Metcalf et al. (1995), Schrijver and van Ballegooijen (2005).
An example of field line tracking is shown in Fig.2.28, using the tracking shown in the previous figures. One can see the small magnetic features, moving around from one frame to another, where a magnetic field-line is automatically drawn from the balltracked positions of the local maxima.

While tracking field lines cannot represent the whole information contained in an extrapolated 3D vector magnetic field, we believe it is a much more consistent method when dealing with time series, compared to other methods.
Indeed, from discussions with users and developers of extrapolation techniques (Wiegelmann et al. 2005b, Thalmann 2010), the two methods usually used to draw field lines are either based on an arbitrary selection of field-lines, designating the footpoints by hand, or using thresholding.
In the former method, one eventually changes the footpoints to obtain the representation that "looks right". In the latter method, all the pixels above a certain threshold, or a coarser grid within them, are used as footpoints. In none of the two methods the time-dependency is explicitly taken into account. Regardless of the extrapolation method used, the Magnetic Balltracking is able to take the time into account when representing time-dependent magnetic field configurations.

2.7 Summary

In this chapter, we have presented our implementation of an efficient method to measure the photospheric flow fields, called "Balltracking". We also used a segmentation algorithm that reveals the supergranular boundaries, out of which we were able to represent the finer dynamic of the supergranular convection by applying it to running averages of the velocity fields. From the Balltracking, we have developed a by-product, called "Magnetic Balltracking" that tracks the magnetic features down to their finest scales. This new algorithm allows us to quantify the evolution of the magnetic flux, and to make time-consistent tracking of magnetic field lines. In the next chapter, we present science studies that make use of Balltracking and of Magnetic Balltracking, with observations of the higher layers of the quiet Sun atmosphere.

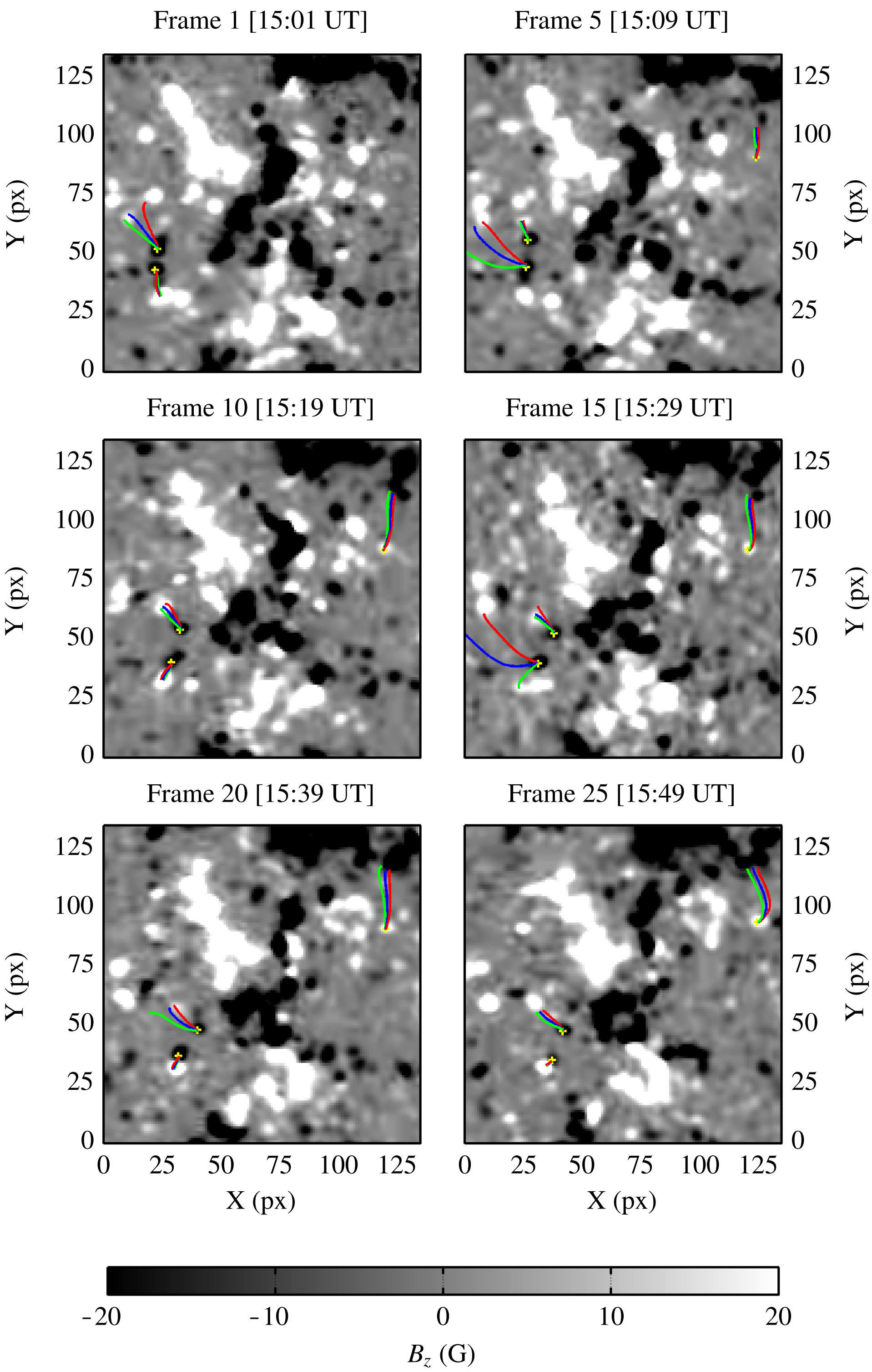

Figure 2.28: *Time-series of magnetograms (gray-scaled background) with magnetic field-lines from a 3D extrapolation. The snapshots are displayed every 5 frames (*15 min*). Green,blue and red correspond (respectively) to* $\alpha = +0.04, 0, -0.04\,Mm^{-1}$ *. The axes are in SOT pixels.* 1 px ≈ 0.2 arcsec ≈ 0.15 Mm.

3 Practical applications on case studies

3.1 Balltracking on granulation

3.1.1 Observations

The Balltracking algorithm was first used for tracking the photospheric flows using continuum images (Potts et al. 2004) from MDI/SoHO. We have adapted the algorithm to process images obtained with the Broad-Band Filter imager of Hinode (BFI). For this analysis, the instrument provided three time series of de-rotated images of the quiet photosphere, i.e, outside of active regions. They both share the same FOV of $\sim 110 \times 110$ arcsec^2 ($\sim 86 \times 86\,\mathrm{Mm}^2$):

- 1-hour time series of blue continuum (granulation) and Ca II images on 10 April 2007 between 17:00 and 18:00 UTC with a cadence of 2 min at disk center.
- 4-hours of contiguous G-band and blue continuum images on 07 Nov 2007 between 1:00 and 5:00 UTC near disk center at a 3 min cadence.
- Ca II images were also taken during the blue continuum time series at the same cadence. They come from the same optical assembly as the granulation images, and co-spatial the granulation images. They are used as a scalar proxy of the magnetic field (Simon and Leighton 1964) co-spatial with the velocity fields derived with Balltracking.

The three datasets were first binned onboard to 0.1 arcsec per pixel (binning 2x2) and then corrected for dark currents, flat-fielding, and instrumental jitter using standard calibration procedures written in Solarsoft. For better computational efficiency, we binned the calibrated images by another factor 2 giving a final pixel size of 0.2 arcsec, which is still 3 times smaller than the resolution of MDI, and resulting in images of $512 \times 512\,\mathrm{px}^2$. With the continuum images, the average width of the visible intergranular lanes is about 2 px, which is the radius that we set for the balls. We also used the Na I stokes V/I of the Narrow-Band-Filter imager (NFI/Hinode) for preliminary estimates of the longitudinal magnetic field.

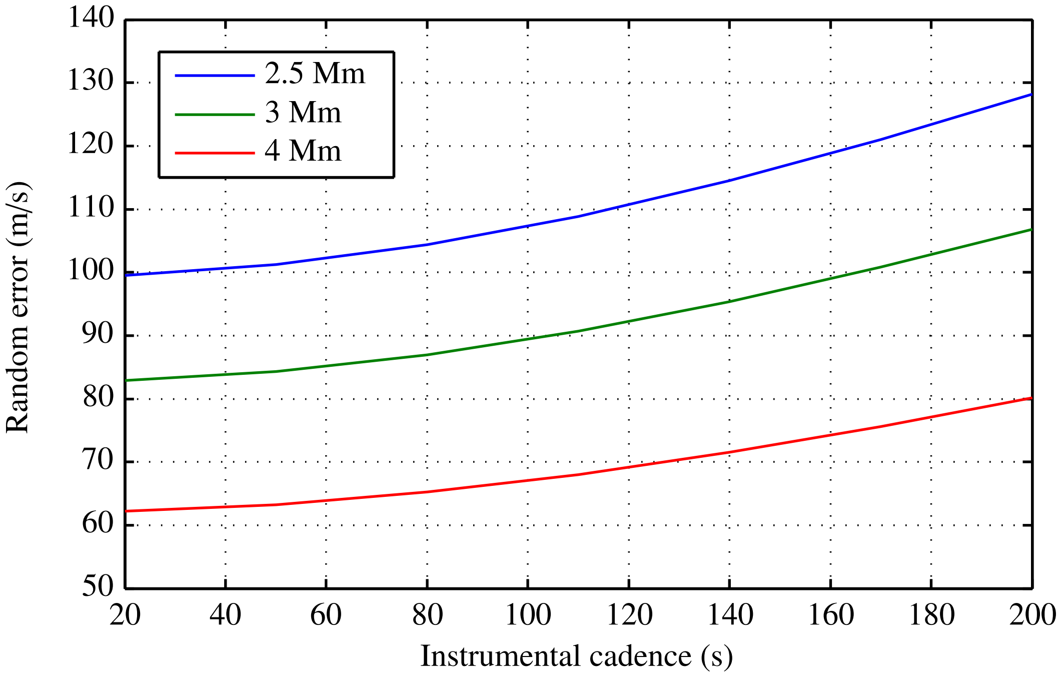

Figure 3.1: *Uncertainty on the velocity measurements* σ_v *at a* 45 min *time averaging for three values of spatial smoothing, with respect to different instrumental cadences (i.e, time interval between each image).*

Since our datasets have a cadence of 2 min and 3 min, the uncertainty on the derived velocities has been recalculated for each, following the definition in Potts et al. (2004):

$$\sigma_v = \frac{\sigma_u}{\sqrt{n_r n_t}} \tag{3.1}$$

where n_r and n_t (respectively) are the effective spatial and temporal numbers of samples, and σ_u is the standard deviation of a Gaussian distribution approximating the velocity distributions of the granules. It is set to 800 m s^{-1} (Roudier et al. 1999). Our velocity fields were spatially smoothed over 4 Mm for both datasets. The results from the 1-hour and 5-hour observation series were averaged over 30 min and 45 min, respectively. The choice of 4 Mm is a compromise between a better accuracy of the velocity measurements and a spatial resolution high enough to distinguish the motions in narrow network lanes. Fig.3.1 shows the random error σ_v on any of the 2 components of the horizontal velocity flow as a function of the instrumental cadence, for different spatial smoothing, and averaging over 45 min. The uncertainty on the velocity flows averaged over 45 min from the 3 min cadence dataset is then ~80 m s^{-1}. At a 2 min cadence and for a 30 min average (not shown here), the uncertainty is similar.

Nevertheless, considering that the mean lifetime of the granules is ~5 min, we believe that the granular motions cannot be properly sampled at cadences of 2 and 3 min. Moreover, the removal of the instrumental jitter needs at least 2 images during the time over which the features do not change significantly. It cannot be guaranteed in these datasets. For these reasons, quantitative results may not be reliable. However, since we consider features on greater scales in time and space than the granular motions, the shape of the underlying velocity field, hypothetically, can still be properly revealed (Potts et al. 2004).

To test this hypothesis, we have compared the effects of different cadences on the final result of Balltracking. As a test, we used another time series of images of 3 hr from 11 November 2007, with a cadence of 20 s from which 3 datasets with a cadence of, respectively, 1, 2, and 3 min were extracted. They were balltracked, smoothed, and averaged over 4 Mm and 30 min with the same sets of input parameters in Balltracking, and the same calibration coefficient (see § 2.2.5) derived from the 1 min-cadence data. Here, the use of the same calibration coefficient is only to set a reference point for the comparison. The velocity distributions are shown in Fig.3.2. The upper panel shows that they are well fitted by a Rayleigh distribution with mean velocities of about, respectively, 370 m s^{-1}, 270 m s^{-1}, 220 m s^{-1} which decreases with the instrumental cadence. Therefore, lowering the cadence from 1 min to 3 min acts as a low-frequency filter in Balltracking, which only picks up slower granules with lifetimes greater than 5 min. We can compensate this, however, by calibrating the velocity fields with three different calibration coefficients associated with the three different cadences (§ 2.2.5). This is shown in the bottom panel of Fig.3.2. There are now very little differences between these distributions, although they are not strictly identical, with mean velocities of, respectively, about 370 m s^{-1}, 370 m s^{-1}, and 380 m s^{-1}. The mean velocities of the first two flow fields are indeed equal. If we account for the measurement errors of ~13% (§ 2.3), these three domains of measurements overlap, which supports our initial hypothesis that even the 3 min-cadence images can still be used to derive meaningful flow fields.

Fig.3.3 represents the distribution of the velocities of the 10 April 2007 dataset. The modal[2] and mean velocities are equal to, respectively, 335 m s^{-1} and 420 m s^{-1}. It is important to note that, by smoothing over 4 Mm, and by averaging over 30 min, our velocities are lower than the usual average speed measured in granular flows. A perfect tracking of the granular flow needs less smoothing and averaging. When the latter are reduced, the modal and mean velocities indeed increase toward higher values that are more consistent with the results in Wang et al. (1995), Berger et al. (1998), and Roudier et al. (1999). For example, the latter measure modal velocities of granules greater than 600 m s^{-1}, using temporal windows of 5 min. In our framework, the granules are only used as tracers of the underlying velocity flow. Therefore, the smoothing and averaging must be increased to reduce the uncertainty introduced by the stochastic nature of the granular motions.

3.1.2 Results

The velocity flows derived from Balltracking on both datasets are shown in Figs.3.4 (April's dataset) and 3.5 (November's dataset). The black arrows are made of several small segments so they can bend along the streamlines to show the direction of the flow (see also close-up in Fig. 3.8). The light blue lanes in the background are the emphasized borders of the supergranular cells derived from the automated lanes recognition algorithm (Potts and Diver 2008a) (see § 2.18). A large-scale converging vortex flow is clearly visible in each dataset (in the red rectangles). The first one is ~15 Mm and the second one is somewhat larger ~20 Mm, although it is not clear where to set the limit of the influence of these vortices. Both of them are located at supergranular junctions as indicated by the blue network lanes. Their relative positions in each field of view are similar but this

---

[2] The modal velocity is the most probable velocity, at the maximum of the probability density.

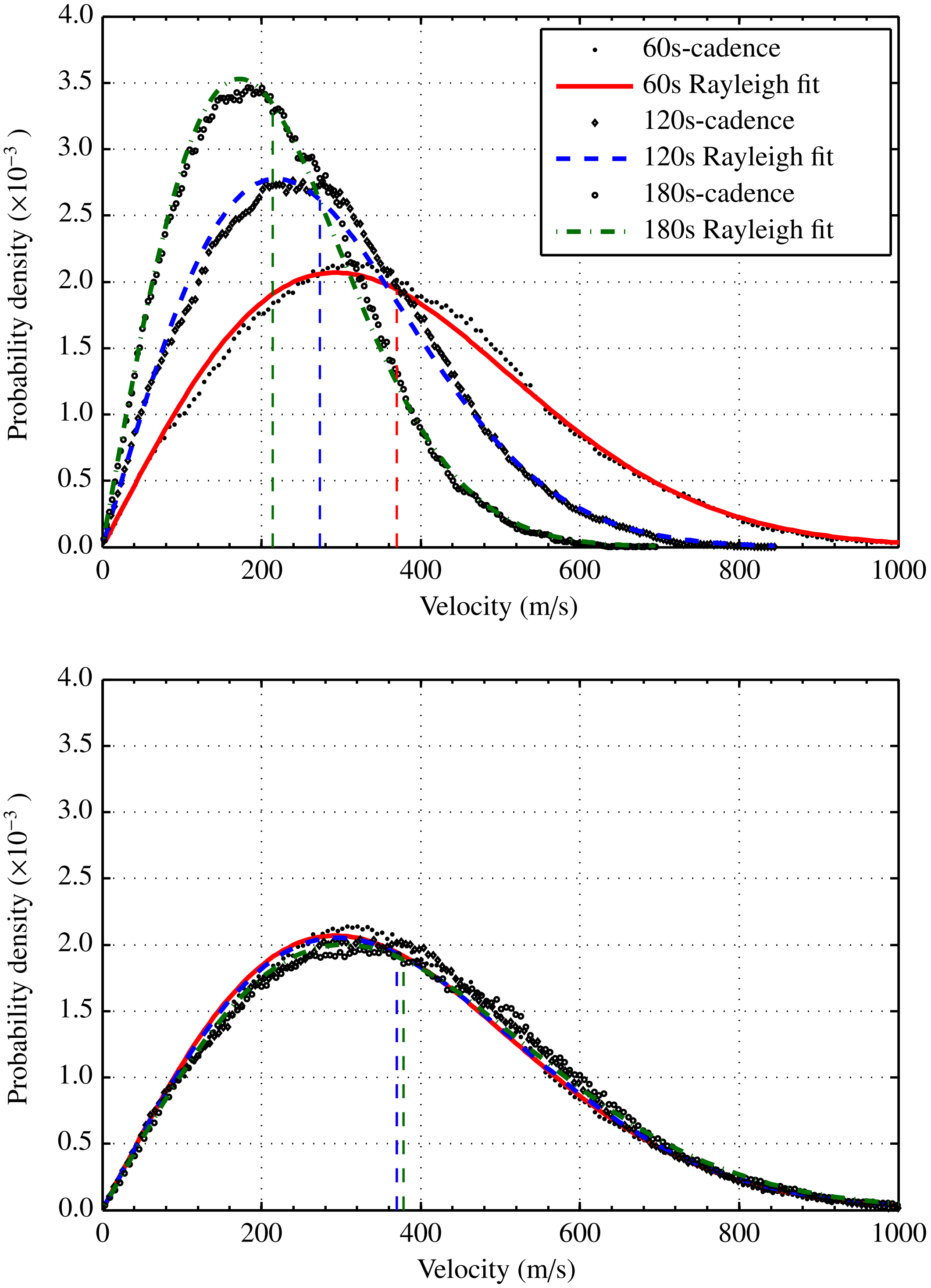

Figure 3.2: *spatial distributions of the horizontal velocity magnitude using test data at 3 different cadences (1, 2, and 3 minutes), on 11 November 2007.*
Top: the calibration of the velocity used, as a reference point, the 1 min*-cadenced data to calibrate the three velocity fields. Bottom: the velocity fields are calibrated independently, to get three calibration coefficients associated with the three instrumentals cadences.*

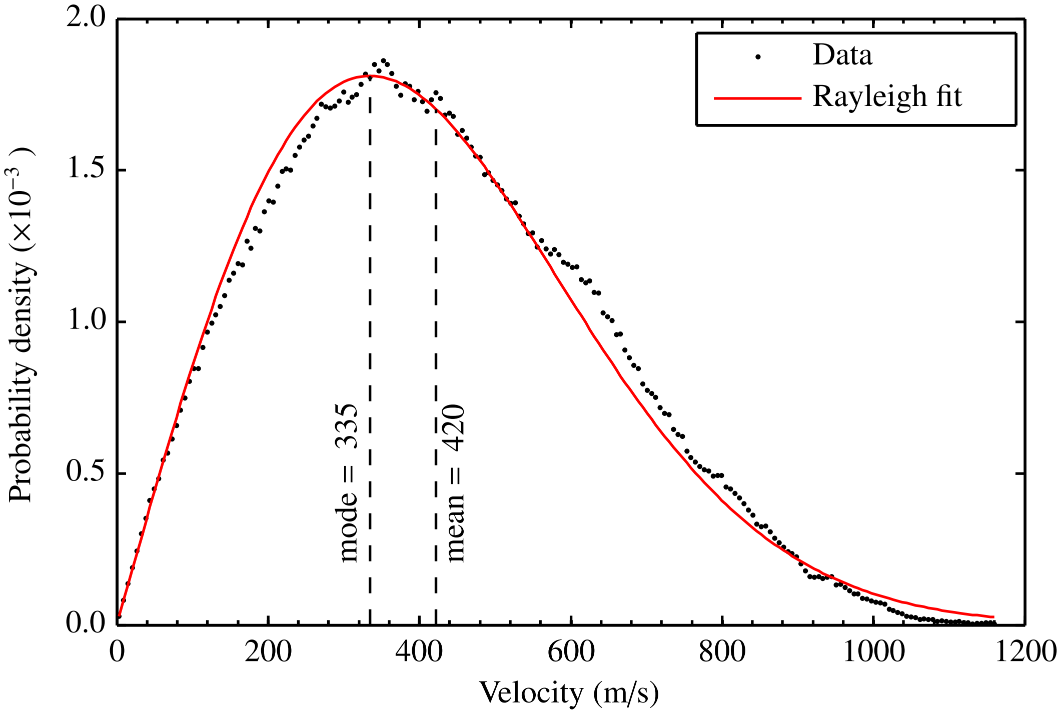

Figure 3.3: *Distribution of the balltracked velocities for the 2007 April 10 dataset. Time average is* 30 min *and spatial smoothing is at a FWHM of* 4 Mm

is only a coincidence. However, these observations were made at similar latitudes and longitudes (near disk center). How it affects the occurrence of these vortex flows may be investigated with more observations to get reliable statistics.

Fig.3.6 sketches how photospheric material (represented by a segmented arrow that can bend) are dragged towards the vortex flow. Fig.3.7 is the Eulerian representation of the velocity field centered on the vortex of Fig.3.5 (red square).

The colored background is the vorticity, normalized to its maximum value. It should only be considered qualitatively (see § 2.5.1). We do not see the beginning of the vortex flow in the first dataset, and it seems to continue longer than the 1 hr time series. In the 2nd dataset, the onset seems to be between 2:30 and 3:10 and to continue past 05:00, which is the end of the time series.

3.1.3 Discussion

We demonstrate the occurrence of steady photospheric vortex flow located at supergranular junctions of the quiet Sun chromospheric network. Their influence extends to a radius of at least 7 Mm from the center of the vortex. The first observations of vortex flow was reported by Brandt et al. (1988) and it had a radius of 2.5 Mm. At granular scales, excess of vorticity has also been observed at the intersections of granular lanes (Zirker 1993, Wang et al. 1995). Magnetic bright points following spirals have been reported by Bonet et al. (2008, 2010). Long-lived vortices are of primary interest because these are the ones in which mixed polarity magnetic fields can become entwined. In the quiet Sun, magnetic fields are swept by the supergranular flows to the boundaries and along the lanes to

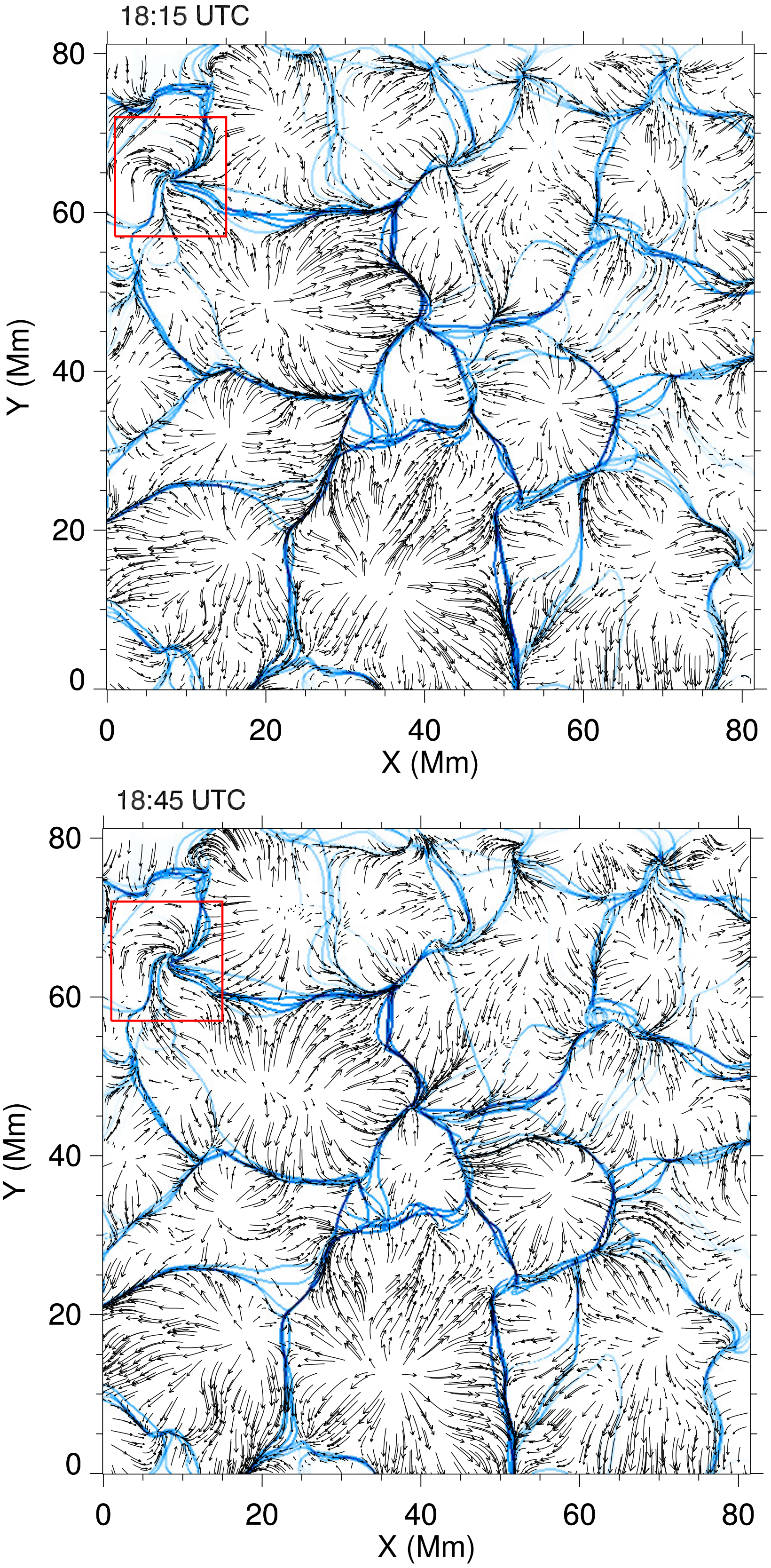

Figure 3.4: *Velocity vector fields of 2007 April 10 centered on 18:15 UTC (top) and 18:45 UTC (bottom). The FOV is* ~$85 \times 85\,\mathrm{Mm}^2$. *Red square :* $15 \times 15\,\mathrm{Mm}^2$. *The mean velocity on this flow map is* ~ $300\,\mathrm{m\,s}^{-1}$.

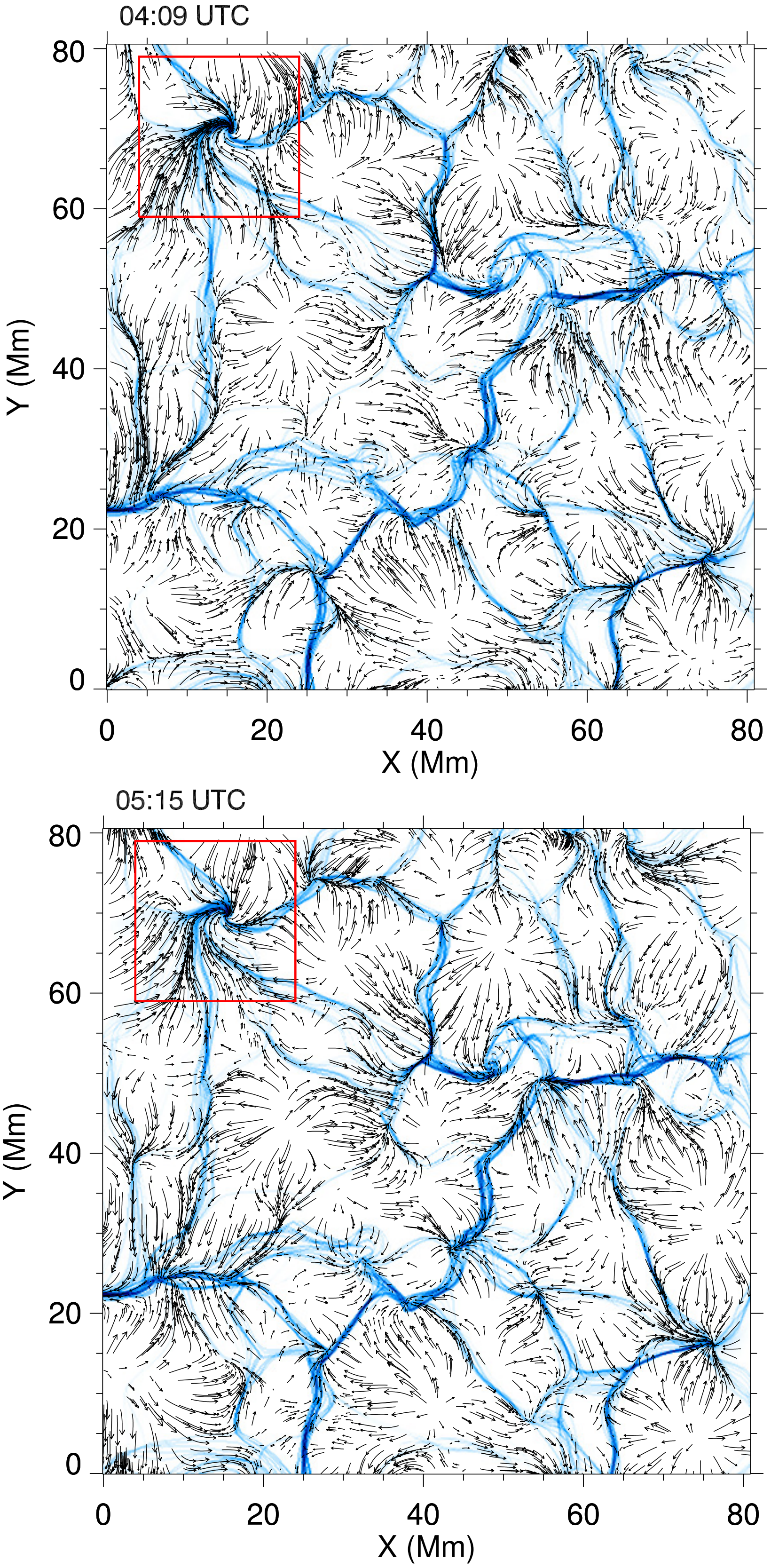

Figure 3.5: *Velocity vector fields of 2007 November 7 centered on 04:09 UTC (top) and 05:15 UTC (bottom). The FOV is* ~$85 \times 85\,\mathrm{Mm}^2$. *Red square :* $15 \times 15\,\mathrm{Mm}^2$. *The mean velocity on this flow map is* ~ $300\,\mathrm{m\,s}^{-1}$

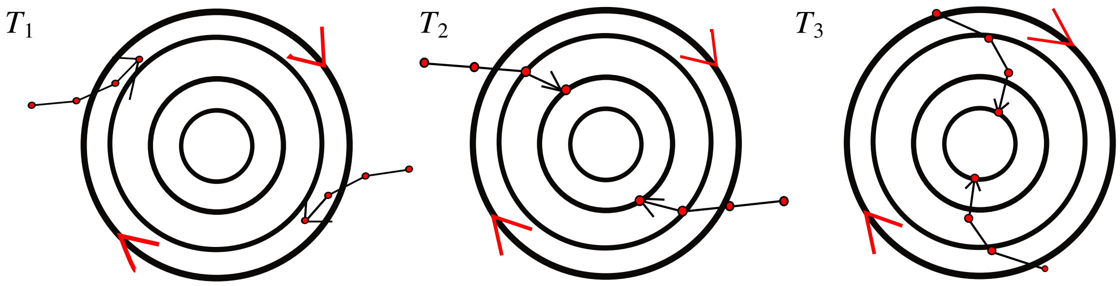

Figure 3.6: *Sketch of an idealized vortex flow in the Lagrangian frame of reference, at three different times T_1, T_2, T_3, increasing from left to right. The concentric circles are fixed, and used as reference. The red arrow heads show the direction of the tangential velocity. The segmented arrows represent massless chained corks advected by the flows, which make the arrows able to "bend" in the presence of differential velocity in the vortex, like in the red squares in Figs.3.4, 3.5 and 3.8.*

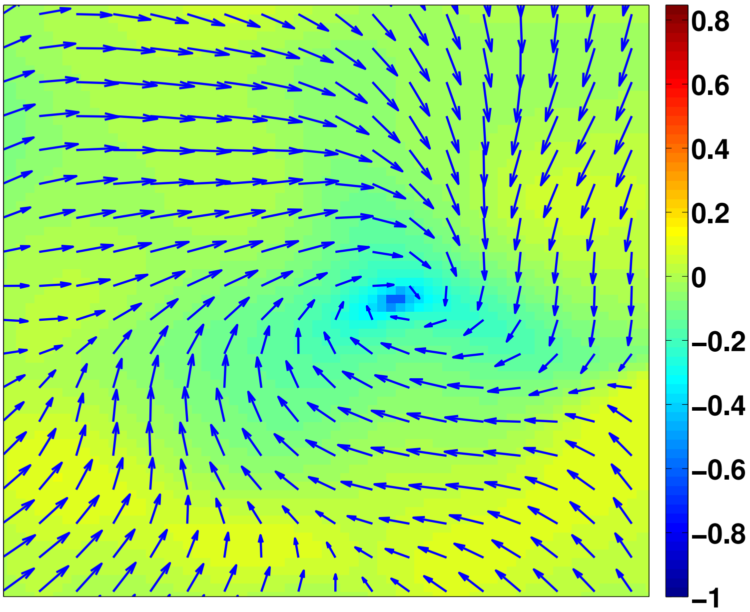

Figure 3.7: *Eulerian representation of the flow in the red square of Fig.3.5. The colored background is the normalized vorticity.*

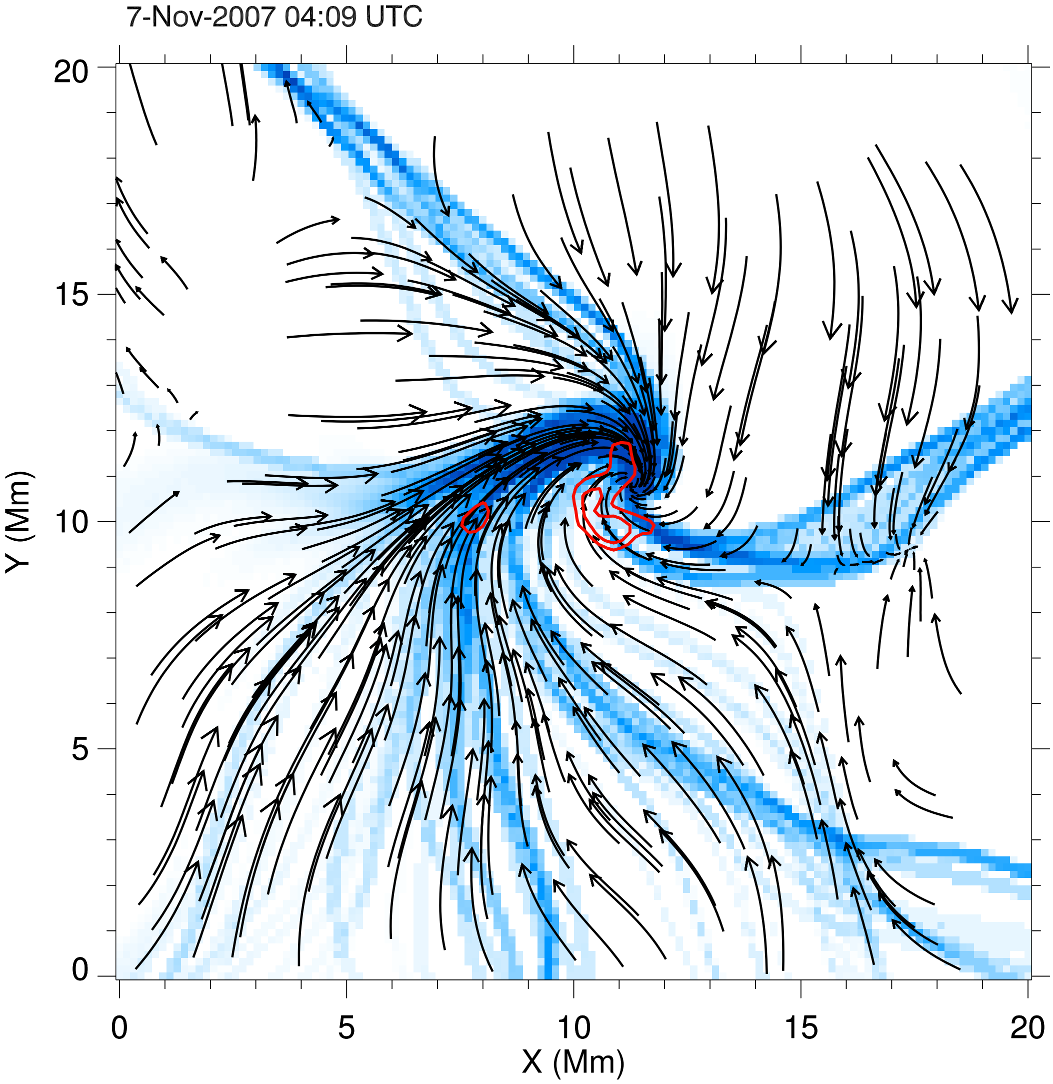

Figure 3.8: *Zoomed-in velocity field of Fig.3.5 with contours of the Ca* II *emission (red) averaged over* 45 min. *The contours are taken above* 900 DN s^{-1}. *The FOV corresponds to the red square in Fig.3.5 and to the patch represented in Fig.3.9*

.

the core of the vortex, provoking flux cancellation and CME-like eruptions (Innes et al. 2009). Figs. 3.8 and 3.9 illustrate the possible connection between the magnetic flux and the vortex flow, in which the magnetic flux looks like it is not just swept out at random places of the supergranular boundaries, but it is literally sucked in at the center of the vortex (red contours in Fig. 3.8) where it seems to accumulate (Fig.3.9).

In Fig.3.9, the black and white colors represent opposite polarities of the line of sight magnetic field. The positive (white) polarity near the image center coincides with the Ca II emission at the center of the vortex in Fig.3.8. In the time series, it is possible to see the negative polarity (black spot indicated by the yellow arrow) moving clockwise around the positive polarity.

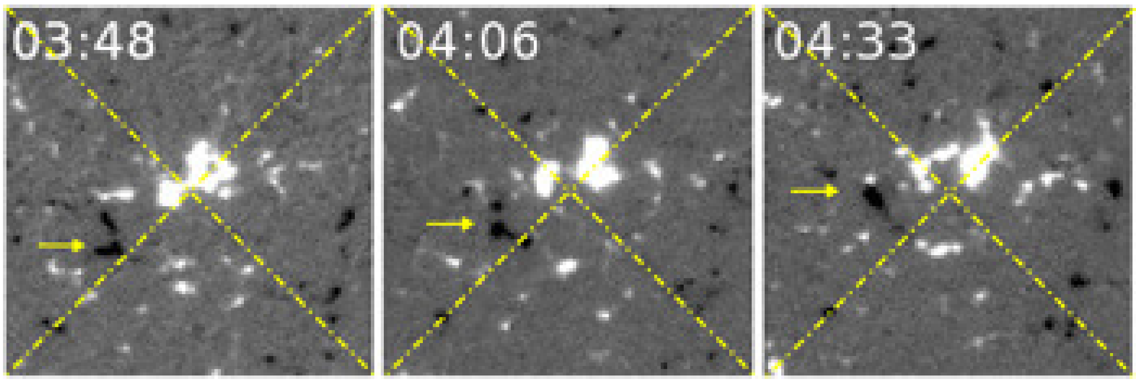

Figure 3.9: *Na I stokes V (FG/SOT) from the November dataset at 3 different times centered on the vortex flows. The FOV of* ~20*x*20 Mm^2 *is designated by the red square in Fig.3.8. The yellow arrow points at a unipolar (black) magnetized fluid element. The dashed cross is a graphical fixed reference to help visualize the relative motions.*

Future observations must be done at higher cadence in order to reduce the uncertainty and to derive quantitative parameters such as the angular velocity and the magnetic helicity (Welsch and Longcope 2003).

3.2 Magnetic Balltracking on flux emergence

3.2.1 Observation of flux emergence

The observations were made on September 26th, 2008, and consist of high-resolution, 1 min-cadence continuum images and magnetograms from MDI (pixel size of 0.6 arcsec), and co-spatial images from Hinode/XRT (Golub et al. 2007) in soft X-ray (pixel size of 1 arcsec), at ~30 s-cadence. The time series last 4 hours, between 15:00 UT until 19:00 UT. Details on the co-alignment are given in the next chapter as a part of a broader science study.

The flux emergence is associated with the rise of X-ray loops observed at the same location, and shown in Fig.3.10 (pointed by the orange arrows). The snapshots are taken in a FOV of 60×60 Mm^2. Balltracking was used to derive the flow fields, and the associated supergranular network lanes are drawn as blue contours. At 15:12 UT, the flux is barely visible in the internetwork, until it emerges as a very clustered, mixed-polarity flux after 16:00 UT (left arrows). The clustered flux then drifts away, and is finally observed with one clearly visible X-ray loop, at 17:55. At 18:12 UT another X-ray loop seems to connect the negative-polarity footpoint (green) from the left side of the network lane in the middle of the frame, to the positive one (red) on the other side. A second, weaker emergence is seen near the bottom right part of the snapshots, starting at 16:42, and also give rise to X-ray loops, visible at 19:05 UT. The time scale of these emergences is a few hours. It is consistent with the time scales of the supergranular flows, here between 300 m s^{-1} and 400 m s^{-1} on average. At this velocity, the fluid elements, and the magnetic flux that they advect take several hours to travel from the internetwork to the lanes (blue). The amount of flux of the emerged bipoles that are observed at the footpoints of the X-ray loops is

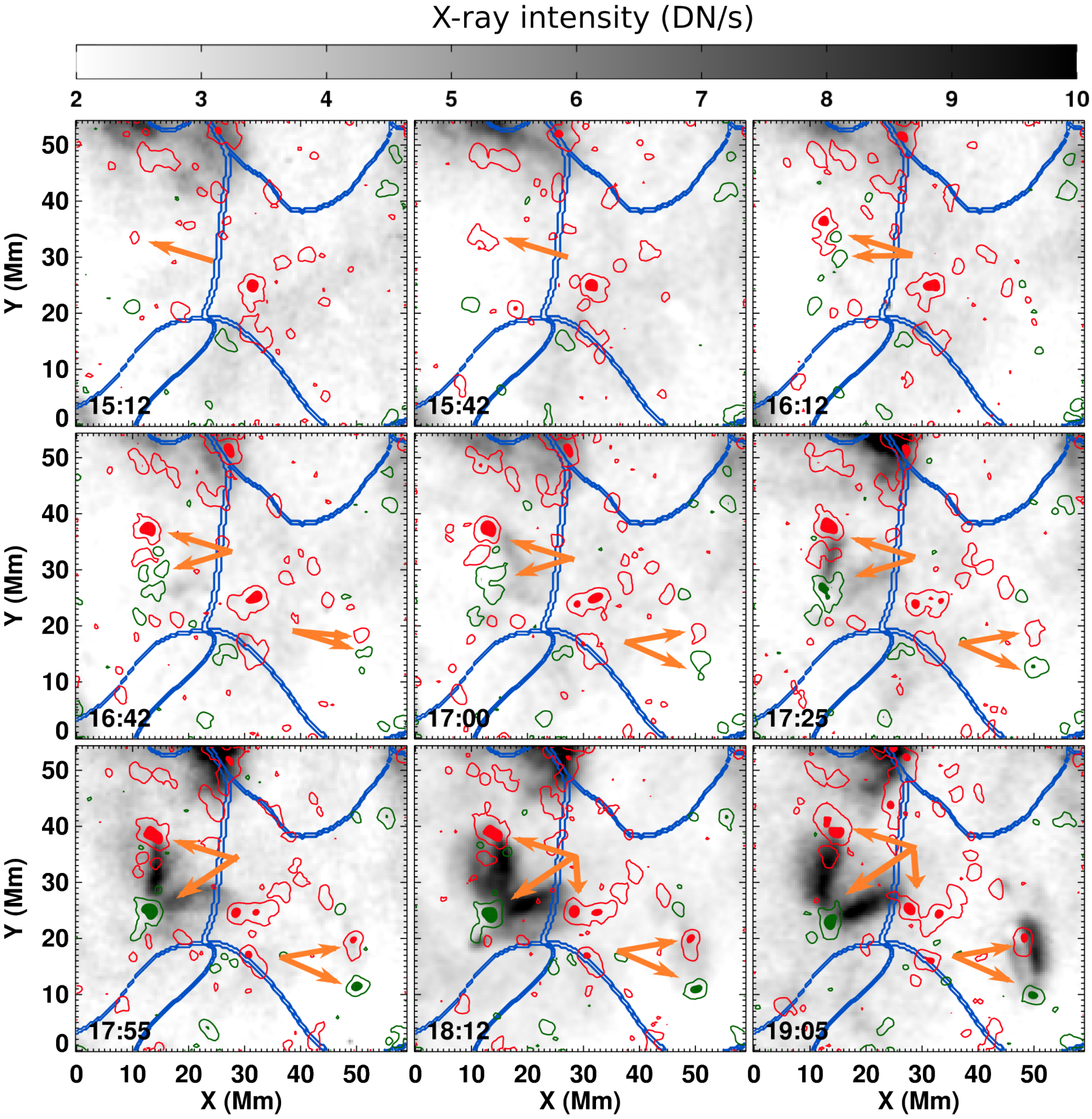

Figure 3.10: *Flux emergence observed at two different places within the displayed field of view. Red/green contours are positive/negative flux (respectively). Thin unfilled contours are at* 10 G, *filled contours are at* 50 G. *The orange arrows point at emerging flux regions that are followed by the rise of X-ray loops*

.

measured with the Magnetic Balltracking, the results are presented in the next section.

3.2.2 Detection and quantification

The Magnetic Balltracking is performed on the FOV of Fig.3.10, followed by the region-growing algorithm. As explained in § 2.6 and § 2.6.5, each ball can act as an identifier of a whole magnetic feature. This makes it easier to detect and isolate only the emerging flux. To do so, we simply associate the tags of the balls that were tracking these features to the flux that is integrated by region-growing. By selecting only the ones with a positive time derivative of the flux, we isolate the features that emerge. In the present case, we selected only the flux that had increased by a factor 10 at the end of the time series, with respect to the value at first detection. This is sufficient to isolate the emerging flux seen in Fig.3.10. The results are plotted in Fig.3.11. The threshold of the detection was set to 20 G, which is about the noise level of the magnetograms in MDI. The pixels with an intensity below this value are ignored by the region-growing.

The first emergence (top) is balanced at the beginning (15:00), during ~40 min with a positive and a negative flux of a bit less than 2×10^{18} Mx. It is unbalanced during ~2.5 hr, until it is balanced again at ~18:15 with an unsigned flux of $\sim 10^{19}$ Mx. The X-ray emission increases by factor ~2.6 of the background intensity, ~1 hr after the emergence is first detected at 15:00, from ~1200 DN s^{-1} up to ~3200 DN s^{-1} after 18:30[3].

In the second case of emergence (Fig.3.11, bottom), the magnetic flux is about 50% weaker than in the first region, with a maximum positive and negative flux (respectively) between 3.5×10^{18} Mx and 4.5×10^{18} Mx. The flux is unbalanced for roughly the first 2 hr, between ~16:40 and ~18:40, although the flux balance is not obvious afterwards. Like in the previous case, this flux emergence is followed by the rise of an X-ray loop. The X-ray emission increases by about 50% from a background level of 1000 DN s^{-1} at 15:00, up to ~1500 DN s^{-1} after 19:00 when the X-ray loop is visible (Fig.3.10, bottom right panel). Note that in the first and second case, there is an X-ray data gap between 18:36 and 19:02. The X-Ray gap is filled with the first value available after the gap (19:02), which is only an arbitrary cosmetic correction.

In order to illustrate further the dynamic topology of the emergence, and to show a science application of the Magnetic Balltracking, we use LFFE to display 3D magnetic loops, and compare them against the X-ray loops. This is represented in Fig.3.12. Similar comparisons have already been done in Wiegelmann et al. (2005b), except that in Fig.3.12, the field lines are drawn using our method of field-lines tracking (§ 2.6.6). The local maxima of the flux, as it emerges, are tracked and used as footpoints for plotting the field lines. Because we make no assumption on the currents, three different values of α are used (including the potential solution $\alpha = 0$), which are represented by three colors (for $\alpha = -0.04, 0, +0.04\,\mathrm{Mm}^{-1}$). For a better visibility of the loops, only the field lines closing in the chosen FOV are automatically kept. This is why some footpoints appear to have missing field lines. For a different value of α, the field line was simply not closing in the present FOV and are ignored when plotting them. The purpose here is to demonstrate an application of the Magnetic Balltracking, it is not an analysis of the coronal magnetic field, although this can still illustrate how different the solutions can get for different

---

[3] DN s^{-1}: Data Number per Second.

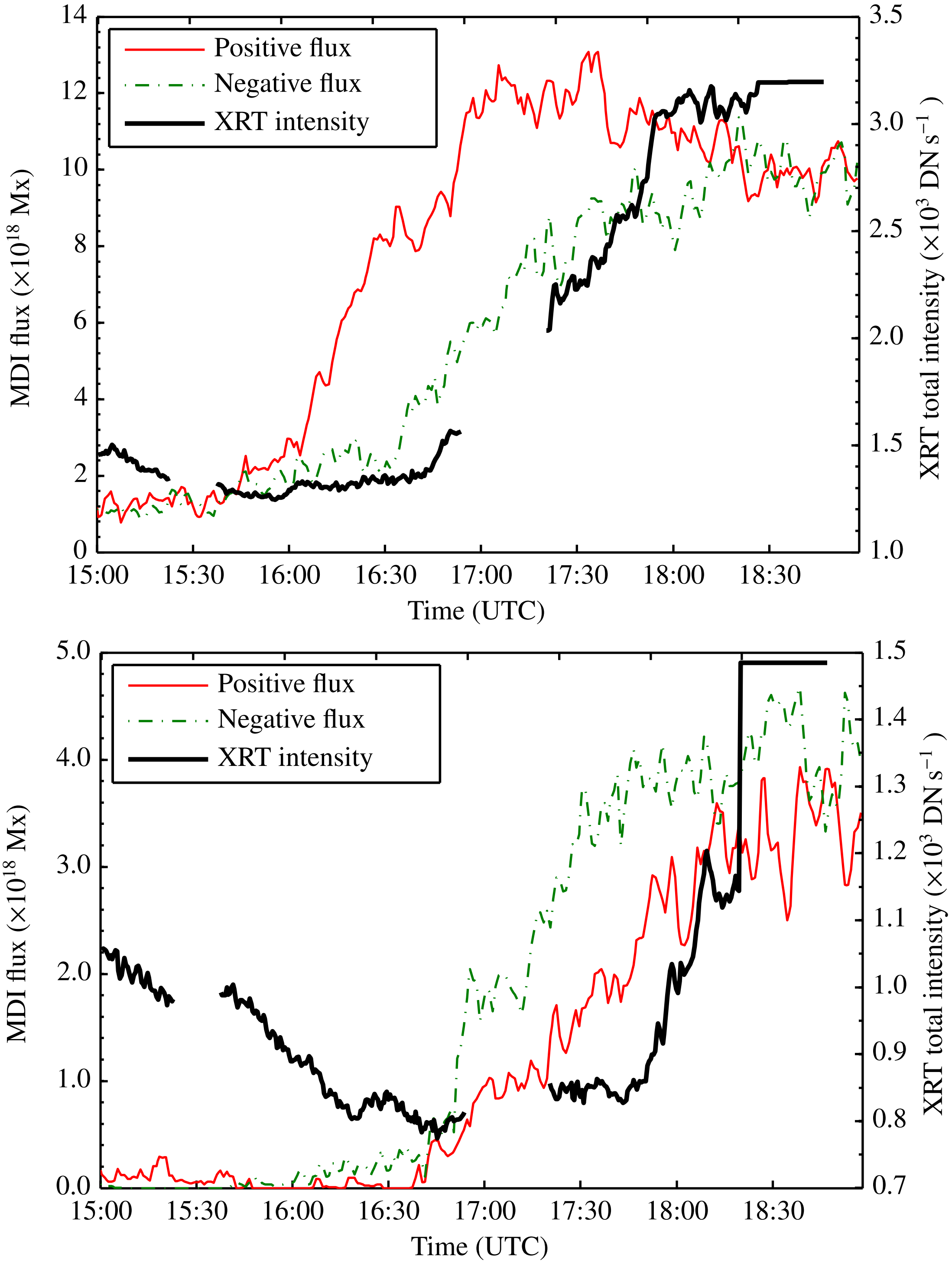

Figure 3.11: *Top: evolution of the X-ray intensity (black line) and the magnetic flux in the region of emerging flux on the left part of the snapshots in Fig.3.10. The colors of the curves of the flux are consistent with the contours. Red is positive flux, green is negative flux (in absolute value). Bottom: Same as the top panel, for the second region of flux emergence in the bottom right of the snapshots in Fig.3.10. There is an X-ray data gap between 18:40 and 19:02 which has been filled in by the first available value after the gap.*

values of the currents, which is well known.
In Fig.3.10, the X-ray loop reaches the other side of the blue network lane at 18:12 (see the group of 3 orange arrows), whereas from Fig.3.12 we see that magnetic field lines appear already connected at the same footpoints, at 15:54 UT, before the X-ray loop becomes visible. As the flux emerges, more field-lines are integrated on the emerging and moving magnetic footpoints. Over several hours, we can keep track of these field lines, and see what they become in relation with the X-ray emission. By simply using the tracked local maxima, which represent only one point for each small clustered magnetic feature, we obtain several lines that match the geometry of the X-ray loop.

3.2.3 About the thresholding

As mentioned in Section 2.6, the threshold of the algorithm was set close to the noise level of the instrument (20 G). In the present case, the threshold in the region-growing algorithm is the same. Nevertheless, note that these two thresholds are defined independently (see § 2.6.2 and § 2.6.5). Otherwise we would loose the flexibility of choosing for instance only stronger flux in the region-growing algorithm (Active Regions, Ephemeral Active Regions, ...), in a specific FOV, and maybe weaker flux in another FOV (quiet Sun, coronal holes,...). Furthermore, isolating flux emergence would be more complicated, as the latter needs a low background level in the extracted feature in order to be able to define an emergence. Thus, in practice, it is more efficient to track at the lowest possible thresholds in order to detect as many features as possible (if not all) on the one hand. On the other hand, the threshold of the region-growing algorithm depends on the science study, and one can perform different region growing on the initially tracked features, without running the main tracking phase at different thresholds over and over again. This saves significant computing time, which is an issue in pipelined computations, e.g, for the long data sets of the Solar Dynamic Observatory (SDO).

3.3 User-friendly software for Balltracking and Magnetic Balltracking

To use the different algorithms in the most flexible manner, and to suit a broad range of different science studies in the future, several modules were created. The Balltracking, the Magnetic Balltracking, the region-growing algorithm, and the tracking of the field lines have been implemented using object-oriented programming. The algorithms are made user-friendly by simply invoking the different modules when they are needed, and do not require any programming skills. For example, a user can apply Magnetic Balltracking to track the magnetic elements in the magnetograms from whichever instrument, and use the tracked positions in whatever extrapolation models the user possesses. Independently, one can use co-spatial observations of the granulation and derive the photospheric flows with the Balltracking module. These modules are presented in the appendix B.

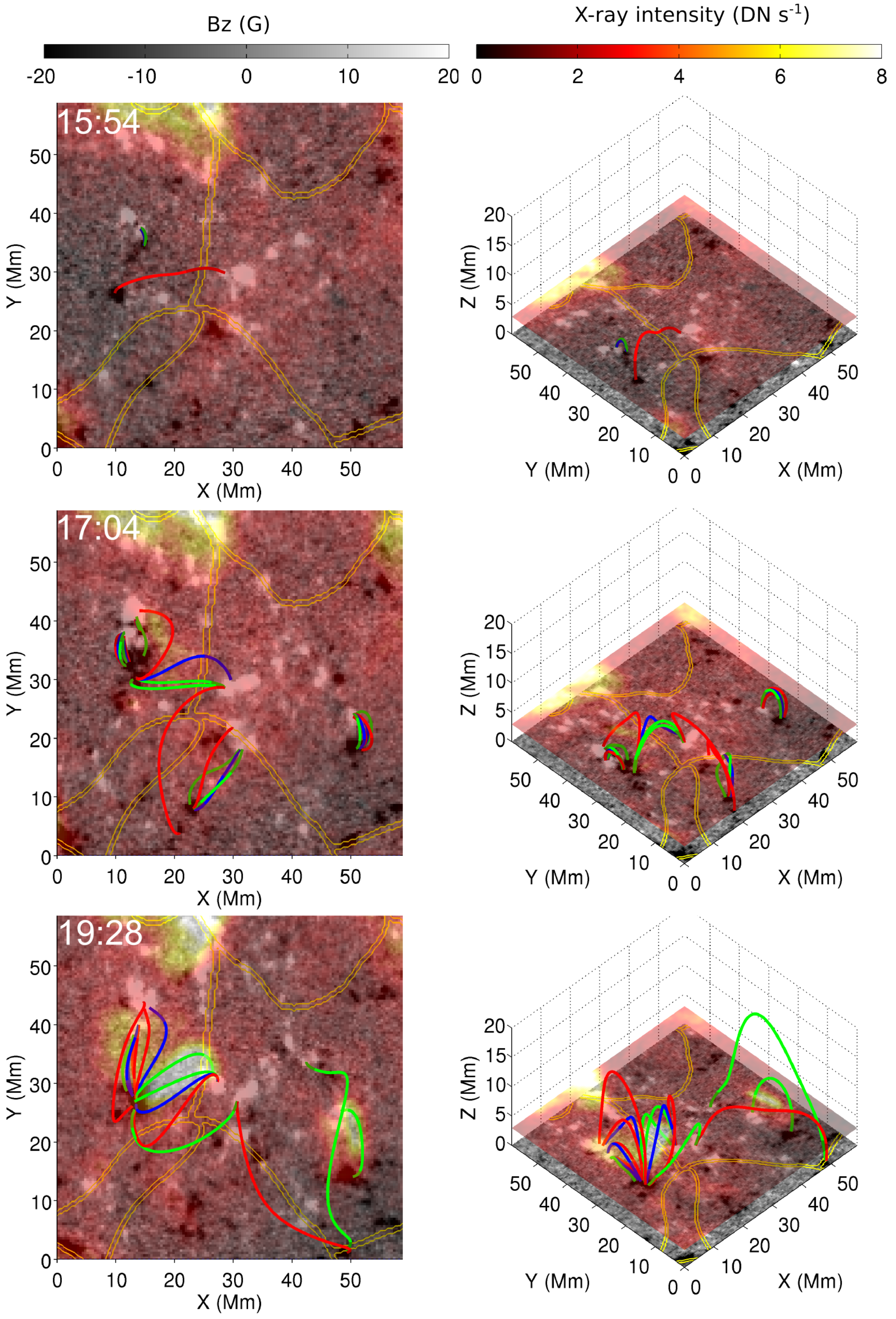

Figure 3.12: MDI magnetograms, with associated 3D extrapolated field lines, overlaid by XRT images (transparent red colortable). The 3 different colors of field lines, (respectively) red, blue, green, correspond to $\alpha = -0.04, 0, +0.04\,\mathrm{Mm}^{-1}$. Both views must be considered, as some field lines can appear open in one view, whereas they are closed from another one, and vice versa. The yellow contour lines are the supergranular lanes.

3.4 Summary

Our implementation of Balltracking on photospheric observations from Hinode data revealed the existence of large scale vortex flows with diameters of $\sim$15 Mm to $\sim$20 Mm. The shape of the supergranular cells was better described with the help of a specific segmentation algorithm developed by Potts and Diver (2008a), and out of which we were able to observe that these vortex flows are centered on the junction of supergranular lanes.

Additionally, the use of Magnetic Balltracking on MDI data allowed us to detect, track, and quantify the evolution of emerging flux between 10^{18} Mx to 10^{19} Mx on a very fine scale of a few Mm, and that are followed by the rise of soft X-ray loops within a few hours. The use of our time-dependent field-lines tracking and of magnetic field extrapolation techniques provided proxies of the magnetic topology that better describes the relationship between the supergranular flows, the flux emergence, and the coronal emission.

The present results are the first case studies of a broader spectrum of investigations of the relationship between the different layers of the solar atmosphere. Such investigations are presented in more detail in the following chapter.

4 Soft-X-ray emission related to photospheric flows and coronal magnetic field

The study of the quiet-Sun has always been limited by the instrumental resolution that is too coarse to reveal the dynamical processes at finer scales. Since the beginning of the SoHO-Hinode era, it is possible to combine long time series with high resolution, simultaneous and co-spatial analyses, from the photosphere, up to the low corona. Finer processes can now be revealed. For example, Innes et al. (2009) revealed the occurrence of small-scale (few Mm) CME-like eruptions using Extreme Ultra-Violet (EUV) observations from STEREO, and the role of the supergranular flows underneath as a possible triggering mechanism is still under investigation (Innes and Teriaca 2013).
In the previous chapters, we have described several methods that provide independent analyses of the solar atmosphere, such as the photospheric flows, the longitudinal magnetic field and its coronal extrapolation, and the observations of the low corona in soft-X-ray. The present chapter provides an additional description by combining all these methods to build a consistent multi-layer analysis of the solar atmosphere. We aim at describing the relationship between the photosphere and the corona, by relating the photospheric flows and the evolution of the magnetic flux to the soft X-ray emission. In Sections 4.1 and 4.2 we describe the observations and their co-alignment.The calibration of the NFI-SOT magnetograms is explained in Section 4.3. In Section 4.4 we present several multi-layer case studies of small-scale X-ray events in the low corona, with the underlying photospheric flows and magnetic flux.

4.1 Multi-instrument observations

Four instruments were involved in co-spatial observations on 26 September, 2008. Each of them provided an 8 hr time series of data, from 15:00 UT to 23:00 UT. They were pointing near disk center. Due to a long data gap in the middle of these observations, this study focuses on the first 4-hour time series. In what follows, the times are given in Universal Time (UT). The observations were carried out as follows:

1. Hinode/XRT (Golub et al. 2007) took images of the quiet Sun in soft X-ray with the C-Poly filter at a cadence of 30 s, at full resolution over a FOV of 384×384 arcsec^2, with a CCD pixel size of $\sim$1 arcsec. The C-Poly filter covers a temperature range of about $1\,\mathrm{MK} < T < 100\,\mathrm{MK}$. Removal of instrumental bias such as pedestal, dark

current, vignetting and misalignments due to satellite jitter were carried out using the XRT software in Solarsoft ("xrt_prep.pro" and "xrt_jitter.pro"). Despite the calibration, contamination spots are still present in the images. Their position were retrieved before co-alignment, using the dedicated procedure of the XRT software ("xrt_tup_contam.pro"), which builds maps of the contamination spots. We used them to acknowledge possible bias when integrating the X-ray fluxes.

2. The Broad-band Filter Imager (BFI) of the Solar Optical Telescope (SOT/Hinode) provided a time series of blue continuum images. Each image was successively taken at two different intervals: 30 s and 90 s. Out of this time series, we extracted two time series with a cadence of 2 min each, the first time series being 30 s ahead of the second one, with the same total duration (4 hr). The FOV of BFI is ~214 × 112 arcsec^2 with a pixel size binned and summed onboard to 0.22 arcsec. For co-alignment purposes, BFI also took Ca II images with the same observing parameters.

3. From the Narrow-band Filter Imager (NFI) of SOT, we took filtergrams of the Stokes V/I every 2 min. The pixel size is 0.3 arcsec. The calibration of SOT data (both NFI and BFI) was done using the dedicated routine "fg_prep.pro" in Solarsoft. By eye, we could not identify any effect of the bubble-shape aberration (Tsuneta et al. 2008).

4. SoHO/MDI (Scherrer et al. 1995) took a time series of high-resolution continuum images and high-resolution (high-res.) magnetograms of the LOS magnetic field. Here the pixel size is ~0.6 arcsec, whereas the resolution is ~1.2 arcsec (2 px). Each time series is taken at a cadence of 1 min. The calibrated continuum images from MDI (level 1.8) were flat-fielded using the method presented in Potts and Diver (2008b), using a time series taken the day after the present observations, and made of more than a thousand images. The instrumental focus and Y-axis offset of the data used for the flat-field are the same as our data. In addition to the high-res. data, MDI provided full-disk observations at a lower resolution (4 arcsec) which are used for co-alignment.

5. Images from the full-disk SoHO/EIT (Extreme-Ultra-Violet Imaging Telescope) (Delaboudinière et al. 1995) are also used for co-aligning the other instruments.

The regions observed by each instrument are presented in Fig.4.1 and 4.2, with (respectively for each figure) EIT and XRT data as the background image. There was no EIT image available at the beginning of the time series, so the displayed image is the closest available, at 19:12, in the 195Å wavelength.

4.2 Protocol for near 1-arcsec co-alignment

This study describes small-scale events happening in both the photosphere and the low-corona, and observed with different instruments. This demands near 1-arcsec accurate co-alignment, whereas the pointing coordinates of Hinode are given with an uncertainty of more than 5 arcsec.

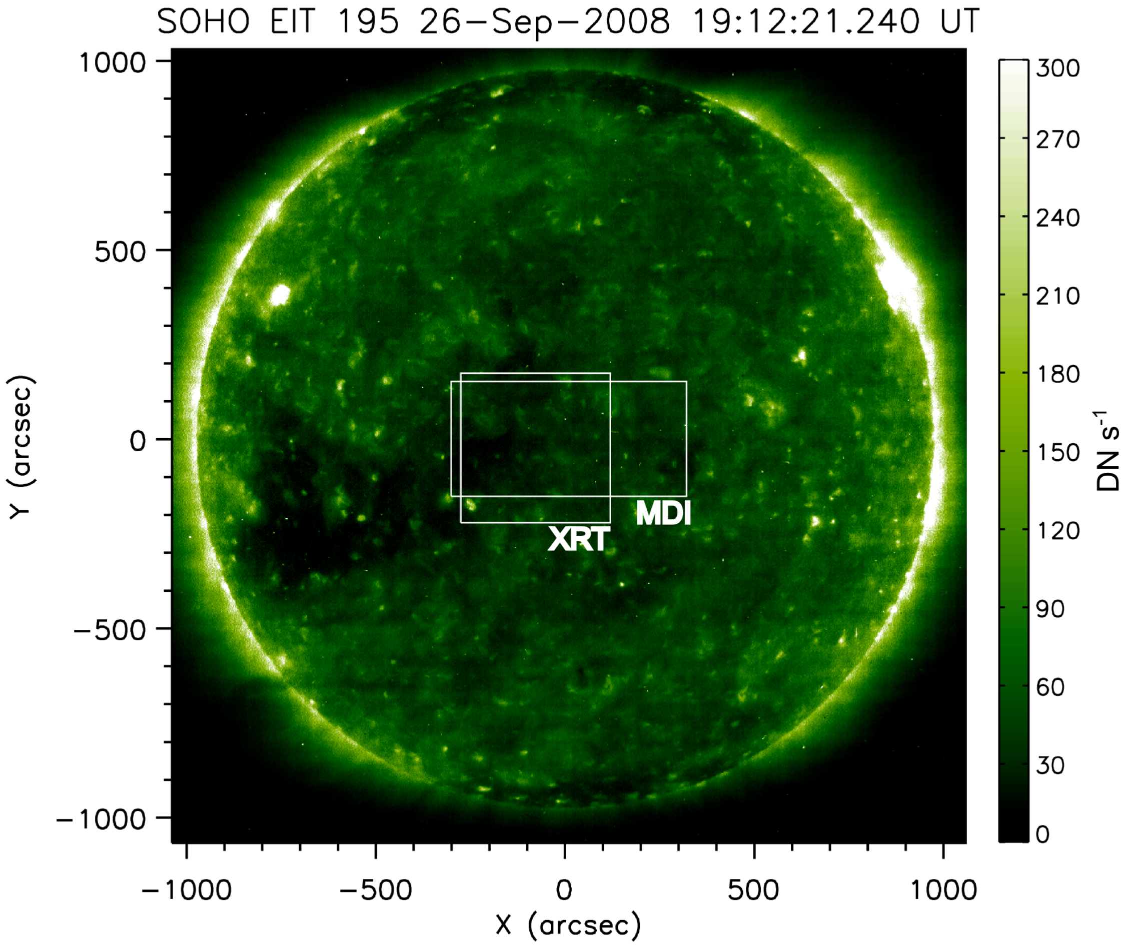

Figure 4.1: EIT full disk context image at 19:12. XRT and MDI FOVs are shown in white rectangles.

When dealing with more than two instruments, the pointing uncertainty of each one adds up, and a fine co-alignment becomes even more complex. For this reason a protocol must be defined and followed carefully. At each step of the co-alignment one must determine the remaining uncertainty, so that in the end, the cumulated uncertainty on the overall co-alignment can be estimated. The present co-alignment consisted in aligning all the observations using MDI data as the reference, as it has the best pointing accuracy (below 1 arcsec). The EIT full disk image taken at the same time as the MDI full disk (19:12) is also used as an intermediate frame of co-alignment. Pointing information is given in the FITS headers of the MDI and EIT data, and is used to directly co-align both instruments. The chart in Fig.4.3 illustrates the different steps of the co-alignment, which are detailed in the next paragraphs. For consistency, we must define some technical vocabulary that will be used often in this chapter:

- Frame: any bi-dimensional observation. Frames can either be images (continuum, EUV,...), 2D flow fields, magnetograms or filtergrams.
- FITS headers: the data are all provided in FITS files. They contain the observations

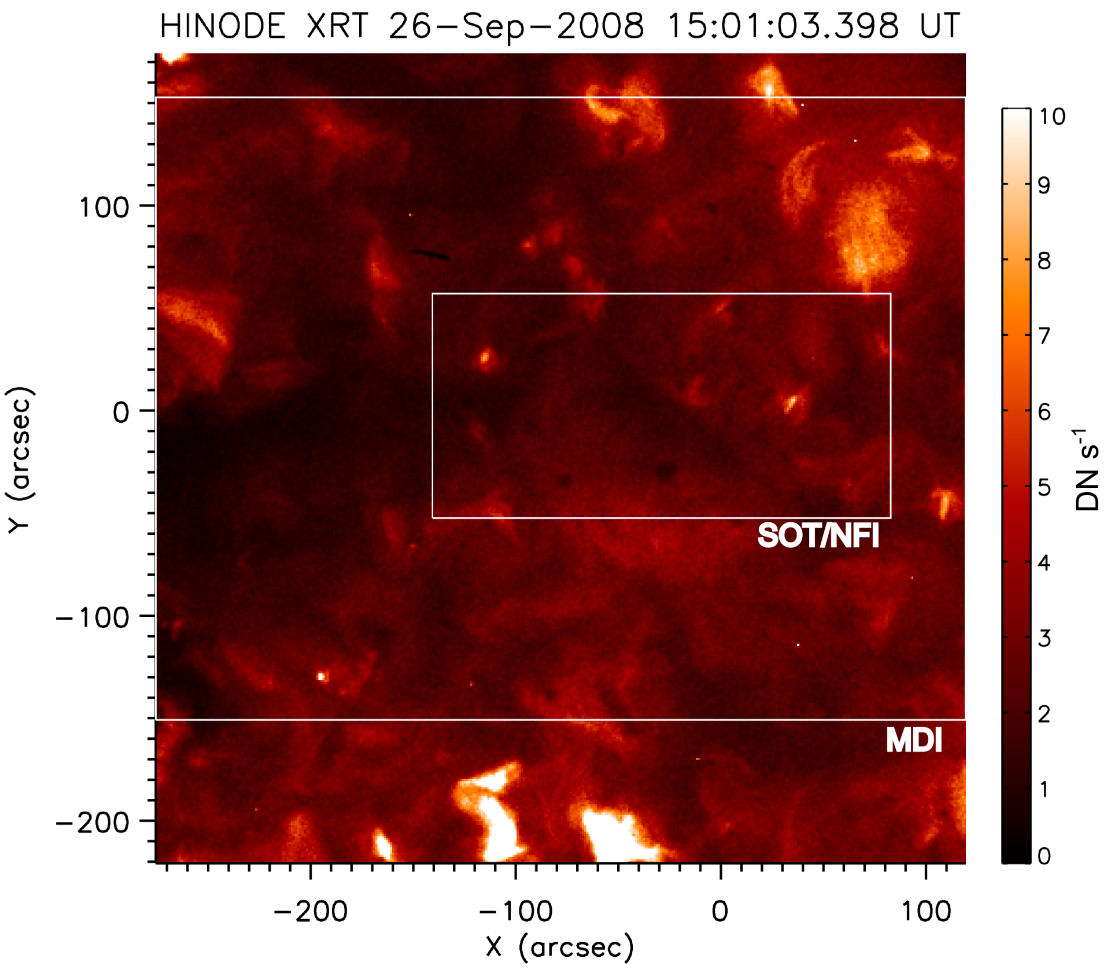

Figure 4.2: *Full XRT FOV of the 4-hour time series. MDI and NFI/SOT are shown in white rectangles. The width of the MDI FOV is larger than XRT's.*

and associated meta-data describing relevant information such as the pointing coordinates, time, roll angle of the instrument, etc... these meta-data are called the FITS header, or header information.

- Co-alignment: co-aligning two frames consists in positioning them at the same position with respect to a common frame of reference. Once co-aligned, the center of both frames have the same coordinates in this frame of reference, and their X and Y axis are parallel. With this definition, two frames can have different sizes (different FOV), but still be co-aligned. We sometimes will use the terms "co-aligned" and "co-spatial", interchangeably.
- Registration: co-alignment of several images of a time series. To register a time series is equivalent as having all of its images co-aligned with each other.

Following these definitions, two (or more) time series are co-aligned if all the images within them are co-aligned, regardless of which time series they belong to.

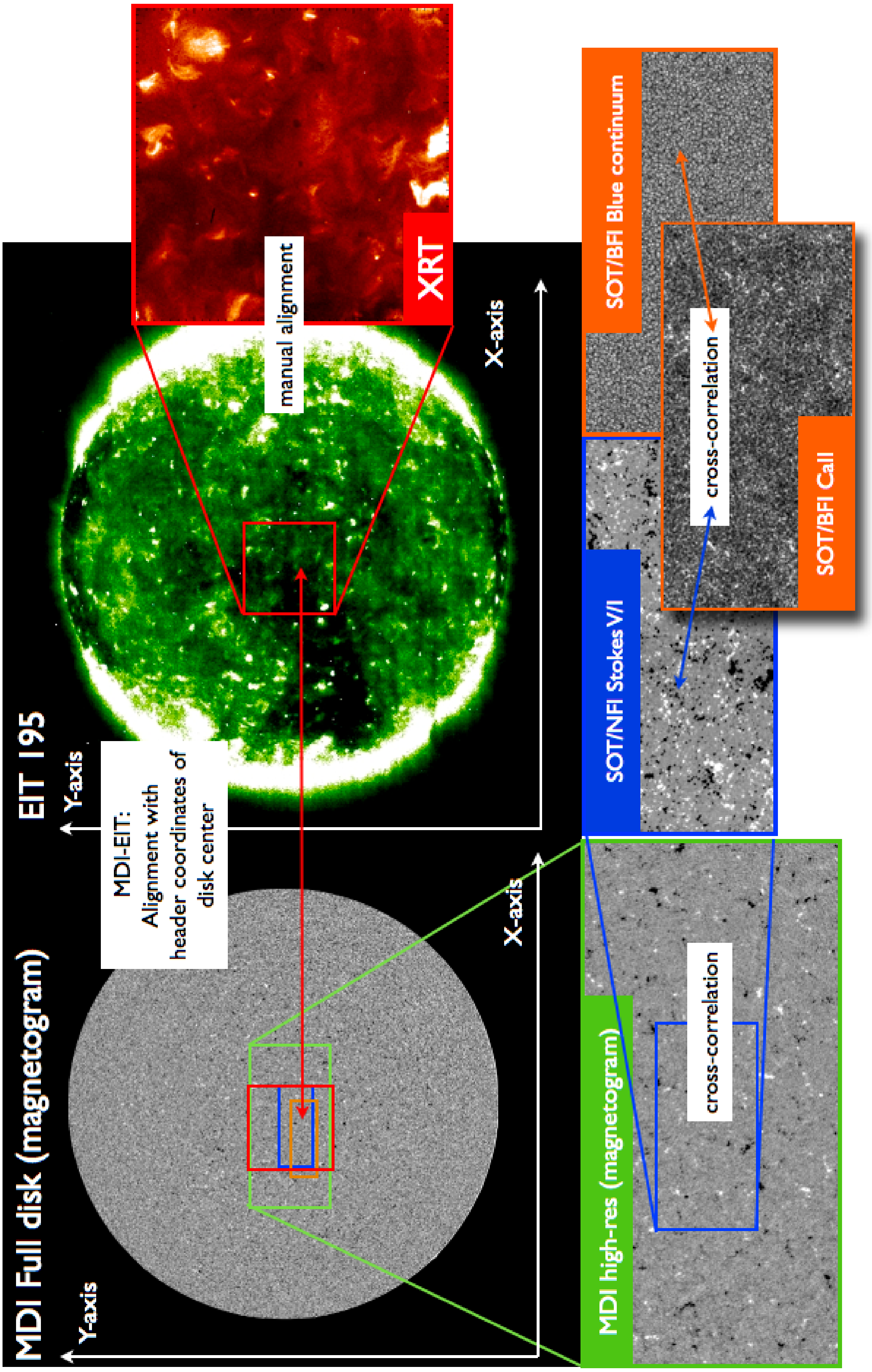

Figure 4.3: Co-alignment chart of all the instruments

4.2.1 Registration of MDI data

MDI took continuum images and magnetograms at a fixed position with respect to the solar disk. Consequently the observed surface moves with respect to the CCD, at the speed of the solar differential rotation. Yet it is necessary to have MDI observations co-rotating with the solar surface. We call this step the "de-rotation[4]". As the same CCD takes co-spatial continuum images and magnetograms, both datasets need to be de-rotated in the exact same manner. Because Hinode is on a polar orbit around Earth, and SoHO is on the Lagrange point L1, the MDI data need to be interpolated to the Earth view by reducing its magnification by a factor of 1.01. This corresponds to the ratio between the distances Earth-Sun and L1-Sun.

Our de-rotation algorithm uses the pointing coordinates given in the FITS header, the time (UT) of each frame, and the orbital parameter of the Sun-Earth orbit to compute the amount of de-rotation needed using the empirical formula of the solar differential rotation from Howard et al. (1990), which gives the angular velocity ω at the latitude ϕ:

$$\omega = A + B sin^2\phi + C sin^4\phi \qquad (\mu\mathrm{rad\,s^{-1}}) \tag{4.1}$$

with $A = 2.89$, $B = -0.43$, $C = -0.37$, in $\mu\mathrm{rad\,s^{-1}}$. Equation 4.1 would yield an angular rotation that varies across the vertical axis of the images. Yet the registration we need to perform must use the same frame of reference for all the pixels. So the rotation rate at the local latitude ϕ at which the central pixel of the CCD is pointing is used to de-rotate the whole frame. Finally, the data are interpolated to the de-rotated coordinates. Doing so, the differential flows (from the differential rotation) are preserved when tracking the flow fields, and the latter are calculated in a frame of reference that is "rigidly" co-rotating with the solar surface.

4.2.2 Registration of BFI/SOT dataset

During an observing sequence, the Hinode pointing follows the solar rotation at the speed of the solar differential rotation. In addition, the SOT instrument has an onboard correlation tracker. The latter takes images of a small FOV (11×11 arcsec^2) of the granulation, with a high-speed (580 Hz) camera, and performs a real-time correlation tracking between them to derive their relative displacement, and correct the pointing accordingly through the Image Stabilization System. The camera operates at 580 Hz, but the corrections are sent to the Stabilization System at a slower rate (every 40 s according to Tsuneta et al. 2008, § 6.1). This keeps the CCD in a small frame of reference moving with this group of granules. The drawback is that within the 11×11 arcsec^2 FOV of the correlation tracker ($\sim 8 \times 8$ Mm^2 near disk center), which is not even half the average size of a supergranule, there are less than a hundred granules, and so their group motion is not necessarily the same as the one of the granulation seen in a wider FOV (see for instance Figs.3.4 and 3.5 in Chapter 3). This forces us to register the images more accurately.

---

[4] the term "tracking" is sometimes used to describe this step on continuum images, whereas "de-rotation" often refers to the removal of solar rotation in dopplergrams. However, to avoid confusion in the present context of flow tracking where the term is used many times (Local Correlation Tracking, Balltracking, Magnetic Balltracking, etc...), we speak of "de-rotation" to specifically designate the removal of the effects of solar rotation in continuum images and magnetograms

The blue continuum images from BFI are separated in two time series, each have a cadence of 2 min. When considering both time series together, the interval between two images changes alternatively from 90s to 30s. As the granules have a mean lifetime of ~5-6 min, most of the granules are still present when changing from one image to the next. Thus it is reasonable to co-align the images by pairs, using cross-correlation. Starting with image 1, image 2 is aligned to it. Image 2 becomes the new reference for image 3, etc... The co-aligned time series can then be separated again to obtain two co-aligned time series with a regular cadence of 2 min, more suitable for Balltracking. This is done with the routine dedicated to the registration of SOT images, called "fg_rigidalign.pro" in Solarsoft. It computes the displacements in the X and Y direction, using a fixed FOV in the images. This FOV must be taken as large as possible. Indeed, the default behavior of this procedure is to consider a small FOV of 256×256 px^2 to perform the cross-correlation, which here corresponds to about one eighth of our image. The main reason of using a smaller FOV as default and not all the pixels of the image is for computational efficiency. This default setup does not give enough accuracy, and can on the contrary worsen the co-alignment. In the BFI images, 256 px corresponds to ~50 arcsec, which is close to the average size of supergranules. Yet on scales of a few hours, a supergranule has an intrinsic motion relative to the whole FOV of the image, which can move up to several arcsec over a few hours. Therefore, using a too small FOV in the procedure would only change the frame of reference of the onboard correlation tracker, that moves with a small group of granules, to another frame of reference (the moving supergranule), somewhat slower, but still in motion with respect to the whole FOV. Either way, any velocity field derived from tracking granules in these registered images would be biased. Note that because of the limited lifetime of the granules, these small effects are impossible to check by eye, but they significantly impairs the velocity fields.

These effects are quantified for the 4 hr-time-series and are reported in Fig.4.4. Compare it with Fig.4.5 that shows the misalignments when using the entire image in the cross-correlation, and note the difference of several pixels in the original shifts. Each figure also displays the result of the alignment-check (right panel). The latter is done by calculating the remaining displacement on each co-aligned dataset, but using the whole available FOV and not just the smaller region. In Fig.4.4, we see that using the smaller region is not enough to make the images steady with respect to each other, with up to 4 px of remaining shift (right panel) between the last and the first image. This also means that the smaller region had a significant net motion different from its surrounding. For this reason, it is important to take the whole image and not a reduced FOV, when using cross-correlation to co-align these images. The remaining alignment error between the frames after this registration is less than ±0.2 arcsec.

Note that so far, the cross-correlation we used only picks up displacements in the X and Y direction. Another misalignment can remain if the images are tilted with respect to each other. As defined earlier, ideal co-alignment requires to have not only the centers of the frames aligned, but their axes must be parallel. The corrections of tilt effects are treated in the next sections.

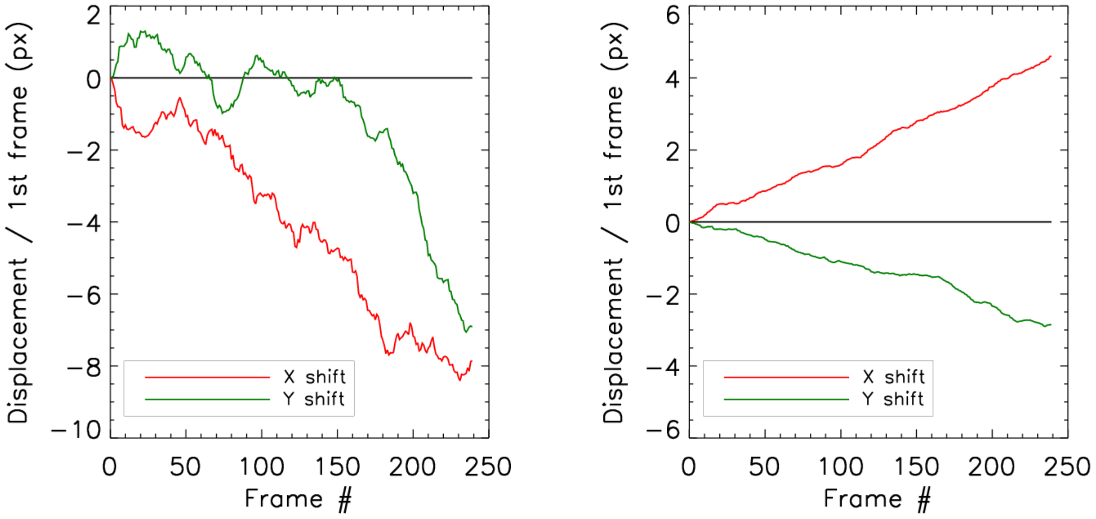

Figure 4.4: *Left: Misalignment curve of the misaligned images, using a small region of* $256x256px^2$ *centered on the images. Right: curve of alignment-check using the entire FOV of the aligned images. The shifts are given with respect to the first frame.* 1 px $\approx$ 0.2 arcsec

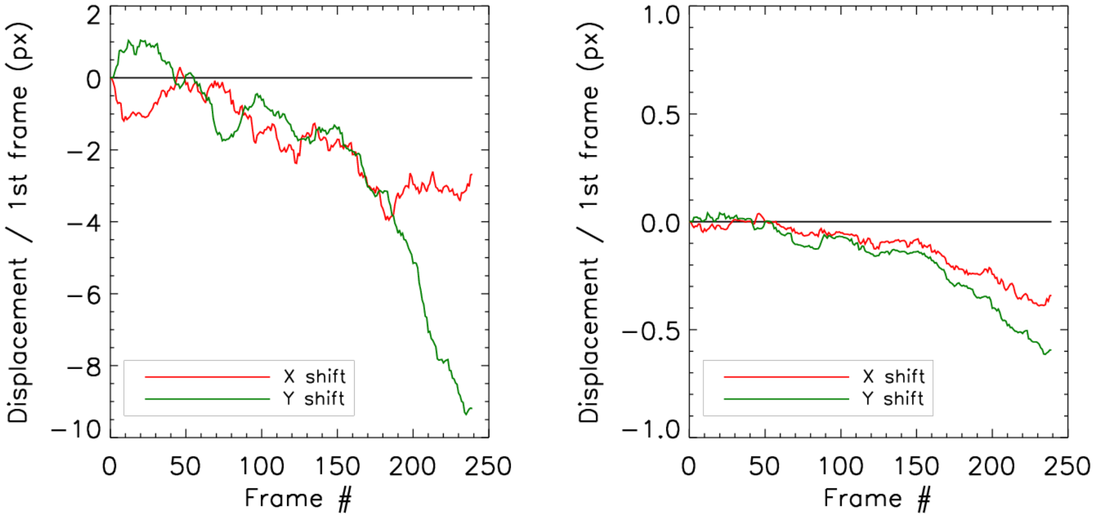

Figure 4.5: *Left: Misalignment curve of the misaligned images using the entire FOV. Right: curve of alignment-check using the entire FOV of the aligned images. The shifts are given with respect to the first frame. Note the reduced y-scale relative to the right panel in Fig.4.4.* 1 px $\approx$ 0.2 arcsec

4.2.3 Co-alignment of NFI/SOT with MDI high-res.

NFI shares the same CCD as BFI, so both instrument cannot record data at the exact same time. In addition, as we explained earlier, the pointing corrections are sent every 40 s to the image stabilization system, while the NFI data are taken every 2 min. Since the small group of granules tracked by the correlation tracker can move at random, the jitter detected in BFI cannot be used here to correct the jitter in NFI. However, each NFI frame can be co-aligned with the MDI high-res. magnetograms taken every minute. Thanks to their very accurate pointing, they offer for each NFI filtergram a very adequate frame of reference for cross-correlation. The time difference between a NFI filtergram and a MDI magnetogram is 30 s at most. Within this time, most of the visible features barely evolve, so we can cross-correlate the MDI-NFI data. Cross-correlating images here only find the best possible alignment by horizontal and vertical translations, because the cross-correlation is done in cartesian space, which is common practice.

Nevertheless, the NFI and MDI are two instruments onboard two different spacecrafts (Hinode and SoHO). Here we assume that the MDI CCD vertical axis is parallel to the solar rotation axis (North-South axis), so the angle between the NFI and MDI reference frames must be checked. This is done by cross-correlation in polar space. Here we define the term "tilt angle" as the angle between the North-South axis of the CCD of SOT and the one of the MDI CCD (assimilated as the solar rotation axis). The value of the NFI tilt angle is given in the FITS header. However, these are nominal values, and it does not always correspond to the real positioning of the axes of the CCD. This is illustrated in Fig.4.6 where the NFI frame were rotated according to the values in the FITS headers. Some misalignment between MDI and NFI is visible, and it increases as one looks away from the frame center (see the green arrows), which is symptomatic of an inaccurate tilt angle. In the FITS header, the tilt angle was $\sim$ 0.4 degrees. We fixed this by cross-correlating the frames in polar space. By calculating the cross-correlation at several angles around the nominal values (FITS header tilt angles), with a resolution of 0.05 degrees, we end up with a more accurate tilt angle of 0.65 degrees. As shown in Fig.4.7, the NFI and MDI frames are better co-aligned with this new angle. The data in Figs. 4.6 and 4.7 are averaged over 30 min. The uncertainty of the co-alignment, including the cartesian cross-correlation, is ±0.3 arcsec.

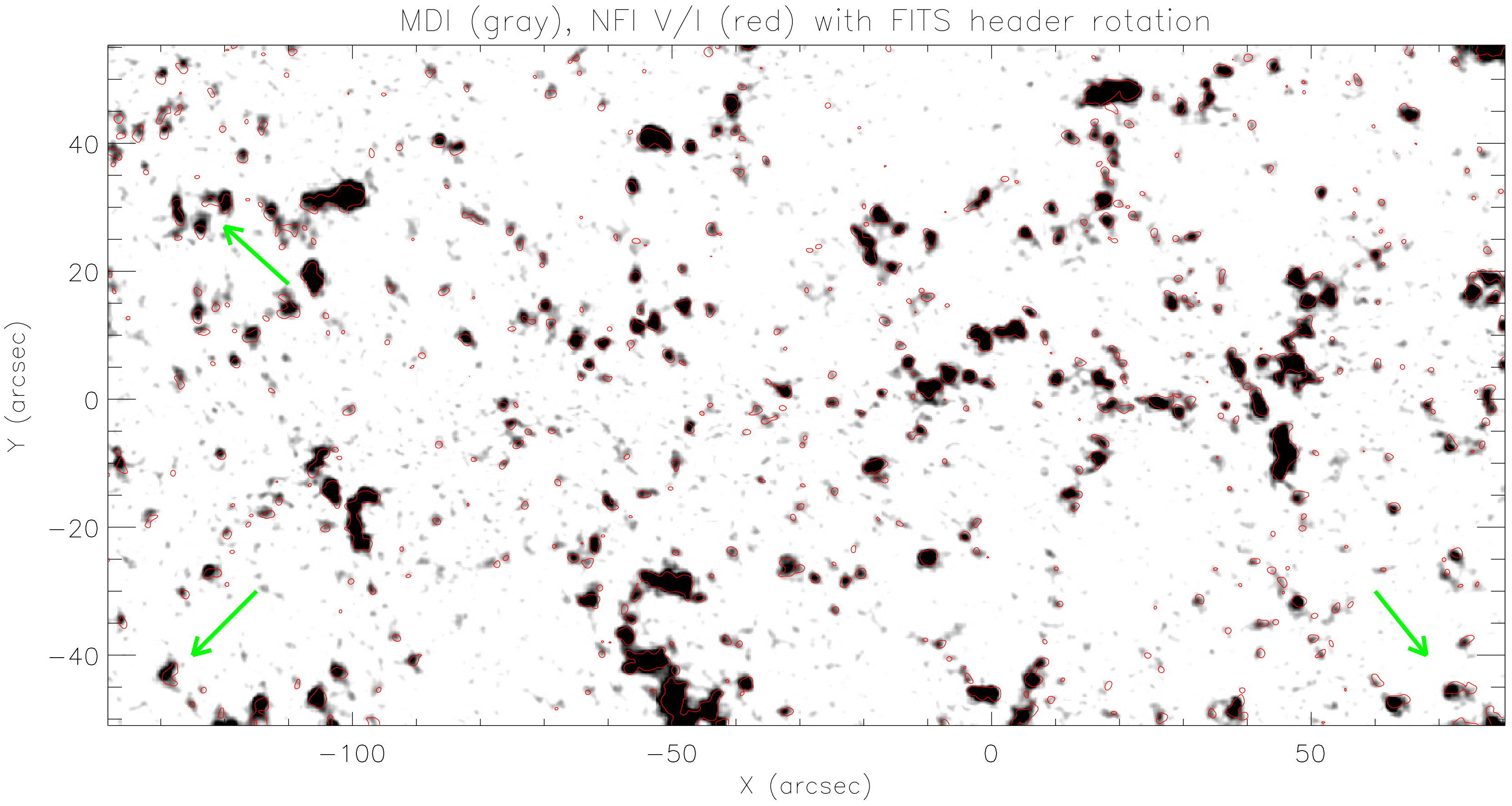

Figure 4.6: *Co-aligned unsigned magnetogram of MDI (gray) and NFI |V/I| (red contours) with a rotation using the original tilt angle from the FITS header. The green arrows are visual references for comparisons of the alignment with Fig.4.7.*

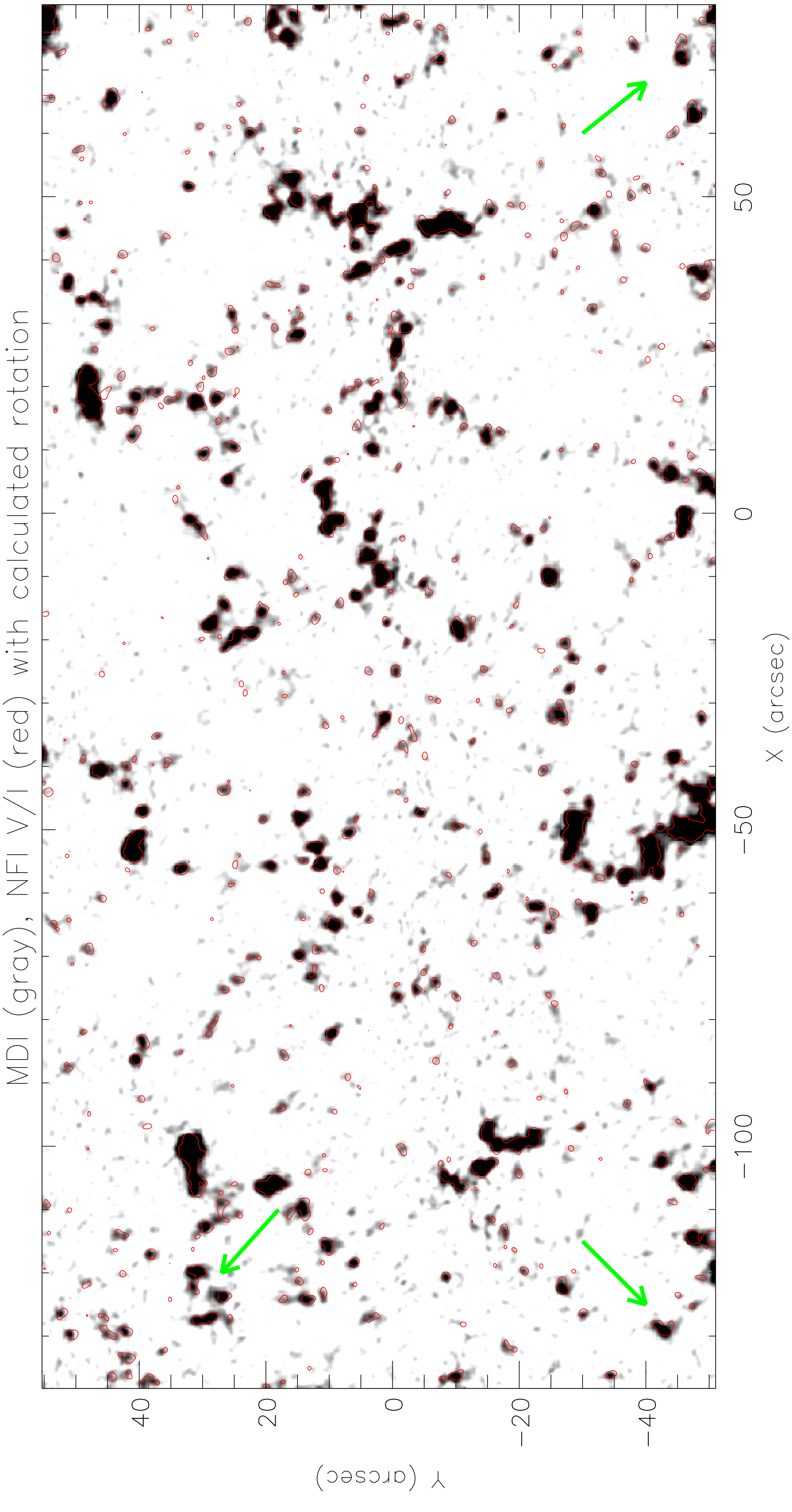

Figure 4.7: *Same as Fig.4.6 with a recalculated tilt. The green arrows are visual references for comparisons of the alignment with Fig.4.6.*

4.2.4 Co-alignment of NFI magnetograms with the Blue continuum images from BFI

The NFI observations and the blue continuum images from BFI also need co-alignment. For this we need the BFI Ca II images as intermediate co-alignment frames.The Ca II images will also be co-aligned with the NFI magnetograms.

BFI Ca II and Blue continuum

The granulation seen in blue continuum with BFI, and the small magnetic cells observed in the NFI magnetograms, are, geometrically speaking, completely different features. In the Ca II emission line, the granulation is seen at hotter temperatures, and their brightness appears reversed (Evans and Catalano 1972, Suemoto et al. 1987). It is identified as "reversed granulation" in Rutten et al. (2004) and reproduced in simulations in Leenaarts and Wedemeyer-Böhm (2005). The intensity is anti-correlated with the photospheric granulation when taking into account a time delay. This time delay is between 2 and 3 min after which the Ca II /Blue anti-correlation is maximum. In addition, the brightest features in Ca II are geometrically similar to the magnetic features in the NFI filtergrams. We use this property to cross-correlate the Ca II images with the blue continuum images (both from BFI) in a similar manner as Rutten et al. (2004). In our data, the time difference between Ca II images does not exceed 90 s, which is also the case for the blue continuum images. In addition, these 2 time series are shifted with each other by ~30 s in time, so we can select, for each blue continuum image, a Ca II image taken after a delay between 2 min and 3 min, and perform a co-alignment by pair. Note that this method only works in quiet Sun, where the granulation is observed with both instruments. Fig.4.8 contains samples of 2 different parts of the images. The Ca II images (red and green contours), are co-aligned onto their time-corresponding blue continuum image (background image). The Ca II intensity has been reverse-scaled in order to compare more directly the granules (bright) and inter-granules (dark) of the continuum image. The red contours are the maximum intensity of the reversed Ca II, whereas the green contours are taken at a lower level for comparisons with the intergranular lanes. This co-alignment is achieved with an uncertainty of ±0.4 arcsec between the two series.

BFI Ca II and NFI magnetograms

The Ca II images are also sensitive to the magnetic field, which is seen as a higher intensity in the Ca II images, and define a low-chromospheric network, similar enough to the one observed in both NFI and MDI magnetograms. Averaging both the Ca II and NFI images over a few minutes is enough to obtain a well contrasted and similar patterns to cross-correlate. The result of the co-alignment is displayed in Fig.4.9, and the error is estimated at ±0.2 arcsec,i.e, the pixel size of BFI.

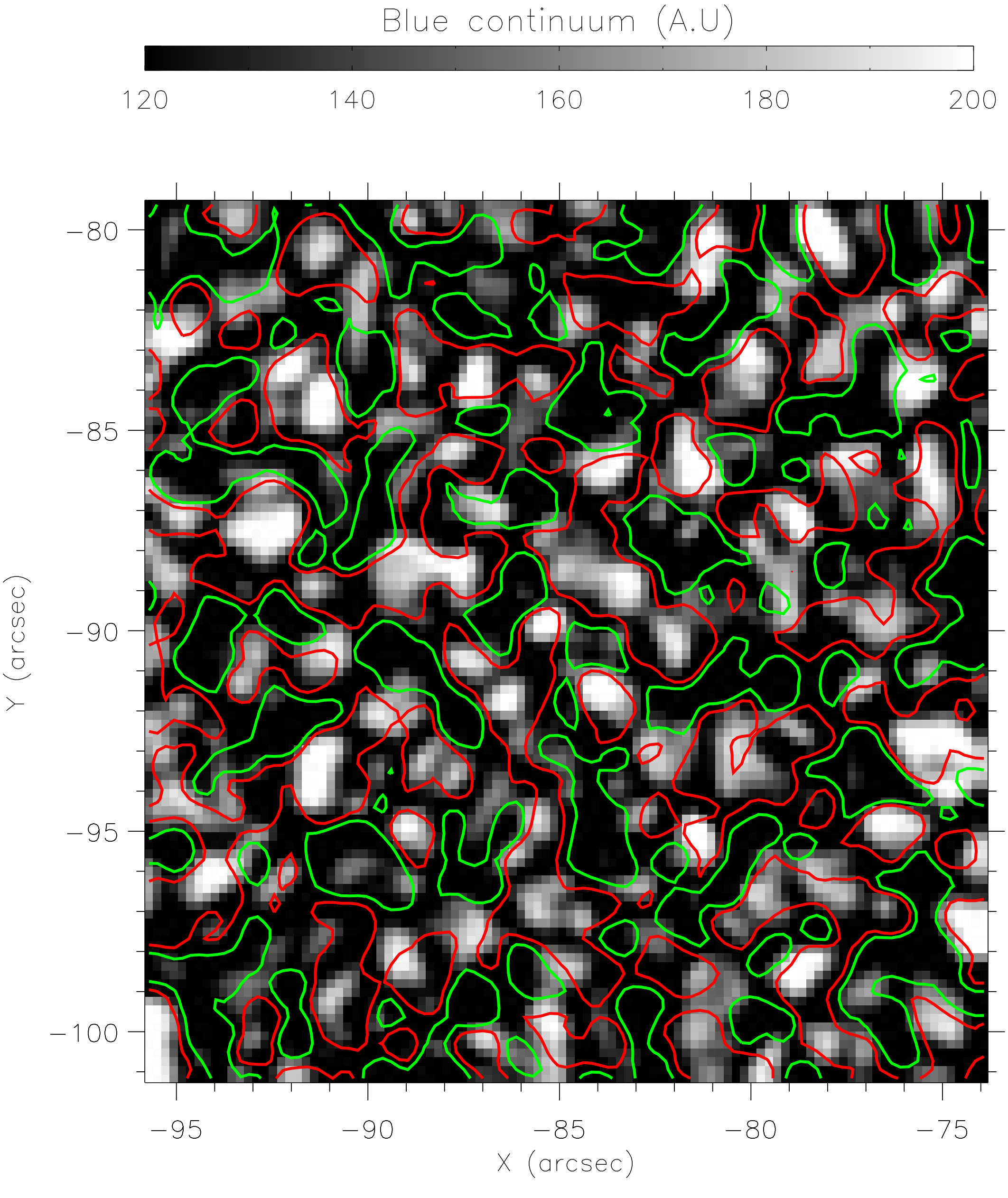

Figure 4.8: *Sample of co-aligned blue continuum image (gray-scaled background in arbitrary units) with contours of the Ca* II *image (red and green. The contrast in the blue continuum image has been enhanced for better visibility of the granular pattern. Red contours are near the maximum intensity of the Ca* II *image and encompass the maximum intensity of the blue continuum image. Green contours are at lower intensity and encompass the darker intergranular lanes in the blue continuum image.*

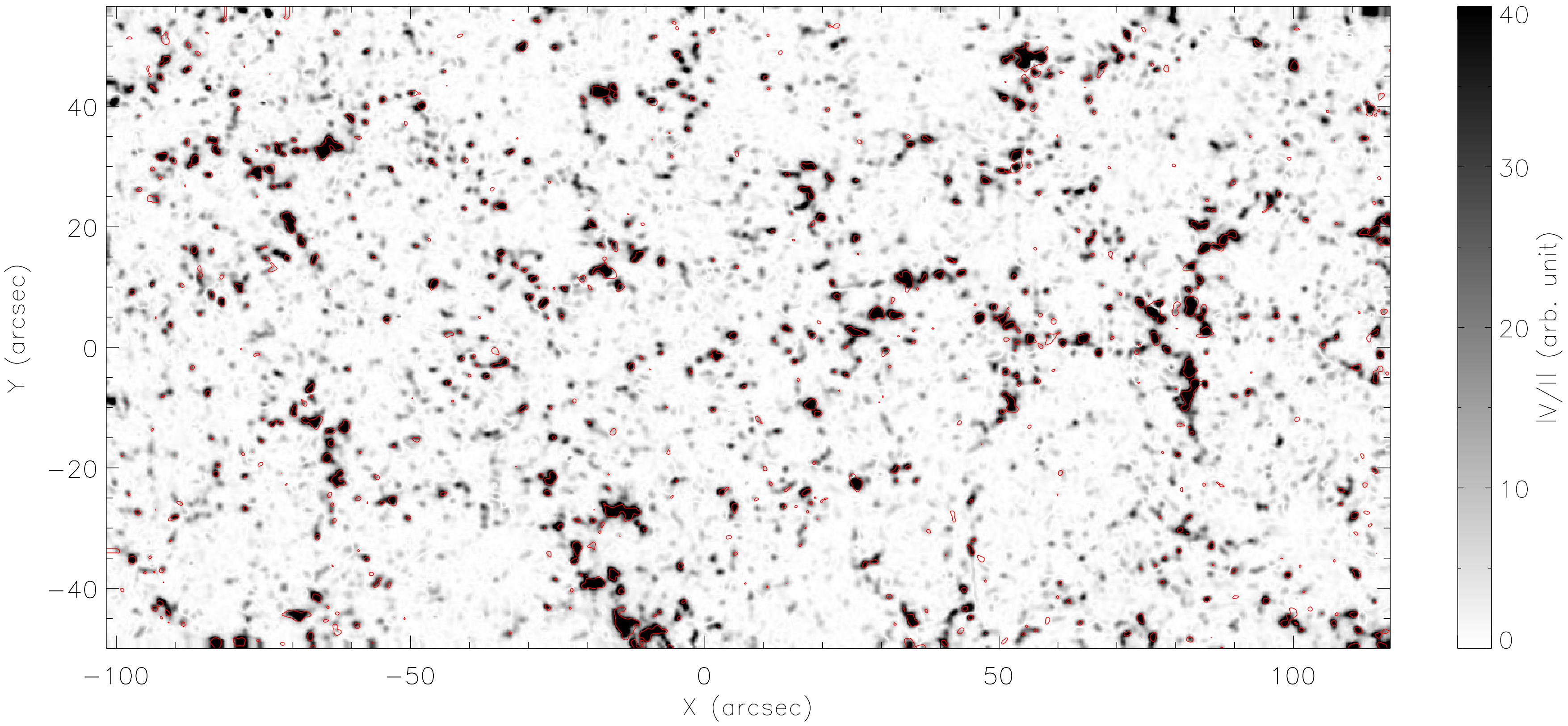

Figure 4.9: *Co-aligned V/I* NFI *filtergram (gray-scaled colortable) and Ca* II *(red contours). Both images result from an average over* 10 min

Instrument pairs	BFI-NFI	NFI-MDI	MDI-EIT	EIT-XRT
Alignment error (arcsec)	0.6	0.3	0.3	0.5

Table 4.1: *Co-alignment random error between the different instruments of Hinode and SoHO. BFI, NFI, and XRT are onboard Hinode. MDI and EIT are onboard SoHO*

Finally, the shifts between the pairs Blue continuum - Ca II , and Ca II - magnetograms (NFI) are summed up to obtain the shifts between the pair Blue continuum (BFI) - magnetograms (NFI). This results in a co-alignment uncertainty of about ±0.6 arcsec.

4.2.5 Co-alignment of the SoHO and Hinode data

The full-disk, low-resolution MDI magnetogram at 18:59 is used as an intermediate reference map (see Fig.4.3), mapped to Earth view, and is interpolated to have the same pixel size as the MDI high-res. magnetogram. The latter, recorded at the same time, is co-aligned to the full disk magnetogram using cross-correlation, with an uncertainty of ±0.3 arcsec.

We estimate the uncertainty of the coordinates of the disk center of both full disk images of MDI and EIT (SoHO) to be negligible compared to the other alignment uncertainties. The alignment of XRT involved the full disk EIT image at 195 Å. This wavelength (among 4 different ones available in EIT) offered the best resemblance with the features visible in XRT. Both regions are taken at the same reference time (18:59). The XRT image could be co-aligned to the EIT image by cross-correlation, as many resolved features were present in both datasets (Fig.4.10). This co-alignment is determined within ±0.5 arcsec.

We then used the shifts of XRT in the EIT frame of reference to project them into the MDI frame of reference, using the coordinates of the disk center in the headers. The XRT images are then co-aligned with the MDI high-res. data.

4.2.6 Overall co-alignment

To summarize, following the methodology of the co-alignment chart in Fig.4.3, we have co-aligned the data series within the co-alignment uncertainty given in Table 4.1.

Note that these are random co-alignment errors. Hence the co-alignment error between any different pair of instruments is obtained by taking the quadratic sum of the relevant errors in Table 4.1. For example between BFI and XRT, frames are co-aligned within a 1σ-uncertainty that quadratically sums up to ±0.9 arcsec.

4.3 Calibration of the magnetograms from NFI/SOT

The observations from the Narrow-band Filter Imager (NFI) are actually the measurements of the line ratio Stokes V/I, which we referred to as "filtergrams". In our data, they

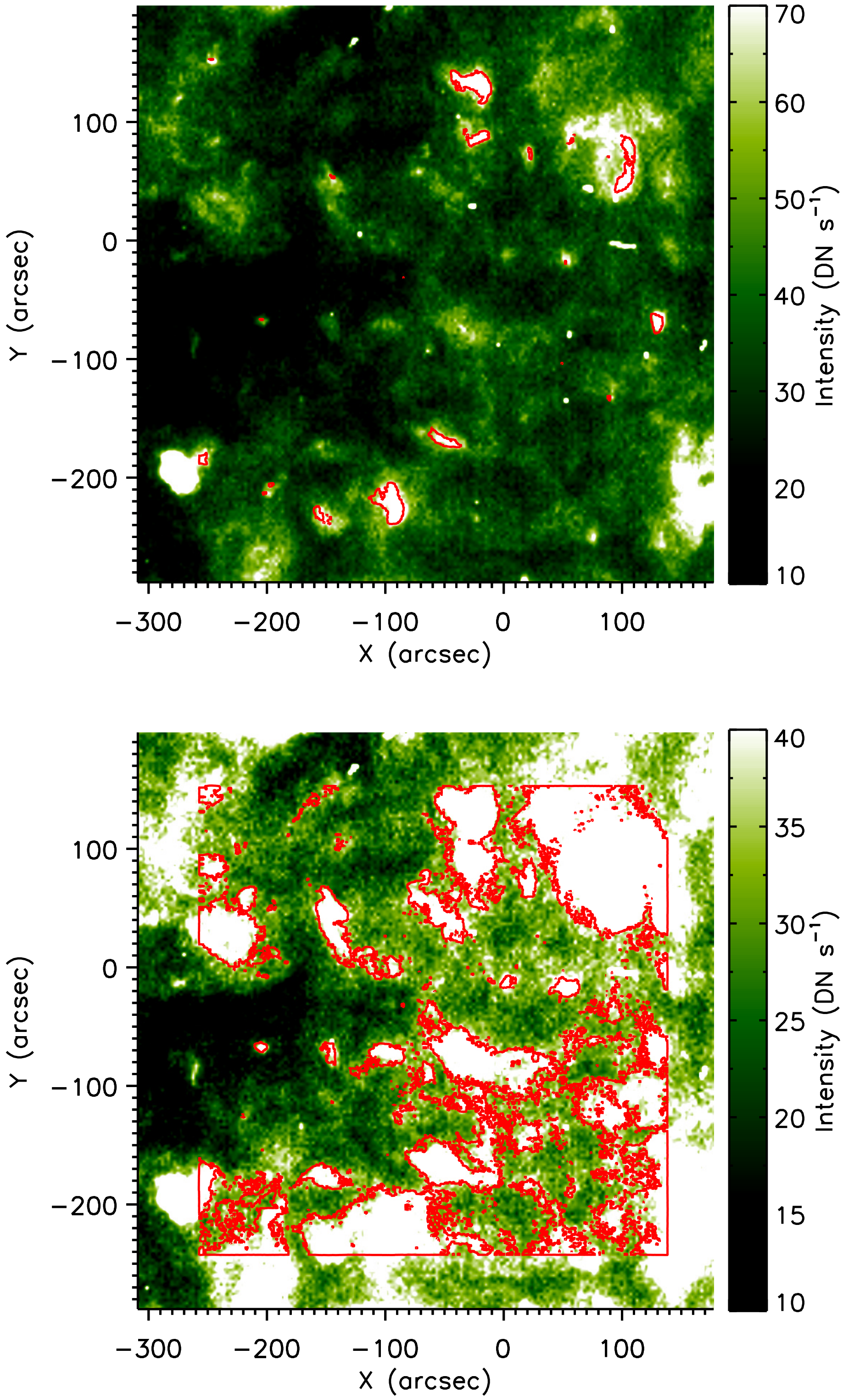

Figure 4.10: *Alignment of XRT (red contours) on EIT (green-scaled background). The field of view of XRT is smaller than EIT, this causes the square shape of the XRT outer contours.*

are given in unphysical, arbitrary units (arb. unit), and with a polarity opposite to those of the MDI magnetograms (i.e, the positive values in MDI correspond to negative values in the NFI filtergrams, and vice versa). An accurate calibration of the filtergrams into units of magnetic field requires the data from the spectro-polarimeter (SP) from SOT/Hinode which provides the line profiles (Chae et al. 2007). Unforturnately, SP observations are not available for the period of time of interest, and we have to revert to another method. Instead, we convert the filtergrams into physical units (G) using the high-resolution MDI magnetograms (SoHO), in a similar manner to Parnell et al. (2008). Note that because our original data were given in different arbitrary units than the one in the latter, our calibration factor will be different. The calibration consists in fitting the NFI data to the MDI data to derive a linear calibration factor, which is used to rescale the units of the NFI filtergrams, which forces both data series to have the same flux density. We remind the reader that the magnetograms used here are bidimensional spatial distributions of the approximated line-of-sight magnetic field. Near the disk center, it is considered parallel to the heliocentric Z-axis (pointing toward the observer), and referred to as B_z, indexed by the name of the instrument with which it is measured (e.g., $B_{z\,\mathrm{MDI}}$, $B_{z\,\mathrm{NFI}}$). Once calibrated, the NFI filtergrams will also be referred to as "magnetograms".

4.3.1 Rejection of artifacts

The NFI uses a CCD that is divided in two parts. In our data, we have noticed that the left-side of the CCD exhibits some time-dependent, and spatially non-uniform artifacts, which impairs the data. It is best visible when averaging the absolute value $|V/I|$, as shown in Fig.4.11. The Stokes I and V are divided onboard to save telemetry, and thus we cannot assess the effect of the removal of dark current and offset signals in both I and V, which makes it difficult to explain the artifact in Fig.4.11. Furthermore, V/I being a line ratio, flat-fielding issues are, by definition, minimized (Stokes I and V are recorded by the CCD almost simultaneously, with a time interval negligible with respect to the time sampling rate of the V/I time series). Because the error stops right at the middle of the CCD, the effect of the air bubbles in the tunable filters are ruled out, as the latter are known to be somewhat circular blemishes that tend to be near the edges of the CCD (for more details, see Tsuneta et al. 2008, § 8). Indeed, when present, the effect of the air bubbles are visible in the images of BFI (Broad-band Filter Imager), which shares the same CCD with NFI. In our case, the BFI images were blemish-free.

This artifact was so far undocumented, and here, it affects about one third of the left half of the CCD. The fact that it is time-dependent, and that it stops precisely at the middle of the CCD makes the data on the left side less reliable for calibration than the data on the right side. Therefore only the latter is used to compute the calibration coefficient.

4.3.2 Least-squares fits

As said earlier, the polarity of the original data are opposite to those of MDI. For simplicity, we first invert the NFI data, which will now be referred to as V/I_{NFI}. Thus note that the correlations derived below are, in fact, anti-correlation with respect to the original, non-inverted data.

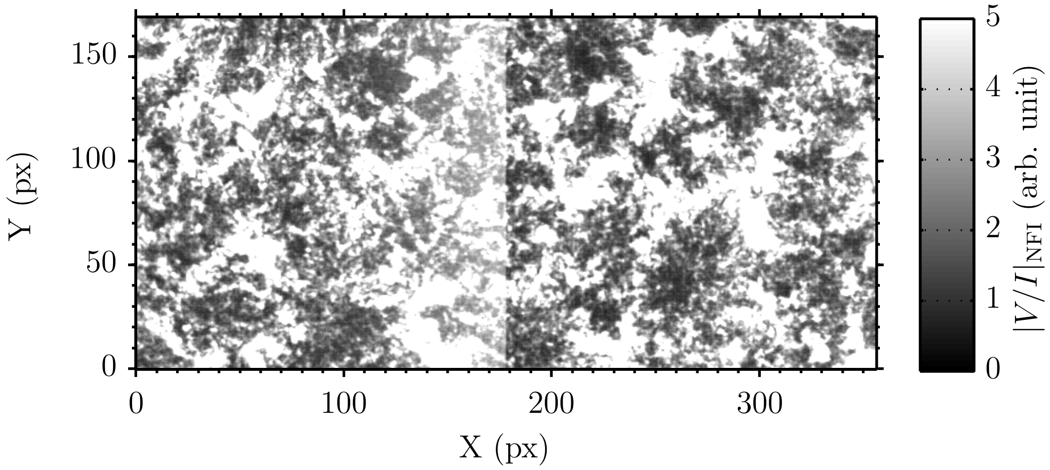

Figure 4.11: *Average filtergram of the absolute value |V/I| (NFI/SOT). The left part of the frame exhibit a non-uniform background signal that stops at the middle of the CCD. The right part is not affected by this error.*

All the NFI data are resampled with the MDI pixel size of 0.6 arcsec. In addition, the resolution is degraded so it is the same as MDI (2 px = 1.2 arcsec), using a gaussian convolution kernel with a FWHM of 1.2 arcsec. Next, in order to decrease the noise level in the MDI magnetograms (~25 G), we averaged both co-spatial data series over simultaneous time windows of 30 min. This decreases the MDI noise level to ~$5G$. Hence the NFI calibration only considers the pixels satisfying $|B_{z\,\rm MDI}| \geq 5$ G. Fig.4.12 (top) shows the areas that were finally used (i.e, the pixels in the magnetic patches within the red contours). In Fig.4.12 (bottom) we have plotted $B_{z\,\rm MDI}$ against $V/I_{\rm NFI}$, pixel to pixel (gray dots). Note the spread of these data. Regardless of other instrumental effects (e.g, cross-talk and doppler shifts in the line profiles), the spread of the scatter plot is mostly caused by the uncertainty of our co-alignment, which makes the NFI frames jitter around the MDI frames within a rather small, but non-negligible distance of ~0.6 arcsec (i.e, displacements of ±0.3 arcsec, see § 4.2.3 or Table 4.1). Indeed, even a displacement of 1 px is enough to make a high flux density of a feature in one instrument correspond to a low flux in another instrument, this is particularly around the sharp edges of the magnetic features. However, we can minimize this spread by taking the mean of the several $V/I_{\rm NFI}$ values that are measured at the same value of $B_{z\,\rm MDI}$ (graphically in Fig.4.12, bottom, this means we average all the values that lie on the same horizontal lines). We obtain $N = 164$ independent pairs of data, plotted as black dots. Note that these points are much less spread out. They are fitted by the red line in Fig.4.12 (bottom). The correlation coefficient is $r \approx 0.997$, the calibration coefficient equals $\beta = 0.75 \pm 0.01$, and the 1σ-uncertainty is $\sigma_{B_z} = 4$ G. Finally, we can rescale the original NFI filtergrams and get proper "magnetograms" using $B_{z\,\rm NFI} = \beta \times V/I_{\rm NFI}$. One should recall, however, that we initially inverted the filtergrams before the calibration. If the latter is applied at once, on the original non-inverted data, β should be inverted and we would use $\beta = -0.75$. We estimate the noise level in these calibrated magnetograms to be ~4 G

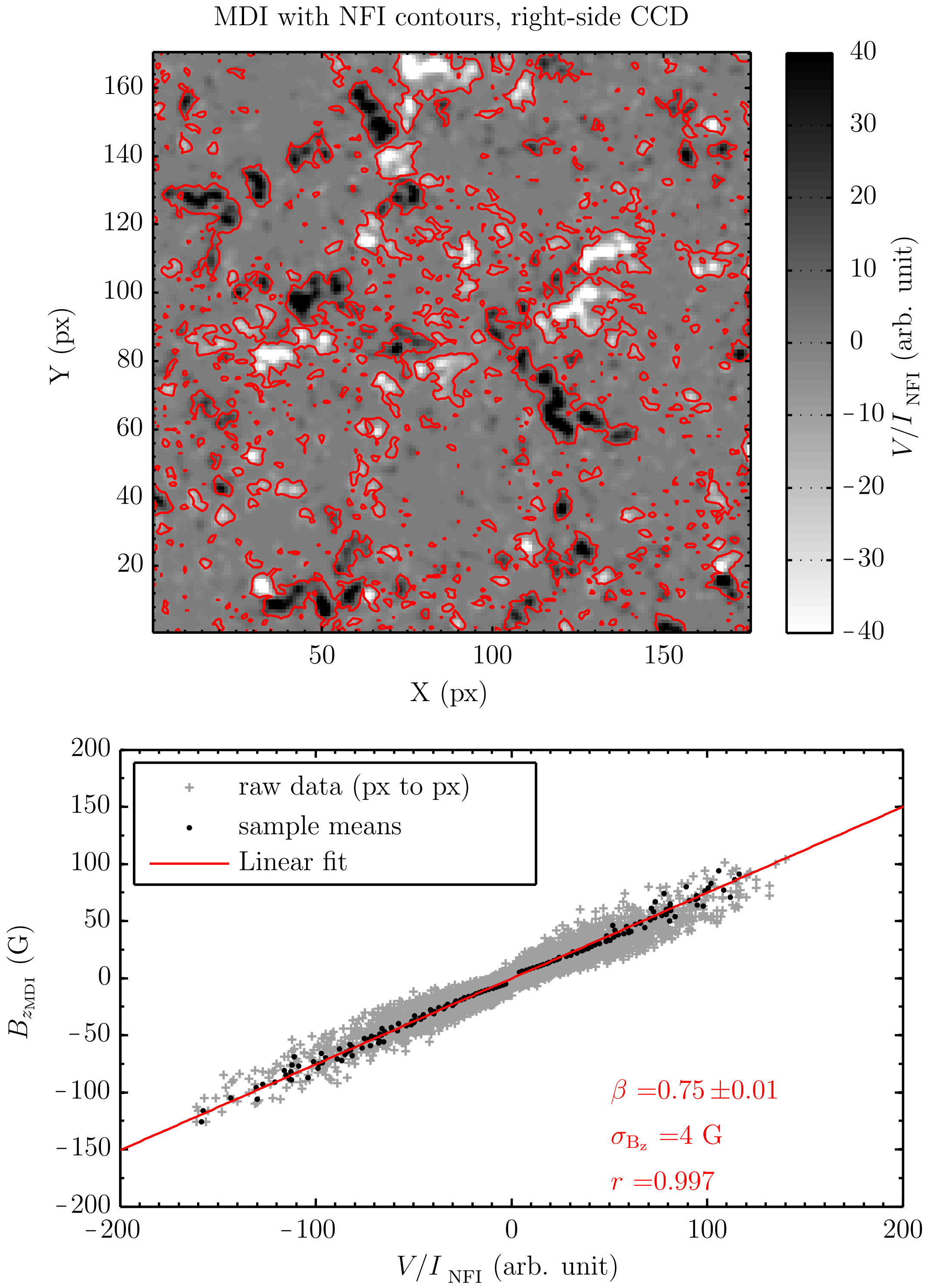

Figure 4.12: *Top: NFI filtergram scaled between* −50 G *and* +50 G *with the red contours of the MDI magnetograms at* $|B_{z\,\mathrm{MDI}}| = 5$ G. *The data are averaged over* 4 hr.
*Bottom: The light-gray crosses are the "*px *to* px*" data. The dark dots are the averages of the* V/I_{NFI} *values that were at the same* $B_{z\,\mathrm{MDI}}$ *values (same horizontal lines). These data are fitted with a least-squares regression (red line). The fit parameters are defined as the slope* β*, the* 1σ*-uncertainty* σ_{B_z} *and the correlation coefficient* r.

4.4 Flows, magnetic field, and X-ray emission

Here we investigate in more details the relationship between the photospheric flows, the magnetic field, and transient X-ray brightenings. First, we need to define the latter. This is detailed in the next section.

4.4.1 Detection of X-ray transients

Fig.4.13 shows the supergranular lanes (blue contours) derived from the 4-hours averaged flow map of MDI, on top of the averaged absolute-running-difference of the XRT images, normalized by the 4 hr-average image. Magnetic contours (red and green) from the averaged MDI magnetogram outline the "magnetic context" of the whole time series. The XRT averaged running-difference enhances all the transient events that occur over 4 hr of observations. The running difference uses a time interval of 3 min between the differentiated images. This processed image, defined as I_{diff}, formally derives as :

$$I_{\mathrm{diff}} = \frac{\sum_{i=1}^{N} |I_{i+\Delta n} - I_i|}{N\bar{I}} \tag{4.2}$$

where $\bar{I}$ is the 4 hr-average XRT image, I_i is the i^{th} original image in a time series of $N = 240$ images, and Δn is the number of frames between two subtracted images. Here, $\Delta n = 6$ with a time interval of 30 s between each frame. Normalizing by the average image $\bar{I}$ has a "flat-fielding" effect, and enhances the contrast of the features even further. Thus I_{diff} has no dimension and is expressed as a normalized intensity ratio. The choice of the ideal time interval was made iteratively, by checking which interval reveals best all the short-lived emission, while smoothing out the long-lasting hot structures like X-ray loops, sigmoids, etc... So any X-ray emission still visible in I_{diff} comes from a source whose emission significantly increases over the background over the time interval Δn of a few minutes or less, and which we call "transients". The latter term is, in fact, relative to the duration of the experiment (4 hr). In I_{diff}, X-ray loops with variable emission may also still be visible.

Next, we look at the events with a rise in the X-ray light curve of more than 15% above the background level, and that last less than an hour. We found 12 transients satisfying these criteria. They are located in the white rectangles in Fig.4.13. There are 6 transients in the MDI FOV, outside the NFI FOV. In the latter, 6 other transients were detected and are located in the wider regions A, B, C, and D which will be treated separately. Some small dots are also visible, and have all the characteristics of cosmic rays (1 pixel wide, present in 1 frame only with saturating intensity). The automated removal of the cosmic rays with the XRT software of Solarsoft is not possible as it also affects the transients of interest. All the transients are located on the network, and are associated with barely resolved bipoles. In this respect they are quite similar to the ones studied in Krucker et al. (1997). We also notice that they are all associated with bipolar structure. The magnetic flux from the MDI magnetograms was too weak to quantify its evolution accurately with Magnetic Balltracking, which here can only be applied to the better resolved magnetograms of SOT/NFI.

Note also that, at this point, we cannot relate these events to those of Innes et al. (2009), as we do not have co-spatial and co-temporal observations to check any EUV counterpart to the observed X-ray transients.

The analysis of the transients is separated in two parts, starting with the ones in the MDI FOV, and followed by those in the SOT FOV with the associated magnetic flux measurements.

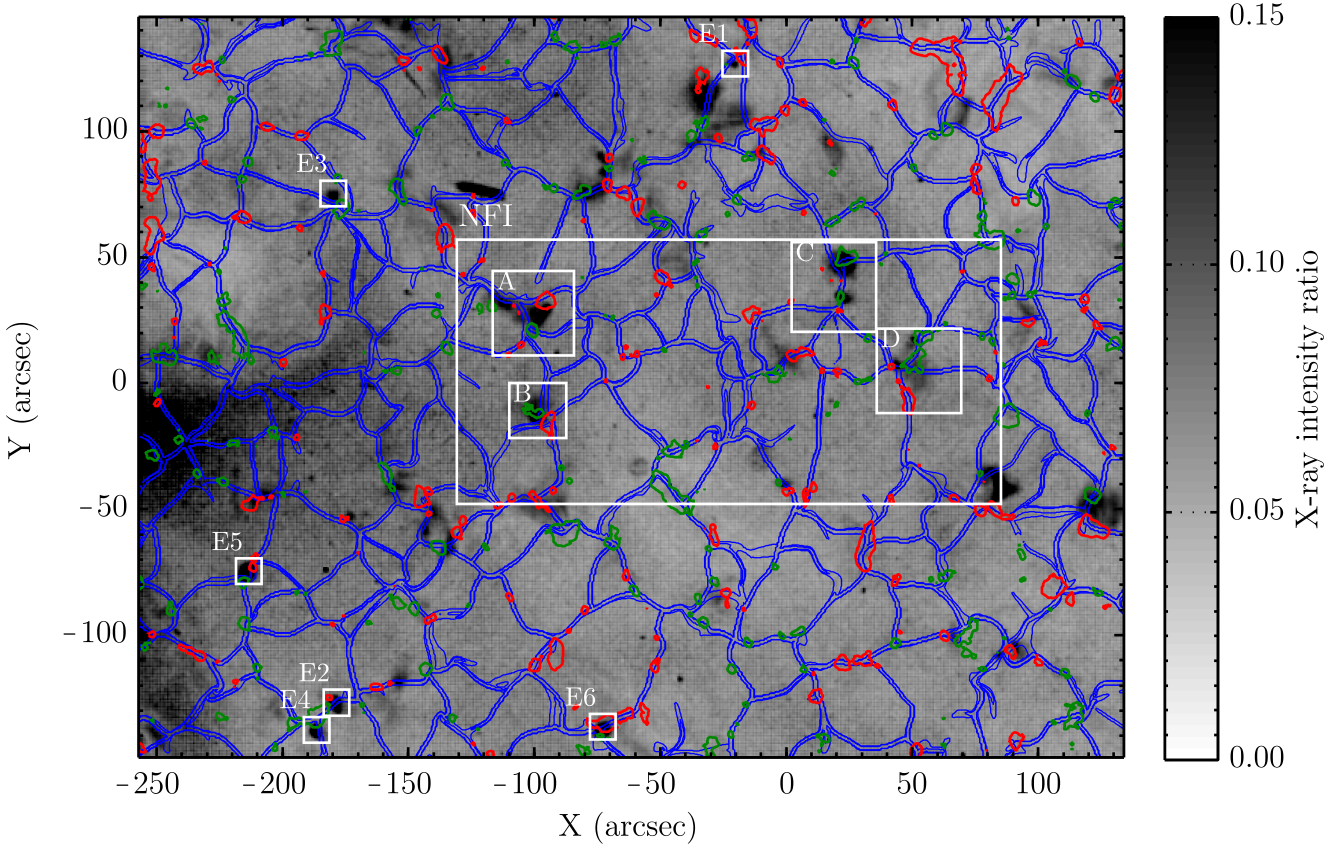

Figure 4.13: *Mean of absolute running-difference XRT images. Each image in the series is taken* 3 min *apart from the previous and the next. The blue contours are the supergranular lanes, from the 4-hours averaged MDI flow field. The green and red contours (respectively) are the magnetic flux at* −10 G / +10 G *from the* 4 hr*-averaged MDI magnetogram. The white rectangle is the FOV of SOT (Figs. 4.16 and 4.17)*

4.4.2 Transients in MDI-XRT FOV

The light curves of the X-ray intensity for each transient are plotted in Fig.4.14. The beginning and the end of the flaring phase is set to the threshold of 15% above the background emission (red crosses). The size of the emitting sources (encompassed by the white rectangles in Fig.4.13) is ~4 XRT pixels (2.8 Mm). The associated flow fields are shown in Fig.4.15, where they are averaged over 1 hr and smoothed over 4 Mm. We can see that the emitting sources E1 to E6 are not just over the network (Fig.4.13), but within groups of converging streamlines which are literally "funneling" the photospheric material right at the footpoints of the X-ray emission. In addition, we can see that they do not occur at random places within the network. Instead, they are located near the intersections of the supergranular network lanes (which we see as the "crossroads" of several blue lanes), with the exception of E2, which may be located in the middle of a network lane (Fig.4.13). These specific locations of the transients can be explained by looking at the detailed view of the streamlines in Fig.4.15. They seem to be the result of at least two combined effects: the first one is the expected motion of the magnetic flux toward the network. The second one is that the funneled flows in the network push flux concentrations together, as they penetrate deeper and deeper into the funnels' streamlines, which join up eventually at the intersection of supergranular flows. This is particularly intriguing with the site E3 caught in one of the funnels of neighboring supergranules whose streamlines get intertwined to form a supergranular vortex flow of about 25 arcsec (~18 Mm).

4.4.3 Transients in SOT-XRT FOV

Balltracking was applied to the 2 min-cadence blue continuum data sets from Hinode/SOT. The velocity fields were smoothed over 4 Mm and averaged over 60 min, and we derived the supergranular network lanes of each flow field. The different "snapshots" of the lanes were averaged over the whole time series, providing a context map of the flows and of the network, in the manner described in Sections 2.5.3 and 2.5.4, and which is displayed in Fig.4.16 (blue lanes). Region A and B contain somewhat elongated features. In regions C and D we identified 4 sites of X-ray transients, tagged in white (C1, C2, D1, D2). The location of their emission peaks are tagged with white crosses. Note the preferred sites of the X-ray transients, with respect to the supergranular lanes: C1, C2, and D2 lie right on top of the intersection of the lanes. D1 is at the middle of a lane,i.e, at mid-course between two intersections. A complementary view of the flow is given in Fig.4.17, averaged over 4 hr, in which the colored background represents the magnitude of the horizontal velocity. The transients are located in the funneled streamlines like we observed previously in the MDI FOV.

Below we describe in more details the observations in the four selected regions. Note that region A and B are observed with the left half of the NFI CCD. There, and as mentioned in Section 4.3.1, calibration issues prevented us from quantitative measurements of the magnetic flux using Magnetic Balltracking. This was only possible in region C and D.

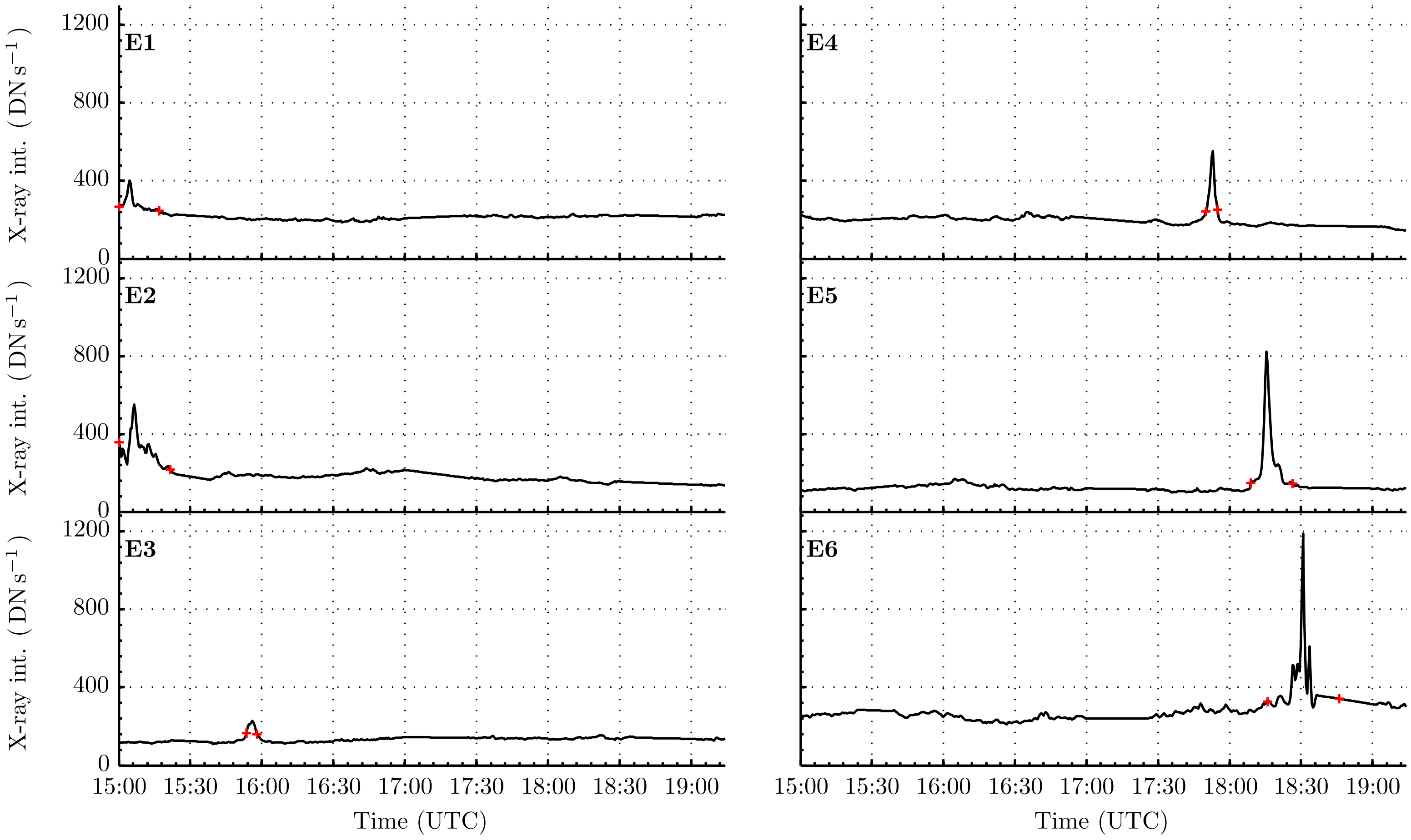

Figure 4.14: *X-ray light curves for events E1 till E6. The red stars mark the beginning and the end of the integration when computing the energy in table. The Y-axis is the same for both columns 4.2*

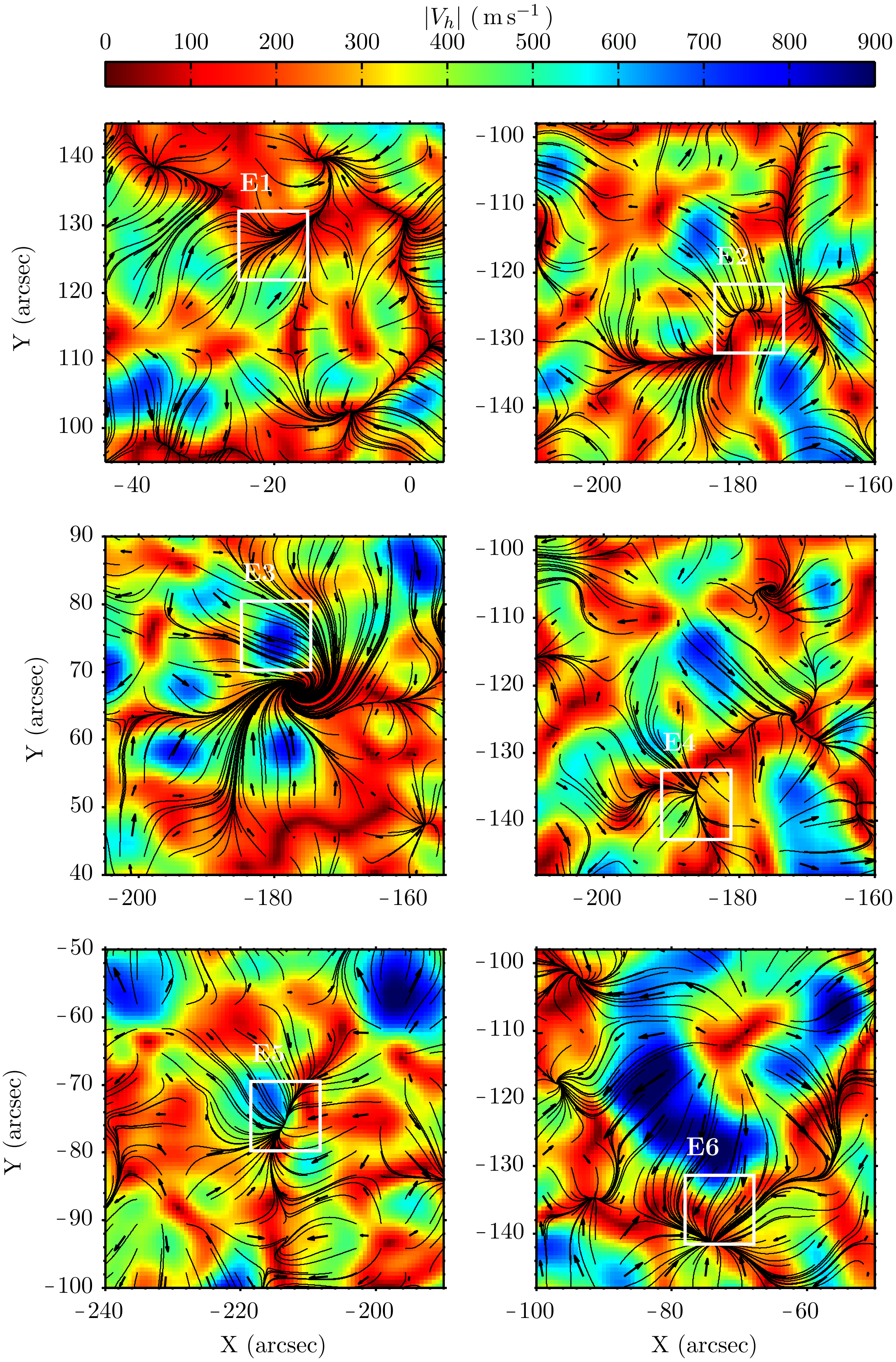

Figure 4.15: *Close-ups on the flow at the sites of the events E1 till E6 shown in Fig.4.13. Flows are averaged over* 1 hr *and smoothed over* 4 Mm.

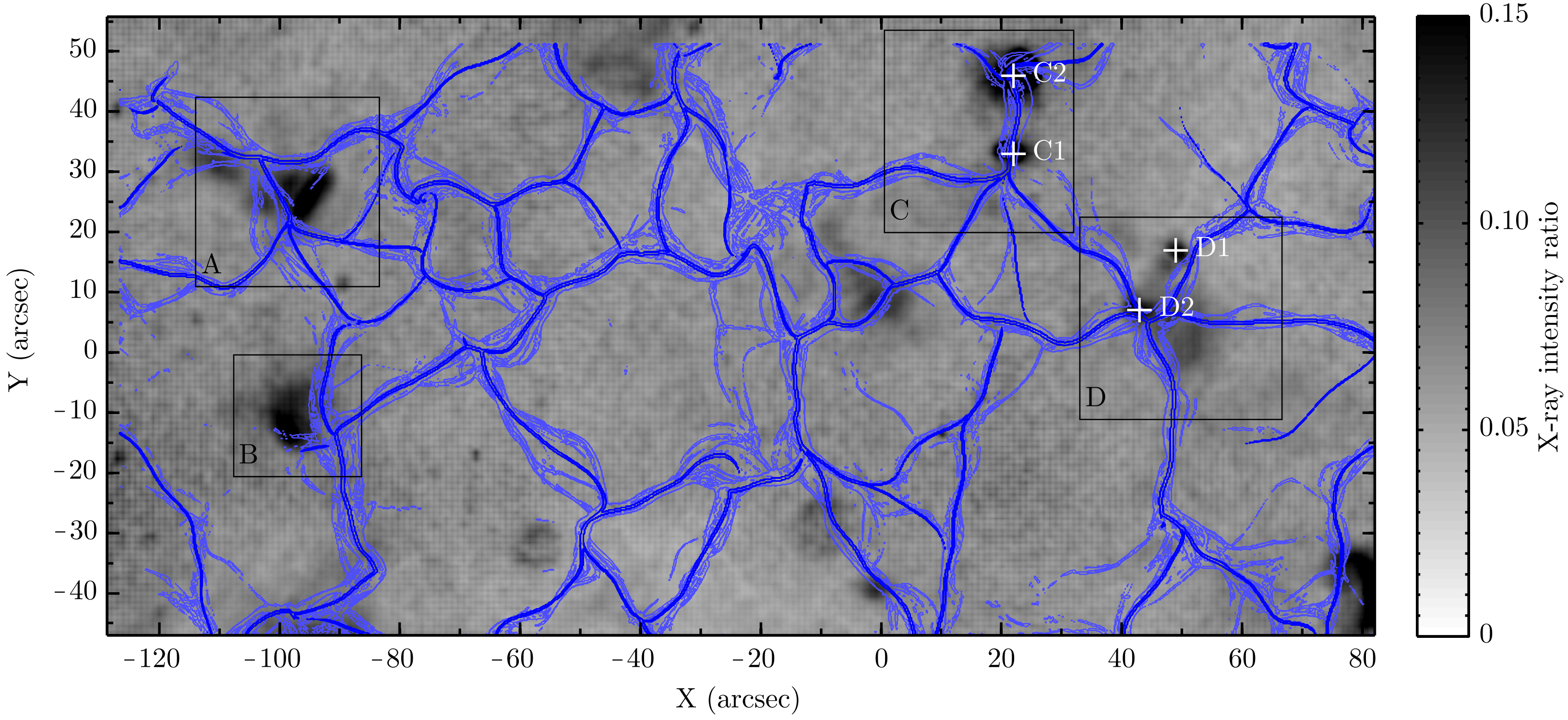

Figure 4.16: *X-ray image from XRT in reversed gray color-table. The blue lanes represent the supergranular network lanes. The gray background is the 4-hours-averaged absolute running-difference image from XRT.*

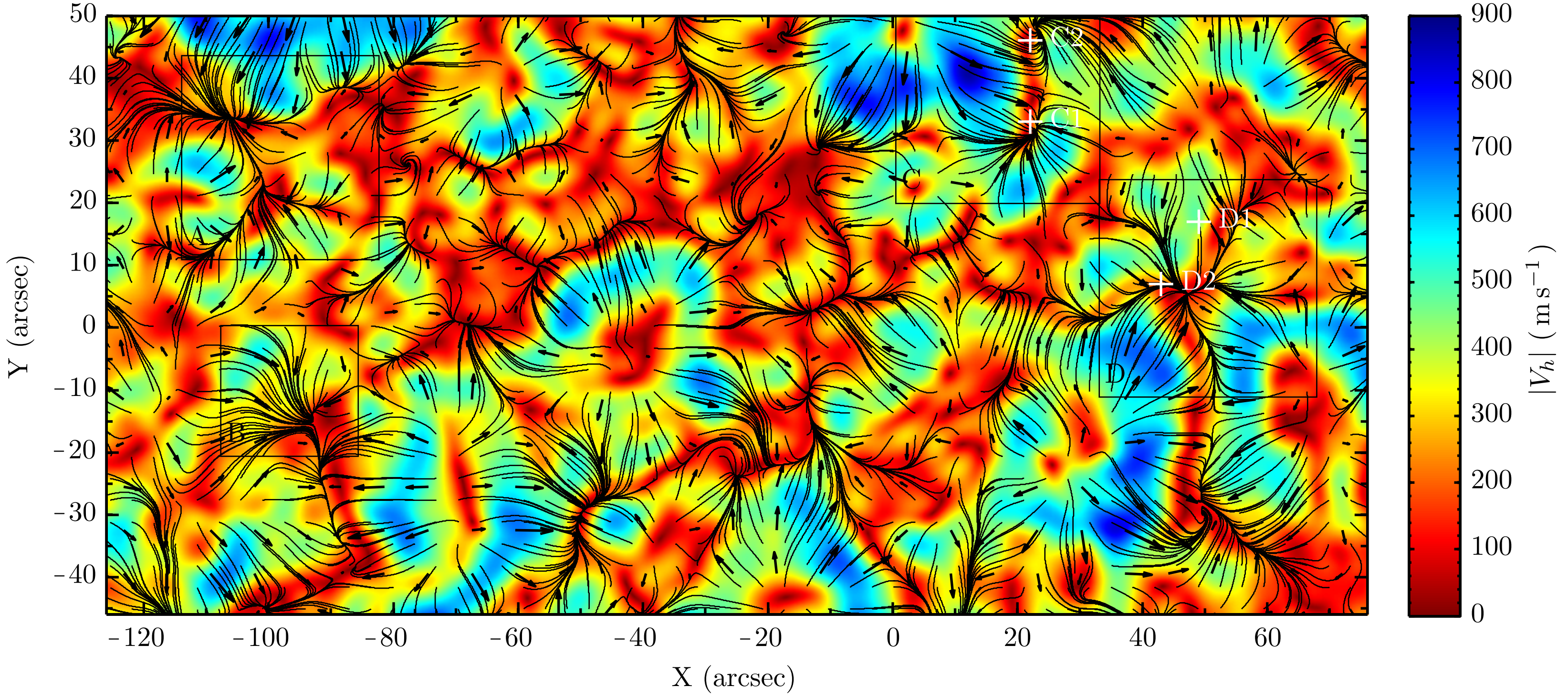

Figure 4.17: *Velocity field associated with the SOT field of view. The flow map is an average over 4-hours. The colored background is the magnitude of the horizontal velocity. The small black arrows show the orientation of the flow*

Region A and B

The bright elongated X-ray emission is located on the edge of a small supergranule (Fig.4.16, region A). In Fig.4.17, we displayed the map of the velocity magnitude with the streamlines. Note the imbalance between the greater magnitude of the northern flows (in region A), compared to the rest of area. In the close-up in Fig.4.18 (top), with a better temporal resolution (1 hr), we also observe this imbalance. The flow in the northern supergranule (above the upper white arrow) is quite fast, above $400\,\mathrm{m\,s^{-1}}$ on average, compared to the small supergranule between the two arrows, with a velocity of less than $300\,\mathrm{m\,s^{-1}}$. This imbalance results in the faster flow pushing the streamlines southward, which might explain the somewhat irregular shape of the slower supergranule. Fig.4.19 (top) is a close-up around the maximum X-ray emission with the vectors (blue arrows) of the 60 min averaged velocity field, and the contours of the magnetic flux. The positions of the blue arrows are integrated along the streamlines, with more arrows where the flow is more converging, like in funnels, and less arrows where the flow is diverging. Their length is proportional to the velocity magnitude (the latter can be inferred from Fig.4.18). We did not see a clear correlation between the magnetic flux and the X-ray emission as a function of time, but one notices that the X-ray thread ends up in the strongest magnetic features of opposite polarities, which suggests it is a poorly resolved X-ray loop. The strongest magnetic concentrations under the footpoints of the X-ray loop appear to be caught in funnels (see the long arrows in the top panels in Figs.4.18 and 4.19 pointing at both of them). This is more visible with the southern funnel, which is longer and wider. The northern one is smaller than the smoothing FWHM of the velocity field (4 Mm) so any particular shape below this size may not be meaningful.

In region B (Fig.4.19, bottom), the brighter soft X-ray emission is also located above[5] a funnel in which a magnetic bipole appears to be caught. It appears more clearly in Fig.4.18 (bottom). The "entrance" of this funnel is more than 10 Mm wide, which is greater than the FWHM (4 Mm) of the smoothing of the flows, and it is visible in both the 1 hr average flow field and in the 4 hr average in Fig.4.17, which makes the description of this funnel more meaningful than the one in region A.

The X-ray emission is slightly fainter than in region A, with only a few Data Number per second (defined as $\mathrm{DN\,s^{-1}}$ in the color bar) but also more variable, such that it remains visible in the absolute running-difference. In this case, it is unclear whether the bright X-ray emission originates from a coronal loop connecting the opposite polarities, or from an X-ray jet. Either way, one footpoint would be located deep inside the funnel, near the middle of the bipole pointed by the yellow arrow.

Region C and D

In what follows, the Magnetic Balltracking combined with the region growing algorithm (§ 2.6.5) was used to measure the flux disappearance underneath the transients. The tracked magnetic features are tagged with red crosses in the magnetograms of Fig.4.21. Note that in all the case studies, including those in region D (Fig.4.29), we can only

---

[5] While the blue arrows of the photospheric flows are plotted on top of the X-ray image in the background, we remind that the X-ray emission originate from the low corona, and thus it is described as being "above" the photospheric flows, i.e, in higher layers of the atmosphere.

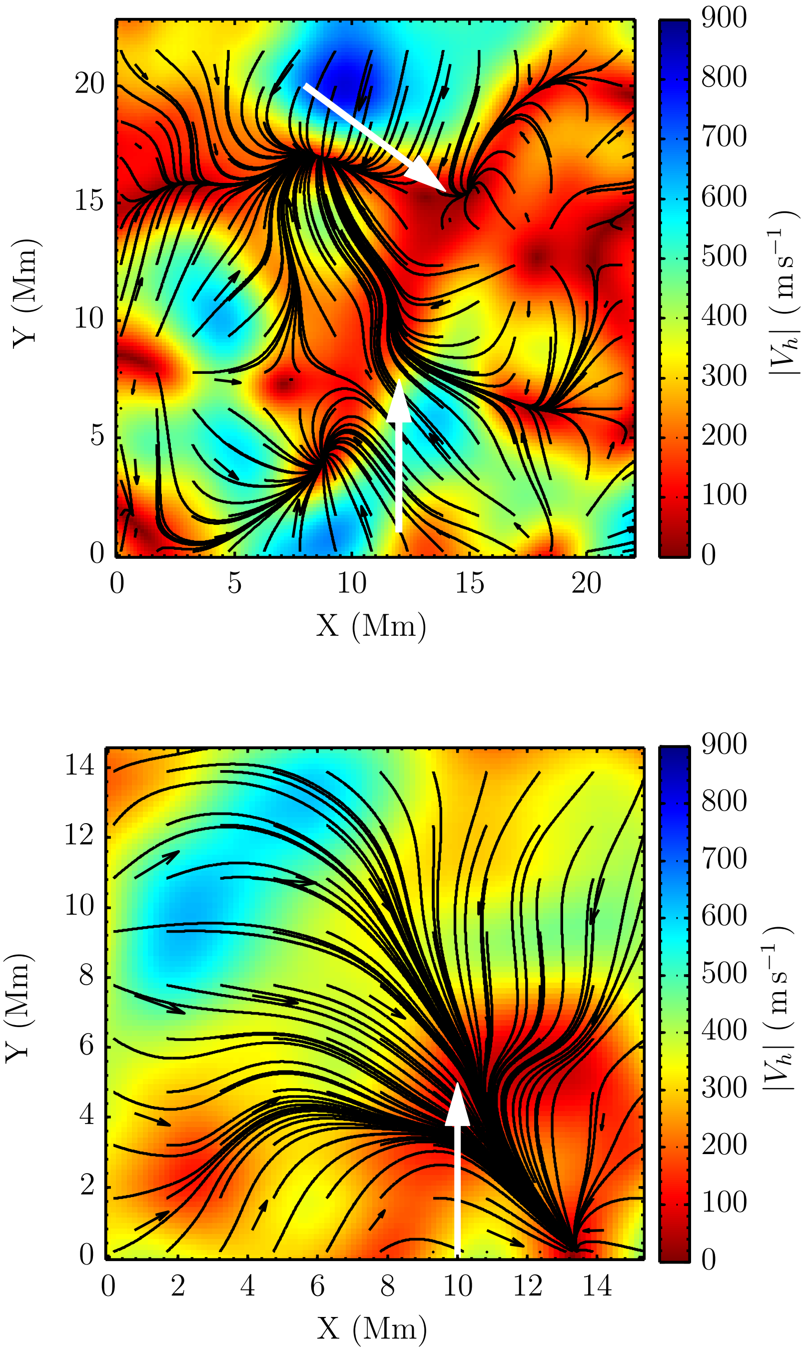

Figure 4.18: *Velocity magnitude in region A (top) and B (bottom), plotted with the streamlines of the flow (black continuous lines). The velocity field is the same as the ones used in Fig.4.19. The white arrows point at the funnel-shaped streamlines, at the same coordinates as the yellow arrows in Fig.4.18.*

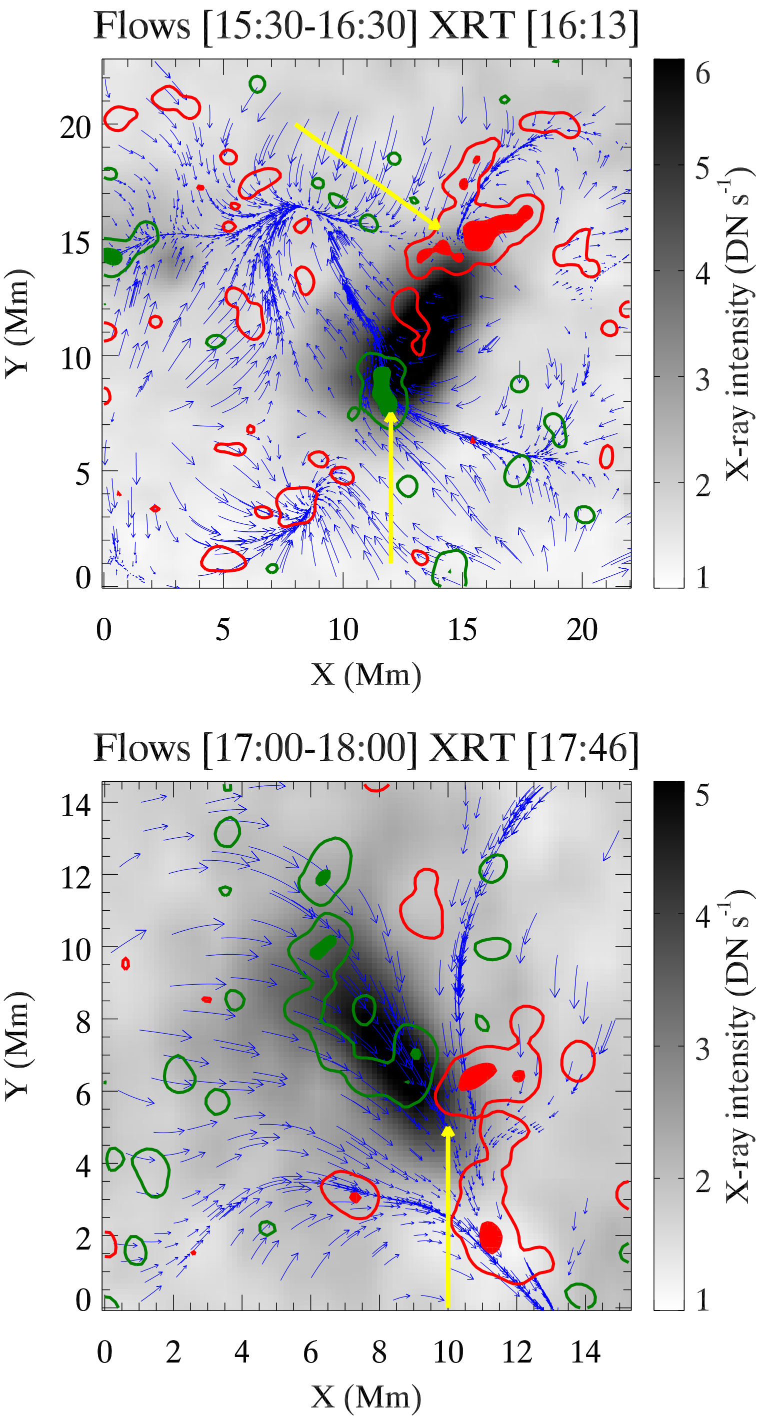

Figure 4.19: *Close-ups on region A (top) and region B (bottom), with vectors (blue) of the the* 60 min *average velocity field. The gray background is the XRT image taken at 16:13 UT (top) and 17:46 UT (bottom). Thin magnetic contours at* $|B_{z\,\mathrm{NFI}}| = 10\,\mathrm{G}$, *filled contours at* $|B_{z\,\mathrm{NFI}}| > 60\,\mathrm{G}$, *red for positive polarity, green for negative polarity. The lengths of the blue arrows are scaled linearly with the magnitude of the flow (the latter are displayed in Fig.4.19), while the body of the arrows can bend to follow the streamlines. Areas with more arrows correspond to a higher convergence of the streamlines. The yellow arrows point at a funneled-shaped streams, they are plotted at the same positions as the white arrow in Fig.4.18.*

extract the positive flux. The negative flux is indeed spread out over too many magnetic elements that cluster out and merge repeatedly, and which covers much larger areas than the disappearing positive flux does. Thus it is not possible to extract any coherent feature of negative flux with the region-growing algorithm which would otherwise extract a much bigger feature with much more flux than the one really involved in the flux disappearance. Indeed, when used locally to track individual magnetic patches, this technique is only meaningful if the tracked magnetic patches keep a coherent shape over time[6]. In region C, the magnetic threshold in the region growing algorithm needed to be set to 10 G. So a small percentage of flux may not be accounted for during the spatial integration. However, in region D, we could set it closer to the noise level.

Several snapshots showing the three transients in region C are displayed in Fig.4.20 (one event per row), with the blue arrows of the 60 min-averaged flow fields, and the X-ray images in the background. The two X-ray outbursts tagged C2a and C2b occur at the same place but at two different times. The three transients are observed between concentrations of positive and negative flux.

The results of the Magnetic Balltracking are given in Figs.4.22, 4.24 and, 4.26. The light curves of the X-ray transients (black) are integrated spatially over the emitting sources. The red curves are the magnetic fluxes derived from the Magnetic Balltracking. The red dashed vertical lines point at the local maximum of the flux, and which defines the beginning of the flux disappearance. The black vertical lines show the beginning and the end of the transient, defined as the time during which the light curve is 15% greater than the averaged background emission. We can see that all the X-ray brightenings in region C occur after the underlying magnetic positive flux has started to decrease.

Transient C1 In Fig.4.22, the flux is maximum at 15:13 with $\sim 1.1\times 10^{17}$ Mx. It has decreased by ~25% after 2 min, when the first X-ray burst starts (15:15), with an emission peak at $\sim 80\,\mathrm{DN\,s^{-1}}$. It is followed by a more intense peak at ~15:24, counting $\sim 160\,\mathrm{DN\,s^{-1}}$, while the underlying positive magnetic feature has almost disappeared, although neighboring clustered flux is still visible. A third burst, peaking above $\sim 120\,\mathrm{DN\,s^{-1}}$ occurs soon after the data gap, at 15:43, whereas the tracked magnetic feature has completely disappeared, although the area is constantly being refilled with new incoming flux. Fig.4.23 shows the 60 min-averaged flows, with the streamlines and the velocity magnitude. The contours of the X-ray image are taken at the time of the maximum emission (15:24). One clearly sees its brightest emission located at the tip of a funnel, which is also near the intersection of the supergranular flows (Fig.4.16), where the velocity is quite slow, below $150\,\mathrm{m\,s^{-1}}$.

Transient C2a Two balls are used to track the magnetic features underneath the transient at 16:50 (Fig.4.20 and 4.21, 2nd row). At first it is a single magnetic feature that ends up broken up in two pieces. When they breakup, the fluxes of both tracked features

---

[6] This does not mean that Magnetic Balltracking cannot track the magnetic features that are merging and breaking up. In fact, tracking those features is precisely why we created it in the first place. The limitation we have stated comes from the segmentation, and the nature of the data, when one wants to integrate the flux. It is possible that vector magnetograms would give more consistent shapes that would be easier to extract, for both positive and negative fluxes.

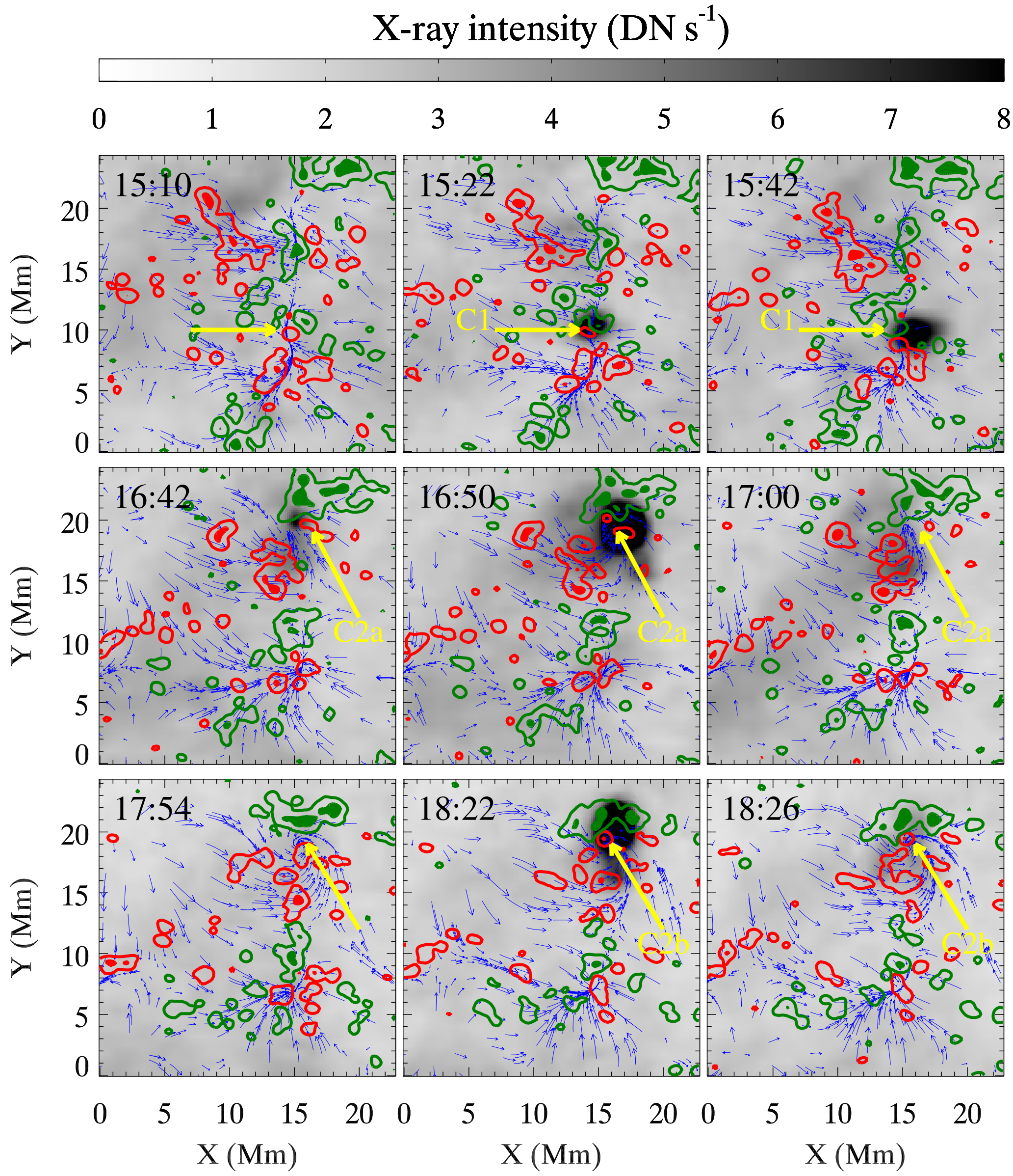

Figure 4.20: *X-ray images (gray reversed-colortable) and contours of the NFI magnetograms in region C of Fig.4.16. Red/green (respectively) is positive/negative polarity. Filled contours at +/-* 40 G, *thin contours at* +/-10 G. *The black arrows are the velocity vectors to show the direction of the flow. Their length is scaled linearly with the magnitude of the flow. The yellow arrows point at the location of the X-ray transient (C1, C2a, C2b).*

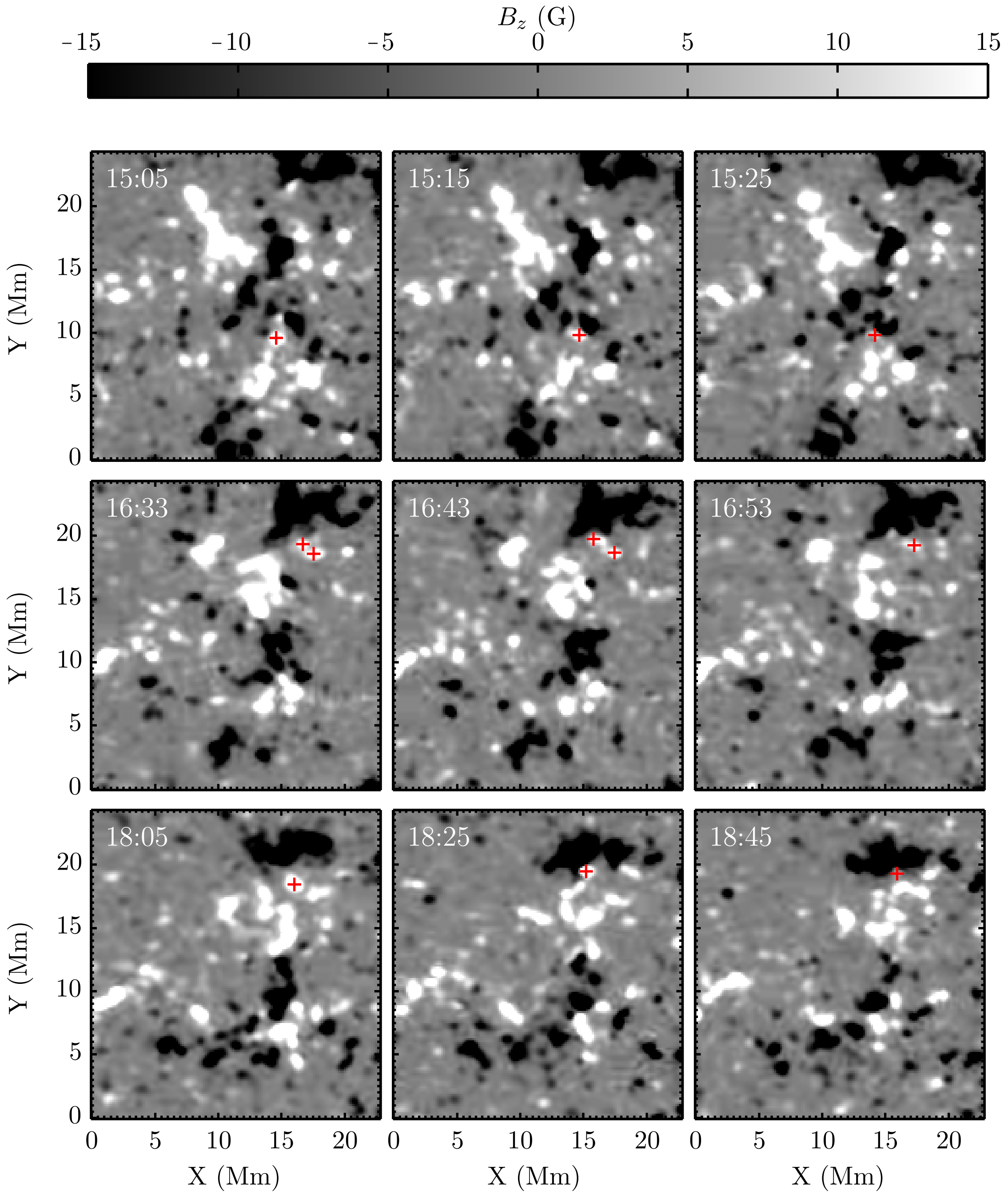

Figure 4.21: *NFI magnetograms as used in the Magnetic Balltracking to track the flux underneath the transients C1, C2a, and C2b, respectively from top to bottom. The red cross shows which magnetic element was tracked.*

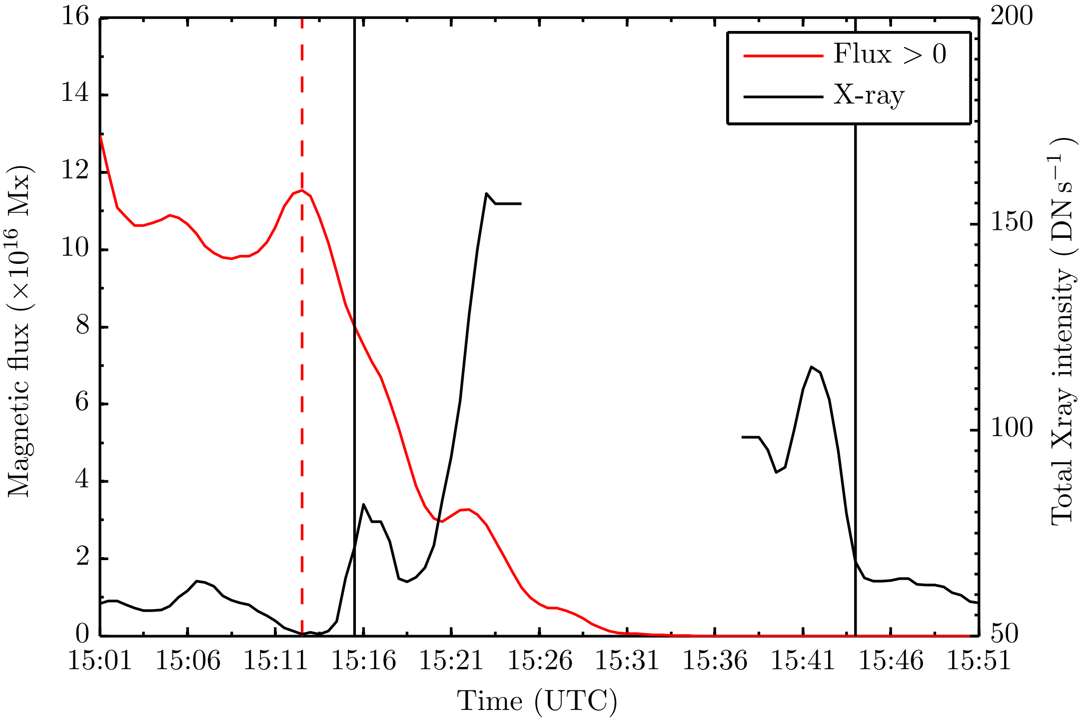

Figure 4.22: *X-ray light curves with associated evolution of canceling magnetic flux for the transient C1. The two black vertical lines define the duration of the X-ray transient, i.e, the time during which the emission is* 15% *above the average background emission.*

are summed up. By doing this, we consider these two magnetic features as a single entity, which the algorithm can extract. In Fig.4.24, the maximum of the positive flux is at 16:41 with ~1.5×10^{17} Mx, and decreases by ~15% over 4 min when the transient begins at 16:45. The X-ray emission is maximum at 16:51, with 650 DN s^{-1}.

In Figs.4.16 and 4.25, one observes that its brightest emission is less than 3 Mm from the northern intersection of supergranular lanes, within the funnels of a flow field whose magnitude is greater than 350 m s^{-1}.

Transient C2b

In Fig.4.26, the positive magnetic flux is maximum at 18:02 with ~2.6×10^{17} Mx. The X-ray transient starts at ~18:14 while the magnetic flux has decreased by ~20%. The X-ray emission is maximum at 18:22 (240 DN s^{-1}). Fig.4.27 provides an interesting picture of the X-ray transient occurring near the center of a vortex flow formed at the northern intersection of the network lanes. The locations of C2a and C2b are close to each other, less than 2 Mm (which is below the 4 Mm resolution of the flow field).

Transient D1 D1 is located in a small funnel (smaller than 4 Mm). The X-ray transient is visible in the second and third snapshot of Fig.4.28. Its location within the flow is also visible as red and white contours in Fig.4.31. Like with C2a, we used two balls to track

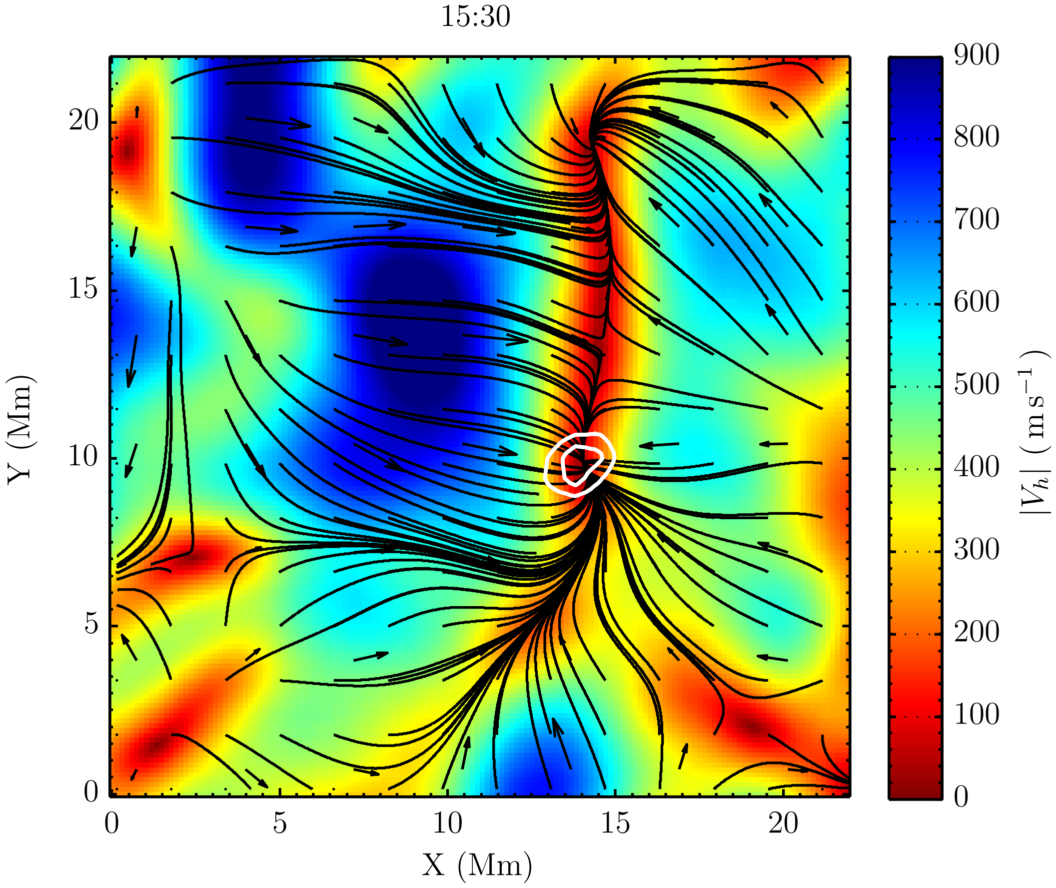

Figure 4.23: Flow field around 15:30 (C1), averaged over 60 min. *The white contours are from the X-ray image at 15:24. X-ray contour levels set to 10 and* 15 DN s^{-1}.

and integrate the disappearing flux (Fig.4.29). In Fig.4.30 (top), the local maximum of the magnetic flux is at 16:19 with ~5.2×10^{16} Mx. It has decreased by ~20% at 16:27 at the beginning of the X-ray transient. The X-ray emission is maximum at 16:33 (195 DN s^{-1}). The threshold in the region-growing algorithm was set to 8 G. We note, however, a secondary, conspicuous maximum of the positive flux, at 16:31, whereas the extracted area of the magnetic feature was still decreasing.

Transient D2 Like in region A, most of the X-ray emission in region D comes from barely resolved X-ray loops in the center of the two first snapshots of Fig.4.28. However the transient D2 is located near the footpoints of these loops. The transient D2 is actually visible in the third snapshot of Fig.4.28. The magnetic elements (positive flux) tracked around the time of the flux disappearance are shown in Fig.4.29 (red crosses). Fig.4.30 shows that the flux is maximum at 16:25 with ~3.4×10^{16} Mx. It has decreased by ~25% at 16:31, when the X-ray transient begins. The X-ray emission is maximum at 16:36 (265 DN s^{-1}). The threshold is set right above the noise level, ~5 G, as the disappearing magnetic feature was well isolated from the rest of the magnetic features. Like with transient D2, exactly at the same time, we note a secondary maximum of the positive flux, at 16:31.

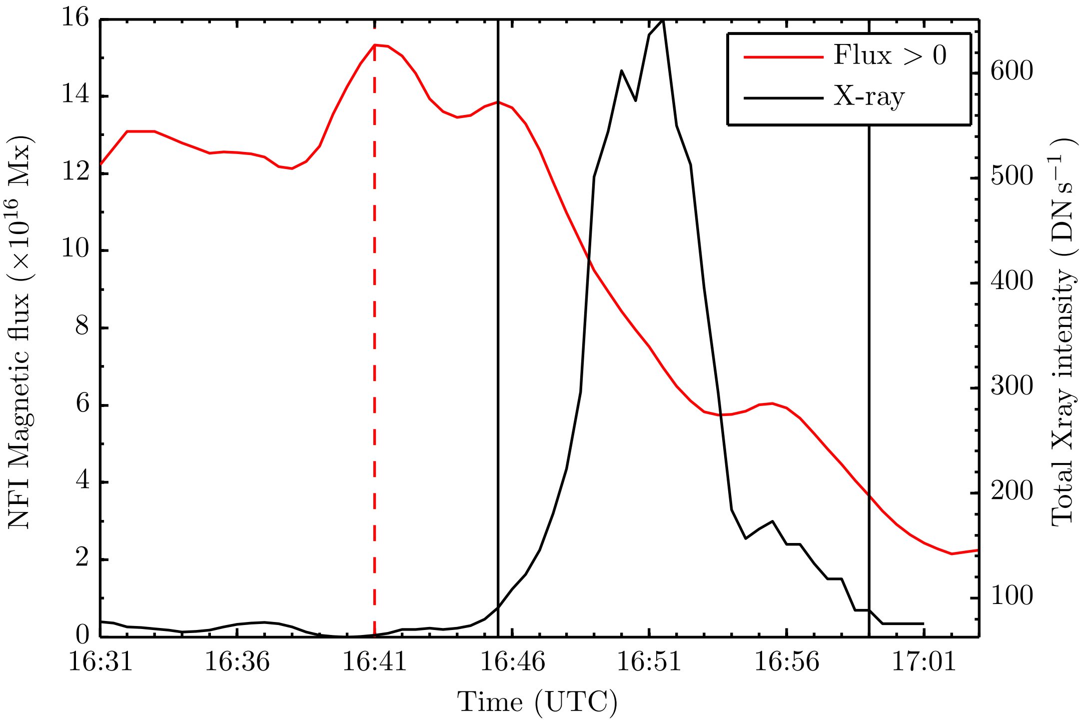

Figure 4.24: *X-ray light curves with associated evolution of canceling magnetic flux for the transient C2a.*

The simultaneous appearance of a secondary maximum of the magnetic flux in transient D1 and D2 at 16:31 comes from oscillations in the whole FOV, and are not specific to these magnetic features. Indeed, in both cases, the 8 G and 5 G thresholds are close to the noise level of these magnetograms (~4 G), and the background intensity in the magnetograms in the whole FOV oscillates with an amplitude of a few G. So the oscillations are more visible here because the flux density of the tracked features is weaker, on average, and integrated over smaller areas than in the previous cases.

This transient (D2) is observed right at the intersection of supergranular lanes according to Figs.4.16 and 4.31. The streamlines seem to twist as they converge. This vortical structure is caused by the unbalanced velocity from either side of the supergranular boundaries. The velocity is on average greater than 550 m s^{-1} within 5 Mm from the supergranular lanes of the lower left supergranule, while it is considerably slower, less than 450 m s^{-1}) in the other supergranules.

Although here we have described the five X-ray transients in the presence of "disappearing" magnetic flux, their occurrence within flux of opposite polarity make us believe it is in fact magnetic cancellation resulting from magnetic reconnection.

4.4.4 Energy of the X-ray transients

Quiet Sun soft X-ray sources in the magnetic network have already been reported in Krucker et al. (1997), and called "network flares". Because of their observational sim-

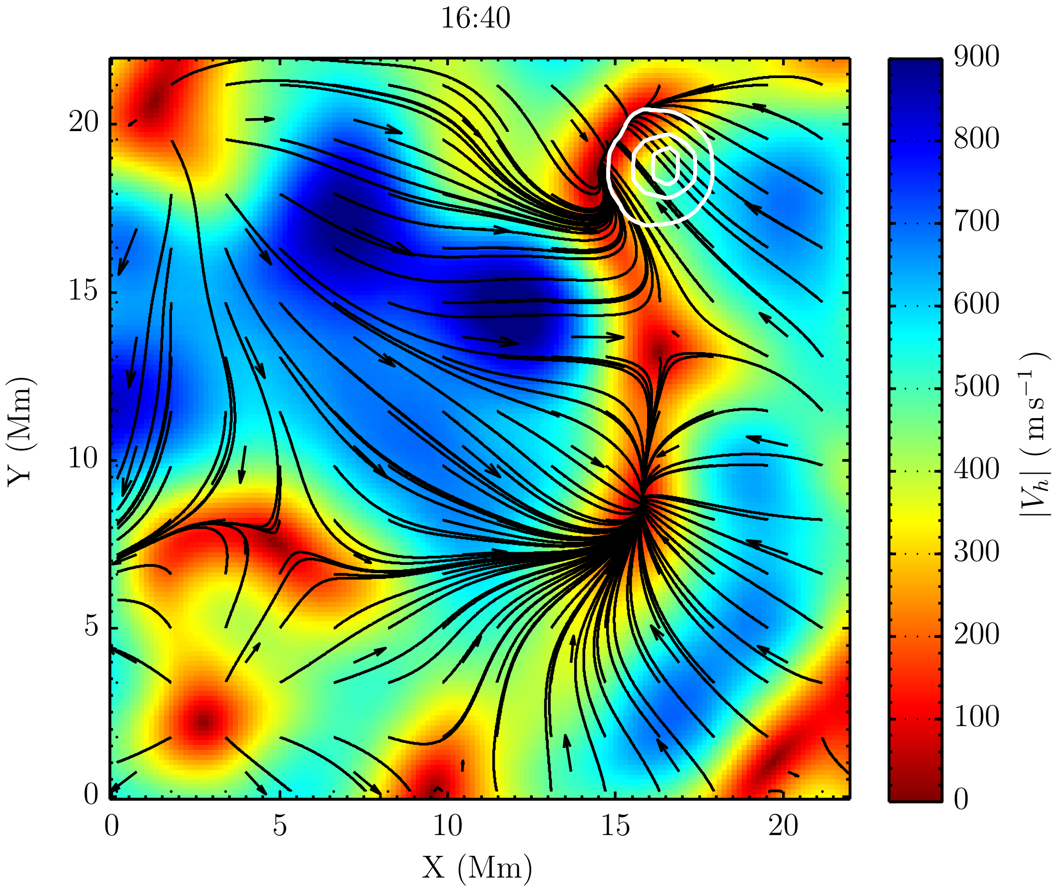

Figure 4.25: *Flow field around 16:50 (C2a), averaged over* 40 min. *The white contours are from the X-ray image at 16:50. Levels set between 15 and* 40 DN s^{-1}.

ilarities (time and spatial scales), we followed the same method to calculate the energy released by these X-ray sources. We assume a temperature $T = 1.2\,\mathrm{MK}$ and we integrate a synthetic coronal spectrum using the CHIANTI package (Dere et al. 1997, 2009), with the XRT response functions corresponding to the C-poly filter, provided by the XRT software in Solarsoft. The emission measure is calculated using the relation

$$I_{obs}^{C_{poly}}(T) \sim EM(T) \int_{\nu(C_{poly})} J_\nu(\nu, T)\ \epsilon(\nu) d\nu \qquad (4.3)$$

where $I_{obs}^{C_{poly}}(T)$ is the observed intensity at a given temperature T, $EM(T)$ is the emission measure, J_ν the synthetic spectrum from CHIANTI, calculated with the procedure "isothermal.pro", and ϵ the spectral response of XRT associated with the C-poly filter. The integral on the right hand side of equation 4.3 is the "temperature response", and is shown in Fig.4.32.

$EM(T)$ is defined along the line-of-sight, and is proportional to the squared density of the electrons $n_e{}^2$ times the depth $\mathrm{d_z}$.

$$EM(T) \approx n_e{}^2 \mathrm{d_z} \quad (\mathrm{cm}^{-5}) \qquad (4.4)$$

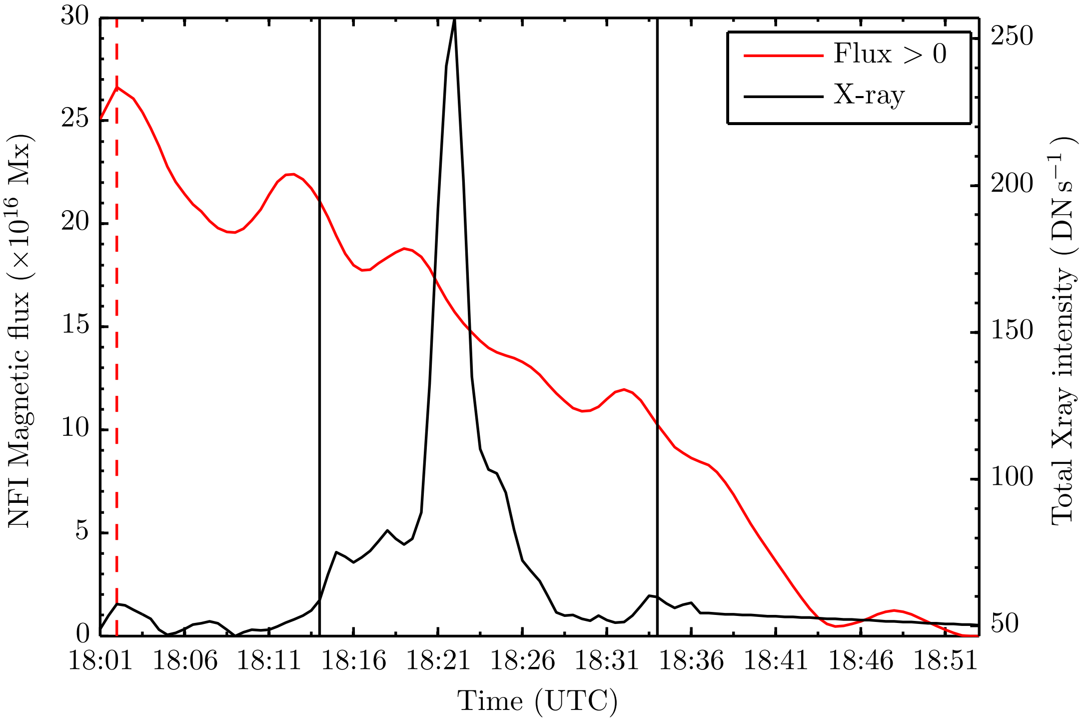

Figure 4.26: *X-ray light curves with associated evolution of canceling magnetic flux for the transient C2b.*

The electron density is therefore $n_e = \sqrt{EM(T)/d_z}$ (cm^{-3}). If we assume that particles have been heated from chromospheric temperatures to provide the X-ray emission, and are filling a cubic volume of side length $d_z = d$, then the total number of particles in the volume would be:

$$N = n_e d^3 = \sqrt{EM(T)d^5} \tag{4.5}$$

Hence the thermal energy of an X-ray emitting source at temperature T on the solar surface, as used for the network flares in Krucker et al. (1997),

$$E_{th} = \frac{3}{2}NkT \approx \frac{3}{2}kT\sqrt{EM(T)\,d^5} \tag{4.6}$$

We only have observations through one filter. So it is not possible to obtain the temperature using filter ratio, and we chose the temperature (1.2 MK) by pure analogy. However, the energy defined in 4.6 has a very weak dependence on the temperature between 1 MK and 10 MK. This is shown in Fig.4.33 where we used $I_{obs}^{C_{poly}}(T) = 1$ DN to compute the energy dependence versus the temperature. For this, we used a source size of $d = 0.15$ Mm (the pixel size of XRT).

Over a large temperature range of 1 to 10 MK, the energy varies by 50%. It seems very unlikely that the temperature(s) of the source exceeds this temperature range. The uncertainty in the thermal energy depends much more on the shape and the size of the source, by a factor of $d^{2.5}$ according to equation 4.6, rather than on the choice of the temperature, provided it stays in the range 1-10 MK. While the horizontal extension of

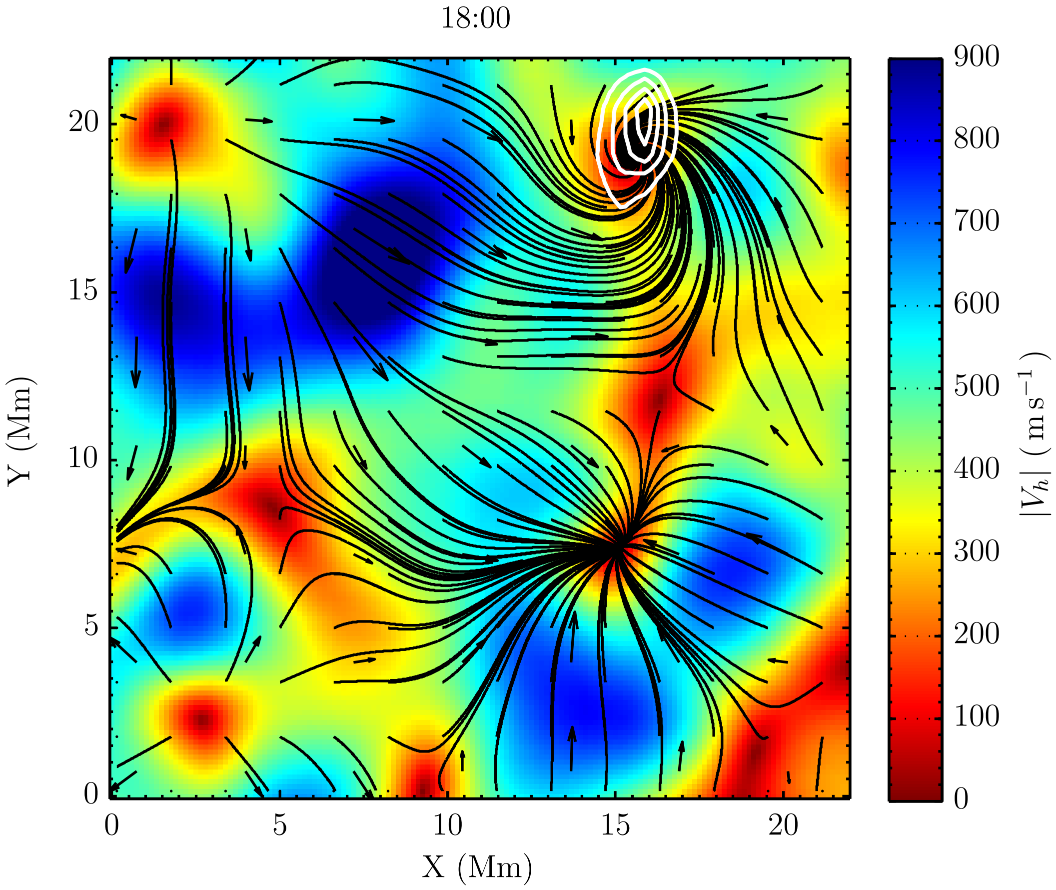

Figure 4.27: Flow field around 18:00 (C2b), averaged over 40 min. *The white contours are from the X-ray image at 18:22. Levels set between 10 and* 25 DN s^{-1}.

the source of several pixels, is a known parameter, its dimension in the line-of-sight (d_z) is unknown. From this we expect an uncertainty of at least one order of magnitude on the energy calculated thereafter.

To compute the energy from the XRT images, the intensity at each pixel is inserted in equation 4.3 to obtain the emission measure $EM(T)$. The emission measure is spatially integrated over a square with side length d. The latter is measured as the averaged Full-Width-at-Half-Maximum of the 2D emitting structure at its maximum emission. The background emission measure is retrieved by averaging $EM(T)$ over the time preceding the flaring phase of the transients. We remind that the flaring phase was previously defined as when the X-ray intensity is 15% above the background. $EM(T)$ is then integrated over the time of the flaring phase, and the background is subtracted. We finally obtain a net increase in emission measure $\Delta EM(T)$ which represents the amount of materials heated to the temperature T, which is inserted in equation 4.6. This process was repeated for each transient, in the MDI FOV and SOT FOV.

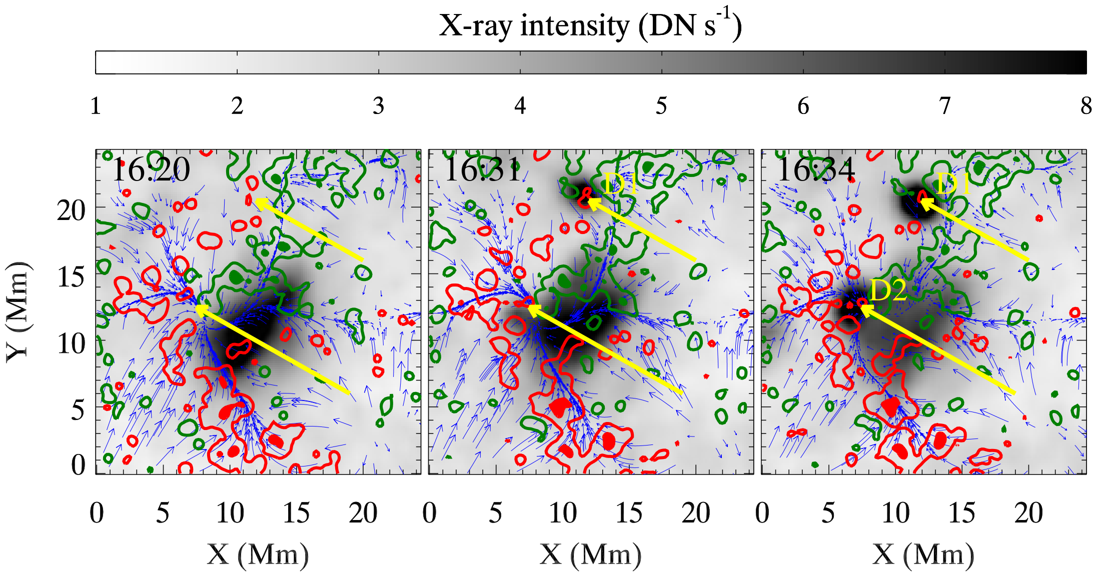

Figure 4.28: *Snapshots of the X-ray time-series in region D. The yellow arrows point at the location of the X-ray transients. Transient D1 is pointed by the top arrow and transient D2 by the bottom arrow.*

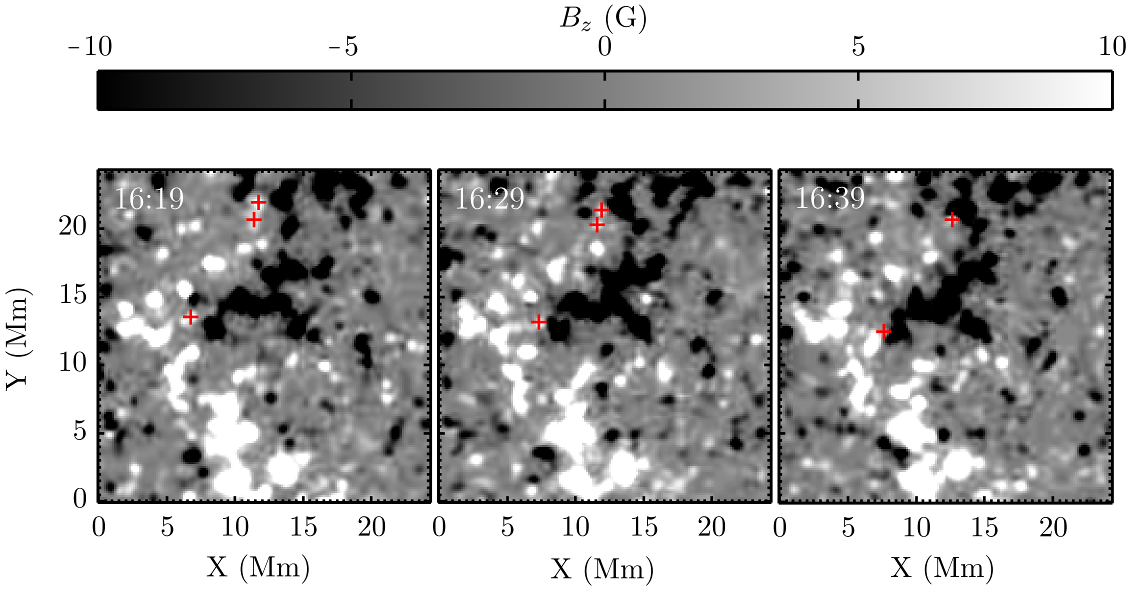

Figure 4.29: *NFI magnetograms as used in the Magnetic Balltracking to track the flux underneath the transient D1 and D2. The red crosses show which magnetic elements were tracked.*

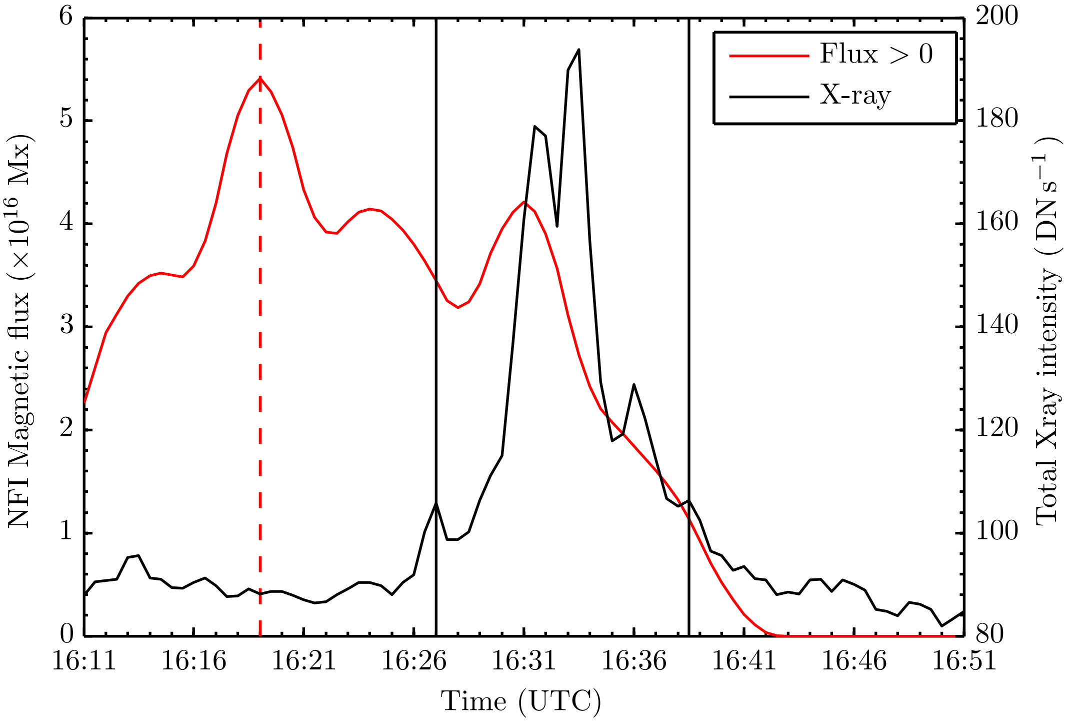

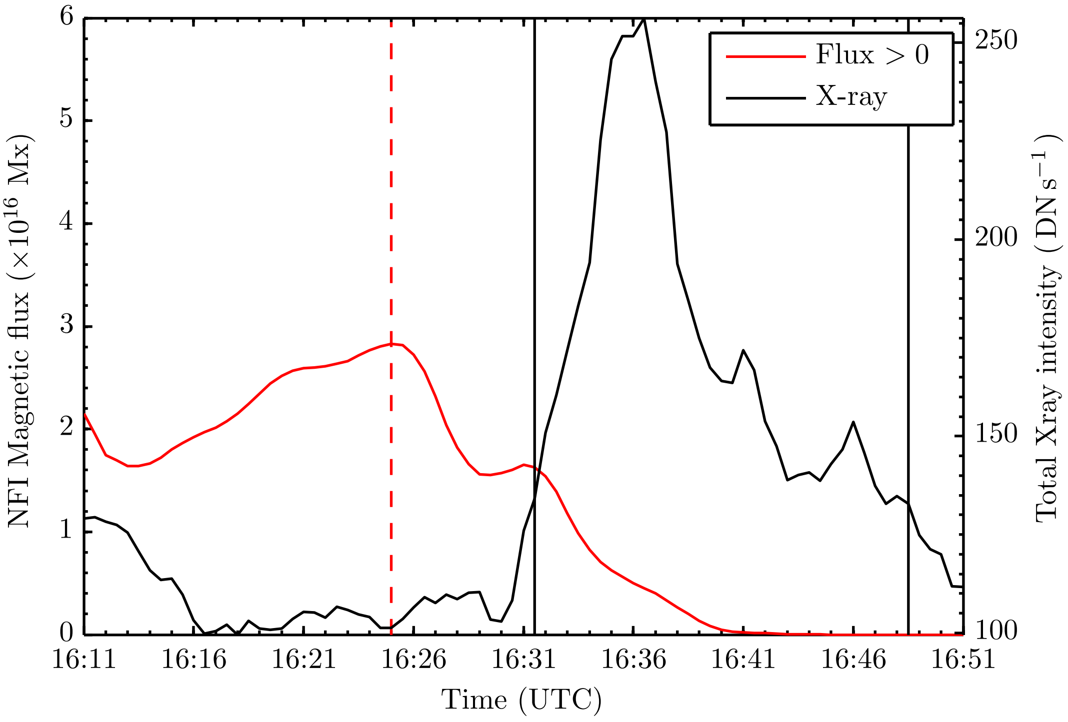

Figure 4.30: *X-ray light curves for the transients in region D, with the associated underlying flux cancellation.*

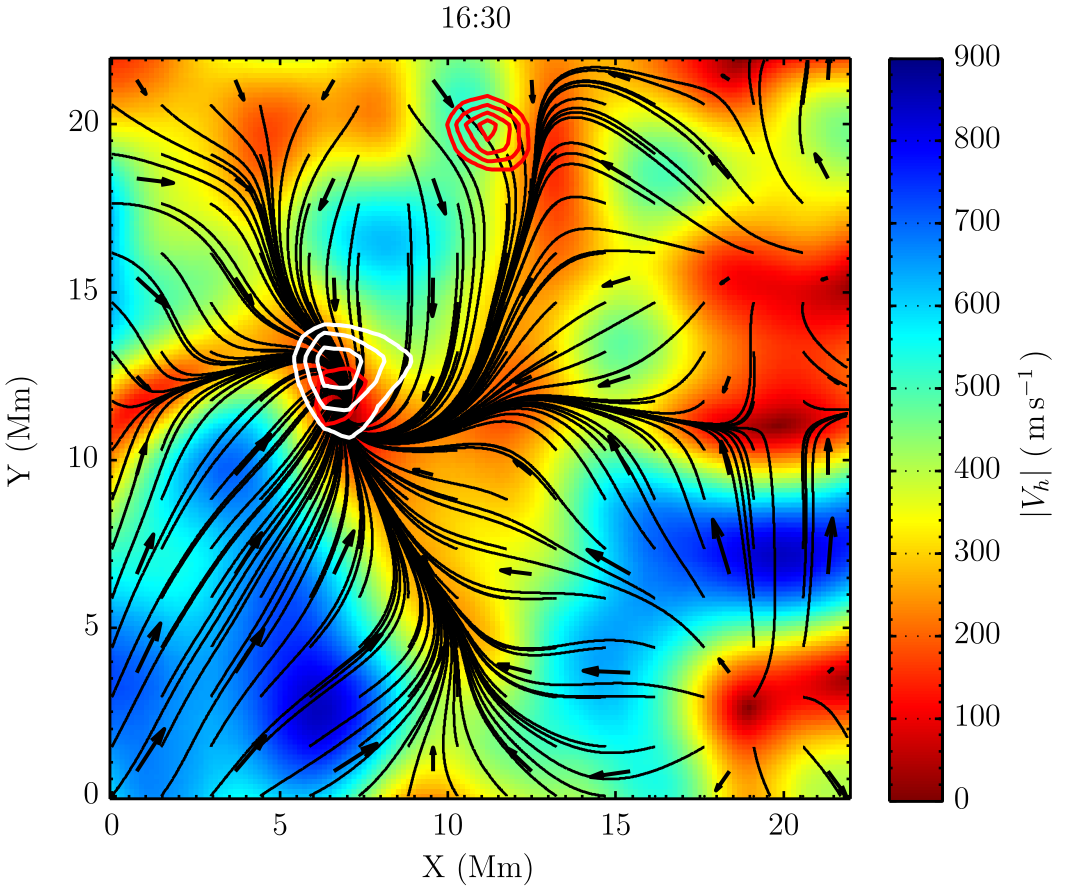

Figure 4.31: *Flow field in region D around 16:30, averaged over* 40 min. *The red contours are from the X-ray image (Fig.4.28) at 16:31, white contours at 16:34. Contour levels are set between* 10 *and* 20 DN s^{-1}.

Results

The results are summarized in tables 4.2 and 4.3, and discussed below. Other parameters relevant to understanding the energetics will be defined and discussed in the next chapter.

The energies of the network flares in the NFI FOV are on average smaller (10^{25} erg, Table 4.3) by one order of magnitude than the ones in the MDI FOV (10^{26} erg, Table 4.2). In each case there is an uncertainty of one order of magnitude due to the longitudinal source size d_z (in the direction of the line-of-sight) that is unknown. The smaller energy in the NFI FOV is mainly due to the smaller dimensions of the sources (at least, on the horizontal dimensions). This difference from one instrument to the other is explained by the fact that Hinode is given a specific "target-region" when planning the observations. In the present case, we asked for "quiet Sun". Therefore, the Hinode science plan induced a selection effect as the pointing was on a region with smaller, less energetic sources than MDI. The latter has a wider FOV and includes relatively more energetic events. With these results, we can calculate the contribution of these network flares to the coronal heating.

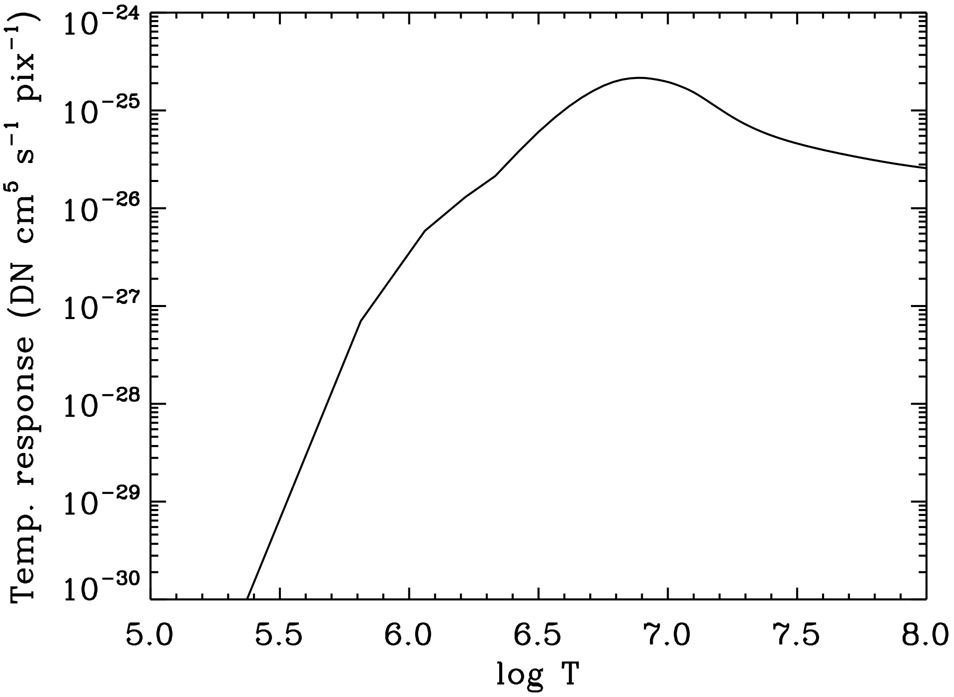

Figure 4.32: *Temperature response of XRT with the C-poly filter.*

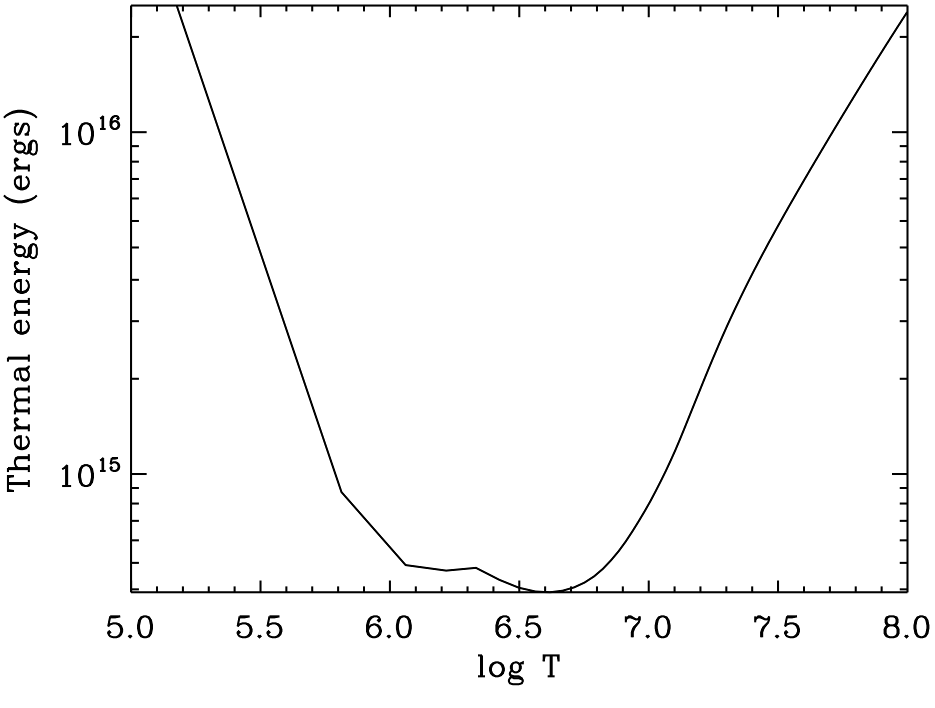

Figure 4.33: *Thermal energy as a function of the temperature for* $I_{obs}^{C_{poly}}(T) = 1\,\mathrm{DN}$ *and* $d = 0.15\,\mathrm{Mm}$.

Transient	E1	E2	E3	E4	E5	E6
$E_{th}(10^{25}$ ergs)	20.4	38.3	23.7	6.7	16.3	30.3
d (Mm)	1.1	1.3	1.7	1.0	1.1	1.2

Table 4.2: *Thermal energy released from sources E1 till E6 assuming a temperature* $T = 1.2\,\mathrm{MK}$.

Transients	E_{th} (10^{25} erg)	d (Mm)	$\Delta\phi_p/\phi_p$ (%)	t_{reac} (min)	Δt_{tr} (min)
C1	1.3	0.4	30	3	29
C2a	1.8	0.4	10	4.5	14
C2b	1.2	0.4	20	12	20
D1	1.9	0.5	35	8	12
D2	2.6	0.7	40	6.5	17

Table 4.3: *Parameters associated with the X-ray transients.* E_{th}*: thermal energy released from the transients in region C and D. d: source size.* $\Delta\phi_p/phi_p$*: percentage of positive flux cancellation.* t_{reac}*: reaction time, i.e, time between the beginning of the X-ray transient and the beginning of the magnetic cancellation.* Δt_{tr}*: transient lifetime. A temperature* $T = 1.2\,\mathrm{MK}$ *is assumed when computing the energy.*

Coronal heating

Here we calculate the average energy flux released by the transients in the NFI FOV, the least energetic, and the energy flux released in the MDI FOV, whose X-ray sources are more intense by about one order of magnitude.

- The NFI FOV covers an area of $6{\times}10^3\,\mathrm{Mm}^2$ of the quiet Sun, during 4 hr of observations. The total energy flux averaged over this area and this time duration, released by the 5 transients C1,C2a, C2b, D1, and D2 is of the order of $10\,\mathrm{erg\,s^{-1}\,cm^{-2}}$.
- The MDI FOV (minus the area covered by the NFI FOV) covers an area of $3.5\,10^4\,\mathrm{Mm}^2$. Which gives an averaged energy flux released by the 6 transients E1 to E6 of the order of $10^2\,\mathrm{erg\,s^{-1}\,cm^{-2}}$.

Note that we only selected transient events whose emission suddenly increases by 15% above the background emission within minutes. They do not represent all the possible sources of X-ray emission. Nevertheless, based on the 11 transients studied here, we have estimated that the average energy flux is between 10 and $10^2\,\mathrm{erg\,s^{-1}\,cm^{-2}}$ in the quiet Sun. This is 10^2 to 10^3 times less than the minimum coronal heating requirement of the quiet Sun (between 10^4 and $10^5\,\mathrm{erg\,s^{-1}\,cm^{-2}}$) (Withbroe and Noyes 1977, Aschwanden 2004).

5 Discussion

In the previous chapter, we have described the relationship between 11 X-ray network flares, and the photospheric flows underneath. With SOT/NFI, we could also quantify the cancellation of the magnetic flux which was followed by the flaring of the X-ray transients. For the 6 other transients, the lower resolution and lower signal-to-noise ratio of the MDI magnetograms only showed bipolar magnetic fields at the flaring sites. Yet we could still define similar patterns in the flows that seem to drive the magnetic flux in an inevitable cancellation. These patterns are sketched in the cartoon of Fig.5.1 that summarizes in a single simplified picture the processes observed for the 11 X-ray transients. Flux cancellation is also observed at more occasions than we observe X-ray transients. However, we have selected here the strongest X-ray transients observed in the MDI and Hinode FOV. They were all related to magnetic cancellation. Flux cancellation not associated with X-ray transient can be explained by submergence, and during which reconnection may not occur, or by reconnection in the photosphere.

In Fig.5.1, we represent the flaring sites at the places where the streamlines of the flow converge. These are the intersection of the supergranular boundaries. As they converge from either side of the network lanes, the streamlines form a funnel. Eventually, the supergranular flow becomes unbalanced, and the velocity in one side of a supergranular lane is greater than in its neighboring supergranule. Consequently, antagonistic flows become asymmetrical with respect to ideal boundaries. The streamlines are reshaped accordingly, and the direction of the resulting flow is determined by the average flow, with streamlines of the "dominant" supergranules pushing back the "weaker" ones. As long as the weaker flow does not accelerate, the directions are kept, and structures like large-scale vortex flows persist. Otherwise, they get disrupted and are barely visible in long-time-average flow fields. When the flow is more balanced, streamlines converge symmetrically to the intersection, forming funnels leading into the intersection.

In the next section, we discuss the possible effects of the observed topology of the flow on the dynamics of the magnetic flux.

5.1 Converging flux model

The mechanism by which the flux decreases is likely to be magnetic reconnection, in a manner that falls within the converging flux model described in Priest et al. (1994). While this model describes the triggering mechanism of X-ray bright points (BPs) at larger scales than the present events, our observations are *a priori* similar: two magnetic fragments of opposite polarities approach each other, cancel out, while an intense X-ray emission is

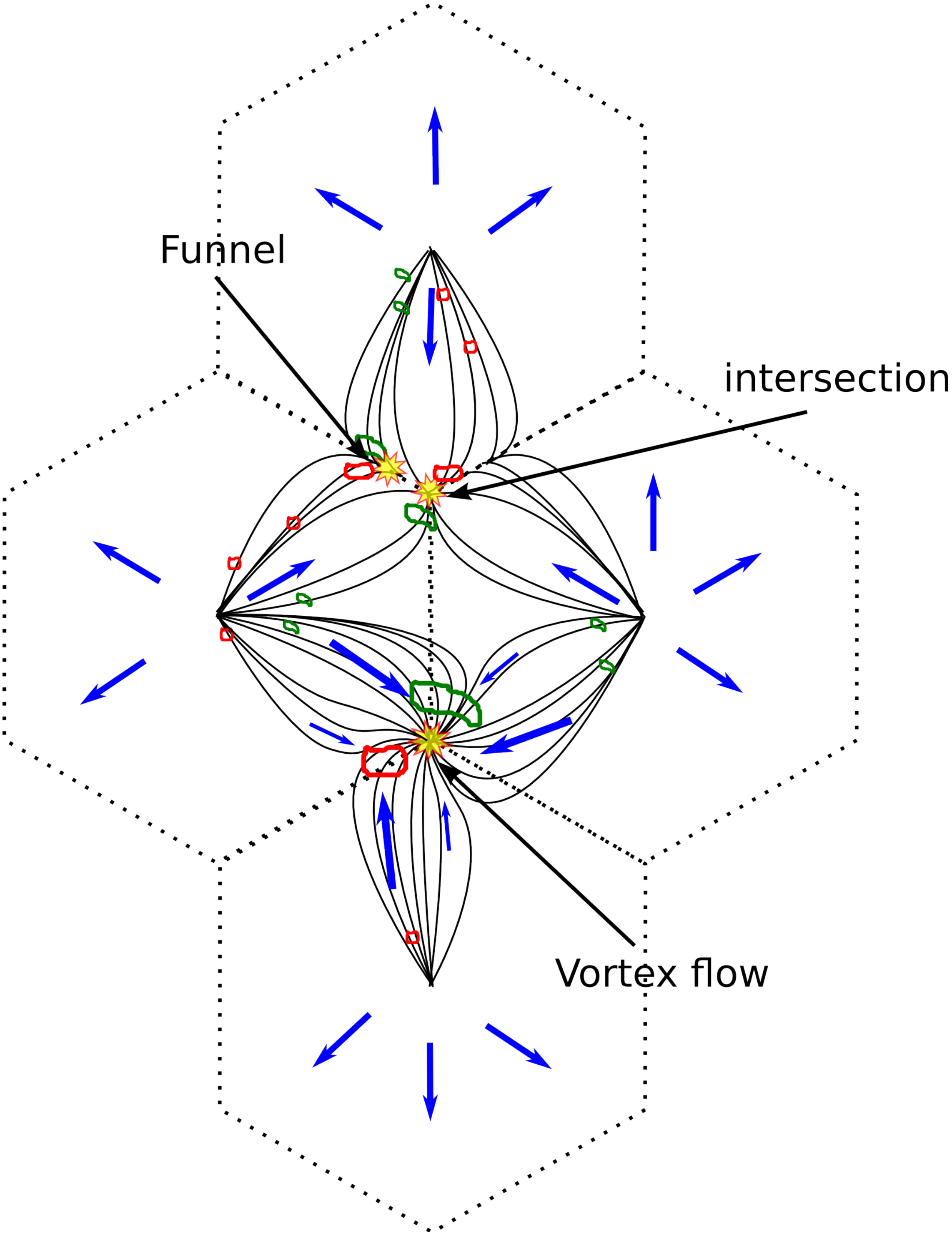

Figure 5.1: Sketch of the different steps leading to an X-ray transient. The hexagonal dashed lines represent idealized supergranular boundaries. The black lines are streamlines of the flow. The blue arrows show the main orientation of the flow. Bigger arrows symbolize faster flows than the smaller arrows. The yellow stars represent X-ray transient events. The green and red thick contours represent magnetic features of opposite polarity.

observed. The model explains the energy release as a result of the interaction of the magnetic fragments with the background field, which eventually leads to the formation of a current sheet and magnetic reconnection in the higher layers. It is followed by photospheric reconnection, resulting in the decrease of the magnetic flux of both fragments. In what follows, we use the Magnetic Balltracking to measure the parameters defined in this model, and to calculate the estimated energy released during the reconnection. We compare it with the energy E_{th} released during the eruption of X-ray network flares (Table.4.3).

5.1.1 Definition of the model parameters

For each event in the NFI FOV, the key parameters of the model are calculated with Magnetic Balltracking. They are:

- The approach speed $-\dot{a}$ of the fragment where $2\,a$ is the distance between the center of two fragments of opposite polarities. Calculating this quantity requires the tracking of the two fragments. As mentioned in the previous chapter, for each of the transients in the NFI FOV, only the positive flux was coherent enough to be extracted by region growing. Although the closest negative patches are wider and clustered out into several pieces, we can still track their positions using a few balls. Their averaged position is more precise and much steadier than the position of a single fragment, and we use this averaged position to derive the relative approach speed $\dot{a}$ of the fragment of positive flux with respect to the fragments of negative flux.

- The interaction distance d^*, defined as the distance at which the reconnection in the higher layers would first occur, and projected onto the photosphere. It can be expressed as:

$$d^* = \sqrt{\frac{f}{\pi B_0}} \tag{5.1}$$

  where f is the flux of the fragment, and B_0 is the intensity of the horizontal background field. In the model, the parameters are defined assuming symmetry, i.e, with the unsigned flux of both fragment being strictly equal. This is not true in our observations and causes an error of more than one order of magnitude. Instead, we can directly use the results of Magnetic Balltracking to measure d^*. We use the geometric definition of d^*, which is the distance between the center of the two canceling fragments and the point (projected onto the photosphere) where the fragment of positive flux starts interacting with the fragment of negative flux. In our data, this is taken as the point (in time and space) when the flux is at its maximum, which is a few minutes before the X-ray transient starts.

- The magnetic fragment width w which is measured with the region-growing algorithm, by taking the average diameter of the extracted area of the fragment.

- The cancellation time τ_c which is the time it takes for the flux of the fragments to completely cancel. It is defined as:

$$\tau_c = \frac{w}{\dot{a}} \tag{5.2}$$

Transients	W_{free} (erg)	$E_{\mathrm{F_p}}$ (erg)	d^* (Mm)	$\dot{a}$ (m.s^{-1})	w (Mm)	τ_c(min)
C1	$3\,10^{23}$	$1\,10^{24}$	0.9	600	1.5	32
C2a	$3\,10^{23}$	$1\,10^{24}$	1.2	800	1.6	24
C2b	$8\,10^{21}$	$1\,10^{25}$	1.4	500	1.6	51
D1	$6\,10^{22}$	$3\,10^{23}$	1.1	500	1.6	57
D2	$9\,10^{20}$	$1\,10^{23}$	0.7	500	0.9	28

Table 5.1: *Parameters related to the converging flux model in Priest et al. (1994).* W_{free} *is the "free" magnetic energy in excess of a potential field configuration.* $d*$ *is the interaction distance,* $\dot{a}$ *is the absolute value of the approach speed,* w *is the average fragment width.* τ_c *is the cancellation time.* $E_{\mathrm{F_p}}$ *is the energy released within sheared flows.*

With the above quantities, the free energy stored in the current sheet W_{free} in excess of a potential field is defined as:

$$W_{\mathrm{free}} = \frac{B_0^2 d^{*3}}{2\mu} F_s(a/d^*) \tag{5.3}$$

where μ is the permeability, $F_s(a/d^*)$ is a scaling factor (determined numerically) that depends on the ratio of a and d^* (Priest et al. 1994, Eq.3.28). The scaling factor varies rapidly with a/d^*. It is equal, respectively, to 0.6, 2.5, and 4.4 when $a/d^* = 0.5$, 0.2, and 0.1 (a/d^* decreases when the fragments approach each other). We use the value of a/d^* at the start time of the reconnection, which is here assumed to be at the beginning of the X-ray network flares. In what follows, a horizontal background field B_0 of 5 G is used. This value is consistent with what we get from potential field extrapolation right above the photosphere in the regions of interest.

5.1.2 Results

The values of the above quantities are summarized in table 5.1. The interaction distance d^* varies from 0.7 Mm to 1.4 Mm. Figs.5.2 and 5.3 represent the positive magnetic flux cancellation (red continuous line) calculated in the previous chapter, along with the distance ratio a/d^* (black discontinuous line) which is used in $F_s(a/d^*)$ to scale the free energy W_{free}. The red discontinuous vertical line shows where the flux cancellation starts, which by definition corresponds to $a/d^* = 1$. The black vertical line marks the beginning of the X-ray transient and sets where we take the value of a/d^* to compute the scaling factor F_s. a/d^* equals (resp.) about 0.6, 0.7, 1.0, 0.8, 1.0 at the start of the transient C1, C2a C2b, D1, and D2 (resp.). It scales W_{free} by $F_s = 4\,10^{-1}, 2\,10^{-1}, 3\,10^{-3}, 5\,10^{-2}, 2\,10^{-3}$ (resp.). Finally we obtain W_{free} of the order (resp.) $10^{23}, 10^{23}, 10^{21}, 10^{22}, 10^{20}$ erg. So the free energy in the transient C2b, D1, and D2 is significantly scaled down. This is due to the fact that the X-ray transient starts too soon after the fragment has moved past the interaction distance (i.e, a/d^* is close to one).

We note however that, apart from C1, the vertical flux of the fragment beneath the transient is unbalanced, with a ratio of negative flux over positive flux equal to 10, and up to 80 in D2. So this is far from the symmetric topology assumed in the model (which assumes a symmetry with respect to the vertical axis). Assuming a symmetric geometry, the reconnection occurs with the horizontal field, which is here quite low (5 G), which results in quite small free energy compared to the thermal energy E_{th}.

5.1.3 Comparisons of E_{th} and W_{free}

The thermal energy E_{th} measured from the X-ray emission and the free magnetic energy W_{free} calculated with the flux convergence model are compared in the bar plot in Fig.5.4. The third energy $\langle F_p \rangle$ will be discussed in the next section. As we mentioned in the previous paragraph, the main source of errors in the calculation of the free energy lies in the actual field topology (unbalance between the positive flux and negative flux) which might be quite different from the ideal case (symmetrical), which affects the estimation of W_{free} as a function of B_0^2. We also recall that there is an uncertainty of one order of magnitude when calculating E_{th} (due to the source height). Nonetheless, on average, the thermal energies are all greater than the free energy. This is particularly clear with C2b, D1, and D2 where the free energy is negligible compared to the thermal energy. Therefore, even if within 1 order of magnitude, the piecewise potential field configuration invoked in the converging flux model provides sufficient energy for a later release during the transients C1 and C2a, it is very unlikely to do so in C2b, D1, and D2. Therefore one must investigate other possible sources of energy.

5.2 Effect of the funnels and the vortices

5.2.1 Shearing motions

Galsgaard and Nordlund (1996) have studied the effect of the shearing of an initial homogenous magnetic field. It was shown that the longer systematic shearing acts on the field, the greater the free energy. This is caused by the exponential growth of currents caused by the field lines bending and converging to a more confined area.

In our observations, we have emphasized the presence of supergranular vortices and twisted funnels. In fact, these are the sites of higher shear than in the relatively more laminar flow of the internetwork. In such configurations, we can consider the time and spatial scales of the funnels and the vortices observed at the erupting sites in region C and D, and apply them to the model of average energy dissipation per unit area and per unit time in Galsgaard and Nordlund (1996), roughly equal to the average Poynting flux $\langle F_p \rangle$ so that, in centimetre-gram-second (cgs) units:

$$\langle F_p \rangle = \frac{B_z^2 \, V_d \, \tan(\phi)}{4\pi} \tag{5.4}$$

where B_z is the intensity of the vertical magnetic field, V_d is the velocity advecting the field lines, and ϕ is the inclination angle of the field lines. Here, we use $B_z =< B_{z\,\text{NFI}} >$,

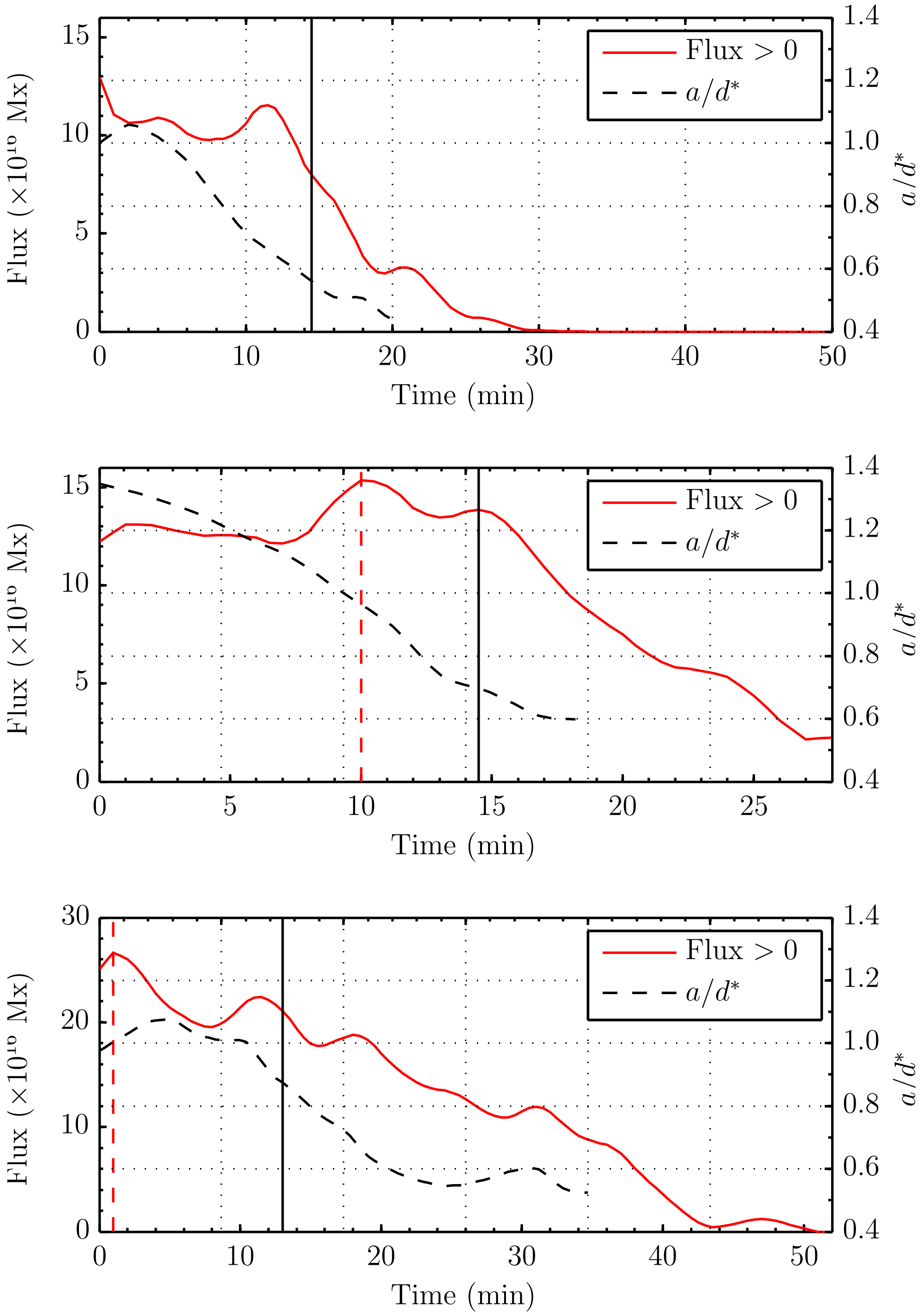

Figure 5.2: *Evolution of the positive flux with a/d^* for the transients in region C. From top to bottom respectively, transient C1, C2a, and C2b. The vertical discontinuous red line is at the maximum of the flux, and $a/d^* = 1$. In C1, that maximum is at* 0 min *so the red line is not plotted. The black vertical line marks the beginning of the X-ray transient.*

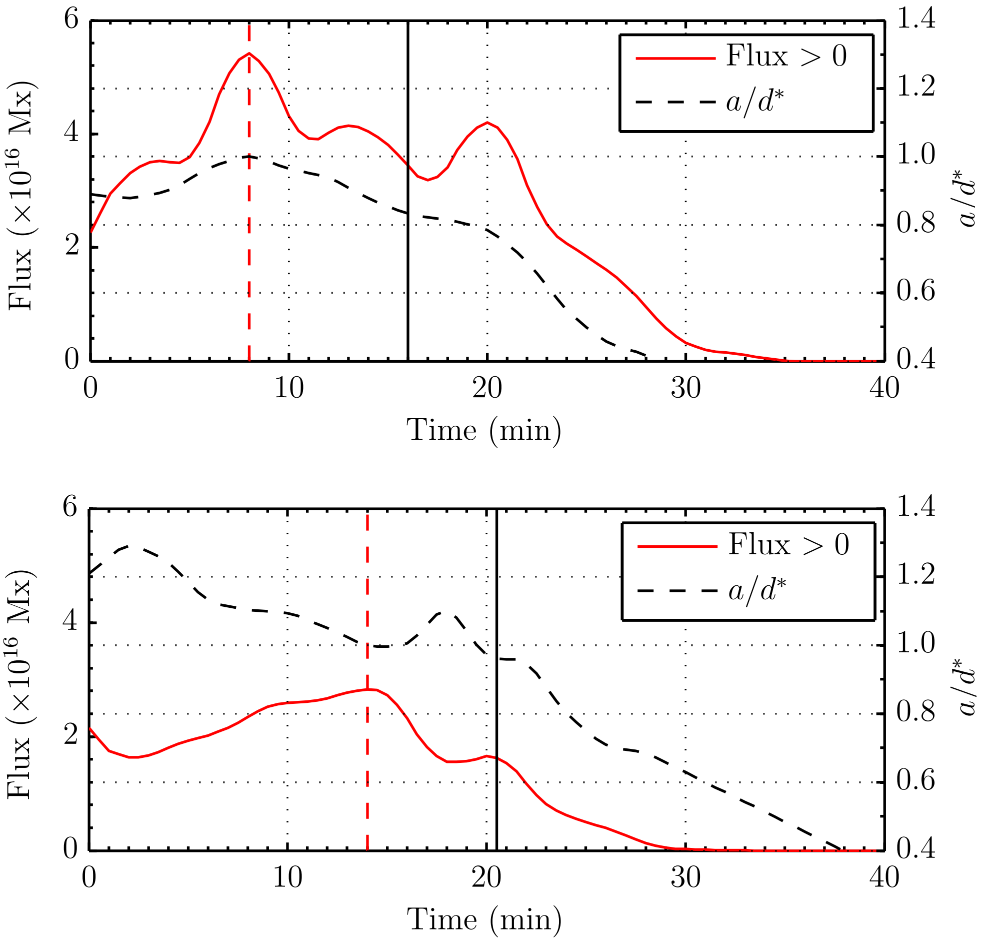

Figure 5.3: *Same as Fig.5.2 for the transients in region D.*

i.e, the mean vertical magnetic field of the fragment with canceling flux. We consider the fragments tracked in region C and D.
tan(ϕ) is approximated by :

$$\tan(\phi) \sim \phi \sim V_d t_d / L \tag{5.5}$$

where t_d is the characteristic time of the shear motions acting on the field lines. L is the characteristic size of the region over which the Pointing flux is integrated. We take $L = 5\,\mathrm{Mm}$, which is the characteristic length of the funnels along which the magnetic fragments are transported.

The above quantities were already calculated in § 5.1.1 (Table 5.1). In fact, we use $t_d = \tau_c$ as a lower limit, where τ_c was defined as the cancellation time, i.e, the time it takes for the flux to vanish. V_d is set to the approach speed $\dot{a}$.

Finally, we integrate the energy flux $\langle F_p \rangle$ over the region of sheared flow (of size L) and over the cancellation time τ_c to get an order of magnitude estimate of the total dissipated energy $E_{\mathrm{F_p}}$ from the magnetic fragments caught in the vortices and the funnels. $E_{\mathrm{F_p}}$ is represented by the third bar plot in Fig.5.4. The energy appears greater than in the converging flux model. However, if we account for the uncertainty in determining the horizontal component of the field in the converging flux model, there is no clear difference

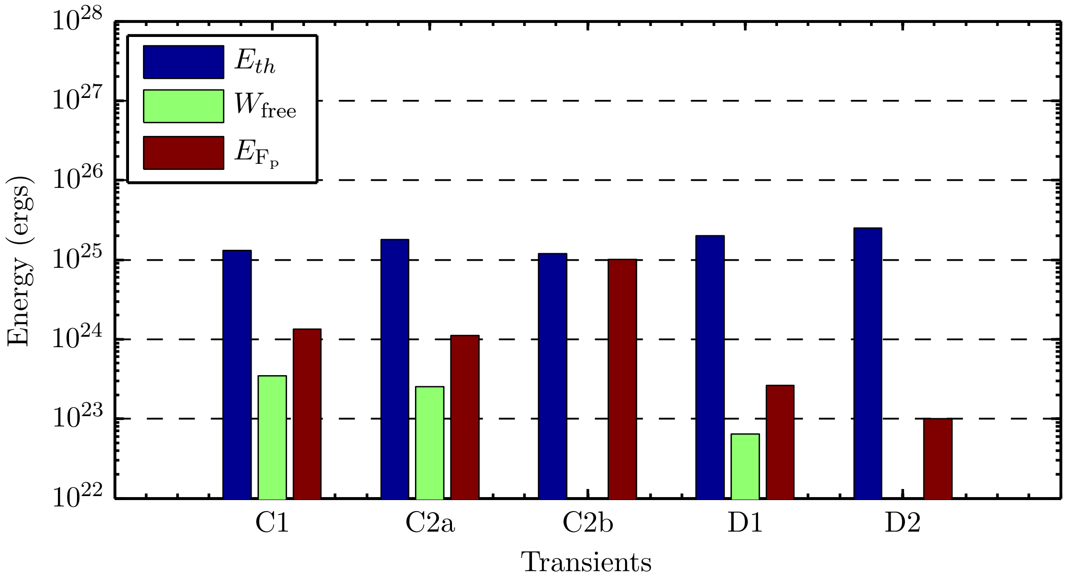

Figure 5.4: *Bar plot of the thermal energy E_{th}, the free energy W_{free} of the converging flux model, and the average Poynting flux $\langle F_p \rangle$ for the transients in region C and D.*

between $W_{\rm free}$ and $E_{\rm F_p}$ in the cases C1 and C2a. Nonetheless, the fact that Eq.5.4 accounts for the actual observed flux (and not the extrapolated horizontal component) leaves much less uncertainty than in the converging flux model, and it becomes clear with C2b, D1, D2 that $E_{\rm F_p}$ is greater than $W_{\rm free}$.

Galsgaard and Nordlund (1996) emphasized that persistent shearing may be the source of a bursty regime of the energy release, and we believe that this indeed is the case for transient C2a and C2b which occur near the center of a vortex flow (see Figs.4.20,4.25,4.27).

5.2.2 Large-scale vortices and funnels

Due to the presence of large-scale vortices and twisted funnels transporting the magnetic flux to the junctions of the lanes, we can also comment on the results of the simulations from Amari et al. (2000, 2003, 2010) with non-zero-helicity magnetic field, that are specific implementations of the more general Flux Cancellation Model from van Ballegooijen and Martens (1989). Although it is applied to coronal mass ejections, the initial states used in the model are in many aspects the same as observed here. In these simulations, the amount of total flux that cancels is within a broad range of 6% to 30%. This broad range is believed to be caused by the different amount of shear given to the magnetic field at the initial state. In the real situation, vortices and funnels are shearing the magnetic field, and a broad range of cancelled magnetic flux could be expected as well. In the 5 X-ray transients that we analyzed (C1, C2a, C2b, D1, D2), the amount of cancelled flux ranges between 10% to 40% (see $\Delta\phi_p/\phi_p$ in Table 4.3). Note that this is only the longitudinal flux, and we do not make any assumption on the amount of cancellation of the transverse component of the flux. In the simulations, the flux cancellation is due to small-scale mixing and reconnection that is followed by the formation of a flux rope, which gets disrupted in the end. While we have no direct observations of the flux rope, the presence of funnels and the vortices at the pre-interactive phase of the converging flux model are conditions quite similar to the simulations, where the same topology of the flows is used.

The energy release is believed to occur through Joule dissipation. The kinetic energy is only indirectly converted into magnetic energy by stressing the magnetic field. Several experiments emulating different driver speeds on interacting fragments were carried out in Galsgaard and Nordlund (1996), Galsgaard et al. (2000), Galsgaard and Parnell (2005) and showed that viscous dissipation was much smaller than Joule dissipation. However, there is one aspect that could make these experiments more realistic, which lies in the dual nature of the photospheric flows. In all the experiments, the magnetic fragment was advected by the flow using an imposed speed. In a real situation, the velocity of the motion of the magnetic fragment is faster than the supergranular flows. Indeed, the approach speed $\dot{a}$ in Table 5.1 can be up to $800\,\mathrm{m\,s^{-1}}$, a typical value for magnetic elements in the quiet Sun (Berger et al. 1998), whereas the mean velocity in supergranular flows and the large-scale vortex flows do not exceed a few hundred of $\mathrm{m\,s^{-1}}$ (Attie et al. 2009).

5.3 Qualitative model of X-ray network flares

To summarize the previous discussions, we use the same base description of the converging flux model, with the evolution of the piecewise potential field, 3D-extrapolated for illustrative purposes. Next, we tune this model by including the effects of funnels and vortices. This aims at qualitatively describing the mechanisms that lead to the 11 X-ray network flares that we observed.

5.3.1 Magnetic field configuration

Following the assumption of piecewise potential evolution in the converging flux model, we use a potential field extrapolation on the NFI magnetograms in region C (Fig.5.5). The footpoints of the field-lines (yellow) were tracked using Magnetic Balltracking (see § 2.6.6). The streamlines of the horizontal flows are shown with blue lines. Here we show three snapshots at three different times (increasing from top to bottom), viewed from two different perspectives (left to right). One sees elongated loops in which smaller loops (a few Mm) are nested. In sites of larger dimensions, like in bright points or active regions, such configurations are known to give rise to so-called "bald patches", where the coronal field becomes tangential to low-lying magnetic loops (Titov et al. 1993, Fletcher et al. 2001).

In the context of the converging flux model, this would eventually result in the reconnection of the small loops with the higher ones (the background field). However, the present extrapolation is not able to show this exact process clearly, but in the third snapshot (16:49), near the X-ray transient C2a seen as red contours, the small green loops in Fig.5.5 are nested within the larger (yellow) overlying loops which could possibly be involved in the reconnection. A very similar configuration is observed around the transient C2b (not shown here). Here (at 16:49), the green loops are rooted in the funnels of the flow, in the same fragments that merge and cancel out under the transient C2a (see

Figs.4.20 and 4.24). Earlier at 15:03 and 15:45, they were connected to different fragments (see the leftmost green loop above the red contours), i.e, before the magnetic flux cancellation.
We remind that we did not select the footpoints at random pixels within the fragment. For tracking the green loops, we have ball-tracked their footpoints, starting at an early phase (15:03). Henceforth, they cluster out and merge again: 3 green loops on 3 fragments at 15:03, 6 green loops on 6 fragments at 15:45, 2 green loops on 2 fragments at 16:49, which results in a smaller patch of loops, heading toward the opposite flux (16:49) that is located northward, at the end of the funnels (see the blue streamlines near the green lines).

The extrapolation also reveals that some large loops have one footpoint in the northern vortex at the northern junction, near the flaring site of transient C2a, and another footpoint in the internetwork, where the flow is more laminar. This configuration can eventually lead to the braiding of these magnetic field lines, and the increase of magnetic stress. We have shown in the previous section that this can be the source of much more energy than in the case of a potential field configuration.

Note also that qualitatively this extrapolation does not change when using linear force free extrapolation. The green lines are still connected to the same fragments. Only the longest lines are affected, and the ones in the vortex flows are still connected to the elongated white magnetic patch (positive polarity) seen in the three snapshots.

5.3.2 Model of X-ray network flares

With the above description, we can finally describe the different steps that lead to the quiet Sun network flares that we have observed in the NFI FOV. Because the other network flares observed in the MDI FOV have the same characteristics (bipolar field underneath, located at the intersection of the supergranular lanes), this description may also apply to transient E1 to E6 (Fig.4.13).

1. **Emergence phase**
   The magnetic flux emerges as small elements, in the internetwork, and appear connected with the other small magnetic patches around, some of them are connected with magnetic patches in the network. This is illustrated in the early phase of transient C2a in Fig.5.5 by the green magnetic field lines at 15:03. Some green lines appear connected to areas with no flux, but this an effect of the scaling of the image. The field there is weak, and barely visible in the snapshots (it is about 10 G).

2. **Pre-interactive phase**
   The magnetic elements follow the funneled streamlines, that are converging toward the vortex. The flux eventually clusters, merges again, and gets squeezed in as the funnels get tighter near the junction. In the presence of vortical flows, magnetic stress is increased and the energy eventually builds up.

3. **Energy release**
   The reconnection of the small core field with the overlying coronal field lines in "bald patches" frees plasma into the higher coronal loops, they are observed in

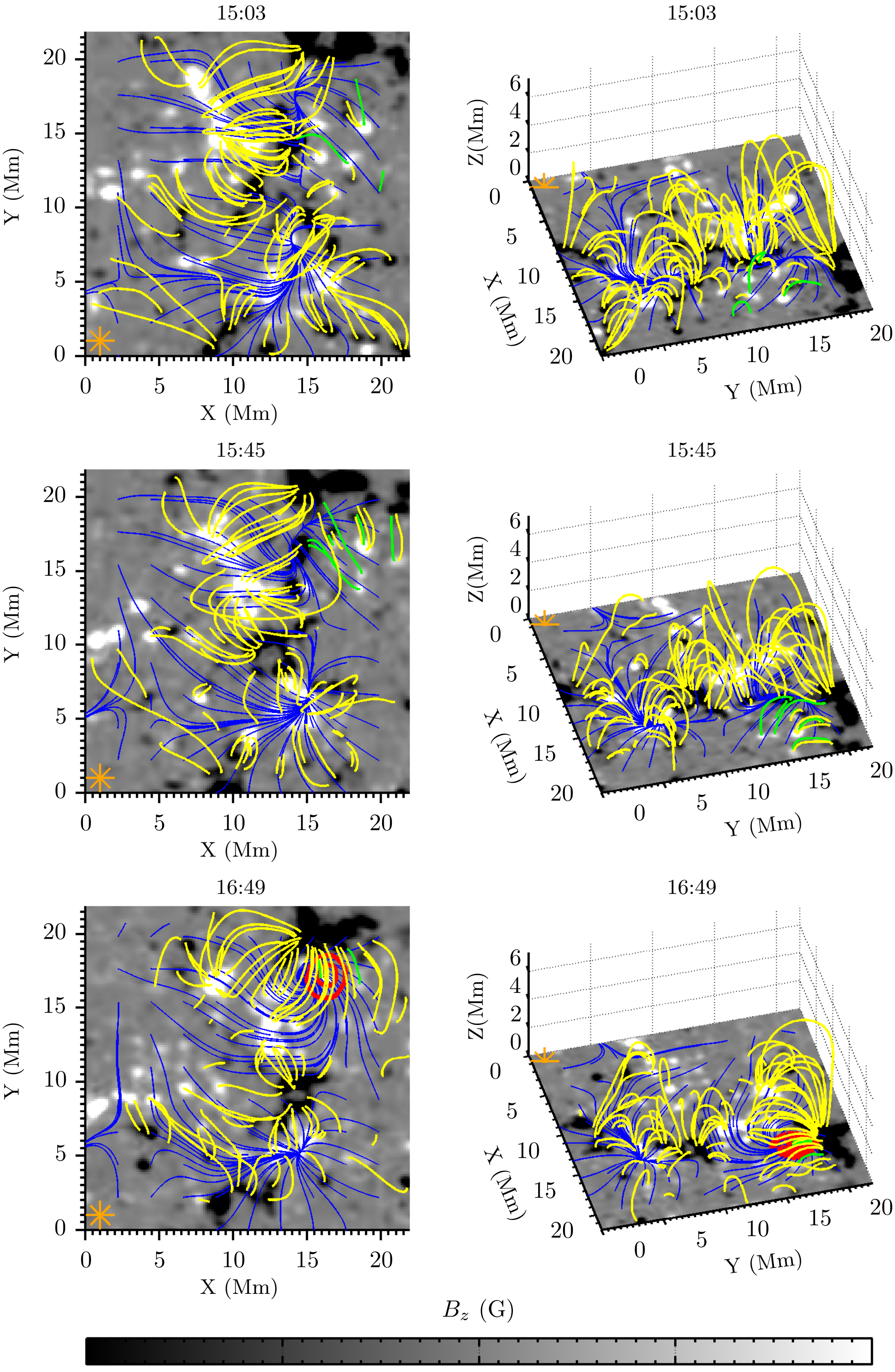

Figure 5.5: *Potential magnetic configuration in region C at three different times (from top to bottom), from 2 different viewing angles (left and right). The orange star in the corner moves rigidly with the axes. The blue lines are the streamlines of the* 1 hr*-averaged flows. The yellow lines are the extrapolated magnetic field lines. The green lines are the magnetic field lines of the fragments involved in the cancellation for the transient C2a, seen as red contours at 16:49.*

X-ray as network flares. From the extrapolations, we cannot be sure of the true topology of the magnetic field; the plasma can be released either to larger coronal loops, or to the interplanetary magnetic field and populate the solar wind.

4. **Flux cancellation**
   As a result of photospheric reconnection enforced by the flows, the flux rapidly decreases. As the interaction distance is very small, the phase of energy release may overlap with the flux cancellation.

From this we can conclude that the quiet Sun network flares require a specific flow pattern sketched in Fig.5.1. Funnels and vortices appear as the elementary flow structures that facilitate the compression of the magnetic elements, causing an increase of the flux density when the magnetic elements have the same polarity. They increase the probability of reconnection and subsequent cancellation when bipolar features are trapped in them. Funnels and vortices may be necessary-but-not-sufficient flow patterns to trigger the network flares. Thus one can anticipate the preferred (if not unique) sites of these localized soft X-ray emission, whatever their actual nature is (micro-, nano-, flares, jets, micro-jets, mini CMEs, etc...). This shall be investigated in future statistical studies.

5.4 Prospects for future studies

5.4.1 Quiet Sun

In Pietarila Graham et al. (2009), the higher resolution magnetograms from Hinode/SOT allowed an unprecedented quantitative, multi-scale study of the magnetic flux in the quiet Sun. More precisely, the self-similar pattern of the magnetic flux is quantified. This self-similar pattern holds for several orders of magnitudes, and includes the small scales in which our study lies, and down to 20 km (below granular scales) using MHD simulations. In addition, we note that one common characteristic between granulation and supergranulation is that they sweep out, mix and disrupt the magnetic field in their respective boundaries. At granular scales, the flow is much faster than the supergranular flow, up to more than $1000\,\mathrm{m\,s^{-1}}$ (Berger et al. 1998) while Brandt et al. (1988) already reported vortical flows in the granulation (see also Bonet et al. 2010). Thus, down-scaling the sketch in Fig.5.1, we can imagine that energy release within the smaller granular lanes also occurs, but at a faster rate and at smaller spatial scales as a result of the same interactions described in the network flares. This shall be investigated through statistical studies using high-resolution instrumentation to resolve the finest structures of the convective flows.
In addition, EUV transient events were reported in Innes et al. (2009) with similar scales (time and size) as the network flares. They are associated with propagating dim clouds, and/or propagating dim shock-waves, which makes them observationally equivalent to CMEs but on the scale of the network flares. The topology of the flows underneath also satisfied the necessary condition that we have assessed here, i.e, presence of vortical flow underneath the eruptions. Combined statistical studies of both EUV transient events and X-ray network flares is a key to better understand the dynamics of the quiet Sun, including their contribution to the coronal heating and to the solar wind. Such a survey is possible

with the combined use of the Atmospheric Imaging Assembly (AIA) and the Helioseismic and Magnetic Imager (HMI) onboard the Solar Dynamic Observatory (SDO).

5.4.2 Active Regions and large scale dynamics

We have explained that X-ray transients can be seen as a by-product of small core-fields reconnecting with the wider coronal loops, and allowing the plasma confined in the lower layers, to populate the higher and hotter layers of the low corona. Without mentioning any geometrical or energetic scales, these observations are in many aspects identical to the triggering mechanism observed in Active Regions (ARs) at much larger scales. The relationship between flares and CMEs, with the longitudinal magnetic flux was investigated by Machado et al. (1988), and later on by Moore et al. (1999), while the so-called Flux Cancelation Model (van Ballegooijen and Martens 1989) was the first model introduced to describe this relationship. In Machado et al. (1988), the disruption of small core-fields are believed to be caused by magnetic reconnection with more distant coronal field. These small core-fields are several orders of magnitude higher than the ones involved in the quiet Sun network flares, yet the mechanisms leading to their massive release of energy are qualitatively similar. It has also been reported that the rotation of sunspots greatly affects the productivity of flares (Zhang et al. 2008, Yan et al. 2008).

More recently (Wedemeyer-Böhm et al. 2012), chromospheric swirls resembling "magnetic tornadoes" have been described as energy channels that reach the upper solar atmosphere, and it has been suggested that they would be the result of rotating magnetic structures. Although these swirls are chromospheric structures, could the supergranular vortex flows that we revealed in this thesis be their photospheric trigger? To what extent are the funnels and the vortices reshaping the Sun's magnetic field topology? Could these flow patterns originate from the deeper layers of the solar atmosphere?

In fact, we are still missing a great component of the solar plasma flows, which are the very long time and spatial scales of the flows underneath Active Regions. We have good hope that these missing blocks will be provided by the inversions of time-distance Helioseismology to derive the flows at greater depths (Gizon et al. 2010), and which can use the photospheric flows as boundary conditions, using HMI/SDO. This will provide more realistic 3D flow maps deeper below the photosphere.

More importantly, this could provide a more detailed description of the dynamics of the plasma flows over the solar disk, during the rising phase of this new solar cycle, with a significant impact on describing the Sun-Earth relationships.

6 Conclusion

In the present thesis, we have used a new tracking technique called Balltracking to derive the photospheric flow fields of the quiet Sun, using images of the granulation. This technique was applied for the first time on Hinode data, which revealed the existence of large-scale photospheric vortex flow at the junction of the supergranular boundaries. Typical dimensions are 20 to 30 Mm in diameter, with a duration of at least 30 min. In addition, we developed a similar algorithm called "Magnetic Balltracking" to track the magnetic flux at unprecedented time (~1 min) and spatial resolutions (below 1 arcsec). The algorithm is able to detect and quantify both flux emergence and flux cancellation, as well as tracking magnetic field lines in combination with magnetic field extrapolation.
With combined observations of MDI and Hinode, we analyzed 11 X-ray network flares, that are intense X-ray emission occurring within a few Mm and lasting ~15 min. These network flares release between 10 to 100 erg s^{-1} cm^{-2} in the quiet Sun. With Magnetic Balltracking, we detected and quantified the cancellation of the longitudinal magnetic flux underneath these X-ray transients, and specific patterns in the flow field were identified. The magnetic flux decreases by 10 to 40% before the X-ray transient starts. The flaring sites are located either in the funnel-shaped streamlines of the horizontal flows, or in large-scale vortices at the junction of the supergranular lanes. The transients are not observed in the absence of such patterns, which we defined as necessary-but-not-sufficient conditions to activate the network flares.
These results and the associated software have motivated future projects: the statistical studies of quiet Sun events, in both X-ray and EUV, and of more energetic processes in and around Active Regions, using Hinode and the Solar Dynamic Observatory (SDO). With the Balltracking algorithm combined with Magnetic Balltracking, we are able to provide a unique survey of the interaction between the plasma flows and the magnetic flux over nearly the whole solar disk.

A Zeeman effect and measurement of photospheric magnetic field

We briefly summarize the quantum origin of the Zeeman effect and how it affects the polarimetric signal. The equations that follow are expressed in CGS units.
First, we consider the total orbital angular momentum **L**, the total spin angular momentum **S**, and the total angular momentum **J** of a n-particles system :

$$\mathbf{L} \equiv \sum_{i=1}^{n} \mathbf{l_i} \tag{A.1}$$

$$\mathbf{S} \equiv \sum_{i=1}^{n} \mathbf{s_i} \tag{A.2}$$

$$\mathbf{J} \equiv \mathbf{L} + \mathbf{S} \tag{A.3}$$

$\mathbf{l_i}$, $\mathbf{s_i}$ are the individual orbital angular momentum and the spin angular momentum of the i^{th} particule. The eigenvalues of the these operators acting on the quantum state $|lsjm_j\rangle$ are defined by :

$$\begin{aligned} \mathbf{L}^2|lsjm_j\rangle &= \hbar^2\, l(l+1)\, |lsjm_j\rangle \\ \mathbf{S}^2|lsjm_j\rangle &= \hbar^2\, s(s+1)\, |lsjm_j\rangle \\ \mathbf{J}^2|lsjm_j\rangle &= \hbar^2\, j(j+1)\, |lsjm_j\rangle \\ \mathbf{J}_z|lsjm_j\rangle &= \hbar\, m_j\, |lsjm_j\rangle \end{aligned} \tag{A.4}$$

The Hamiltonian **H** of the system is:

$$\mathbf{H} \equiv \mathbf{H_0} + \mathbf{H_B} \tag{A.5}$$

where H_0 is the Hamiltonian in the absence of external magnetic field, and acting on the quantum state $|lsjm_j\rangle$

$$\mathbf{H_0}|lsjm_j\rangle = E_j|lsjm_j\rangle \tag{A.6}$$

H_B is the magnetic Hamiltonian due to an external magnetic field **B**.

$$\mathbf{H_B} = \mu \cdot \mathbf{B} \tag{A.7}$$

where the terms in B^2 are neglected, thus restricting the development to weak field, which is accurate enough for the quiet Sun. μ is defined as the intrinsic magnetic moment of the atom:

$$\mu = \mu_0(\mathbf{J} + \mathbf{S}) \tag{A.8}$$

with $\mu_0 = \frac{h\nu_L}{B}$, and $\nu_l \equiv \frac{e_0 B}{4\pi m_e c}$ the larmor frequency, with m_e the mass of the electron, c the speed of light in vacuum, and e_0 the charge of the electron.

We can express $\mathbf{J}+\mathbf{S}$ in terms of $\mathbf{J}^2$, $\mathbf{S}^2$ and $\mathbf{L}^2$:

$$\mathbf{J}+\mathbf{S} = \frac{(\mathbf{J}+\mathbf{S})\cdot\mathbf{J}}{\mathbf{J}^2}\,\mathbf{J} \tag{A.9}$$

From the definition (A.3) of $\mathbf{J}$, to the square , we have $\mathbf{S}\cdot\mathbf{J} = \frac{1}{2}(\mathbf{J}^2+\mathbf{S}^2-\mathbf{L}^2)$ from which we obtain a practical definition of μ :

$$\mu = \mu_0(3/2 + \frac{\mathbf{J}^2+\mathbf{S}^2-\mathbf{L}^2}{\mathbf{J}^2})\,\mathbf{J}\cdot\mathbf{B} \tag{A.10}$$

If we conveniently arrange the axis so the z-axis is in the direction of $\mathbf{B}$, and using equation A.4, the diagonal elements of the magnetic Hamiltonian give :

$$\langle lsjm_j|\mathbf{H_B}|lsjm_j\rangle = m_j\mu_0 gB \tag{A.11}$$

where we introduced the Landé factor $g = \frac{3}{2} + \frac{s(s+1)-l(l+1)}{2j(j+1)}$, for$j \neq 0$.

In weak field approximation, the non-diagonal terms of the hamiltonian are negligible with respect to the diagonal terms. We finally obtain the eigenvalues for $\mathbf{H}$:

$$\langle lsjm_j|\mathbf{H_0}+\mathbf{H_B})|lsjm_j\rangle = (E_j + m_j g\mu_0 B) \tag{A.12}$$

There is a separation of the level of energy E_j in $2j+1$ degenerated components, as illustrated in figure A.1. Each new energy level depends on both j and m_j. Quantum selection rules are such that the difference between the quantum number of the upper level j_u and the lower level j_l obeys $\Delta j = 0, \pm 1$, and the atomic transition such that $j_u = j_l = 0$ is not allowed. The difference in wavelength of the new atomic transitions is also changed. If we define m_{ju}, g_u and m_{jl},g_l, as the quantum numbers m_j and the Landé factor for the upper and lower energy level of the transition, we have :

$$\begin{aligned} \Delta\lambda &= (m_{jl}g_l - m_{ju}g_u)\,\lambda_B \\ \lambda_B &\equiv \frac{\lambda_0^2 e_0}{4\pi m_e c^2}B \end{aligned} \tag{A.13}$$

λ_B is called the Zeeman wavelength splitting. When the total spin $s = 0$, the Landé factor equals to unity, and $m_{jl} - m_{ju} = 1$ which gives $\Delta\lambda = \lambda_B$. The splitting is referred as the "normal" Zeeman triplet for historical reasons. All the other cases are called "anomalous" splitting. λ_B also defines the unity in the Lorentz units of Zeeman splitting.

Equation A.13 shows that by measuring the Zeeman splitting, one can infer the strength of the magnetic field.

In the solar atmosphere, the spectral lines are broadened due to Doppler shifts and collisions, such that the splitting can only be inferred with polarimetric measurements of the Stokes parameters I, V. We define the angles (θ, ϕ) where θ is the inclination angle of $\mathbf{B}$ with respect to the line-of-sight, and ϕ the azimuth angle. In this geometry, the triplet consists of three different states of polarization:

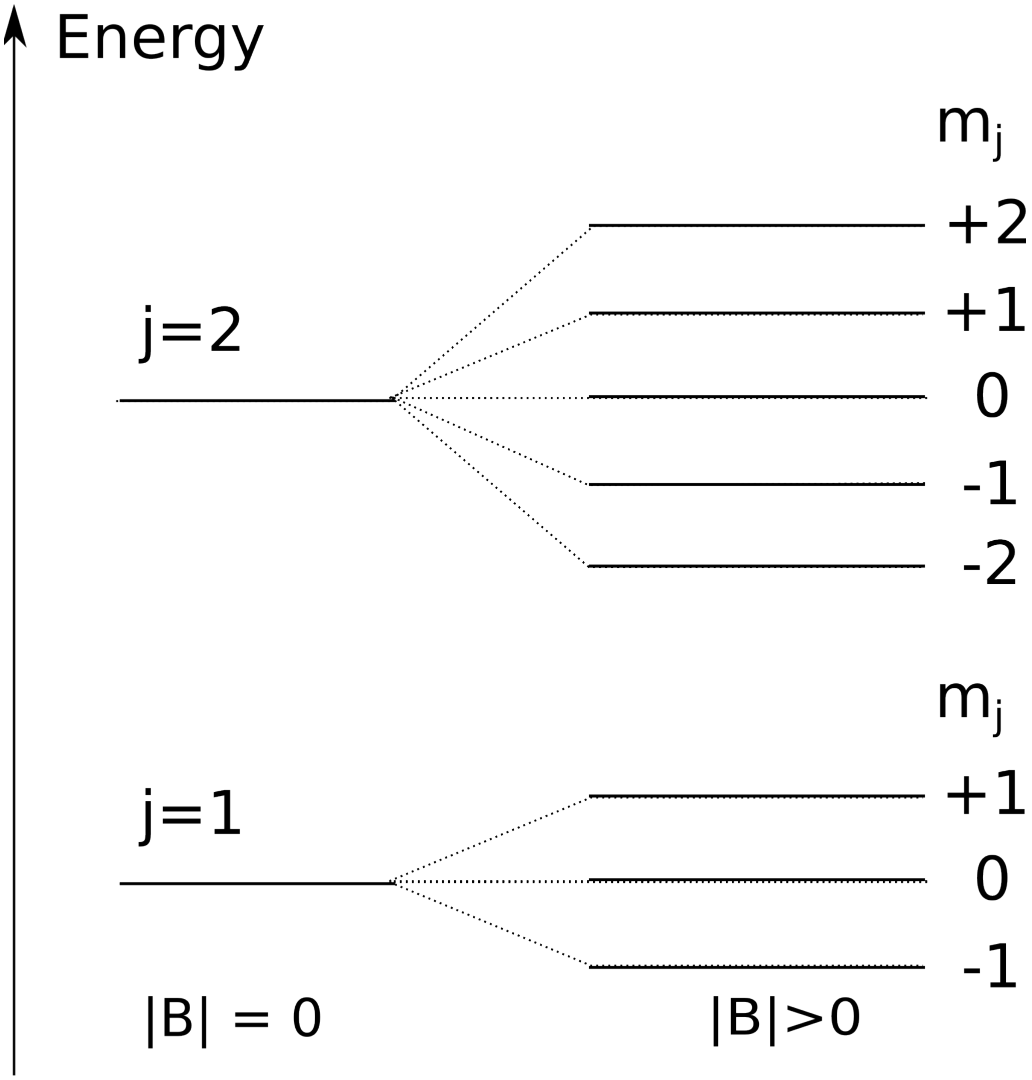

Figure A.1: *Splitting of the unperturbed energy level (no magnetic field, left) for the quantum number j, into 2j+1 degenerated components due to the magnetic field (right).*

- The π component, unshifted, and linearly polarized along the direction of **B**. It partly bears the transverse field through Stokes Q and U where $Q \propto B^2 sin2\theta \cos 2\phi$ and $U \propto B^2 \sin 2\theta \sin 2\phi$. As we do not dispose of such measurements for the present study, it is not discussed further.
- The two σ components, shifted, can be elliptically or even linearly polarized and are also present in transverse effect.

A common technique to infer the Zeeman splitting is called the Center-of-Gravity method (COG), and consists in computing the residual intensity profile from spectro-polarimetric data. Further details can be found for recent instrumentation like Hinode in Chae et al. (2007), while details on the general technique can be found in Rees and Semel (1979) and the references therein.

B Object-oriented implementation of the Balltracking algorithms

The Balltracking algorithm was originally programmed in Matlab for MDI, and for very specific purposes. In addition, the constant interaction of the input data and the results, their visualization, along with their interpretation, as well as inherent debugging, prevented the code from being implemented in low-level programming language like C or Fortran.

In our implementation, however, the main algorithm was written in C and Fortran, and interfaced with Matlab using MEX functions so we can easily interact with it using high-level programming, while keeping the low-level efficiency of Fortran and C. The original code could only be used by users experienced with Matlab programming. Therefore, the code needed to be completely reviewed for our purposes, and we chose to implement the code so that everyone could use it. The advantage of using Matlab with respect to using IDL is that it is highly object-oriented. Thus it is intrinsically programmed to ease the design and programming of GUIs (Graphical User Interfaces). All the algorithm used in this thesis has a GUI that any user is free to use, without any knowledge of Matlab programming. The output of the algorithms are made cross-platform, and are in forms of fits files essentially using the CFITSIO library, so it can also be used in IDL, or any other software recognizing fits files.

B.1 GUI for Balltracking

Figure B.1 is a snapshot of the user-friendly GUI for using Balltracking. Different modules are present and are used for quick look on hydrodynamic-related analyzes of the flow maps (divergence, curl, streamlines, etc...), although they can be ignored by the user who only wishes to restrict to the Balltracking part. In the figure, each entry of the interface has a legend which shows what they do in the algorithm. Most of the functionalities and parameters visible on the interface were detailed in the first chapter. Usage of the basic functionalities of the interface is meant to be intuitive provided that the basic principles of Balltracking are known. For example, to perform only the Balltracking part, and output the averaged flows, one would only focus on the panel "pre-processing" and "Smoothing parameters" of this GUI. Note that Balltracking itself is done before any averaging, which gives the flexibility to compute the flow maps at several scales, with only one run of Balltracking. Mandatory inputs are the information regarding the path and names of the data, the geometric parameters of the balls, and the averaging parameters of the flow maps.

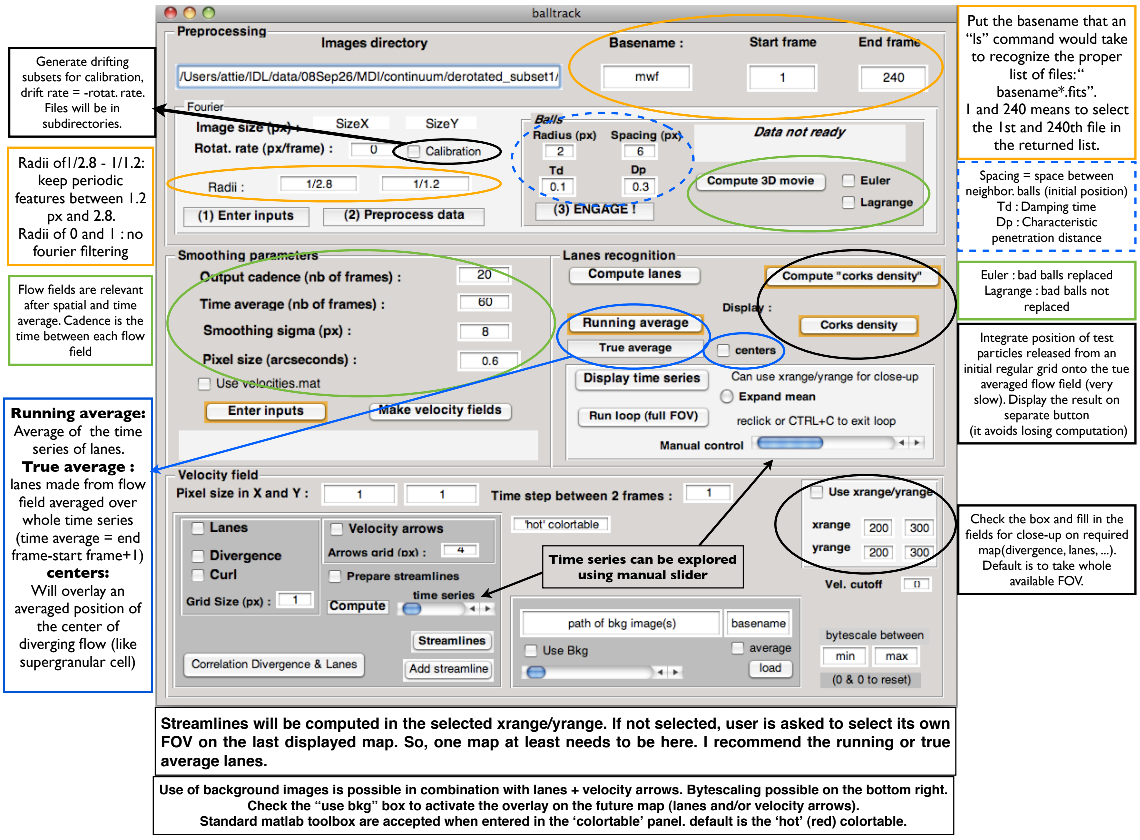

balltrack

Preprocessing

Images directory: /Users/attie/IDL/data/08Sep26/MDI/continuum/derotated_subset1/

Basename : mwf

Start frame: 1

End frame: 240

Fourier

Image size (px) : SizeX SizeY

Rotat. rate (px/frame) : 0 ☐ Calibration

Radii : 1/2.8 1/1.2

Balls

Radius (px): 2

Spacing (px): 6

Td: 0.1

Dp: 0.3

Data not ready

☐ Euler

☐ Lagrange

Smoothing parameters

Output cadence (nb of frames) : 20

Time average (nb of frames) : 60

Smoothing sigma (px) : 8

Pixel size (arcseconds) : 0.6

☐ Use velocities.mat

Lanes recognition

Display :

☐ centers

Can use xrange/yrange for close-up

○ Expand mean

reclick or CTRL+C to exit loop

Velocity field

Pixel size in X and Y : 1 1

Time step between 2 frames : 1

'hot' colortable

☐ Lanes

☐ Divergence

☐ Curl

Grid Size (px) : 1

☐ Velocity arrows

Arrows grid (px) : 4

☐ Prepare streamlines

☐ Use xrange/yrange

xrange 200 300

yrange 200 300

Vel. cutoff 0

☐ Use Bkg

☐ average

bytescale between min max

(0 & 0 to reset)

Generate drifting subsets for calibration, drift rate = -rotat. rate. Files will be in subdirectories.

Radii of1/2.8 - 1/1.2: keep periodic features between 1.2 px and 2.8. Radii of 0 and 1 : no fourier filtering

Flow fields are relevant after spatial and time average. Cadence is the time between each flow field

Running average: Average of the time series of lanes. **True average :** lanes made from flow field averaged over whole time series (time average = end frame-start frame+1) **centers:** Will overlay an averaged position of the center of diverging flow (like supergranular cell)

Put the basename that an "ls" command would take to recognize the proper list of files:" basename*.fits". 1 and 240 means to select the 1st and 240th file in the returned list.

Spacing = space between neighbor. balls (initial position) Td : Damping time Dp : Characteristic penetration distance

Euler : bad balls replaced Lagrange : bad balls not replaced

Integrate position of test particles released from an initial regular grid onto the tue averaged flow field (very slow). Display the result on separate button (it avoids losing computation)

Check the box and fill in the fields for close-up on required map(divergence, lanes, ...). Default is to take whole available FOV.

Time series can be explored using manual slider

Streamlines will be computed in the selected xrange/yrange. If not selected, user is asked to select its own FOV on the last displayed map. So, one map at least needs to be here. I recommend the running or true average lanes.

Use of background images is possible in combination with lanes + velocity arrows. Bytescaling possible on the bottom right. Check the "use bkg" box to activate the overlay on the future map (lanes and/or velocity arrows). Standard matlab toolbox are accepted when entered in the 'colortable' panel. default is the 'hot' (red) colortable.

Figure B.1: *Graphical User Interface (GUI) for user-specific science studies with Balltracking. The GUI is programmed with Matlab, but its usage does not require any knowledge of the Matlab language*

The job is started by clicking on the button "Make velocities fields". When it finishes, the user is notified and the fits files are exported in subdirectories of the images' directory. To compute the supergranular lanes on the previous output (the fits files of the flow map), one simply computes the lanes in the panel "Lanes recognition". The results can be visualized as averaged maps, or by looking at the time series of the individual maps. We remind that each individual map is an average on at least 30-min of tracking. Once again, here, the images of the lanes are made as FITS files.

B.2 GUI for Magnetic Balltracking

B.2.1 module of Magnetic Balltracking and region-growing algorithm

Figure B.2 is the graphical interface of Magnetic Balltracking. It also contains the module of the region-growing algorithm in the bottom. The upper panel has many parameters in common with the previous interface of the normal Balltracking. However, here, the user can perform different case studies on different FOVs within the same magnetogram.

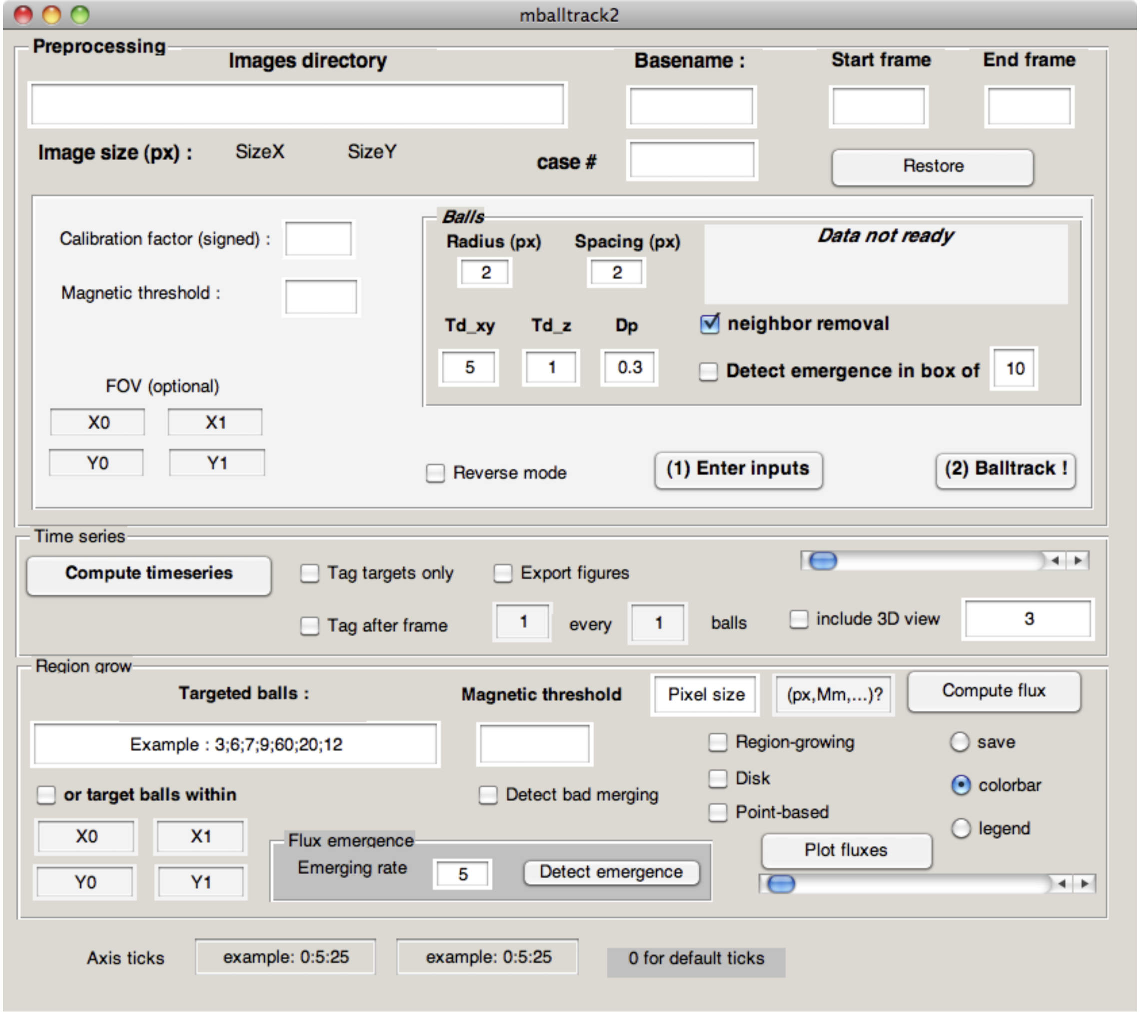
mballtrack2

Data not ready

Radius (px): 2

Spacing (px): 2

Td_xy: 5

Td_z: 1

Dp: 0.3

☑ neighbor removal

☐ Detect emergence in box of 10

☐ Reverse mode

☐ Tag targets only

☐ Export figures

☐ Tag after frame 1 every 1 balls

☐ include 3D view 3

Targeted balls : Example : 3;6;7;9;60;20;12

☐ or target balls within

☐ Detect bad merging

☐ Region-growing

☐ Disk

☐ Point-based

○ save

● colorbar

○ legend

Emerging rate 5

Axis ticks example: 0:5:25 example: 0:5:25 0 for default ticks

Figure B.2: Graphical User Interface (GUI) for Magnetic Balltracking.

B.2.2 Module for field-lines tracking

To track magnetic field-lines like in figure 2.28, one uses the interface of figure B.3 right after the module of Magnetic Balltracking. The field lines are drawn from a user-supplied 3D arrays defining the magnetic field vector in the solar atmosphere. If such an array is not (yet) available, we have embedded the analytical solution of the Linear-Force-Free Extrapolation (LFFE) from Seehafer (1978) combined with a 4^{th} order Runge-Kutta integration of the equation of field-lines:

$$\frac{\partial \mathbf{r}}{\partial \tau} = \mathbf{B}$$

The foot-points of the lines are directly taken from the output of the previous interface B.2. From the latter, the "targeted balls", tagged with a unique number, can define a more customized subset of foot-points although we tend to avoid this, as the algorithm aims at reducing the arbitrary choice of field lines to draw. The panel on the right is only here to display co-spatial observations at different layers of the atmosphere (X-ray, EUV, etc...) to relate the magnetic field lines with emission in X-ray, EUV, etc... like it is performed

Figure B.3: *Graphical User Interface (GUI) for the field-line tracking.*

throughout this thesis. Again, this module is only here to give the user some confidence on the quality of the output. Bad data in the input may give incorrect extrapolated field lines, and this can be corrected early enough with these little modules.

B.2.3 Computing power

One could argue that computing a lot of field lines in a 3D vector field in Matlab or IDL could be time consuming. However, the equation of the field-lines are independent of each other. This is used to parallelize their computation, which significantly improves the processing time in multi-cpu architecture. Furthermore, using GPU (Graphics Processing Unit) parallel computation in addition to CPU parallel computation, the processing can be even faster. This is why we experimented on six identical GPUs (generation of year 2006-2007) to assemble an experimental GPU cluster in our institute. With this, we managed to speed up by more than 40 times the processing of 3D magnetic field vectors from MDI/SoHO magnetograms and NFI/Hinode magnetograms, using the embedded solution of LFFE (including potential field extrapolation, $\alpha = 0$). Current technology of GPUs has significantly improved in the last four years and speed-up of at least 2 orders of magnitudes are expected. Figure B.4 shows the speed-up of GPU computation against pure CPU computation, at increasing size of the 3D box. The speed up goes up to 43 when the height $NZ = 192$ px. The GPU cards were too old to compute a bigger box. However, this was enough for our study, and it made our interface even more suitable for systematically printing out quick visualizations of the results.

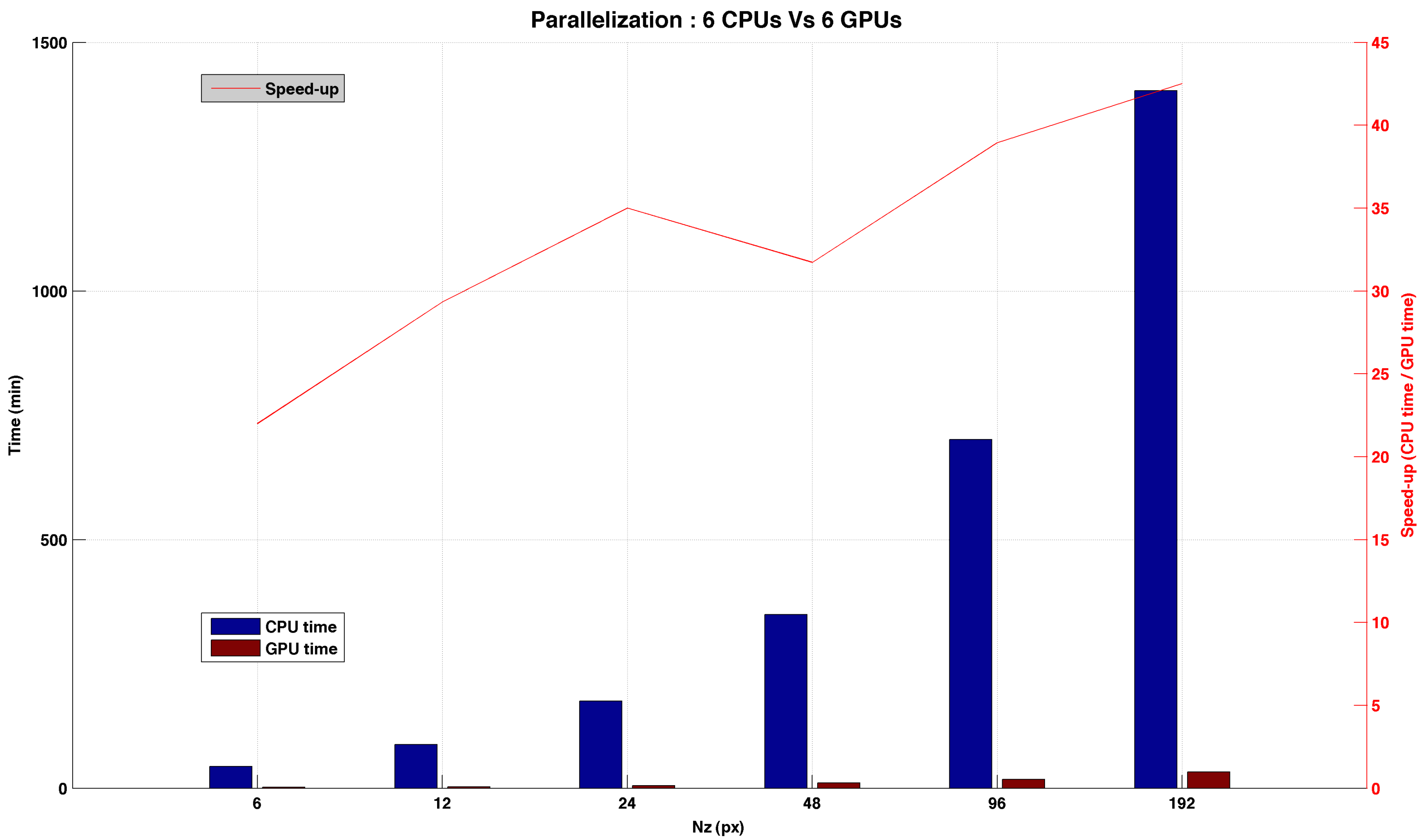

Figure B.4: *Benchmark of LFFE on MDI magnetograms* $(1000 \times 500\,\mathrm{px}^2)$*. The left bars are the processing time when using 6 CPUs, the right bars are the processing time when using 6 GPUs, as a function of the length of the* 3^{rd} *dimension (NZ) of the computation box* $(NX = 1000\,\mathrm{px},\ NY = 500\,\mathrm{px})$.

Bibliography

Amari, T., Luciani, J. F., Mikic, Z., Linker, J., 2000, A Twisted Flux Rope Model for Coronal Mass Ejections and Two-Ribbon Flares, ApJ, 529, 49

Amari, T., Luciani, J. F., Aly, J. J., Mikic, Z., Linker, J., 2003, Coronal Mass Ejection: Initiation, Magnetic Helicity, and Flux Ropes. I. Boundary Motion-driven Evolution, ApJ, 585, 1073–1086

Amari, T., Aly, J., Mikic, Z., Linker, J., 2010, Coronal Mass Ejection Initiation: On the Nature of the Flux Cancellation Model, ApJ Lett., 717, 26–30

Aschwanden, M. J., 2004, Physics of the Solar Corona. An Introduction, Praxis Publishing Ltd

Attie, R., Innes, D. E., Potts, H. E., 2009, Evidence of photospheric vortex flows at supergranular junctions observed by FG/SOT (Hinode), A&A, 493, L13–L16

Berger, T. E., Löfdahl, M. G., Shine, R. A., Title, A. M., 1998, Measurements of Solar Magnetic Element Dispersal, ApJ, 506, 439–449

Bevington, P., 1969, Data reduction and error analysis for the physical sciences, McGraw-Hill

Bonet, J. A., Márquez, I., Sánchez Almeida, J., Cabello, I., Domingo, V., 2008, Convectively Driven Vortex Flows in the Sun, ApJ Lett., 687, L131–L134

Bonet, J. A., Márquez, I., Sánchez Almeida, J., Palacios, J., Martínez Pillet, V., Solanki, S. K., del Toro Iniesta, J. C., Domingo, V., Berkefeld, T., Schmidt, W., Gandorfer, A., Barthol, P., Knölker, M., 2010, Sunrise/imax observations of convectively driven vortex flows in the sun, ApJ Lett., 723, L139–L143

Brandt, P. N., Scharmer, G. B., Ferguson, S., Shine, R. A., Tarbell, T. D., 1988, Vortex flow in the solar photosphere, Nat, 335, 238

Chae, J., Moon, Y., Park, Y., Ichimoto, K., Sakurai, T., Suematsu, Y., Tsuneta, S., Katsukawa, Y., Shimizu, T., Shine, R. A., Tarbell, T. D., Title, A. M., Lites, B., Kubo, M., Nagata, S., Yokoyama, T., 2007, Initial Results on Line-of-Sight Field Calibrations of SP/NFI Data Taken by SOT/Hinode, PASJ, 59, 619–624

Condon, E. U., Shortley, G. H., 1963, The theory of atomic spectra, Cambridge University Press del Toro Iniesta, J. C., 2003, Introduction to Spectropolarimetry, Cambridge University Press

Delaboudinière, J., Artzner, G. E., Brunaud, J., Gabriel, A. H., Hochedez, J. F., Millier, F., Song, X. Y., Au, B., Dere, K. P., Howard, R. A., Kreplin, R., Michels, D. J., Moses, J. D., Defise, J. M., Jamar, C., Rochus, P., Chauvineau, J. P., Marioge, J. P., Catura, R. C., Lemen, J. R., Shing, L., Stern, R. A., Gurman, J. B., Neupert, W. M., Maucherat, A., Clette, F., Cugnon, P., van Dessel, E. L., 1995, EIT: Extreme-Ultraviolet Imaging Telescope for the SOHO Mission, Sol. Phys., 162, 291–312

Démoulin, P., Berger, M. A., 2003, Magnetic Energy and Helicity Fluxes at the Photospheric Level, Sol. Phys., 215, 203–215

Dere, K. P., Landi, E., Mason, H. E., Monsignori Fossi, B. C., Young, P. R., 1997, CHIANTI - an atomic database for emission lines, aas, 125, 149–173

Dere, K. P., Landi, E., Young, P. R., Del Zanna, G., Landini, M., Mason, H. E., 2009, CHIANTI - an atomic database for emission lines. IX. Ionization rates, recombination rates, ionization equilibria for the elements hydrogen through zinc and updated atomic data, A&A, 498, 915–929

Emonet, T., Cattaneo, F., 2001, Small-scale photospheric fields: Observational evidence and numerical simulations, ApJ Lett., 560, L197–L200

Evans, J. W., Catalano, C. P., 1972, Observed Oddities in the Lines H, K, b and Hβ, Sol. Phys., 27, 299–302

Fletcher, L., López Fuentes, M. C., Mandrini, C. H., Schmieder, B., Démoulin, P., Mason, H. E., Young, P. R., Nitta, N., 2001, A Relationship Between Transition Region Brightenings, Abundances, and Magnetic Topology, Sol. Phys., 203, 255–287

Galsgaard, K., Nordlund, Å., 1996, Heating and activity of the solar corona 1. Boundary shearing of an initially homogeneous magnetic field, J. Geophys. Res., 101, 13 445–13 460

Galsgaard, K., Parnell, C. E., 2005, Elementary heating events - magnetic interactions between two flux sources. III. Energy considerations, A&A, 439, 335–349

Galsgaard, K., Parnell, C. E., Blaizot, J., 2000, Elementary heating events - Magnetic interactions between two flux sources, A&A, 362, 395–405

Gierasch, P. J., 1985, On the energetics of the solar supergranulation, ApJ, 288, 795–800

Gizon, L., Duvall, T. L., Schou, J., 2003, erratum: Wave-like properties of solar supergranulation, Nat, 421, 764

Gizon, L., Birch, A. C., Spruit, H. C., 2010, Local Helioseismology: Three Dimensional Imaging of the Solar Interior, ARA&A, 48, 289–338

Golub, L., Deluca, E., Austin, G., Bookbinder, J., Caldwell, D., Cheimets, P., Cirtain, J., Cosmo, M., Reid, P., Sette, A., Weber, M., Sakao, T., Kano, R., Shibasaki, K., Hara, H., Tsuneta, S., Kumagai, K., Tamura, T., Shimojo, M., McCracken, J., Carpenter, J., Haight, H., Siler, R., Wright, E., Tucker, J., Rutledge, H., Barbera, M., Peres, G., Varisco, S., 2007, The X-Ray Telescope (XRT) for the Hinode Mission, Sol. Phys., 243, 63

Gonzalez, R., Woods, R., 2008, Digital Image Processing, Pearson/Prentice Hall, 3rd edition edn., ISBN 9780131687288

Howard, R. F., Harvey, J. W., Forgach, S., 1990, Solar surface velocity fields determined from small magnetic features, Sol. Phys., 130, 295–311

Innes, D. E., Teriaca, L., 2013, Quiet sun explosive events: Jets, splashes, and eruptions, Sol. Phys., 282, 453–469

Innes, D. E., Genetelli, A., Attie, R., Potts, H. E., 2009, Quiet Sun mini-coronal mass ejections activated by supergranular flows, A&A, 495, 319–323

Krucker, S., Benz, A. O., Bastian, T. S., Acton, L. W., 1997, X-Ray Network Flares of the Quiet Sun, ApJ, 488, 499–505

Leenaarts, J., Wedemeyer-Böhm, S., 2005, DOT tomography of the solar atmosphere. III. Observations and simulations of reversed granulation, A&A, 431, 687–692

Leighton, R. B., Noyes, R. W., Simon, G. W., 1962, Velocity Fields in the Solar Atmosphere. I. Preliminary Report., ApJ, 135, 474–499

Machado, M. E., Moore, R. L., Hernandez, A. M., Rovira, M. G., Hagyard, M. J., Smith, J. B., 1988, The observed characteristics of flare energy release. I - Magnetic structure at the energy release site, ApJ, 326, 425–450

Metcalf, T. R., Jiao, L., McClymont, A. N., Canfield, R. C., Uitenbroek, H., 1995, Is the solar chromospheric magnetic field force-free?, ApJ, 439, 474–481

Moore, R. L., Falconer, D. A., Porter, J. G., Suess, S. T., 1999, On Heating the Sun's Corona by Magnetic Explosions: Feasibility in Active Regions and Prospects for Quiet Regions and Coronal Holes, ApJ, 526, 505–522

November, L. J., Simon, G. W., 1988, Precise proper-motion measurement of solar granulation, ApJ, 333, 427–442

November, L. J., Toomre, J., Gebbie, K. B., Simon, G. W., 1981, The detection of mesogranulation on the sun, ApJ Lett., 245, L123–L126

Parnell, C. E., Deforest, C. E., Hagenaar, H. J., Lamb, D. A., Welsch, B. T., 2008, Quiet-Sun: A Comparison of MDI and SOT Fluxes, in First Results From Hinode, (Eds.) S. A. Matthews, J. M. Davis, L. K. Harra, vol. 397 of Astronomical Society of the Pacific Conference Series, pp. 31–34

Pietarila Graham, J., Danilovic, S., Schuessler, M., 2009, Turbulent magnetic fields in the quiet Sun: implications of Hinode observations and small-scale dynamo simulations, ApJ, 693, 1728–1735

Potts, H. E., Diver, D. A., 2008a, Automatic Recognition and Characterisation of Supergranular Cells from Photospheric Velocity Fields, Sol. Phys., 248, 263–275

Potts, H. E., Diver, D. A., 2008b, Post-hoc derivation of SOHO Michelson doppler imager flat fields, A&A, 492, 863–871

Potts, H. E., Barrett, R. K., Diver, D. A., 2004, Balltracking: An highly efficient method for tracking flow fields, A&A, 424, 253–262

Priest, E. R., Parnell, C. E., Martin, S. F., 1994, A converging flux model of an X-ray bright point and an associated canceling magnetic feature, ApJ, 427, 459

Rast, M. P., 1995, On the nature of 'exploding' granules and granule fragmentation, ApJ, 443, 863–868

Rast, M. P., 2003, The Scales of Granulation, Mesogranulation, and Supergranulation, ApJ, 597, 1200–1210

Rees, D. E., Semel, M. D., 1979, Line formation in an unresolved magnetic element - A test of the centre of gravity method, A&A, 74, 1–5

Rieutord, M., Rincon, F., 2010, The Sun's Supergranulation, Living Reviews in Solar Physics, 7, 2

Rieutord, M., Roudier, T., Malherbe, J. M., Rincon, F., 2000, On mesogranulation, network formation and supergranulation, A&A, 357, 1063–1072

Rieutord, M., Roudier, T., Ludwig, H.-G., Nordlund, Å., Stein, R., 2001, Are granules good tracers of solar surface velocity fields?, A&A, 377, L14–L17

Roudier, T., Rieutord, M., Malherbe, J. M., Vigneau, J., 1999, Determination of horizontal velocity fields at the sun's surface with high spatial and temporal resolution, A&A, 349, 301–311

Rutten, R. J., de Wijn, A. G., Sütterlin, P., 2004, DOT tomography of the solar atmosphere. II. Reversed granulation in Ca II H, A&A, 416, 333–340

Scherrer, P. H., Bogart, R. S., Bush, R. I., Hoeksema, J. T., Kosovichev, A. G., Schou, J., Rosenberg, W., Springer, L., Tarbell, T. D., Title, A., Wolfson, C. J., Zayer, I., MDI Engineering Team, 1995, The solar oscillations investigation - michelson doppler imager, Sol. Phys., 162, 129–188

Schrijver, C. J., van Ballegooijen, A. A., 2005, Is the Quiet-Sun Corona a Quasi-steady, Force-free Environment?, ApJ, 630, 552–560

Seehafer, N., 1978, Determination of constant alpha force-free solar magnetic fields from magnetograph data, Sol. Phys., 58, 215–223

Simon, G. W., Leighton, R. B., 1964, Velocity Fields in the Solar Atmosphere. III. Large-Scale Motions, the Chromospheric Network, and Magnetic Fields., ApJ, 140, 1120–1147

Simon, G. W., Weiss, N. O., 1968, Supergranules and the Hydrogen Convection Zone, zap, 69, 435–450

Solanki, S. K., 1993, Small-scale Solar Magnetic Fields - an Overview, Space Sci. Rev., 63, 1–188

Stein, R. F., Nordlund, A., 1989, Topology of convection beneath the solar surface, ApJ Lett., 342, L95–L98

Stenflo, J. O., Keller, C. U., Gandorfer, A., 1998, Differential hanle effect and the spatial variation of turbulent magnetic fields on the sun, A&A, 329, 319–328

Stix, M., 1989, The Sun. an Introduction, Springer Berlin Heidelberg

Suemoto, Z., Hiei, E., Nakagomi, Y., 1987, Bright threads in the inner wing of solar CA II K line, Sol. Phys., 112, 59–66

Taylor, J. R., 1996, An Introduction to Error Analysis: The Study of Uncertainties in Physical Measurements, University Science Books

Thalmann, J. K., 2010, Evolution of coronal magnetic fields, Ph.D. thesis, T.U Braunschweig

Titov, V. S., Priest, E. R., Demoulin, P., 1993, Conditions for the appearance of ”bald patches” at the solar surface, A&A, 276, 564–570

Tsuneta, S., Ichimoto, K., Katsukawa, Y., Nagata, S., Otsubo, M., Shimizu, T., Suematsu, Y., Nakagiri, M., Noguchi, M., Tarbell, T., Title, A., Shine, R., Rosenberg, W., Hoffmann, C., Jurcevich, B., Kushner, G., Levay, M., Lites, B., Elmore, D., Matsushita, T., Kawaguchi, N., Saito, H., Mikami, I., Hill, L. D., Owens, J. K., 2008, The Solar Optical Telescope for the Hinode Mission: An Overview, Sol. Phys., 249, 167

van Ballegooijen, A. A., Martens, P. C. H., 1989, Formation and eruption of solar prominences, ApJ, 343, 971–984

van der Borght, R., 1979, Finite-amplitude convection in a compressible medium and its application to supergranulation, MNRAS, 188, 615–624

Vickers, G. T., 1971, On the Formation of Giant Cells and Supergranules, ApJ, 163, 363–374

Wang, Y., Noyes, R. W., Tarbell, T. D., Title, A. M., 1995, Vorticity and Divergence in the Solar Photosphere, ApJ, 447, 419

Wedemeyer-Böhm, S., Scullion, E., Steiner, O., Rouppe van der Voort, L., de La Cruz Rodriguez, J., Fedun, V., Erdélyi, R., 2012, Magnetic tornadoes as energy channels into the solar corona, Nat, 484, 505–508

Welsch, B. T., Longcope, D. W., 2003, Magnetic Helicity Injection by Horizontal Flows in the Quiet Sun. I. Mutual-Helicity Flux, ApJ, 588, 620–629

Welsch, B. T., Fisher, G. H., Abbett, W. P., Regnier, S., 2004, ILCT: Recovering Photospheric Velocities from Magnetograms by Combining the Induction Equation with Local Correlation Tracking, ApJ, 610, 1148–1156

Wiegelmann, T., Inhester, B., Lagg, A., Solanki, S. K., 2005a, How To Use Magnetic Field Information For Coronal Loop Identification, Sol. Phys., 228, 67–78

Wiegelmann, T., Lagg, A., Solanki, S. K., Inhester, B., Woch, J., 2005b, Comparing magnetic field extrapolations with measurements of magnetic loops, A&A, 433, 701–705

Withbroe, G. L., Noyes, R. W., 1977, Mass and energy flow in the solar chromosphere and corona, ARA&A, 15, 363–387

Yan, X., Qu, Z., Kong, D., 2008, Relationship between rotating sunspots and flare productivity, MNRAS, 391, 1887–1892

Zhang, Y., Liu, J., Zhang, H., 2008, Relationship between Rotating Sunspots and Flares, Sol. Phys., 247, 39–52

Zirker, J. B., 1993, Photospheric vortices and coronal heating, Sol. Phys., 147, 47–53

Acknowledgements

I would like to thank the Max-Planck-Institut für Sonnensystemforschung and the International Max Planck Research School (IMPRS) in Katlenburg-Lindau for providing the environment and the fundings which made this thesis possible.

My thanks go particularly to Dr. Davina Innes for her continuous guidance throughout this entire Ph.D thesis. Without your patience, your constant support and understanding every step of the way, this work would not have been possible. I also thank Prof. Dr. Sami Solanki for supporting my thesis, and for giving a more sensible perspective to my work when it was needed.

I am grateful to Dr. Thomas Wiegelmann and my colleague Dr. Julia Thalmann for helping me with many important scientific, and technical aspects in this thesis. Thanks also to Prof. Dr. Laurent Gizon for the support, as well as the helpful and friendly discussions within his research team. I am very thankful to Borut Podlipnik for the technical help on computer issues. The friendly coffee breaks in your office meant a lot to me.

Many thanks to Prof. Dr. Karl-Heinz Glaßmeier and Dr. Sonja Schuh who have been really helpful, particularly at the end of this journey.

I would also like to express my most sincere and deepest gratitude to Dr. Dieter Schmitt. Your wisdom and your kindness will always be in my heart.

Finally I am eternally grateful to my beloved family, whose continuous support, despite the distance, has always driven my will. You have been supportive despite the toughest moments you had to face. Your unbowed strength has inspired me in carrying out this endeavor, which I dedicate to you all.

CURRICULUM VITAE: RAPHAEL ATTIE

Born in Bayonne (France), 1983

WORK EXPERIENCE

2011–current Physics teacher, Spesup — Lille, France

Spesup (France)

Teaching physics to undergraduate students.

Jan–Mar 2011 Research assistant, University of Glasgow

University of Glasgow (UK)

Data analyses from satellite observations of the solar magnetic field.

Oct-Dec 2010 IT specialist, Max-Planck-Institute for Solar System Research — Germany

Max-Planck-Institute for Solar System Research (Germany)

Automation of data analyses for the Solar Dynamic Observatory (SDO).

2007 - 2010 Ph.D student, Max-Planck-Institute for Solar System Research — Germany

Max-Planck-Institute for Solar System Research (Germany)

Research on the evolution of solar photospheric flow fields and magnetic field. Analyses of observations using space telescopes (SoHO, SDO, Hinode), using satellite imaging, spectroscopy and spectro-polarimetry.

Summer 2005 Summer Intern, Space Sciences Laboratory (SSL) — Berkeley

Space Sciences Laboratory (Berkeley)

Data analyses of *in situ* measurements of the Earth magnetosphere from the Cluster satellites.

EDUCATION

2007-2010 Ph.D student at the International Max Planck Research School, Katlenburg-Lindau, Germany

Thesis: *The relationship between supergranulations flows, magnetic field evolution and network flares*
Supervisor: Pr. Dr. Sami Solanki

2006 Master of Science (astrophysics) at Université Paul Sabatier, Toulouse, France

Thesis: *Analysis of Cluster data of energetic events in the foreshock of the Earth magnetosphere.*
Hosted by the Centre d'Etude Spatiale des Rayonnements (CESR) in Toulouse.
Supervisor: Dr. Christian Mazelle

2004 Bachelor's degree (physics) at Université Paul Sabatier, Toulouse, France

Degree on fundamental physics at the Université Paul Sabatier in Toulouse.

2008	Attie, R., Innes, D., 2008, Explosive Event in the Quiet Sun Seen by XRT-EIS and SUMER, in First Results From Hinode, (Eds.) S. A. Matthews, J. M. Davis, L. K. Harra, vol. 397 of Astronomical Society of the Pacific Conference Series, pp. 155
2008	Innes, D. E., Attie, R., Hara, H., Madjarska, M. S., 2008, EIS/ Hinode Observations of Doppler Flow Seen through the 40 arcsec Wide-Slit, Sol. Phys., 252, 283-292
2009	Attie, R., Innes, D. E., Potts, H. E., 2009, Evidence of photospheric vortex flows at super- granular junctions observed by FG/SOT (Hinode), A&A, 493, L13-L16
2009	Innes, D. E., Genetelli, A., Attie, R., Potts, H. E., 2009, Quiet Sun mini-coronal mass ejections activated by supergranular flows, A&A, 495, 319-323
2014	Attie, R., Innes, D. E., 2014, Magnetic Balltracking: tracking the photospheric magnetic flux, A&A (submitted)